Interplay of Broken Symmetries and Quantum Criticality in Correlated Electronic Systems

A dissertation presented

by

Debanjan Chowdhury

to

The Department of Physics

in partial fulfillment of the requirements

for the degree of

Doctor of Philosophy

in the subject of

Physics

Harvard University

Cambridge, Massachusetts

April 2016

Thesis advisor

Subir Sachdev

Author

Debanjan Chowdhury

Interplay of Broken Symmetries and Quantum Criticality in Correlated Electronic Systems

Abstract

This thesis delves into a study of phases of strongly correlated quantum matter confined to two spatial dimensions. The thesis can broadly be divided into three parts. In the first part, comprising of chapters 2 and 3, we investigate some interesting aspects of symmetry breaking and quantum criticality in the superconducting phase of the iron-based superconductors. In particular, motivated by tunneling microscopy measurements on FeSe, in chapter 2 we study the effect of spontaneously broken rotational symmetry on the structure of the superconducting vortex. In chapter 3, we study the critical singularities associated with the superfluid-density at a wide class of symmetry-breaking and topological phase transitions in a clean superconductor. Inspired by experiments on $BaFe_2(As_{1-x}P_x)_2$, we also analyze the effect of quenched disorder on the superfluid-density in the vicinity of magnetic quantum critical points.

The second part of this thesis, consisting of chapters 4 and 5, is devoted to a study of the *pseudogap* phase in the underdoped cuprates. In chapter 4 we study the effect of thermal fluctuations of various competing order parameters, including preformed superconductivity and short-ranged charge-density wave, on the electronic excitations. In chapter 5 we analyze the feedback of pairing fluctuations on the landscape

of various competing charge-density wave order parameters within the framework of fermi-liquid theory.

In the final part of the thesis, consisting of chapters 6 and 7, we propose an alternative picture for describing the pseudogap metal. In chapter 6, we study a *quantum-disordered* phase of matter—the fractionalized fermi-liquid (FL*)—where the electrons are coupled to the fractionalized excitations of a strongly fluctuating antiferromagnet and propose it to be a candidate state for the pseudogap. We investigate instabilities of the FL* to density-wave order and compare with experiments. In chapter 7, we describe a framework for describing a novel quantum phase transition without any broken-symmetries—a *Higgs* transition—that describes a transition from a conventional fermi-liquid to a parent phase of the FL* state via an intermediate non-fermi liquid. We discuss its possible connection to the optimal doping critical point in the cuprates.

Contents

Citations to Previously Published Work

Most of the chapters of this thesis have appeared in print elsewhere. By chapter number, they are:

- **Chapter 1**:
  Partly based on "*The Enigma of the Pseudogap Phase of the Cuprate Superconductors,*" in *Quantum criticality in condensed matter*, 50th Karpacz Winter School of Theoretical Physics, edited by J. Jedrzejewski (World Scientific, 2015), ISBN: 978-981-4704-08-3; `arXiv:1501.00002`.

- **Chapter 2**:
  "*Nematic order in the vicinity of a vortex in superconducting FeSe,*" Debanjan Chowdhury, E. Berg and Subir Sachdev, **Phys. Rev. B 84, 205113 (2011)**; `arXiv:1109.2600`

- **Chapter 3**:
  "*Singularity of the London penetration depth at quantum critical points in superconductors,*" Debanjan Chowdhury, B. Swingle, E. Berg and Subir Sachdev, **Phys. Rev. Lett. 111, 157004 (2013)**; `arXiv:1305.2918`.

  "*Phase transition beneath the superconducting dome in $BaFe_2(As_{1-x}P_x)_2$,*" Debanjan Chowdhury, J. Orenstein, S. Sachdev and T. Senthil, **Phys. Rev. B 92, 081113 (R) (2015)**; `arXiv:1502.04122`.

- **Chapter 4**:
  Partly based on "*Connecting high-field quantum oscillations to zero-field electron spectral functions in the underdoped cuprates,*" A. Allais, Debanjan Chowdhury and Subir Sachdev, **Nature Communications 5, 5771 (2014)**; `arXiv:1406.0503`.

- **Chapter 5**:
  "*Feedback of superconducting fluctuations on charge order in the underdoped cuprates,*" Debanjan Chowdhury and Subir Sachdev, **Phys. Rev. B 90, 134516 (2014)**; `arXiv:1404.6532`.

- **Chapter 6**:
  "*Density wave instabilities of fractionalized Fermi liquids,*" Debanjan Chowdhury and Subir Sachdev, **Phys. Rev. B 90, 245136 (2014)**; `arXiv:1409.5430`.

- **Chapter 7**:
  "*Higgs criticality in a two-dimensional metal,*" Debanjan Chowdhury and Subir

Sachdev, **Phys. Rev. B 91, 115123 (2015)**; `arXiv:1412.1086`.

Some additional work, which is not presented in this thesis, has appeared in:

- "*Breakdown of Fermi liquid behavior at the* $(\pi, \pi) = 2k_F$ *spin-density wave quantum critical point: the case of electron-doped cuprates,*" D. Bergeron, Debanjan Chowdhury, M. Punk, S. Sachdev and A.-M.S. Tremblay, **Phys. Rev. B 86, 155123 (2012)**; `arXiv:1207.1106`.

- "*Multipoint correlators of conformal field theories: implications for quantum critical transport,*" Debanjan Chowdhury, S. Raju, S. Sachdev, A. Singh and P. Strack, **Phys. Rev. B 87, 085138 (2013)**; `arXiv:1210.5247`.

- "*Topological excitations and the dynamic structure factor of spin liquids on the kagome lattice,*" M. Punk, Debanjan Chowdhury and S. Sachdev, **Nature Physics 10, 289-293 (2014)**; `arXiv:1308.2222`.

- "*Fluctuating charge order in the cuprates: spatial anisotropy and feedback from superconductivity,*" Y. Wang, Debanjan Chowdhury and A.V. Chubukov, **Phys. Rev. B 92, 161103(R) (2015)**; `arXiv:1508.03636`.

- "*Confinement transition to density wave order in metallic doped spin liquids*", A.A. Patel, Debanjan Chowdhury, A. Allais and S. Sachdev, **Phys. Rev. B 93, 165139 (2016)**; `arXiv:1602.05954`.

Electronic preprints (shown in `typewriter font`) are available on the Internet at the following URL:
`http://arXiv.org`

Acknowledgments

It has been almost six years since I came to Harvard and it only feels like yesterday! My journey in graduate school has been an enriching experience, with its fair share of bittersweet moments. We were told at the outset that the pursuit of a PhD is not a sprint but a marathon. A number of people have helped me reach the finish line and the least I can do now is express my gratitude towards them. Omissions, if any, are entirely unintentional!

The work reported in this thesis would not have been possible without the guidance of my advisor Professor Subir Sachdev. I consider myself to be extremely fortunate to have been his student. Subir's intuition for any given problem, combined with his extraordinary technical skills are awe-inspiring. I must thank him for igniting my interest in superconductivity and spin-liquids from early on, since it has been great fun thinking about these subjects! Subir has supported me in far too many endeavors to list here and I will remain eternally grateful to him for them. I hope that our association will continue in the future and lead to many more successful collaborations. I would also like to thank Subir and Usha for having been wonderful hosts of several get-togethers that kept us in good spirits during this arduous journey!

I thank the other members of my thesis committee: Professor Eugene Demler, Professor Amir Yacoby and Professor Philip Kim. They have always provided useful feedback during the course of my PhD. In particular, I would like to thank Eugene for teaching us three advanced quantum many-body courses during my first two years at Harvard; my training in the subject would have remained incomplete had it not been for these courses. I also thank Professor Bertrand Halperin for giving me multiple opportunities to be a teaching fellow in his courses. It has been an honor to learn

from and interact with him. I hope that I will get an opportunity to work more closely with all of them in the coming years.

I have been enormously influenced by two brilliant mentors (and "academic siblings"!), Professor Andrey Chubukov and Professor T. Senthil, and have had the extraordinary privilege of collaborating with both of them during the course of my PhD. I have known them personally for more than four years now and their research continues to inspire and guide my own research. I would like to thank them for all the useful advice that I have received from them. I hope to be able to continue collaborating with Andrey and Senthil on topics of mutual interest.

It was also great to be able to collaborate with Professor Andre-Marie Tremblay and Professor Joseph Orenstein. I was exposed for the first time to non-fermi liquid physics in quantum critical metals while collaborating with Andre-Marie. Working with Joe was a great learning experience for me — it continues to be the only time during my PhD when I analyzed real data from experiments!

One of the best things about my experience at Harvard has been the opportunity to collaborate with a group of exceptional people, which have led to some great collaborations. In this regard, I would especially like to thank two of my early mentors and friends, who helped me in my early days as a graduate student — Erez Berg and Matthias Punk. It has also been a wonderful experience to discuss various aspects of Physics (and life, in general!) with Andrea Allais, Jay Sau and Brian Swingle.

I have benefitted enormously from discussions with a number of people while attending conferences, workshops and visiting other institutions. I would especially like to acknowledge Professor Ehud Altman, Professor Seamus Davis, Professor Rafael

Fernandes, Professor Eduardo Fradkin, Professor Steven Kivelson, Professor Patrick Lee, Professor Yuji Matsuda, Professor Mohit Randeria and Professor Suchitra Sebastian for discussions and comments on my work that have greatly clarified my thinking. I would also like to thank three of my undergraduate research supervisors—Professor Michael Cross, Professor Stephan Grill and Professor Amit Dutta for introducing me to research at an early stage and motivating me to excel in life.

During the course of my time at Harvard, I have had the immense privilege of discussing and learning from a number of young colleagues. They include Dima Abanin, Johannes Bauer, Mehrtash Babadi, Andreas Eberlein, Wenbo Fu, Sarang Gopalakrishnan, Fabian Grusdt, Mo Hamidian, Yejin Huh, Liza Huijse, Janet Hung, Michael Knap, Junhyun Lee, Tony Lee, Andy Lucas, Max Metlitski, Eun-Gook Moon, Marton Kanasz-Nagy, Aavishkar Patel, Susanne Pielawa, Yang Qi, William Witczak-Krempa, Philipp Strack, Chong Wang and Liujun Zou. Some of my friends in the long and arduous journey through graduate school, who have helped me keep my sanity, include Kartiek Agarwal, Shubhayu Chatterjee, Ilya Feige, Lauren Forbes, Saloni Jain, Szilvia Kiriakov, Peter Komar and Prahar Mitra. I have also learned a great deal from my friends outside of Harvard: Tarun Grover, Tim Hsieh, Sam Lederer, Akash Maharaj, Laimei Nie, Yoni Schattner and Yuxuan Wang.

I thank Dr. Jacob Barandes and Dr. David Morin for helping me with numerous aspects of life in the Physics department. The staff at Harvard has also been an invaluable resource in times of distress. I sincerely thank Jennifer Bastin, Gerard Byrne, Lisa Cacciabaudo, Carol Davis, Sheila Ferguson, Dayle Maynard, Clare Poucha, Sarah Roberts, Marina Werbeloff and Darryl Zeigler for all their help.

My research has been funded by grants from the U.S. National Science Foundation, by a Purcell fellowship from the Physics department and by a Term-time merit fellowship from the Graduate School of Arts and Sciences at Harvard University. I also thank the hospitality of the Perimeter Institute of Theoretical Physics, Waterloo and the Max-Planck Institut für Physik Komplexer Systeme, Dresden, where I spent a considerable amount of time during the summers of 2014 and 2015.

Last, but in no way the least, I would like to thank the three most important people in my life. This thesis might not have taken its current form without their constant support and encouragement during graduate school. No amount of words are enough to express my gratitude for my parents. My father, a physicist himself, instilled in me a passion for Physics from an early age. My mother took exceptionally good care of various aspects of my life up until I left for graduate school in the U.S. They have been a source of steadfast support, unconditional love and just the right amount of criticism (whenever required!). The past eighteen months of my life have been especially amazing, thanks to Priyanka! In spite of the long geographical distance separating us and only the occasional transcontinental trips, she has been a source of constant love and support. I dedicate this thesis to all three of them.

Dedicated to my parents, Debashish and Indrani,
and my fiancé, Priyanka.

Chapter 1

Introduction

"The beginning is the most important part of the work." - *Plato*, The Republic

1.1 Preliminaries

Two of the unifying themes in the study of quantum matter are *emergence* and *universality*. Emergence corresponds to the idea that the "whole is greater than the sum of its parts", meaning that an assembly of billions of interacting electrons may display non-trivial phenomena that are fundamentally different from what one might expect from an ensemble of non-interacting electrons. Universality refers to the observation that distinct physical systems often show remarkably similar long-distance, or low-energy, properties. The physics of universal features typically requires an emergent length scale, ξ, that is significantly larger than any other microscopic length scale in the problem.

One of the most influential minds of the 20th century, Lev D. Landau, laid the

foundation stone for much of theoretical condensed matter physics by proposing two ideas that have been central to the field [141]. These include:

- An *order parameter* description of phase transitions and spontaneously broken symmetries. The critical singularities observed at phase transitions are then attributed to the long wavelength fluctuations of these order-parameter degrees of freedom. The development of renormalization group techniques [246] in the second half of the last century led to an immensely powerful 'Landau-Ginzburg-Wilson' paradigm of symmetry breaking and phase transitions.

- The concept of *quasiparticles*, where even in the presence of strong electron-electron interactions, the excitations above the ground state retain a long-lived, particle-like form. In other words, there is a notion of adiabatic continuity, where the sole effect of the interactions is to dress the original electron with a cloud of excitations, and it is this composite object that behaves as a quasi-particle. This idea formed the basis of Landau's Fermi liquid theory and has been immensely successful in describing the phenomenology of many electronic systems.

The above ideas have played an influential role in describing the physics of metals, superfluids, BCS superconductors, semiconductors etc. However, the discovery of a wide range of exotic phenomena in the past three decades, such as the fractional quantum hall effect, high-temperature superconductivity and frustrated magnetism challenge the applicability of the above ideas. We shall delve into the intricacies of many of the above unconventional phases in this thesis later. But first, let us briefly review some essential concepts related to critical phenomena and fermi-liquids.

1.1.1 Quantum Criticality

We begin by recalling certain essential features associated with *critical* systems, identified by a diverging correlation length, ξ. The standard theoretical machinery for tackling the universal aspects of this problem were developed to study the finite temperature (T) continuous phase transitions [246]. The critical singularity associated with ξ at such transitions is given by a power law of the form,

$$\xi \sim (T - T_c)^{-\nu} \tag{1.1}$$

where T_c is the critical temperature of the transition, and ν is the correlation length exponent. The specific-heat, order parameter, susceptibility, and other thermodynamic quantities also show universal power-law behavior in the vicinity of the transition with exponents that are fixed by the underlying symmetry of the problem, form of disorder etc. The well developed 'Landau-Ginzburg-Wilson paradigm' can be used to compute these exponents in a controlled fashion.

Classical phase transitions are driven by purely thermal fluctuations. In the past two decades, a lot of effort has been devoted to the study of criticality at zero temperature, where phase transitions are driven by purely quantum fluctuations; the ground state of the system undergoes a singular reorganization across such a *quantum critical point* (QCP). Moreover, the criticality is not necessarily restricted merely to a point; there are examples of entire phases being critical. With an advancement in experimental techniques, evidence for quantum criticality has appeared in a number of correlated electronic phases as a function of non-thermal parameters (g), such as chemical doping, pressure and magnetic field.

Even in the quantum setting, the correlation length continues to have a divergence

of the form $\xi \sim |g - g_c|^{-\nu}$, where $g = g_c$ is the critical point. Associated with the diverging correlation length is a diverging time-scale,

$$\xi_\tau \sim \xi^z, \tag{1.2}$$

where z is known as the dynamical critical exponent. Equivalently, this means that at the QCP, there are gapless excitations dispersing as $\omega \sim k^z$, where k is the momentum. Therefore at $T = 0$, in a system defined in $d-$spatial dimensions, the 'effective-dimensionality' is $d + z$. There is a characteristic energy scale, Δ, which vanishes at the QCP as,

$$\Delta \sim \xi_\tau^{-1} \sim |g - g_c|^{\nu z}. \tag{1.3}$$

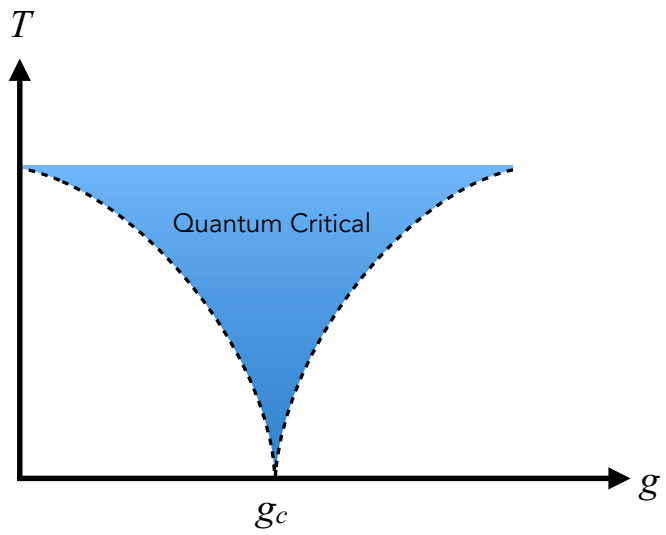

Figure 1.1: A cartoon phase diagram as a function of temperature (T) and a generic control-parameter (g) for a system close to a quantum critical point. The dashed lines could be phase-transitions or crossovers depending upon the specific system under consideration. In the shaded region marked 'Quantum critical', $k_B T$ is much bigger than Δ, and hence it is influenced strongly by the underlying QCP at $g = g_c$.

Thus far we have discussed the physics associated with quantum criticality at

$T = 0$, where it is sharply defined. This also raises the question whether quantum criticality is purely of academic interest or whether it has any role to play in real life at non-zero (but low) temperatures. From our study of quantum statistical mechanics, we know that a non-zero temperature introduces a finite length scale along the time-direction, and thus necessarily requires one to carry out an analog of finite size scaling, familiar from classical criticality. This leads to an appearance of the well known 'quantum critical fan' above the QCP (see fig. 1.1). The boundaries of the fan can be obtained approximately by $k_B T \sim \Delta \sim \xi_\tau^{-1} (\sim |g - g_c|^{\nu z})$. Far away from the boundaries ($k_B T \gg \Delta$), the system is completely unaware of the finite gap, Δ, since the finite extent of the temporal direction, $\beta = 1/k_B T \ll \xi_\tau$. Therefore, the higher we move up in temperature, the system becomes less aware of the finite gap and becomes more 'critical'. This is why the influence of the QCP affects a large region of the phase diagram as we move higher up in temperature. The quantum critical region is also identified by the absence of well defined quasiparticles [193].

The strength of quantum fluctuations is stronger in low-dimensions, and fascinating quantum critical phenomena are therefore most likely to appear in (quasi-)two dimensional systems. We shall focus on such systems, with a special emphasis on their experimental connections during much of the discussion in this thesis. We note that quantum phase transitions involve physics that is unbeknownst to the world of classical phase transitions. For instance, some of the most dramatic consequences of quantum criticality arise in problems with gapless fermi-surfaces coupled to Bosonic order-parameters. We shall see later how this is a problem relevant for studying various aspects of high-temperature superconductivity. Even in magnetic insulators,

it is possible to have continuous quantum phase transitions that are forbidden in a strict Landau-sense. The quantum critical point in such examples has emergent fractionalized excitations, even in dimensions greater than one. The general framework for describing such exotic critical points was developed in the theory of 'deconfined criticality' [214].

1.1.2 Fermi-liquids and Luttinger's theorem

Fermi liquids are ubiquitous in nature—from an elemental metal such as copper to high-temperature superconducting materials (far away from magnetism), they have been observed in a wide variety of systems. In this subsection, we introduce some of the key properties of fermi-liquids, as this will serve as a convenient point of departure later in the thesis for describing gapless phases of matter that are not adiabatically related to fermi-liquids. In momentum space, the Hamiltonian for a collection of 'non-interacting' electrons may be expressed as,

$$H = \sum_{\boldsymbol{k}} (\varepsilon_{\boldsymbol{k}} - \mu) c^{\dagger}_{\boldsymbol{k}\sigma} c_{\boldsymbol{k}\sigma}, \tag{1.4}$$

where $c_{\boldsymbol{k}\sigma}$ is the destruction operator for an electron with momentum $\boldsymbol{k}$ and spin σ. The underlying microscopic physics determines the band-structure, $\varepsilon_{\boldsymbol{k}}$, and μ is the chemical potential. In the ground state, as a result of the Pauli principle, all the states with $\varepsilon_{\boldsymbol{k}} < \mu$ are filled while states with $\varepsilon_{\boldsymbol{k}} > \mu$ are empty. There is a sharp surface in momentum-space, $\varepsilon_{\boldsymbol{k}} = \mu$ (of dimension $d-1$, embedded in a $d-$dimensional system), which separates the occupied from the unoccupied states and is known as the 'fermi-surface'. For the remainder of this thesis, we shall focus on Fermi surfaces in two spatial dimensions (see fig. 1.2 for an example).

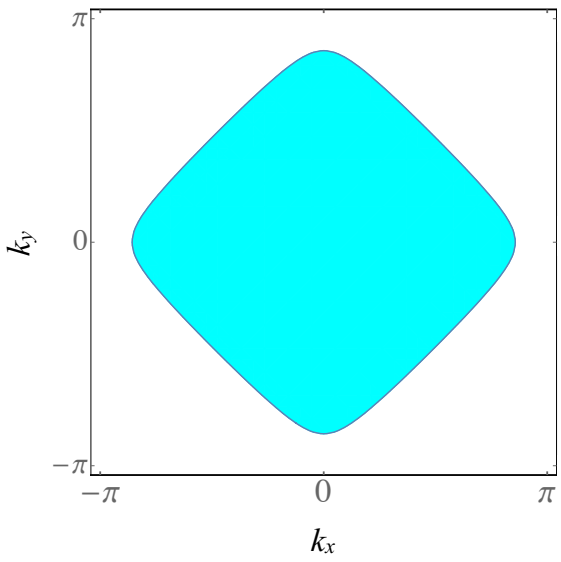

Figure 1.2: An example of a fermi-surface of a two dimensional metal with C_4 rotational symmetry. The states shaded in cyan are filled.

The low energy excitations above the ground state consist of spinful particles and holes near the fermi-surface. Close to the fermi-surface, it is sufficient to linearize the dispersion of these excitations as,

$$(\varepsilon_{\boldsymbol{k}} - \mu) \approx v_F(\hat{k})k, \tag{1.5}$$

where $v_F(\hat{k}) = |\nabla_{\boldsymbol{k}}\varepsilon_{\boldsymbol{k}}|$ is the Fermi velocity and k measures the distance from the fermi-surface. We have allowed for a velocity that depends on the position along the fermi-surface.

A quantity that is going to be used throughout this thesis is the imaginary time electronic Green's function, defined as,

$$G(\boldsymbol{k}, i\omega_m) = -\int d\tau \langle c_{\boldsymbol{k}\sigma}(\tau) c^\dagger_{\boldsymbol{k}\sigma}(0)\rangle e^{i\omega_m \tau}, \tag{1.6}$$

where $i\omega_m$ correspond to the Matsubara frequencies. In the vicinity of the fermi-

surface,

$$G(\boldsymbol{k}, i\omega_m) = \frac{1}{i\omega_m - v_F(\hat{k})k}. \tag{1.7}$$

So far we have only discussed the non-interacting fermi-gas, ignoring any electron-electron interactions. Landau boldly *hypothesized* that if the interactions are turned on adiabatically, and if during this process the system does not undergo any phase transition, then the low energy excitations in the interacting fluid are similar to those in the non-interacting gas, apart from a few modifications as highlighted below. The resulting state was dubbed the (Landau) fermi-liquid.

The notion of the fermi-surface continues to survive in the fermi-liquid, as do the particle and hole like excitations in the immediate vicinity of the fermi-surface. However, the excitations are not the bare electrons anymore but are dressed excitations, introduced previously as 'quasiparticles'. The electronic Green's function is now modified to,

$$G(\boldsymbol{k}, i\omega_m) = \frac{Z(\hat{k})}{i\omega_m - v_F^*(\hat{k})k}, \tag{1.8}$$

where $v_F^*(\hat{k})$ is the renormalized Fermi velocity as a result of the interactions and $Z(\hat{k})$ is a quasiparticle residue, measuring the overlap between the new quasiparticle state and the original free electron. Equivalently, Z also measures the strength of the 'jump' in the quasiparticle distribution, $n(\boldsymbol{k})$, at the fermi-surface. Both of these quantities are measurable in experiments on real materials, as will become clear during our subsequent discussions.

Due to the abundance of gapless particle-hole excitations around the fermi-surface, the Fermi liquid is a 'critical' phase. It is therefore important to address whether the

quasiparticle introduced above survives as a stable excitation or if it decays into the particle-hole continuum. A straightforward computation of the inverse lifetime as a function of the deviation from the fermi-surface ($\delta\varepsilon_{\boldsymbol{k}}$) of a quasiparticle in $d > 1$ gives,

$$\frac{1}{\tau_{\boldsymbol{k}}} \sim \delta\varepsilon_{\boldsymbol{k}}^2 \ (\ll \delta\varepsilon_{\boldsymbol{k}}, \text{ for } \delta\varepsilon_{\boldsymbol{k}} \text{ small}), \tag{1.9}$$

with an additional logarithmic correction in two dimensions. Since the inverse lifetime vanishes much faster than the energy itself as $\varepsilon_{\boldsymbol{k}} \to 0$ (i.e. upon approaching the fermi-surface), the decay processes are irrelevant near the fermi-surface and the quasiparticle survives as a well defined excitation.

A defining feature of a fermi-liquid is a relationship between the volume (or, area in two dimensions) enclosed within the fermi-surface and the total density (ν) of electrons,

$$\nu = 2 \int_{k \in \text{FS}} \frac{d^d k}{(2\pi)^d}, \tag{1.10}$$

where the factor of 2 accounts for electron spin. The above statement, trivial for a non-interacting fermi-gas, is highly non-trivial for an interacting fermi-liquid and is known as the 'Luttinger's theorem'. It was originally proven to all orders in perturbation theory [142]. We note here that this is a property of the fermi-liquid that can also be verified in experiments; the Hall-coefficient (R_H) directly measures ν^{-1}.

There is an elegant non-perturbative proof [173, 175] of the Luttinger's theorem using a 'momentum-balance argument', whose essential steps we reproduce below in brief. The discussion will closely follow Ref. [175].

Let us start by defining the system, with N particles of charge $\mathcal{Q}$ on a lattice of dimensions $L_x \times L_y$ with periodic boundary conditions, i.e. on a torus (fig. 1.3).

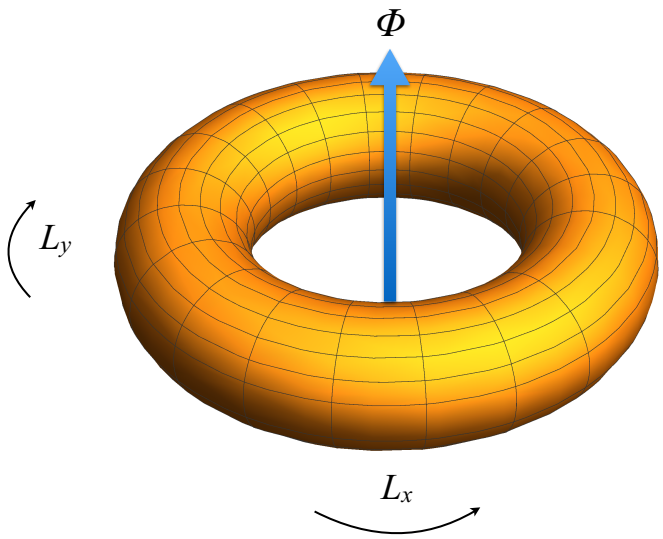

Figure 1.3: The system with N particles defined on a $L_x \times L_y$ lattice with periodic boundary conditions (i.e. torus). A flux, Φ, is introduced adiabatically through one of the holes of the torus.

The density of particles is then $\nu = N/L_x L_y$. The argument relies on adiabatically inserting a flux, $\Phi = hc/\mathcal{Q}$, through one of the holes of the torus over a period of time $t = \tau$ and keeping track of the change in the 'crystal momentum' during this process. The change in the crystal momentum is evaluated using two different methods: first, in an almost trivial way, independent of the phase that the system is in and which only depends on the filling. In the second method, one uses essential information about the phase that the system is in and its excitations to compute the change in the momentum. By equating the two, one recovers Luttinger's theorem for the fermi-liquid.

We begin by evaluating the momentum change using the first method. As a result of the flux-threading, the initial and final Hamiltonians are different, but related by

a gauge-transformation, $\mathcal{U}_G$, i.e.,

$$\mathcal{U}_G H_f \mathcal{U}_G^{-1} = H_i, \;\; \mathcal{U}_G = \exp\left(\frac{2\pi i}{L_x}\sum_i x_i \hat{n}_i\right), \tag{1.11}$$

where $\hat{n}_i$ is the number-operator. The final wavefunction of the system is related to the initial wavefunction by $|\Psi_f\rangle = \mathcal{U}_G\mathcal{U}_\tau|\Psi_i\rangle$, where $\mathcal{U}_\tau$ is the unitary time evolution operator. We are interested in computing the change in crystal momenta, $\Delta P = P_f - P_i$, where

$$\hat{T}|\Psi_i\rangle = e^{-iP_i}|\Psi_i\rangle, \;\; \hat{T}|\Psi_f\rangle = e^{-iP_f}|\Psi_f\rangle, \tag{1.12}$$

and $\hat{T}$ is the unit translation operator. It is straightforward to show that,

$$\hat{T}\mathcal{U}_G\hat{T}^{-1} = \exp\left(-\frac{2\pi i N}{L_x}\right)\mathcal{U}_G, \tag{1.13}$$

and so naturally,

$$P_f = P_i + \frac{2\pi N}{L_x}(\text{mod } 2\pi) = P_i + 2\pi\nu L_y(\text{mod } 2\pi). \tag{1.14}$$

This concludes the computation of the change in crystal momentum, obtained in a rather general setting.

Let us now compute the momentum difference for a fermi-liquid, where the assumption is that the only low energy excitations are quasiparticles near the fermi-surface. These quasiparticles are adiabatically related to the bare non-interacting fermions. As a result of the flux-threading, each quasiparticle picks up a uniform shift of $\Delta p_x = 2\pi/L_x$, leading to a displacement of the fermi-sea. The total change is then given by,

$$\Delta P_x = \sum_p p_x \delta n_p, \tag{1.15}$$

where $\delta n_p = \pm 1$ on a shell of thickness $\delta \boldsymbol{p} \cdot d\boldsymbol{S_p}$ ($d\boldsymbol{S_p}$ is normal to the Fermi surface). Then,

$$\Delta P_x = \oint_{\rm FS} p_x \frac{L_x L_y \ \delta \boldsymbol{p} \cdot d\boldsymbol{S_p}}{(2\pi)^2}. \tag{1.16}$$

Using the divergence theorem, the above can be converted to a volume integral leading to,

$$\Delta P_x = \frac{2\pi}{L_x} \frac{L_x L_y}{4\pi^2} V_{\rm FS}, \ \Delta P_y = \frac{2\pi}{L_y} \frac{L_x L_y}{4\pi^2} V_{\rm FS}. \tag{1.17}$$

Finally, comes the crucial step of equating ΔP evaluated using the two different approaches,

$$\Delta P_x = 2\pi\nu L_y = \frac{2\pi}{L_x} \frac{L_x L_y}{4\pi^2} V_{\rm FS} + 2\pi m_x, \tag{1.18}$$

$$\Delta P_y = 2\pi\nu L_x = \frac{2\pi}{L_y} \frac{L_x L_y}{4\pi^2} V_{\rm FS} + 2\pi m_y, \tag{1.19}$$

for $m_x, m_y \in$ Integers. The above equations can be recast as,

$$L_x m_x = N - L_x L_y \frac{V_{\rm FS}}{4\pi^2}, \tag{1.20}$$

$$L_y m_y = N - L_x L_y \frac{V_{\rm FS}}{4\pi^2}. \tag{1.21}$$

The strongest constraint can be obtained in the situation when L_x, L_y are mutually prime integers, so that they can only be integer multiples of $L_x L_y$, i.e. $L_x m_x = L_y m_y = p L_x L_y$, for p an integer. Then,

$$\nu = \frac{V_{\rm FS}}{4\pi^2} + p, \tag{1.22}$$

which is the statement of Luttinger's theorem, and we have allowed for filled bands represented by p.

Based on our proof of Luttinger's theorem for the fermi-liquid, it is clear that in order to violate the theorem for a phase with electron-like quasiparticles with a fermi-surface, other global excitations need to be present in the system that can carry away non-trivial crystal momentum. This will modify the momentum balance argument for the electronic quasiparticles. We shall see an example of such a phase in our subsequent discussion.

1.2 Beyond conventional condensed-matter physics

Now that we have reviewed some of the elementary concepts that will be used quite frequently, let us list some challenging questions that will be raised during the course of our discussion. While many of these questions have received a lot of attention in the past couple of years and much understanding has been gained, a lot still remains to be understood.

- Does a quantum phase transition necessarily require an order parameter? Equivalently, is symmetry breaking involving a physical symmetry the only route to 'ordering'?

- Do electrons have to retain their identity as well-defined quasiparticles in the presence of strong correlations? If they do (and in the absence of superconductivity), can they realize a phase not adiabatically related to the fermi-liquid?

- Do the critical singularities at phase transitions always arise from the long-wavelength fluctuations of an order parameter?

- In the absence of superconductivity and disorder, are we guaranteed to have a sharp Fermi surface at zero temperature?

Many of the above questions arise naturally in the context of high-temperature superconductivity, which will be a major focus of this thesis. The answers will often be quite counter-intuitive and will require a serious modification of lessons from conventional solid-state physics. With the above set of questions in mind, let us now introduce some of the key phenomenology associated with the high-temperature superconductors before moving on to discussing some specific issues in the subsequent sections.

1.2.1 High-temperature superconductivity

There are a number of different 'families' of high-temperature, or, unconventional superconductors at this point, some of which were discovered more than three decades ago. However, in this thesis we shall focus mostly on the copper-oxide and iron-based superconducting families; these are possibly the most well studied families and have some of the highest superconducting transition temperatures. The other families that display similar phenomenology include the heavy Fermion and organic superconductors. In general, most of these materials have complex crystal structures, but contain quasi two-dimensional layers of square arrays of $d-$ or $f-$electrons (see fig. 1.4). In their phase-diagrams, as a function of temperature and doping, or other control-parameters, superconductivity usually arises upon suppressing a parent phase that is antiferromagnetic; there is evidence for sufficient overlap of the two phases in some systems (fig.1.5). There are however fundamental differences in the nature of

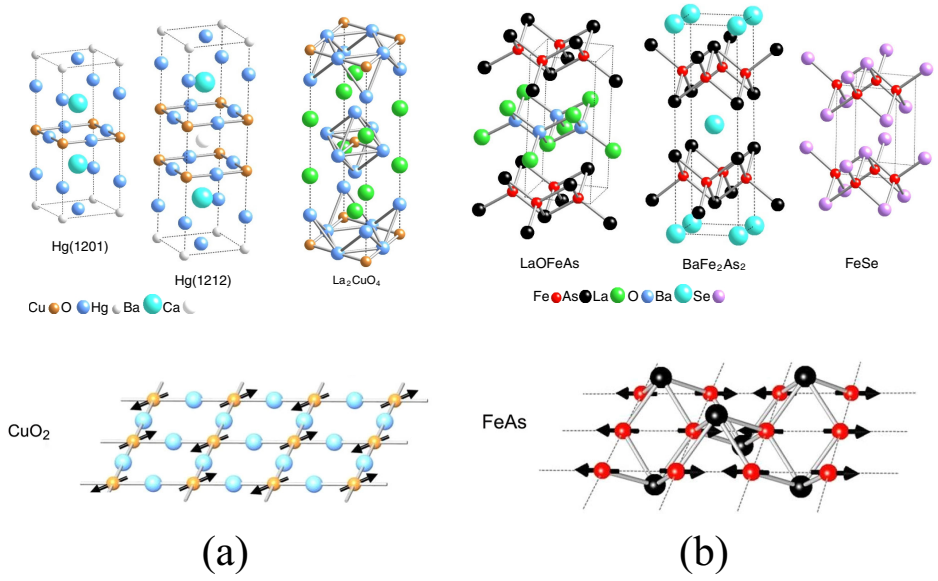

Figure 1.4: (a) Crystal structures of different members of the copper-oxide family of superconductors (top). The quasi-two dimensional layers of CuO_2 determine most universal aspects of the phenomenology; the parent state is an antiferromagnetic Mott insulator with the orinetation of spins on the Cu sites as shown (bottom). (b) Crystal structures of different members of the iron-based superconductors (top). The 'puckered' quasi-two dimensional layers of iron and the associated pattern of SDW ordering (bottom). Adapted from Ref.[200].

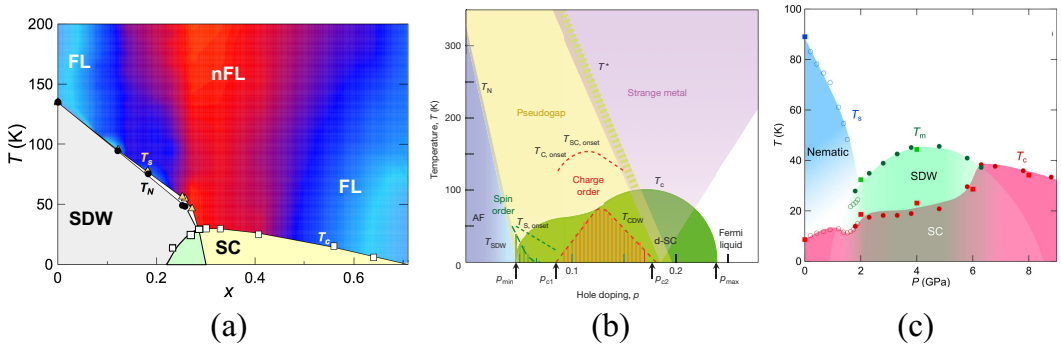

Figure 1.5: Phase-diagrams of (a) isovalently substituted $BaFe_2As_2$ (Adapted from Ref. [112]). (b) hole-doped cuprates (Adapted from Ref. [119]). (c) bulk FeSe under hydrostatic pressure (Adapted from Ref.[226]). In all three cases, superconductivity occurs in the vicinity of (and often coexists with) magnetism. In bulk FeSe, the magnetic phase is absent at ambient pressure but superconductivity occurs in the presence of spontaneously broken rotational symmetry ('nematic').

the parent states between the two families, as explained below.

The parent compound in the iron-based superconductors is metallic—the high temperature phase is a tetragonal metal (see fig. 1.5a and fig. 1.6) and undergoes a transition to a metallic *spin-density wave* (SDW) with broken C_4 lattice symmetry at a temperature T_N. In the SDW phase, the moments are oriented antiferromagnetically along one direction and ferromagnetically along the other, thereby explicitly breaking the rotational symmetry. Note that breaking the discrete C_4 symmetry down to C_2 is an Ising transition and can be split from the breaking of spin-rotation symmetry. The breaking of the rotational symmetry naturally induces a structural transition to an orthorhombic state. This structural transition, driven by electronic correlations, occurs at a temperature, T_S, that is slightly higher than T_N in many of the materials. There is at least one exception to this general observation in bulk stoichiometric FeSe (fig.1.5c), where at ambient pressure no magnetic phase occurs. There is only a

structural transition to a nematic metal, followed by a transition to a nematic superconducting state at low temperatures. In chapter 2, we shall study some interesting consequences of the interplay between the nematic order and superconductivity.

With increased hole-, electron-, or, isovalent-doping, both the structural and SDW transitions are suppressed, eventually giving rise to superconductivity. There is growing evidence that for a range of dopings, many of these materials host a region in the phase-diagram with microscopic coexistence of superconductivity and SDW. One of the interesting questions that we shall address in section 1.2.2 is whether the T_N or T_S lines terminate at a zero temperature QCP, as this may serve as a way of associating the huge fan-shaped non-Fermi liquid regime with the quantum critical fan of the $T = 0$ QCP. Chapter 3 will take a closer look at the question of whether existing experimental measurements of various quantities shed any light on the fate of these transitions deep in the superconducting phase.

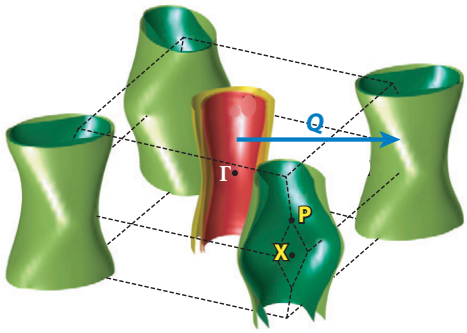

Figure 1.6: The Fermi surface of $BaFe_2As_2$ in the tetragonal, paramagnetic metallic state. The Fermi surfaces have a weak dispersion along the $z-$direction. There are three hole sheets near the Γ point (zone center) and two electron sheets near the X point (zone corner); the sheets are (quasi-)nested by the wavevector $\boldsymbol{Q}$ of the SDW. Adapted from Ref.[218].

Unlike the itinerant, metallic state discussed above, the parent state of the cuprates

are Mott charge-transfer antiferromagnetic insulators (fig.1.5b). In the insulating CuO_2 layer, Cu^{2+} has a $3d^9$ configuration. As a result of the crystal field effects, the $d_{x^2-y^2}$ orbital has the highest energy and is half filled; the Coulomb interaction energy on the Cu sites is large. The $2p$ orbitals on O sites mediate an exchange interaction between the Cu spins leading to long-range antiferromagnetic order. The gap in the undoped insulator is set by the difference in energy between the $2p$ orbital of the O and the $d_{x^2-y^2}$ orbital of the Cu. When doped with holes, the cuprates display superconductivity with fairly high T_c's beyond a critical doping. However, the more enigmatic states obtained upon doping are the metallic states about T_c in the 'underdoped' and optimally doped cuprates. In the former case, the metallic state thus obtained is dubbed as the *pseudogap*, and has only disconnected Fermi 'arcs' in momentum space (see fig. 1.7). The low-energy excitations are hole-like, carrying both physical charge and spin. On the other hand, the metallic state existing over a wide fan-shaped region above optimal doping does not have coherent particle like excitations and displays a number of transport anomalies; it is appropriately referred to as the *strange-metal*. Chapters 4, 5, 6 will be devoted to the study of the pseudogap metal and the low temperature symmetry broken phases that have been the subject of much discussion in recent years [42, 74]. Chapter 7 will describe a QPT of novel kind in a metallic phase, without any broken symmetries, and its possible relevance for the strange-metal phenomenology.

We note however, that in both the families, sufficiently far away from the parent antiferromagnetic phase, there is a well behaved fermi-liquid state with 'large' fermi-surfaces satisfying Luttinger's theorem. This observation often serves as a mo-

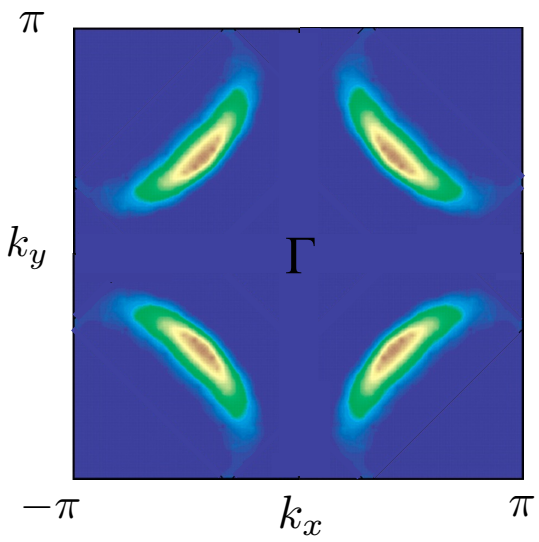

Figure 1.7: Measurements of the spectral function, obtained from photoemission experiments, in the pseudogap phase. The disconnected 'arcs' are clearly visible along the zone diagonals, with no low-energy excitations in the vicinity of $(\pi, 0)$, $(0, \pi)$ and symmetry related points. Adapted from Ref.[217]

tivation for unifying the physics of unconventional superconductivity, by approaching the problem from the conventional fermi-liquid side and building in the correlations as the antiferromagnetic phase is approached [200].

In the next two sections, we shall review some of the specific experimental puzzles that will be addressed during the course of this thesis.

1.2.2 Quantum criticality in the pnictide superconductors

Given the remarkable similarity in the basic structure of the phase-diagrams of the different families of unconventional superconductors, and the large non-Fermi liquid "fan" extending in temperature above the optimal transition temperatures, it is interesting to consider the possibility of an underlying quantum critical point

being at the heart of the mystery. A careful look at figs. 1.1 and the phase-diagrams in fig.1.5 would seem to suggest that the putative QCP corresponds to the onset of a broken symmetry in a metal. Of course, it is natural to ask what the broken symmetries are, if any, on the ordered side of the transition and if the QCP survives even in the presence of superconductivity.

Experimentally, it is usually known what the broken symmetries are on the ordered side of the transition. However, it is extremely hard to ascertain whether there is a QCP beneath the superconducting dome. Most experiments suppress superconductivity by applying a large magnetic field and study properties associated with the metallic normal state. This has been done systematically, for example, on a prototypical member of the iron-pnictide family: P-doped $BaFe_2As_2$. In fig. 1.8(a) we show the phase-diagram of this material as a function of isovalent P-doping, x, and a summary of some of the measurements in the normal state.

The magnetic response in the metallic state above the superconducting T_c was probed by measuring the ^{31}P NMR relaxation rate, $1/T_1$. We know that,

$$\frac{1}{T_1 T} \propto \frac{1}{\omega_0} \sum_{\boldsymbol{k}} |A(\boldsymbol{k})|^2 \chi''(\boldsymbol{k}, \omega_0), \tag{1.23}$$

where $A(\boldsymbol{k})$ is the hyperfine coupling between the ^{31}P nuclear spin and the neighboring electrons, ω_0 is the NMR frequency and $\chi''(\boldsymbol{k}, \omega_0)$ is the imaginary part of the dynamical spin-susceptibility. In the presence of strong antiferromagnetic fluctuations, there is a strong enhancement of $1/T_1T$ and deviation from the usual Korringa relation. [1] In particular, near $x_c \approx 0.3$, $1/T_1T \sim 1/T$, i.e. the experimentally extracted Curie-Weiss temperature (θ) goes to zero. This is quite suggestive of there

[1]Korringa relation relates $1/T_1T \sim K^2$, where K is the Knight-shift.

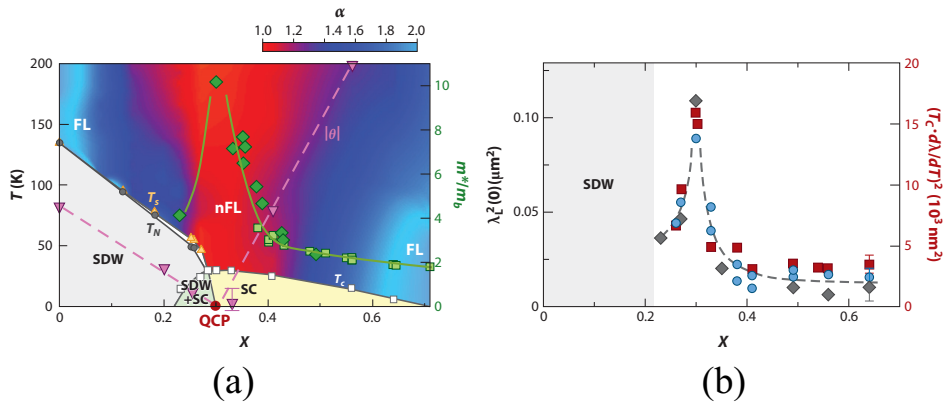

Figure 1.8: (a) Experimental phase diagram of $BaFe_2(As_{1-x}P_x)_2$. The exponent α determines the temperature dependence of the resistivity. T_s, T_N and T_c represent the structural, magnetic and superconducting transition temperatures, respectively. $|\theta|$ is the Weiss temperature determined by the nuclear magnetic resonance relaxation rate and the light green squares and dark green diamonds represent the effective mass extracted from quantum-oscillations and jump in the specific-heat at T_c, respectively. (b) The experimental data for the square of the (zero-temperature) London penetration depth, or inverse of the superfluid-density, as determined by three different techniques. Adapted from Ref.[218].

being an antiferromagnetic QCP in the metallic state at x_c.

The effective mass, m^*, in the metallic state was extracted experimentally using two different techniques. The effective cyclotron mass, $m^*_{\rm QO}$, was extracted from quantum-oscillations by fitting the temperature-dependent amplitude of the oscillations to the standard Lifshitz-Kosevich formalism. Specifically, the cyclotron mass is given by an angular average,

$$m^*_{\rm QO} = \frac{1}{2\pi} \oint \frac{dk}{v^*_F(\theta)}, \tag{1.24}$$

where $v^*_F(\theta)$ is the fermi-velocity introduced earlier in eqn.1.8 and dk is the line element in momentum space along the fermi-surface. Remarkably, the experimentally obtained $m^*_{\rm QO}$ tends to diverge upon approaching x_c from the fermi-liquid side. If

the effective mass gets enhanced locally, as a function of θ, but along a wide enough segment of the Fermi surface, then it leads to an enhancement in $m^*_{\rm QO}$. For example, at the onset of a SDW transition, the Landau quasiparticles are destroyed at points on the fermi-surface that are connected by the ordering wavevector (i.e. the 'hot-spots'), which is accompanied by a diverging effective mass. On the other hand, nematic fluctuations that couple uniformly to the fermi-surface and destroy quasiparticles everywhere also lead to a divergence in $m^*_{\rm QO}$. Since the material under question has both types of fluctuations, it is challenging to identify the source of the divergence in $m^*_{\rm QO}$. It is worth noting that the critical divergence in a measurable observable here is arising not merely from the long-wavelength fluctuations of an 'order-parameter', but from the underlying gapless fermi-surface.

The effective mass was also extracted from a measurement of the $\gamma \propto m^*_{\rm C}$ term (i.e. Sommerfeld coefficient) in the electronic specific heat. In particular, the doping dependence of $m^*_{\rm C}$ was extracted by carefully measuring the jump in the specific heat at T_c, $\gamma = \Delta C/\alpha T_c$, where ΔC is the jump and $\alpha = \mathcal{O}(1)$ is a numerical prefactor. The experimentally extracted $m^*_{\rm C}$ has a strong enhancement upon approaching x_c from either side of the putative transition.

All of the above results indeed seem to indicate the presence of at least one QCP in the metallic state. However, deep in the superconducting state, when the fermionic degrees of freedom are gapped out, there is no guarantee for the quantum criticality to survive. The transition(s) could become first-order inside the dome, accompanied by phase-separation. In order to ascertain the presence of pristine quantum criticality in the paired state, experiments were carried out to measure a property of the

superconductor, namely the London penetration depth, $\lambda_L^2(0)$, or inverse superfluid density. Interestingly, the penetration depth shows an anomalous peak in the vicinity of x_c (see fig. 1.8(b)), which was interpreted as a 'smoking-gun' evidence for the QCP surviving beneath the superconducting dome. Whether this interpretation is correct, or if it is at odds with theoretical expectations will be explored in chapter 3 in great detail, both in the presence and absence of disorder.

Finally, we note that the problem of a metal in two spatial dimensions coupled to gapless order-parameters, carrying a finite or zero momentum (eg. density-wave orders vs. nematic order), remains 'unsolved' in the sense that there is no controlled method of studying the low-energy field theory. However, in recent years, there has been a great deal of progress in studying these problems numerically using quantum-Monte carlo techniques on models that do not suffer from the infamous sign-problem. For the problem of a fermi-surface coupled to a SDW order parameter, preliminary studies find phase-diagrams (see fig. 1.9 and Refs.[30, 204]) that are remarkably similar to the experimental phase-diagram of the pnictides; they find a dome of sign-changing superconductivity and a SDW phase, including a regime with overlapping orders. The dynamical properties remain to be analyzed and will hopefully shed light on the nature of the spectral functions in future studies. However, the fate of the SDW QCP at low temperatures and in the superconducting state remains unclear within this numerical study [204].

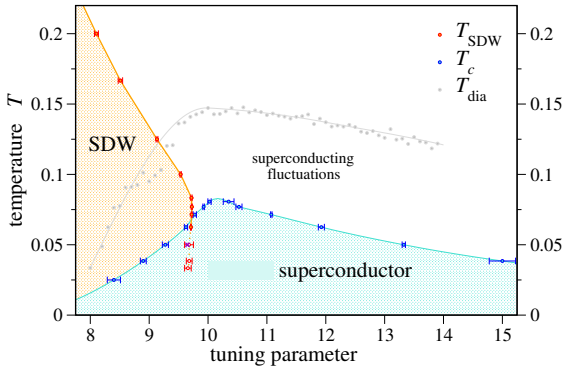

Figure 1.9: Phase diagram of a 'sign-problem free' model of fermions coupled to critical fluctuations of a SDW order parameter obtained using quantum-Monte Carlo simulations. Different lines represent the transition temperatures: $T_{\rm SDW}$, the superconducting T_c, and the onset of diamagnetism at $T_{\rm dia}$. The nature of the SDW transition *inside* the SC dome, marked by a dashed line, is unclear and could possibly be a weakly first-order transition. Adapted from Ref.[204].

1.2.3 The enigma of the cuprate superconductors

Ever since their discovery [26] in 1986, the cuprate high-temperature superconductors (SC) have been among the most well-studied correlated electron materials, both theoretically and experimentally. These materials show a number of different phases as a function of hole doping (see fig.1.5b). The parent antiferromagnetic Mott insulator, the d-wave superconductor and the Fermi liquid state at large doping are reasonably well understood at this point. On the other hand, the phases that continue to elude an explanation, and occupy a large portion of the phase diagram (see fig. 1.10 for a simplified 'cartoon' phase-diagram), are the pseudogap and the strange-metal. It is essential to develop a microscopic understanding of these phases in order to resolve the mystery of cuprate superconductivity, as they are the 'normal' states out of which superconductivity (and various other ordering tendencies) arise at low

temperatures.

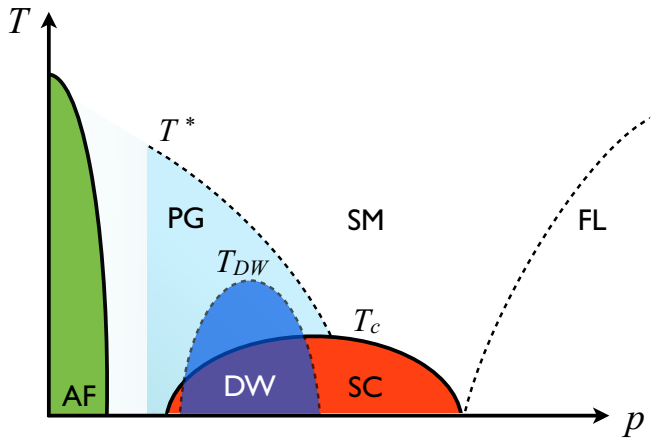

Figure 1.10: A temperature (T) vs. hole-doping (p) phase diagram for the non-La-based cuprates. The parent state is an antiferromagnetic (AF) Mott insulator which upon being doped leads to a d-wave superconductor (SC) with transition temperature, T_c. The extremely overdoped phase is a familiar fermi-liquid (FL). The two mysterious phases are the pseudogap (PG), which onsets at a high temperature (T^*), and the strange-metal (SM), occupying a wide fan-shaped region. Multiple recent experiments have investigated the nature of the lower ($T_{DW} < T^*$) temperature density-wave (DW) phase in the underdoped cuprates.

Although we don't have a complete understanding of these phases, a lot is now known phenomenologically about the pseudogap regime of the underdoped cuprates. The first signatures of the 'high'-temperature pseudogap ($T < T^*$) came from measurements of the Knight-shift [12], followed by other spectroscopic measurements [58], which showed evidence for a suppression in the density of states at the fermi-level along specific regions of the Brillouin zone. However, there is no clear evidence for any broken symmetry in this regime. On the other hand, in recent years many remarkable experiments have revealed the nature of the 'low'-temperature pseudogap ($T < T_{DW} < T^*$), where a number of broken symmetries have, in fact, been ob-

served below a temperature, T_{DW}. A major breakthrough was the initial observation of quantum oscillations at high magnetic-fields and very low temperatures, followed by the subsequent discovery of short-ranged charge-order even at zero field in the underdoped regime. This was marked by initial optimism that, perhaps, the "hidden" broken-symmetry phase responsible for giving rise to the pseudogap has finally been identified. However, a more systematic study has now made it quite clear that the somewhat fragile charge density wave itself can't be responsible for causing the pseudogap; but it possibly arises at low temperatures out of the *normal* pseudogap phase with no broken symmetry (there may be broken discrete symmetries, such as time-reversal or nematicity [74], at higher temperatures, but these have little direct effect on the electronic structure or spin excitations). One might then ask, what have we really learnt post the discovery of charge order? Could it perhaps serve as a "window" into the nature of the pseudogap state itself?

In chapters 5 and 6, we shall take the point of view that, indeed, the *microstructure* of the charge-order, namely its 'form-factor' and (doping-dependent) wavevector, shall provide us important clues about the nature of the higher temperature pseudogap phase. We will investigate low-energy particle-hole instabilities of possible normal states, and this will help us identify the necessary features required to give rise to a state that is qualitatively similar to the one observed in the experiments. This will also aid us in distinguishing between some of the different approaches that have been used to describe the pseudogap phase.

Broadly speaking, theoretical approaches for characterizing the pseudogap can be classified into two major categories. In the first category, the build up of antiferro-

magnetic correlations and the opening of a spin-gap [12] at T^* signal the onset of a quantum spin liquid [135, 254, 148, 183, 240]. Moreover, as a function of decreasing temperature, there could be multiple crossovers within the metallic spin-liquid and there could also be instabilities to other symmetry-broken phases[2] at lower temperatures. However, in order for this to be a useful and precise characterization, there should be remnants of the 'topological order' of the spin liquid at high temperatures. [3] One possibility is the presence of closed Fermi pockets which violate the Luttinger theorem constraining the total area enclosed by the Fermi surface [253], and this may be related to photoemission spectra which have intensity only on open arcs in the Brillouin zone. In this approach, the pseudogap metal found at high temperatures is a novel quantum state which, with moderate changes, could be stable at low temperatures for suitable model Hamiltonians.

In the second category [122, 194, 205, 239], the antiferromagnetic correlations are precursors to the appearance of antiferromagnetism, superconductivity, charge density-wave, and possibly other conventional orders at low temperatures. In the pseudogap regime, we then have primarily thermal and classical, rather than quantum, fluctuations of these orders. This raises an immediate question: why don't other unconventional superconductors, many of which have a robust antiferromagnetic phase [200], also display pseudogap behavior due to the precursor thermal fluctuations? What is so different about the hole-doped cuprates?

[2]Though clearly important for describing some of the phenomenology, we shall ignore the effects arising due to the presence of *quenched disorder*, which in some cases forbids a true symmetry breaking in two spatial dimensions.

[3]By 'topological order', we mean states with emergent gauge excitations; for states with an energy gap, there are non-trivial ground state degeneracies on a torus.

In this thesis, we shall delve into discussing some of the merits of both approaches. However, hopefully by the end of our discussion on cuprates, it will become clear to the reader that we believe that the spin liquid approach provides a more coherent picture of the hole-doped side of the phase diagram.

Let us now outline the scope of our focus. There are already a number of excellent reviews that discuss much of the previously known phenomenology of the pseudogap phase [172, 122, 135]. Our emphasis here will be on the more recent experiments, particularly with regard to the discovery of charge order in the non-Lanthanum-based cuprates, and the implications of these experiments on the nature of the high temperature pseudogap phase. We shall not explicitly consider experimental reports of nematic order [74]: this order can be an ancillary consequence of our low and high temperature models of the pseudogap, but we do not believe it is crucial to the basic phenomenology. We shall not discuss any of the signatures of time-reversal symmetry-breaking either that have possibly been seen via polarized neutron scattering [140] and Kerr-rotation [250] experiments, but surprisingly not in μSR or NMR experiments. While these are clearly interesting experiments that need a theoretical explanation in the future, we shall choose not to discuss them any further in this thesis.

With the above goals in mind, let us raise a few sharp questions with regard to the pseudogap phase, and the charge density wave in particular, that we hope to address in this thesis:

- What is the normal state out of which the charge density wave emerges? In other words, can the charge density wave help us identify the nature of the parent pseudogap state?

- What is the modulation wavevector and the internal symmetry ('form-factor') of the charge density wave?
- What is the nature of the onset, and in particular, the temperature dependence of the charge density wave correlations? Does this have any consequence on the fermionic spectral functions?
- Is there an underlying quantum-critical point that controls the physics of the strange-metal region, and if so, what are the two phases on either side of this QCP?

Most of these questions, while easy to state, might not have a complete answer at present. However, we shall argue that based on a body of work done over the past few years, it is at least partially possible to answer some of them. Some of the above questions will necessarily require us to speculate, with the hope that future work will help us address these issues further.

Review of experiments

In the past few years, a number of remarkable experiments have given both direct and indirect evidence for the appearance of charge-order in the underdoped cuprates. Charge (and spin)-stripes have been known to exist in the Lanthanum-based cuprates [232, 122] for a long time now. In these materials, close to a hole-doping of $p = 1/8$, the spin and charge stripes are known to have the most pronounced signatures; this is also where the superconducting T_c goes all the way to zero. However, in this thesis we shall focus only on the non-La-based cuprates, where charge-order is not accompanied

by any spin-order. There are important differences between the properties of these two 'classes' of cuprates.

A preliminary indication of charge-order in $Bi_2Sr_2CaCu_2O_{8+\delta}$ came from STM experiments, which imaged the periodic modulation in the density of states near the vortex cores in the Meissner state [96] and in the high-temperature pseudogap state [235]. In $YBa_2Cu_3O_y$, NMR measurements have been able to detect field-induced long-range static charge order, predominantly on the oxygen sites, without any sign of spin-order [248, 249]. Ultrasound measurements at high-fields [132] have further corroborated a transition to a long-range charge ordered state. The most clear signatures of any charge density wave correlations should come from X-ray. Indeed, incommensurate charge order has now been detected with resonant [78, 5] and hard [39] X-ray scattering, both at zero and high fields. The wave vector has consistently been found to be directed along the copper-oxygen bonds and decreases with increasing hole-doping [31], a trend that is the exact opposite of what has been known to be the case in the La-based-cuprates [239]. Moreover, there are strong indications that the charge modulation is highest on the bonds connecting the Cu sites [125, 3]. A conclusion that is safe to draw from all of these experiments is that there exist incommensurate charge density wave correlations in the CuO_2 plane, which become static and (reasonably) long-ranged upon the application of a high magnetic field, and in general compete with superconductivity.

Some of the key experimental data that have shed light on the nature of the charge-order in the underdoped cuprates, is reproduced in fig. 1.11. Fig. 1.11a from Ref. [78] shows a peak in the total intensity at an incommensurate wavevector $\approx 2\pi(0.3, 0)$,

in the superconducting phase. In order to study the interplay between charge-order and superconductivity, Chang *et al.* [39], studied the onset of scattering intensity as a function of temperature both at zero and finite fields (fig.1.11b). They observed a gradual onset of charge density wave correlations at $T_{\rm CDW}$ (where $T_c < T_{\rm CDW} < T^*$), with a subsequent decrease in the intensity below T_c at zero-field. The feature for $T \leq T_c$ highlights the competition between the two order-parameters, which goes away when superconductivity is suppressed by a reasonably large magnetic field. The field-induced transition in the charge-order has also been investigated using NQR experiments[249] (fig.1.11c). At moderate fields, such as those used in the X-ray and NQR experiments, the charge-order likely develops in the large 'halos' surrounding the superconducting vortices[4] in the mixed-state. The field-induced transition occurs when the halos start to overlap, 'locking' the orientation of the charge density wave over long distances.

Finally, STM measurements show that the primary modulation resides on the Cu-O bonds and has a non-trivial pattern in real space (fig. 1.11d,e). The exact symmetry properties associated with this modulation have only been unveiled recently [77], as we shall discuss shortly.

A key question now is whether the presence of the charge density wave order may also explain the quantum oscillations observed at low temperatures and high magnetic fields [65, 207]. This topic will be discussed briefly later, but it is worthwhile to also review some of the most striking experimental aspects here. The first observation of quantum-oscillations [65] provided clear signatures of a *reconstructed* pocket with an

[4]In the extreme type-II limit ($\kappa = \lambda/\xi_{\rm SC} \to \infty$; λ being the London penetration depth and $\xi_{\rm SC}$ the superconducting coherence length), the vortices really correspond to 'superfluid' vortices [62].

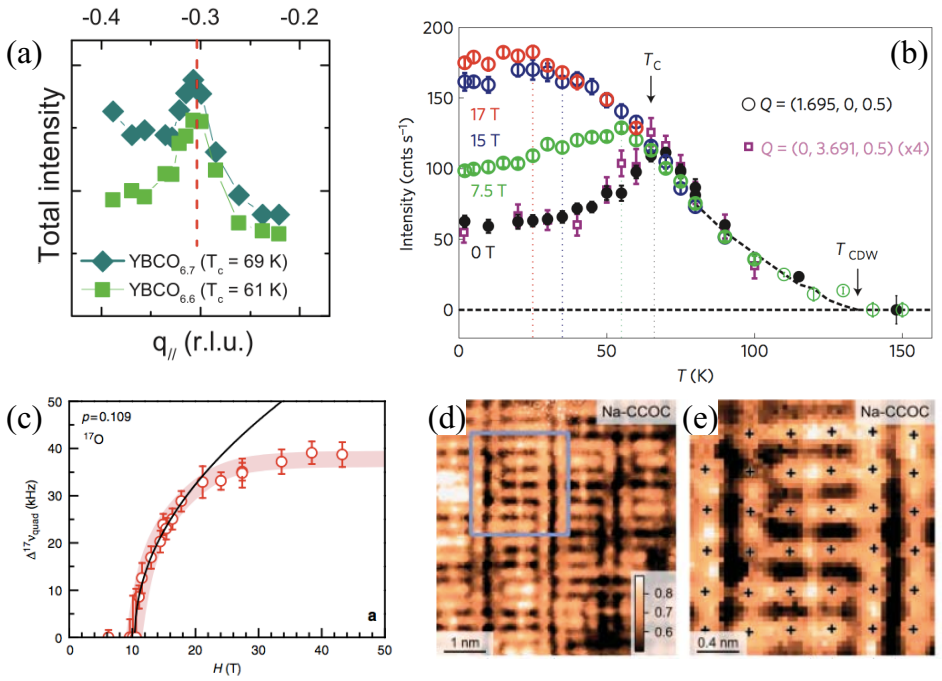

Figure 1.11: (a) Dependence of the CDW intensity at 15 K, showing a finite correlation length (as inferred from the width of the peak). Adapted from Ref. [78]. (b) Temperature dependence of the peak intensity as a function of magnetic field. The onset shows a gradual non-mean-field like behavior. At zero-field, the intensity decreases below the superconducting T_c, showing competition between the two order-parameters. Adapted from Ref. [39]. (c) Quadrupole part of the splitting of the O line showing a field-induced transition. Adapted from Ref. [249]. (d), (e) R-Maps taken at 150 mV. Adapted from Ref. [125].

area approximately 2% of the Brillouin zone (corresponding to a frequency $\sim$ 530T; see fig.1.12a). This is fundamentally different from the observations in extremely overdoped cuprates, where quantum-oscillations observed a 'large' Fermi surface [236]. The key question then was to figure out the density-wave order responsible for giving rise to the reconstruction in the underdoped cuprates. An interesting fact that was realized soon after the initial discovery of oscillations, is related to the nature of carriers in the system. In spite of doping holes into the system, transport-properties

were most consistent with the presence of primarily electron-like quasiparticles, as evidenced by the *negative* Hall coefficient [131] (fig.1.12b). This prompted the search for a small *electron-pocket*, that would explain both of these observations.

It is not entirely clear what the upper critical field, H_{c2}, is for the underdoped cuprates and if the fields, $B \sim 40$T, where oscillations are first observed are already higher than H_{c2}. Moreover, whether the application of large fields completely suppresses the pseudogap is also a topic of ongoing debate. These are questions that need to be resolved in order to realize *what* gets reconstructed to give rise to the small electron-pocket. It is nevertheless a reasonable starting point to study the problem of reconstruction on top of a 'large' Fermi surface in the presence of a (sufficiently) long-ranged BDW [11]. [5]

More recently, by extracting the effective cyclotron mass ($m^*_{\rm QO}$) of the electron-like quasiparticles[6] and by noting the critical dopings where they appear to diverge (fig.1.12c), the location of the underlying quantum critical points, corresponding to the onset of charge-order, have been determined [207, 187]. These QCPs also coincide with the dopings around which the $T_c(B)$-domes, as deduced from the resistive transition in a field (B), are centered about. It has been argued [209] that the critical like divergence arises from the angle-dependent fermi-velocity, $v^*_F(\theta)$, along the electron-pocket, and is in fact dominated by the corners of the pocket (i.e. the vicinity of the hot-spots). However, signatures of this divergence are absent in any measurement performed at zero field, that is dominated by the 'light' nodal quasiparticles, such

[5] Such that the cyclotron-radius associated with an applied magnetic field is smaller than the correlation length of the BDW.

[6] By studying the temperature dependence of the oscillation amplitudes and fitting to the Lifshitz-Kosevich form.

as transport. We direct the readers to some recent review articles for further details regarding the quantum oscillation experiments [207, 237].

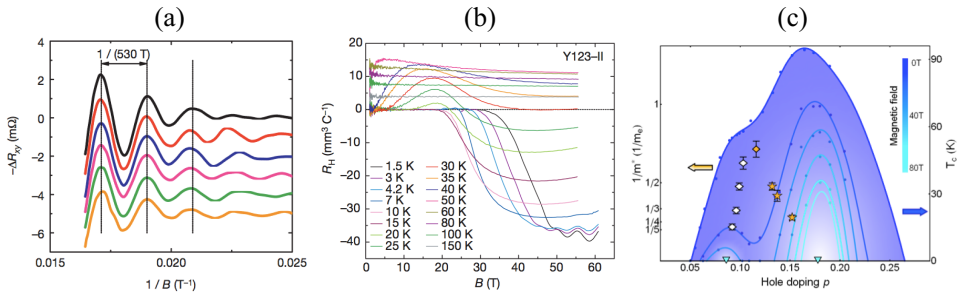

Figure 1.12: (a) The oscillatory part of the Hall resistance (after subtracting the monotonic background at $T = 2$ K), as a function of inverse magnetic field, $1/B$. Adapted from Ref. [65]. (b) The Hall coefficient as a function of B at different temperatures. Adapted from Ref. [131]. (c) The blue curves represent T_c, at different B and are supposed to highlight the connection between effective mass enhancement and the strength of superconductivity. Adapted from Ref. [187].

Charge density wave order in the underdoped cuprates

A significant portion of this thesis is devoted to the study of density-wave order in the underdoped cuprates and its interplay with related phenomenology. It is therefore useful to start by prescribing a systematic approach to express the charge-modulation on a two-dimensional square lattice. The charge density wave, or more appropriately *bond-density wave* (BDW), can be expressed as a bond-observable defined on sites i, j,

$$P_{ij} = \langle c^\dagger_{i\alpha} c_{j\alpha} \rangle = \sum_{\boldsymbol{Q}} \left[\sum_{\boldsymbol{k}} P_{\boldsymbol{Q}}(\boldsymbol{k})\ e^{i\boldsymbol{k}\cdot(\boldsymbol{r}_i - \boldsymbol{r}_j)} \right] e^{i\boldsymbol{Q}\cdot(\boldsymbol{r}_i + \boldsymbol{r}_j)/2}, \tag{1.25}$$

where $c^\dagger_{i\alpha}$ creates an electron at site i with spin $\alpha(=\uparrow,\downarrow)$. The action of various symmetry operations become quite transparent for the above parametrization in mo-

mentum space in terms of a relative momentum, $\boldsymbol{k}$, and a center-of-mass momentum $\boldsymbol{Q}$, as emphasized in Ref. [8]. In momentum space, we can write Eq. (1.25) as,

$$\left\langle c^{\dagger}_{\boldsymbol{k}-\boldsymbol{Q}/2,\alpha} c_{\boldsymbol{k}+\boldsymbol{Q}/2,\alpha} \right\rangle = P_{\boldsymbol{Q}}(\boldsymbol{k}). \tag{1.26}$$

In contrast, the early work of Nayak [170], and numerous analyses since [37, 36, 241, 138, 60, 216], have used the parameterization

$$\left\langle c^{\dagger}_{\boldsymbol{k},\alpha} c_{\boldsymbol{k}+\boldsymbol{Q},\alpha} \right\rangle = F_{\boldsymbol{Q}}(\boldsymbol{k}). \tag{1.27}$$

Of course, we can easily go back and forth between (1.26) and (1.27). However when we write $P_{\boldsymbol{Q}}(\boldsymbol{k})$ as a periodic function of $\boldsymbol{k}$ alone, then the equivalent $F_{\boldsymbol{Q}}(\boldsymbol{k})$ also depends upon $\boldsymbol{Q}$. In particular the state described by $P_{\boldsymbol{Q}}(\boldsymbol{k}) \sim \cos(k_x) - \cos(k_y)$, proposed in Refs. [196, 154], is a d-form factor bond density wave which preserves time-reversal and which will play an important experimental role shortly. In contrast, the state $F_{\boldsymbol{Q}}(\boldsymbol{k}) \sim \cos(k_x) - \cos(k_y)$, considered by others, is a different state; for general $\boldsymbol{Q}$, it is a mixture of components that are both even and odd under time-reversal, and so it is not a useful starting point for a symmetry analysis.

Conventional charge density waves with $P_{\boldsymbol{Q}}(\boldsymbol{k})$ independent of $\boldsymbol{k}$ lead only to an on-site charge modulation, with the overall modulation period set by $2\pi/|\boldsymbol{Q}|$. However, this is not the case in the context of the cuprates. The experiments on at least two different families of the cuprates (BSSCO and Na-CCOC), which involves phase-sensitive STM [77] and X-ray [52] measurements, have now unveiled the form factor $P_{\boldsymbol{Q}}(\boldsymbol{k})$ to be predominantly of a d-wave nature, i.e. $P_{\boldsymbol{Q}}(\boldsymbol{k}) \sim (\cos k_x - \cos k_y)$. In addition, as already mentioned above, almost all the experiments point towards a strong evidence for the wavevector $\boldsymbol{Q}$ to be along the Cu-O bonds, i.e. $(\pm Q_0, 0)$

and $(0, \pm Q_0)$, where Q_0 decreases with increasing hole-doping (and is therefore, incommensurate). For an underlying 'large' putative Fermi surface, which is absent in this regime (as known from photoemission experiments, which only see fermi-'arcs'), these wavevectors would nest regions in the vicinity of, but away from the antinodes: $(\pi, 0)$ and $(0, \pi)$.

On the other hand, there is a recent X-ray observation [4] in the La-based cuprates, which seems to indicate a dominant $s'-$form factor (where $P_{\boldsymbol{Q}}(\boldsymbol{k}) \sim (\cos k_x + \cos k_y)$), and this has been ascribed to the presence of magnetic stripe order in these compounds [231, 20]. The nature of the bond-density waves seen in the two different 'classes' of cuprate superconductors is therefore qualitatively different—both in terms of the predominant form-factor, and, in terms of the doping dependence of the wavevector.

In fig. 1.13 we provide an illustration of unidirectional BDWs with different components of $P_{\boldsymbol{Q}}(\boldsymbol{k})$ in real space for both commensurate as well as incommensurate wavevectors. It is not a coincidence that the patterns of fig.1.13 (c), (f) and the data of Kohsaka et al. [125] in fig.1.11(d), (e) look remarkably similar. This comparison has recently been carried out to a remarkable degree of precision in the phase-sensitive work of Fujita et al.[77], which has pinned down the symmetry to be predominantly d-wave.

Recent computations of quantum-oscillations due to the BDW order coupled to a 'large' fermi-surface are broadly consistent [11] with the presence of a *nodal electron-pocket* and many of the other experimental observations. However, despite this agreement, there are a number of outstanding puzzles that remain. There are a number of 'open fermi-sheets' that are bound to be present as long as the weak BDW potential

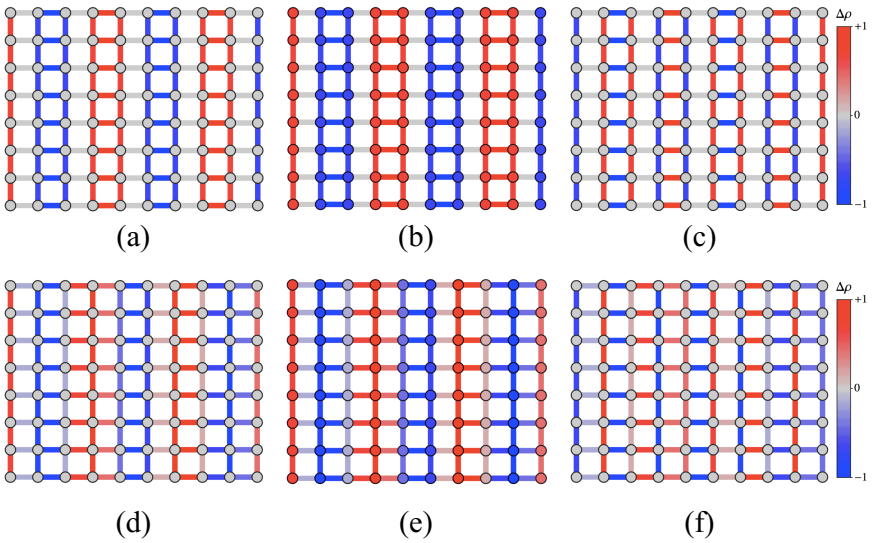

Figure 1.13: Real-space visualization of unidirectional BDW (charge-stripe) with components: $P_s(\boldsymbol{k}) = P_s, P_{s'}(\boldsymbol{k}) = P_{s'}(\cos k_x + \cos k_y)$, and $P_d(\boldsymbol{k}) = P_d(\cos k_x - \cos k_y)$. (a)-(c) we plot the charge modulation for a commensurate wavevector, $\boldsymbol{Q} = 2\pi(\frac{1}{4}, 0)$, while (d)-(f) plot the same quantity for an incommensurate wavevector, $\boldsymbol{Q} = 2\pi(0.3, 0)$. The parameters used are: (a), (d) $P_s = 0, P_{s'} = 1, P_d = 0$. (b), (e) $P_s = 1, P_{s'} = 1, P_d = 0$. (c),(f) $P_s = 0, P_{s'} = 0, P_d = 1$. We have included phases in the definitions of $P_{s,s',d}$ in order to make the charge distribution bond-centered for the case of the commensurate wavevector; however, other choices of the phases are also allowed. Adapted from Ref. [44].

reconstructs a large fermi-surface. Even though these don't contribute to oscillations, the large density of states along these sheets would contribute to various thermodynamic measurements. However, recent measurements of the Knight-shift [116] and specific heat [190] in fields of upto $\sim$ 45 T do not seem to be consistent with the availability of such large density of states at the fermi-level. One could argue that if the BDW potential were to be arbitrarily large, it could gap out these portions of the Fermi surface as well. However, in the presence of such strong *incommensurate* density-wave order, quantum oscillations are likely to be disrupted completely [260].

The above thermodynamics experiments seem to suggest that whatever is causing

the pseudogap to open up close to the antinodes remains unaffected at low to intermediate fields. This leaves us with two options: (*i*) The reconstruction occurs on top of a 'pseudogapped' Fermi surface, so that it is really the arc that gets reconstructed, or, (*ii*) The reconstruction happens in a 'vortex-liquid' phase, where the vortices associated with *d*-wave superconductivity are fluctuating [24]. However, within either of these two scenarios, the nodal electron-pocket is likely to survive, since this region of the Fermi surface remains unaffected, both by *d*-wave superconductivity and by the pseudogap.

Another issue that remains to be resolved with regard to the nature of the charge-order responsible for the oscillations at high fields is as follows. Experiments at zero-fields seem to suggest the presence of a stripe-like order, while the nodal electron-pocket scenario requires a nearly checkerboard order. In order to relate these two regimes, there could be two possibilities: (*i*) There is a field induced transition from a stripe-like BDW at zero or low-fields to a nearly checkerboard-like BDW at high-fields, or, (*ii*) The system actually consists of differently oriented domains with stripe-like order, either within each CuO_2 plane, or within different planes (but with a strong interlayer tunneling) [143], where the typical domain sizes, $\xi_{\rm domain}$, are smaller than the cyclotron-radius. Future experiments will hopefully be able to shed light on this issue.

1.3 Correlated antiferromagnetic metals

A substantial portion of the work reported in this thesis concerns a description of the pseudogap metal and its relation to the forms of broken symmetry observed at low

temperatures in the underdoped cuprates. In section 1.3.1, we introduce a metallic phase where the electrons coexist with a 'quantum-disordered' antiferromagnet. This will be followed by a discussion of the instabilities of a conventional fermi-liquid in the presence of strong antiferromagnetic fluctuations. While this is perhaps not directly relevant for describing the pseudogap phase of the hole-doped cuprates, it leads to key insights on the nature of the symmetry-broken phases observed in the experiments.

1.3.1 Fractionalized Fermi liquid

We now turn to the higher temperature regime just below T^*, significantly above temperatures at which there is any indication of appreciable fluctuating order. Here, as we have discussed earlier, the primary experimental indications of the pseudogap are the suppression in the spin susceptibility, and the appearance of 'Fermi arc' spectra in the electron spectral function (see fig. 1.7).

We review a model of this pseudogap metal as a 'fractionalized Fermi liquid' (FL*). While related states have been derived by many different theoretical methods [245, 254, 113, 184], we begin with a simple toy model description [182] which generalizes the quantum dimer models [123, 191] of insulating spin liquids. [7]

Consider a doped antiferromagnet with p holes per unit cell, as shown in fig. 1.14a. Note that there are p holes with respect to the antiferromagnet, but the number of holes with respect to the filled band insulator is $1 + p$. As p increases, we imagine that the antiferromagnetic order is quickly destroyed, and we obtain a state with p holes in a spin liquid background as shown in fig. 1.14b. Now all the spins of the

[7] We believe that recent results from dynamical mean field theory [72, 80] also point to a low energy effective theory of the pseudogap in terms of such a dimer model [182]

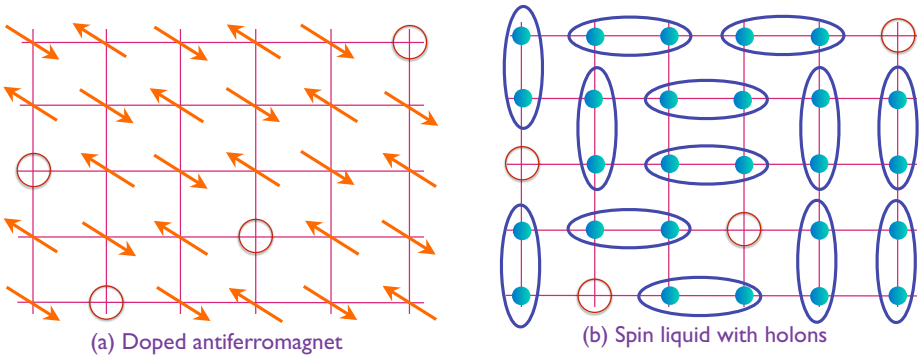

Figure 1.14: (a) A density of p holes per unit cell in an ordered antiferromagnet. The holes are the open circles, while the arrows denote the orientation of the electron spins on the remaining sites. Note that there is a density of $1+p$ holes with respect to the band insulator in which there are 2 electrons on each site. (b) Spin liquid with a density p of spinless holons of charge $+e$. The ellipses represent spin-singlet pairs of electrons in the state $\left(|\uparrow\downarrow\rangle - |\downarrow\uparrow\rangle\right)/\sqrt{2}$.

antiferromagnet have been paired into singlets, and these singlets can resonate with each other [16]. The holes in this spin liquid background carry no spin and charge $+e$ as they move around: so these are 'holons'. This doped spin liquid state also has neutral $S = 1/2$ excitations known as 'spinons', as shown in fig. 1.15a.

So far we have just described the well-known structure of a doped spin liquid. To obtain the FL*, we need one further step: suppose there is an attractive potential between the holons and spinons so that they form bound states with charge $+e$ and spin $S = 1/2$ (a rationale for this attractive potential is given in the caption of fig. 1.15a). For simplicity, let us take the strong coupling limit in which this bound state involves only nearest neighbor sites, and so can be represented by a dimer, as shown[8] in fig. 1.15b. If the binding energy is large enough, every holon will pay the

[8] The bound state is represented in fig. 1.15b by an arrow, and this represents an electron which is in a bonding orbital between the two sites. In a three-band model, this can be associated with an electron on the O orbital between the Cu orbitals. However, our analysis does not require the three-band model, and applies equally to the one-band Hubbard model.

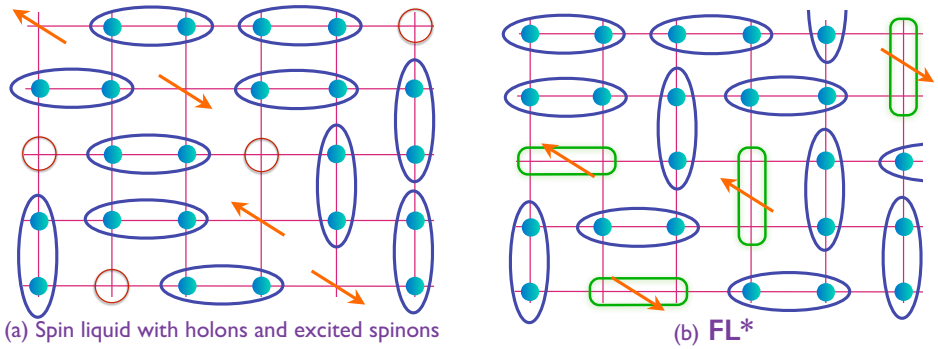

Figure 1.15: (a) An excited state of the doped spin liquid, with neutral $S = 1/2$ spinon excitations represented by the arrows. Both the holons and the spinons can move independently in the spin liquid background. Note the holon and spinon on nearest neighbors in the middle of the figure: the electron can easily exchange positions between these sites, and this can lead to a holon-spinon bound state in which the electron is in a bonding orbital between the two sites. (b) The FL* state: All holons have paid the energy cost to create a spinon from the spin liquid, and the resulting bound state is represented by the green dimers. The green dimers are fermions carrying charge $+e$ and spin $S = 1/2$, and their motion in the spin liquid background realizes a metal with Fermi surfaces enclosing an area equivalent to a density of p fermions of spin $S = 1/2$.

energy cost needed to create a spinon out of the spin liquid background, and we obtain a spin liquid doped only by fermionic dimers carrying charge $+e$ and spin $S = 1/2$.

The dynamics of this FL* is now described by a quantum dimer model [182] in which the fermionic dimers and the original spin singlet pairs resonate with each other. This leads to motion of the fermionic dimers, and as there is a dilute gas of them, we can expect them to form a metallic state with a Fermi surface. The quasiparticles near the Fermi surface will now have the same quantum numbers as in a Fermi liquid, but they differ in key aspects:

- The volume enclosed by the Fermi surface in a FL* is equivalent to a density of p spin $S = 1/2$ particles of charge $+e$. In contrast, in a Landau Fermi liquid

the equivalent density would be $1 + p$.

- The FL* has a second independent sector of low energy 'topological' excitations. In the quantum dimer model, these are associated with the resonances of the spin-singlet dimers, which are represented in analytical formulations by emergent gauge fields.

- The quasiparticles near the Fermi surface are neutral under the emergent gauge field. In the quantum dimer model presented here, this is a consequence of the fact that the fermions are themselves also dimers. Indeed, the fermions couple to the gauge field non-minimally as *dipoles*. This coupling is not strong enough to disrupt the quasiparticle nature of the Fermi surface excitations.

The dimer model picture demonstrates the inevitability of the above characteristics of the FL*: the fermionic dimers have density p, while the remaining sites are required to have spin-singlet dimers representing the gauge field. In Ref. [173, 215, 175], general arguments have been given which demonstrate that any violation by a Fermi surface of the $1 + p$ Luttinger volume requires the presence of low energy topological excitations.

The following subsections will move beyond this dimer toy-model picture of the FL* phase, and review field theoretic analyses which yield a metallic state with the same basic characteristics. Such analyses allow us to compute the Fermi surface structure, understand potential low T instabilities of the FL* metal, and also connect to other phases in the global cuprate phase diagram; these will be carried out in chapter 6.

Field-theoretic description

We begin our description of the FL* metal by first reviewing a standard description for the evolution of antiferromagnetism in metallic phases of the one-band Hubbard model. This model is widely believed to contain the essential physics of the cuprates [16], for electrons hopping on the sites of a square lattice,

$$H_{\rm hubbard} = H_t + H_U, \tag{1.28}$$

$$H_t = -\sum_{i<j} t_{ij} c^\dagger_{i\alpha} c_{j\alpha} - \mu \sum_i c^\dagger_{i\alpha} c_{i\alpha}, \tag{1.29}$$

$$H_U = U \sum_i \left(n_{i\uparrow} - \frac{1}{2} \right) \left(n_{i\downarrow} - \frac{1}{2} \right), \tag{1.30}$$

where t_{ij} represent the hopping parameters, U is the on-site Coulomb repulsion, μ represents the chemical potential and $\alpha = \uparrow, \downarrow$ are the spin-indices. The fermions satisfy the standard anti-commutation relations, $\{c_{i\alpha}, c^\dagger_{j\beta}\} = \delta_{ij}\delta_{\alpha\beta}$ and $\{c_{i\alpha}, c_{j\beta}\} = 0$. This completely defines the problem at hand that has eluded an exact solution.

Anticipating the metallic state to be in the vicinity of an antiferromagnetic instability close to half-filling, we use the exact operator equation,

$$U \left(n_{i\uparrow} - \frac{1}{2} \right) \left(n_{i\downarrow} - \frac{1}{2} \right) = -\frac{2U}{3} \boldsymbol{S}_i^2 + \frac{U}{4}, \tag{1.31}$$

valid on each site, i, and where $\boldsymbol{S}_i = c^\dagger_{i\alpha} \boldsymbol{\sigma}_{\alpha\beta} c_{i\beta}/2$. Upon decoupling the interaction via a Hubbard-Stratanovich transformation, we obtain

$$\exp\left(\frac{2U}{3} \sum_i \int d\tau \boldsymbol{S}_i^2 \right) = \int \mathcal{D}\boldsymbol{J}_i(\tau) \exp\left(-\sum_i \int d\tau \left[\frac{3}{8U} \boldsymbol{J}_i^2 - \boldsymbol{J}_i \cdot \boldsymbol{S}_i \right] \right). \tag{1.32}$$

We can now integrate out the fermions from the action and look for the saddle point of the resulting action for $\boldsymbol{J}_i$. This leads to the Néel state with a wavevector, $\mathbf{K} = (\pi, \pi)$.

In the long-wavelength limit, it is then useful to introduce a field, $\boldsymbol{\varphi}_i$,

$$\boldsymbol{J}_i = \boldsymbol{\varphi}_i e^{i\mathbf{K}\cdot\boldsymbol{r}_i}. \tag{1.33}$$

This is then the familiar route towards arriving at the "spin-fermion" model,

$$\mathcal{Z} = \int \mathcal{D}c_\alpha \mathcal{D}\boldsymbol{\varphi}\, \exp(-\mathcal{S}), \tag{1.34}$$

$$\mathcal{S} = \int d\tau \left[\sum_{\boldsymbol{k}} c^\dagger_{\boldsymbol{k}\alpha}(\partial_\tau - \varepsilon_{\boldsymbol{k}}) c_{\boldsymbol{k}\alpha} - \lambda \sum_i c^\dagger_{i\alpha} \boldsymbol{\varphi}_i \cdot \boldsymbol{\sigma}_{\alpha\beta} c_{i\beta} e^{i\mathbf{K}\cdot\boldsymbol{r}_i} \right] + \int d\tau\, d^2\boldsymbol{r} \left[\frac{\mathrm{v}^2}{2}(\nabla_{\boldsymbol{r}}\boldsymbol{\varphi})^2 + \frac{1}{2}(\partial_\tau \boldsymbol{\varphi})^2 + \frac{s}{2}\boldsymbol{\varphi}^2 + \frac{u}{4}(\boldsymbol{\varphi}^2)^2 \right]. \tag{1.35}$$

The first term in $\mathcal{S}$ is just the kinetic energy of the fermions, and the second term

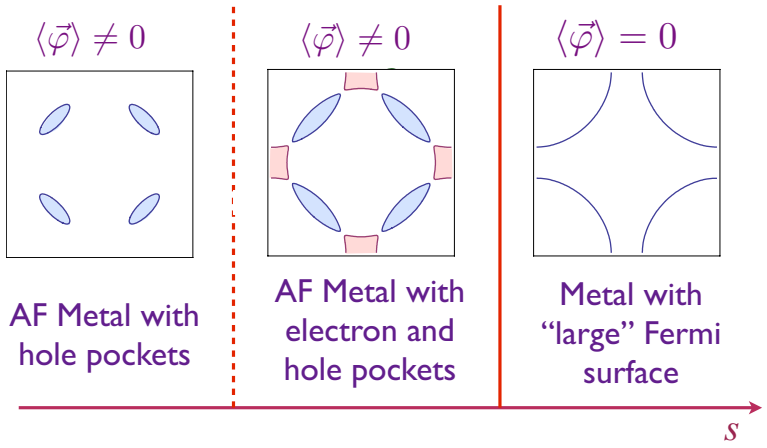

Figure 1.16: The evolution from a 'large' Fermi surface (for $\langle\boldsymbol{\varphi}\rangle = 0,\ s > s_c$) to a reconstructed Fermi surface with electron (red) and hole (blue) pockets in the presence of antiferromagnetic (AF) order with a finite $\langle\boldsymbol{\varphi}\rangle \neq 0$ ($s < s_c$) across a SDW QCP at $s = s_c$. By moving sufficiently deep inside the SDW phase, one has a metallic state with only hole-pockets in the presence of a large $\langle\boldsymbol{\varphi}\rangle$.

is the "Yukawa" coupling term that leads to the spin-fluctuation mediated scattering of fermions from one portion of the Fermi surface to the other. The momentum of the boson, $\boldsymbol{\varphi}$, is small, and v represents a characteristic spin-wave velocity. The last line in the above action is just the φ^4- field theory for an $N = 3$ order-parameter.

At mean-field level, as we tune the value of s, we go from a metallic fermi-liquid phase with a 'large' Fermi surface ($s > s_c$) to a metal with reconstructed electron and hole pockets ($s < s_c$). The gap due to the SDW order parameter opens up at the 'hot-spots', where $\varepsilon_{\boldsymbol{k}} = \varepsilon_{\boldsymbol{k}+\mathbf{K}} = 0$. With a decreasing s, as $\langle \boldsymbol{\varphi} \rangle$ increases in magnitude, only the hole pockets remain (fig.1.16).

So far, apart from possible exotic behavior at quantum critical points, we have only obtained conventional Fermi liquid phases. To obtain the FL*, we have to switch from the above description of SDW order by a "soft-spin" $\boldsymbol{\varphi}$ field with large amplitude fluctuations, to a "hard-spin" perspective in which we have primarily *angular* fluctuations of the antiferromagnetic order. So we replace $\boldsymbol{\varphi}$ by a unit vector field $\mathbf{n}$,

$$\boldsymbol{\varphi} \Rightarrow \mathbf{n} \quad , \quad \mathbf{n}^2 = 1. \tag{1.36}$$

The key utility of such a formulation in terms of the unit-length $\mathbf{n}$ field is that it allows us to consider a route to "quantum-disordering" the SDW order in which topological "hedgehog" tunneling events are suppressed [165]. In contrast, the perturbative analysis of the soft-spin theory necessarily proliferates hedgehogs at the zeros of the $\boldsymbol{\varphi}$ field. In such a hard-spin theory, we argue that the evolution of phases in fig. 1.16 can be replaced by the more exotic route shown in fig. 1.17. Now there is an intermediate phase in which there are hole pockets enclosing a volume equivalent to fermions with density p, but without antiferromagnetic order: this is the FL* phase.

Let us turn to an explicit presentation of the theory of a metal with angular fluctuations of antiferromagnetic order. We are only interested in the long-wavelength fluctuations of $\mathbf{n}_i$ while retaining the full lattice dispersions for the fermions. Applying

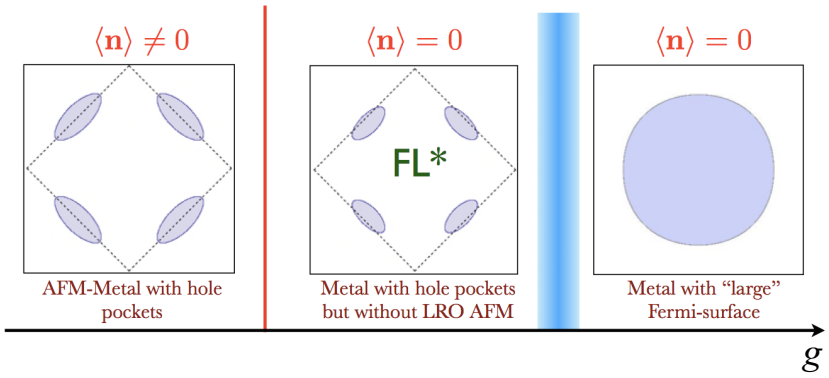

Figure 1.17: Alternative route to fig. 1.16 for the loss of antiferromagnetic order in a metal in a theory with *angular* fluctuations of the fixed-length order $\mathbf{n}$. The middle phase is FL*. The evolution from FL* to the large Fermi surface Fermi liquid on the right is addressed in Ref. [46].

(1.36) to (1.35) we obtain the imaginary time Lagrangian, $\mathcal{L} = \mathcal{L}_f + \mathcal{L}_n + \mathcal{L}_{fn}$, with

$$\mathcal{L}_f = \sum_{i,j} c^\dagger_{i\alpha}\Big[(\partial_\tau - \mu)\delta_{ij} - t_{ij}\Big]c_{j\alpha} + \text{h.c.}, \tag{1.37}$$

$$\mathcal{L}_n = \frac{1}{2g}\int d^2\boldsymbol{r}\ [(\partial_\tau \mathbf{n})^2 + \mathrm{v}^2(\nabla\mathbf{n})^2], \tag{1.38}$$

$$\mathcal{L}_{fn} = \lambda\sum_i e^{i\mathbf{K}\cdot\boldsymbol{r}_i}\ \mathbf{n}_i \cdot c^\dagger_{i\alpha}\boldsymbol{\sigma}_{\alpha\beta}c_{i\beta}. \tag{1.39}$$

Now s has been replaced by g to tune the strength of quantum fluctuations associated with the AFM order parameter. We assume g is a generic coupling measuring the degree of frustration in the insulating antiferromagnet, which can drive the insulator into a non-magnetic state with valence bond solid (VBS) order across a deconfined quantum critical point [214]. It is therefore useful to consider the phase diagram of a general class of frustrated doped antiferromagnets, as a function of the coupling g and the charge density p. This will be discussed in detail in chapter 6.

It is useful to note that for $g < g_c$, the above model has long-range antiferromagnetic order, $\langle\mathbf{n}\rangle \neq 0$ (with a correlation length, $\xi \to \infty$), which reconstructs the large

Fermi surface. The interesting regime is when $g \geq g_c$, which we argue is relevant to the physics of the non-La-based cuprates. The deconfined critical point $g = g_c$ and $p = 0$ is expressed not in terms of the $\mathbf{n}$ fields, but in terms of the spinor z_α, with $\mathbf{n}_i = z^*_{i\alpha}\boldsymbol{\sigma}_{\alpha\beta}z_{i\beta}$ and a U(1) gauge field A_μ. At the same time [184], one tranforms the underlying electrons, $c_{i\alpha}$, to a new set of spinless fermions, ψ_{ip},

$$c_{i\alpha} = R^i_{\alpha p}\psi_{ip}, \quad \text{where} \tag{1.40}$$

$$R^i_{\alpha p} = \begin{pmatrix} z_{i\uparrow} & -z^*_{i\downarrow} \\ z_{i\downarrow} & z^*_{i\uparrow} \end{pmatrix}, \tag{1.41}$$

is a spacetime dependent SU(2) matrix ($\sum_\alpha |z_{i\alpha}|^2 = 1$) and the fermions ψ_{ip} carry opposite charges $p = \pm 1$ under the same emergent U(1) gauge transformation. Note that the above parametrization introduces a large SU(2) 'gauge' redundancy and it is possible to embed the U(1) gauge-theory within the larger SU(2) gauge structure. Some interesting consequences of this SU(2) structure, and their relation to metallic quantum criticality without broken-symmetries, will be discussed in chapter 7.

While we defer the technical details of constructing the FL* state to chapter 6, we note here that a strong attractive force, which is naturally present in the field-theory construction, binds the z_α and ψ_p quanta into gauge-neutral fermions [113, 115, 184]. These gauge-neutral fermions start to notice each other via the Pauli principle, and so they form Fermi surfaces leading to the FL* state (see fig.1.18a). The FL* is a conventional fermi-liquid phase, as far as its transport, thermodynamic or spectral properties are concerned. However, as noted above, the subtle difference arises from the presence of topological order. The spectral weight on the 'back-side' of these pockets is suppressed strongly. It has been argued that the fermi-arcs in the pseudogap

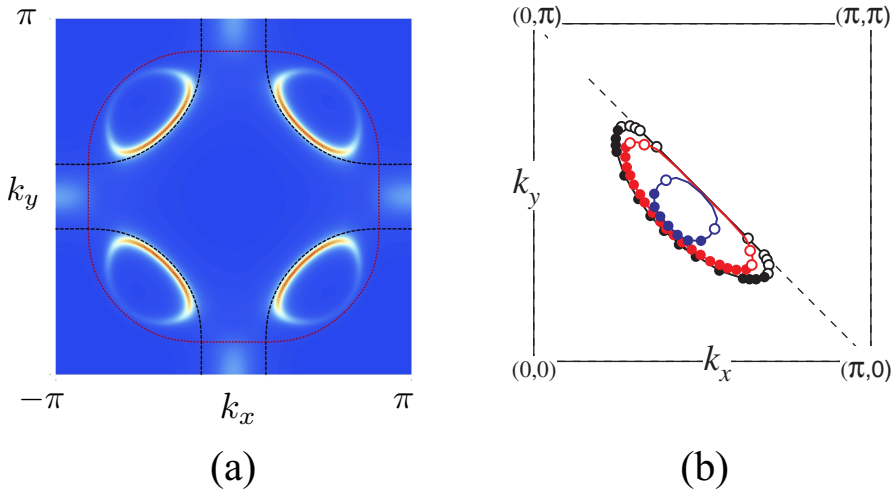

Figure 1.18: (a) Spectral function of the FL* state computed in Ref. [184]. (b) Photoemission measurements of the pseudogap phase for three different samples by Yang *et al.* in Ref. [253]. Note that only filled circles correspond to measured data-points.

regime could in fact be modeled as pockets whose back-sides are (almost) invisible (see fig. 1.18b and Refs. [254, 253]). However, clear signatures of the 'back-sides' are currently lacking in experiments.

Finally, we note a recent experiment [21], which sheds new light on the nature of the metallic states as a function of hole-doping, p. Measurements of the Hall-coefficient at high-fields and low-temperature reveal some interesting, and perhaps, surprising results. As a function of decreasing p, there are two separate transitions (see fig. 1.19). At higher-doping ($p_h \approx 19\%$), there is a transition from a conventional fermi-liquid, with $1 + p$ carriers, to a metallic state with p carriers and no broken translational symmetry. The metallic state with only p carriers would be consistent with an FL* with reconstructed hole-pockets; the presence of a background spin-liquid is crucial for the reconstruction and violation of Luttinger's theorem as noted above

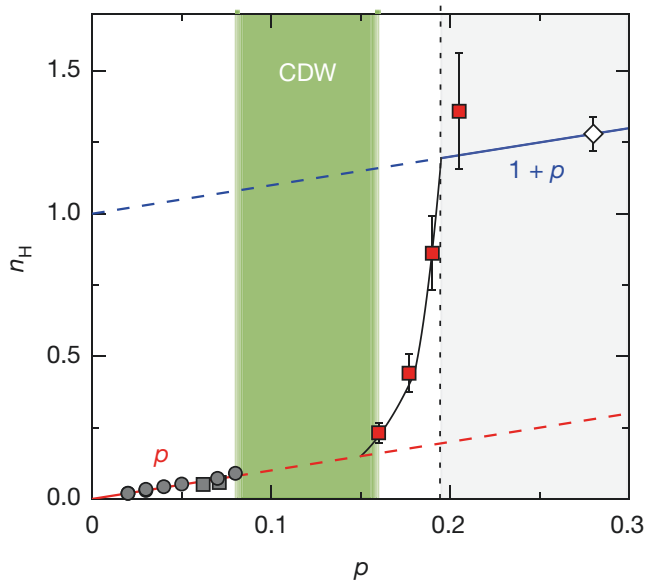

Figure 1.19: Doping dependence of the Hall number, $n_H = V/(eR_H)$, in hole-doped cuprates at a field of 80T. Adapted from Ref.[21].

[173, 215, 175]. The subsequent transition at lower doping ($p_l \approx 16\%$), corresponds to the onset of quasi long-ranged charge density wave and an associated change in sign of the Hall-coefficient.

1.3.2 Instabilities of a Fermi liquid with antiferromagnetic correlations

For the sake of completeness it is useful to review the instabilities of a conventional Fermi liquid state in the presence of antiferromagnetic interactions. This will be useful when studying the instabilities of the FL* state discussed above in chapter 6. We return now to the soft-spin theory in Eq. (1.16) for the properties of a Landau Fermi liquid in the presence of amplitude fluctuations of a SDW order. Starting from

Eq. (1.16) it is useful to focus on the low energy theory for fermions near the 'hot spots' on the Fermi surface, shown in fig. 1.20. Such a Lagrangian is given by,

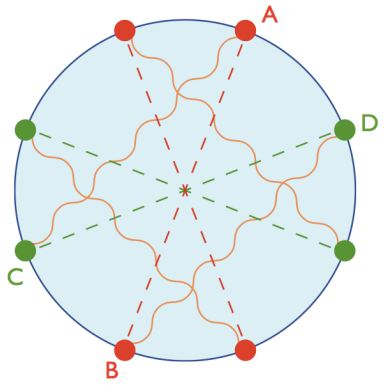

Figure 1.20: A cartoon of a large Fermi surface, with the filled electronic states in blue. The red and green circles represent the 'hot-spots' connected by $\mathbf{K}$ (shown as wavy lines).

$$\begin{aligned}
\mathcal{L}_{sdw} &= \mathcal{L}_f + \mathcal{L}_\varphi + \mathcal{L}_{f\varphi}, \\
\mathcal{L}_f &= \psi_{1p}^{\dagger m}(\partial_\tau - i\boldsymbol{v}_1^m \cdot \nabla)\psi_{1p}^m + \psi_{2p}^{\dagger m}(\partial_\tau - i\boldsymbol{v}_2^m \cdot \nabla)\psi_{2p}^m, \\
\mathcal{L}_{f\varphi} &= \frac{\lambda}{\sqrt{N_f}}\,\boldsymbol{\varphi} \cdot (\psi_{1p}^{\dagger m}\boldsymbol{\sigma}_{pp'}\psi_{2p'}^m + \psi_{2p}^{\dagger m}\boldsymbol{\sigma}_{pp'}\psi_{1p'}^m),
\end{aligned} \tag{1.42}$$

and where $\mathcal{L}_\varphi$ part of the action was already written down in Eq.1.35. In the above, $\boldsymbol{v}_1^m$, $\boldsymbol{v}_2^m$ represent the velocities at the hot-spots labelled 'A', 'C' or 'B', 'D' within each hot-spot pair (denoted by 'm').

Before proceeding any further, let us first digress for a bit and discuss an interesting (exact) symmetry associated with the exchange-interactions [7, 135, 56], that also manifests itself as an emergent symmetry [154] of the hot-spot theory. To start

with, consider just the nearest neighbor Heisenberg term,

$$H_J = \sum_{i<j} J_{ij} \boldsymbol{S}_i \cdot \boldsymbol{S}_j, \tag{1.43}$$

where $\boldsymbol{S}_i$ is expressed in terms of the underlying electronic operators in the usual way. If we, for instance, make the transformation, $c^\dagger_{i\uparrow} \to c_{i\downarrow}$, $c^\dagger_{i\downarrow} \to -c_{i\uparrow}$, then $S^z_i = n_{i\uparrow} - n_{i\downarrow} \to S^z_i$ and similarly for $S^\pm_i$. The above particle-hole transformation carried out on every site leaves the Hamiltonian invariant.

It is possible to generalize the above transformations to arbitrary SU(2) rotations in particle-hole space. In order to do this, let us introduce the Nambu spinors,

$$\Psi_{i\uparrow} = \begin{pmatrix} c_{i\uparrow} \\ c^\dagger_{i\downarrow} \end{pmatrix}, \quad \Psi_{i\downarrow} = \begin{pmatrix} c_{i\downarrow} \\ -c^\dagger_{i\uparrow} \end{pmatrix}. \tag{1.44}$$

Then, H_J can be re-expressed as,

$$H_J = \frac{1}{8} \sum_{i<j} J_{ij} \left(\Psi^\dagger_{i\alpha a} \boldsymbol{\sigma}_{\alpha\beta} \Psi_{i\beta a} \right) \cdot \left(\Psi^\dagger_{j\gamma b} \boldsymbol{\sigma}_{\gamma\delta} \Psi_{j\delta b} \right), \tag{1.45}$$

where a, b are Nambu indices. It is now a trivial matter to see that H_J is invariant under independent SU(2) pseudospin transformations acting on each lattice site of the form $\Psi_{i\alpha a} \to U_{i,ab} \Psi_{i\alpha b}$.

We note that this pseudospin symmetry is broken explicitly by terms involving Coulomb repulsion and a finite chemical potential (except when we are at a fine-tuned, half-filled state). However, an interesting feature of the low-energy critical theory in Eq.1.42 is that the SU(2) symmetry re-emerges. To see this, note that in Eq.1.42, if we carry out the following transformations,

$$\psi^\dagger_{1\uparrow} \to \psi_{1\downarrow},\ \psi^\dagger_{1\downarrow} \to -\psi_{1\uparrow},\ \psi^\dagger_{2\uparrow} \to \psi_{2\downarrow},\ \psi^\dagger_{2\downarrow} \to -\psi_{2\uparrow}, \boldsymbol{\varphi} \to \boldsymbol{\varphi}, \tag{1.46}$$

then $\mathcal{L}_{sdw}$ is invariant because,

$$\psi^\dagger_{1\uparrow}(\boldsymbol{v}_1\cdot\nabla)\psi_{1\uparrow}\to\psi^\dagger_{1\downarrow}(\boldsymbol{v}_1\cdot\nabla)\psi_{1\downarrow}=\psi_{1\downarrow}(\boldsymbol{v}_1\cdot\nabla)\psi^\dagger_{1\downarrow}=\psi^\dagger_{1\downarrow}(\boldsymbol{v}_1\cdot\nabla)\psi_{1\downarrow}, \tag{1.47}$$

where we have used integration-by-parts. The remaining terms can be simplified similarly. Note that it is crucial for the curvature-terms to be absent in order for this symmetry to manifest itself. The SDW theory with 4 pairs of hot-spots therefore has an emergent $[\mathrm{SU}(2)]^4$ symmetry, in addition to the usual spin SU(2) rotation symmetry.

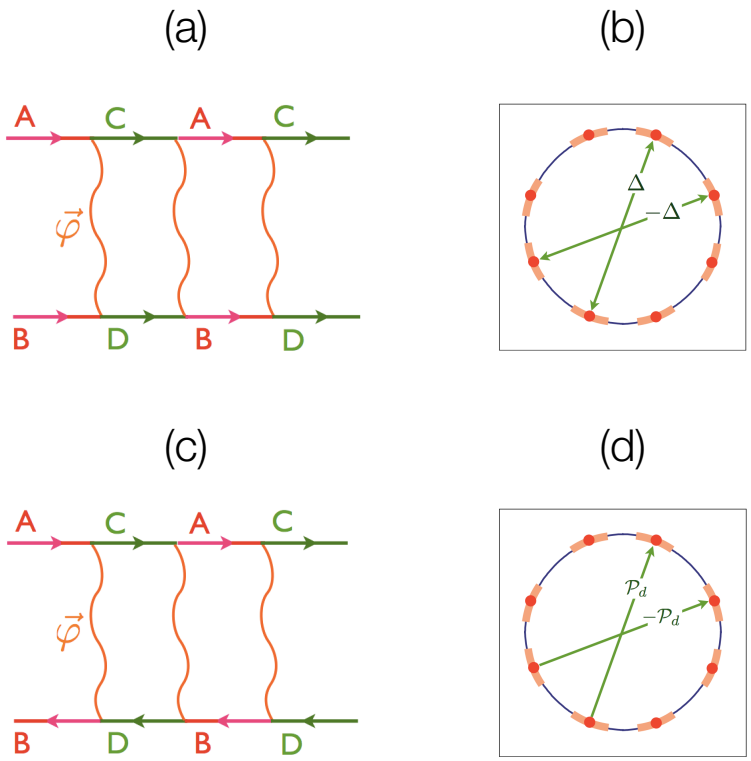

Figure 1.21: (a) 'Cooperon'-diagram in the particle-particle channel leads to (b) d-wave pairing with a relative phase-shift between pairs 'A-B' and 'C-D'. (c) 'Diffuson'-diagram in the particle-hole channel, obtained from (a) by carrying out the SU(2) transformation on only half of the hot-spot pairs leads to (d) d-form factor density wave with $\boldsymbol{Q}=2k_F$ and a relative phase-shift between pairs 'A-B' and 'C-D'.

Returning to the problem of a fermi-liquid in the presence of SDW fluctuations, we recall a result that has now been known for almost three decades. The spin-fluctuations give rise to a pairing-glue in the $d_{x^2-y^2}$ channel [201, 158], as can be seen by explicitly evaluating the 'Cooperon' diagram (fig.1.21(a), (b)). The underlying reason for the attraction in the sign-changing d-wave channel can be traced back to the BCS gap-equation for the pairing gap $\Delta_{\boldsymbol{k}}$:

$$\Delta_{\boldsymbol{k}} = -\sum_{\boldsymbol{p}} \frac{\chi(\boldsymbol{p}-\boldsymbol{k})}{2E_{\boldsymbol{p}}}\ \Delta_{\boldsymbol{p}}. \tag{1.48}$$

$\chi(\boldsymbol{p}-\boldsymbol{k})$ is the SDW susceptibility, peaked at $\boldsymbol{p}-\boldsymbol{k}=\mathbf{K}$, the momentum carried by the SDW order-parameter and $E_{\boldsymbol{p}} = \sqrt{\varepsilon_{\boldsymbol{p}}^2 + \Delta_{\boldsymbol{p}}^2}$ is the dispersion for the Bogoliubov quasiparticles. In order for the above equation to have a non-trivial solution, $\mathrm{sgn}(\Delta_{\boldsymbol{k}}) = -\mathrm{sgn}(\Delta_{\boldsymbol{p}})$, whenever $\boldsymbol{p}-\boldsymbol{k}=\mathbf{K}$.

We can now use the SU(2) symmetry to carry out a particle-hole transformation on only the electrons in the vicinity of 'B' and 'D' (fig.1.20). This then suggests that the same antiferromagnetic fluctuations would give rise to 'pairing' in the particle-hole channel as well, as shown by the 'diffuson' diagram in fig.1.21(c). The particle-hole condensate, $\langle c^{\dagger}_{\boldsymbol{k}-\boldsymbol{Q}/2,\alpha} c_{\boldsymbol{k}+\boldsymbol{Q}/2,\alpha}\rangle$, now carries a finite center-of-mass momentum, $|\boldsymbol{Q}| = 2k_F$ and there is an internal $d_{x^2-y^2}$ form-factor, $\mathcal{P}_d$ (fig.1.21 (d)). Note that this wavevector will always be oriented along a diagonal direction, i.e. it is of the form $\boldsymbol{Q} = (Q_0, \pm Q_0)$.

For the hot-spot theory, the superconducting and density-wave instabilities are exactly degenerate. However, a finite curvature which breaks the SU(2) symmetry will lift this degeracy. While the superconducting instability remains unaffected (since $\pm\boldsymbol{k}$ are always 'nested'), the density-wave instability becomes sub-leading to

superconductivity.

The most natural question, in light of our discussion so far, is as follows: *Is there any relation between the density-wave instability found above in the vicinity of a SDW quantum-critical point to the state unveiled in the underdoped cuprates?*

We shall first address the above question, within a 'weak-coupling' picture, in chapter 5, where we shall also study the feedback of superconducting fluctuations on the density-wave order. However, various discrepancies between theory and experiment will lead us to investigate the instabilities of a 'normal' state that already has a well-developed pseudogap, without any symmetry-breaking, i.e. investigate the instabilities of a state that has fermi-'arcs', and not a large Fermi surface. This will leads us to investigate the instabilities of the FL* introduced earlier in chapter 6.

We note however that computing the ordering instabilities of the FL* metal is a far more complicated task than that for the Fermi liquid described above. Apart from instabilities associated with particle-particle and particle-hole excitations near the Fermi surface, we also have to consider the instabilities associated with the gauge sector. For the U(1)-FL* case, the latter contain monopole tunneling events which necessarily lead to confinement and broken symmetries at low temperatures. There has been partial progress on these difficult issues [176], but we shall not review them here.

In Section 1.3.1, both prescriptions of arriving at the FL* relied on starting from the antiferromagnetic insulator and doping it with charge-carriers. A natural question to ask is how to connect the metallic FL* phase with a 'small' Fermi surface to the 'large' Fermi surface metal. We shall investigate a possible route towards studying

this transition in chapter 7.

1.4 Organization of thesis

In the remainder of this thesis we will study in close detail many of the problems that have been discussed in previous sections. We summarize the main findings of the chapters below.

The thesis consists of three parts. In chapters 2 and 3, we have analyzed various aspects of symmetry breaking and quantum criticality in the superconducting phase of the iron-based superconductors. In chapter 2, motivated by STM experiments on FeSe, we will construct a phenomenological theory for the competition between nematic order and superconductivity in the vicinity of a vortex induced by an applied magnetic field. We find that when there is weak bulk nematic order at zero magnetic field, the field-induced eccentricity of the vortex core has a slow power-law decay away from the core. Conversely, if the nematic order is field induced, then the eccentricity is confined to the vortex core.

In chapter 3, we first present a general theory of the singularity in the London penetration depth at symmetry-breaking and topological quantum critical points within a superconducting phase. We find that while the critical exponents and ratios of amplitudes on the two sides of the transition are universal, an overall sign depends upon the interplay between the critical theory and the underlying Fermi surface. For the case of SDW critical point, we note implications for the maximum observed in the London penetration depth in P-doped $BaFe_2As_2$ at optimal doping. In particular, we find that there is no maximum in the penetration depth at the QCP; instead there

is merely a change in the sign of the second derivative. Therefore, in the second part of this chapter, we argue that the transition possibly becomes weakly first order in the vicinity of optimal doping, and disorder induces puddles of superconducting and antiferromagnetic regions at short length scales; thus, the system becomes an electronic *microemulsion*. We propose that frustrated Josephson couplings between the superconducting grains suppress the superfluid-density and additionally give rise to a highly nontrivial feature in the low-frequency optical response.

In the second part, in chapters 4 and 5, we have analyzed the role of thermal fluctuations on the pseudogap and the associated density-wave phenomenology. In chapter 4, we compute the electronic spectrum in the presence of thermally fluctuating charge-density and superconducting orders in the zero-field and intermediate temperature regime. Our results are compatible with some of the experimental trends as a function of energy, angle around the fermi-surface and temperature. In chapter 5, we explore the landscape of the (sub-)leading density-wave instabilities of a metal interacting via antiferromagnetic fluctuations. For a cuprate-like large fermi-surface, the leading instability in the particle-hole channel is to a $d-$form factor density wave with a diagonal wavevector, with a subleading instability to a predominantly $d-$form factor density wave with axial wavevector. By examining the feedback of superconducting fluctuations on all the allowed charge-density wave states, we find that over at least a small temperature window, they prefer the experimentally observed wave vector.

In the final section of the thesis, in chapters 6 and 7, we present an alternative view of the pseudogap. In chapter 6, we present an analysis of the charge ordering instabil-

ities in a FL* metal, where the electronic excitations are coupled to the fractionalized excitations of a quantum fluctuating antiferromagnet on the square lattice. The resulting state, a BDW*, has predominantly $d-$form factor and wavevectors along the axial direction, in agreement with experiments on a number of different families of the cuprates. We therefore propose that the pseudogap regime can be described by such a FL* metal at least over intermediate length and energy scales. In chapter 7, we analyze a novel quantum phase transition without any broken symmetries between metals with large and small Fermi surfaces of spinless fermions carrying the electromagnetic charge of the electron. The two metals have emergent SU(2) and U(1) gauge fields respectively, and the transition is driven by the condensation of a real Higgs field, carrying a finite lattice momentum and an adjoint SU(2) gauge charge. This Higgs field measures the local antiferromagnetic correlations in a "rotating reference frame."

Chapter 2

Nematic order in the vicinity of a superconducting vortex

"Symmetry is what we see at a glance; based on the fact that there is no reason for any difference..." - Blaise Pascal, Pensées

2.1 Introduction

In the preceding chapter, we saw that unconventional superconductors typically have an exceedingly rich phase diagram, determined by the interplay of multiple competing, or coexisting, types of order. Nematic order (which breaks the C_4 symmetry of the underlying square lattice down to C_2) has been shown to emerge in certain regimes of the phase diagrams of the copper-oxide [18, 94, 125, 59, 130, 151] and the iron-based [68, 251, 49, 48, 255, 168, 256] superconductors. In the latter case, the nematic order accompanies (and in some cases, precedes) the magnetic order which

occurs at a wavevector that breaks the lattice rotational symmetry.

Recently, the structure of the vortex cores in the mixed state of clean FeSe films was studied by means of scanning tunneling microscopy (STM) [224]. Strong anisotropy was observed in the zero bias conductance map around the cores, which have an eccentricity of the order of unity. Although the lattice structure of FeSe at low temperature is orthorhombic[146], it has been claimed [224] that the crystalline anisotropy (of the order of a few tenths of a percent) is too small to explain the large anisotropy of the vortex cores, which is likely to have an electronic origin.

This experiment raises several questions, some of which we address in this paper: assuming that there is an electronic nematic order in superconducting FeSe, what is its microscopic origin? What is its relation to superconductivity - *e.g.*, are these two types of order competing? Is the nematic order localized in the vortex cores (and hence stabilized by the application of the magnetic field), or does it extend throughout the system (and is only apparent in the STM spectrum near the cores)?

In this chapter, we study the structure of the vortex core using a phenomenological Landau-Ginzburg (LG) theory in terms of two competing order parameters. Using our LG analysis we have calculated the structure of an isolated vortex in the presence of the nematic order. Our main result is that by looking at the profile of the gap near the vortex core, it is possible to distinguish between two different configurations of the nematic order, namely the presence of a localized nematic order within the superconducting vortex as opposed to the presence of a long range nematic order in the system. If the nematic order is localized at the core, the superconducting gap should be anisotropic only near the core and the anisotropy decays exponentially as

we move away from the core. On the other hand, if the nematic order is long-ranged, the superconducting gap should exhibit an anisotropy which decays as a power law. If the nematic order is near its critical point, there is a large region in which the anisotropy of the gap depends logarithmically on the distance, eventually crossing over to a power law. Moreover, we find qualitative differences in the shape of the contours of constant gap around the core in the different cases. If the nematic order exists only in the cores, the equal-gap contours tend to be elliptical; if the nematic order is long-ranged, we find that the gap function tends to develop a "four-lobe" structure, with more pronounced higher harmonics. These features can be sought in STM experiments by mapping the magnitude of the gap around the core as a function of position.

We note at the outset that the Fermionic degrees of freedom, which have been ignored in the study here, are important near the vortex core. In order to deal with them, one has to go beyond the Ginzburg-Landau formalism. We would however like to stress on the fact that even though the GL formalism is not perfectly valid deep in the vortex core, our results for the asymptotic behavior away from the vortex core are robust. Therefore one of our main predictions, which is the difference in the behavior of the gap function far away from the core remains qualitatively valid even though the GL formalism breaks down inside the core [104].

The chapter is organized as follows: In section 2.2 we introduce the LG functional with the two competing order parameters and carry out a preliminary analysis in the absence of the anisotropy. In section 2.3.1, we investigate the mean-field phase diagram of a single vortex. In section 2.3.2, we introduce the anisotropy and perform

a numerical minimization of the functional, commenting on the interesting features. Finally, in section 2.3.3, we present our analytical results explaining the various interesting features observed by minimizing the free energy. Some additional technical details are summarized in appendix A.

2.2 Model

We consider a LG type free energy for two competing order parameters: a complex field Ψ, describing the superconducting order parameter, and a real field ϕ, which describes a nematic order that competes with the superconducting order parameter. The form of the free energy density is given by

$$\mathcal{F} = \mathcal{F}_s + \mathcal{F}_\phi + \mathcal{F}_a + \frac{\gamma}{2}|\Psi|^2\phi^2, \tag{2.1}$$

$$\mathcal{F}_s = \frac{\kappa_\psi}{2}|(-i\nabla - e^*\mathbf{A})\Psi|^2 - \frac{\psi_0^2}{2}|\Psi|^2 + \frac{1}{4}|\Psi|^4, \tag{2.2}$$

$$\mathcal{F}_\phi = \frac{\kappa_\phi}{2}(\nabla\phi)^2 - \frac{\phi_0^2}{2}\phi^2 + \frac{1}{4}\phi^4, \tag{2.3}$$

$$\mathcal{F}_a = \frac{\lambda_1}{2}\phi\left[|(-i\partial_x - e^*A_x)\Psi|^2 - |(-i\partial_y - e^*A_y)\Psi|^2\right] + \frac{\lambda_2}{2}\phi\left[(\partial_x\phi)^2 - (\partial_y\phi)^2\right]. \tag{2.4}$$

Apart from the standard free energy contributions arising due to ϕ and Ψ, we have a competition term, controlled by γ (> 0), and a term that gives rise to different effective masses for Ψ in the two directions, which is controlled by λ_1. $\mathcal{F}$ is invariant under a rotation by 90 degrees, represented by

$$x \to y,\ y \to -x,\ \phi \to -\phi. \tag{2.5}$$

We will be interested in the limit of $\lambda_L(0) \to \infty$, where $\lambda_L(0)$ is the London penetration depth, so that we can neglect the coupling to the electromagnetic field. At the outset, we set $\lambda_2 = 0$, since the λ_2 term is small compared to the λ_1 term in the limit where ϕ is small. It is convenient to define the coherence length of Ψ and the healing length of ϕ as

$$l_\psi = \sqrt{\frac{\kappa_\psi}{\psi_0^2}}, l_\phi = \sqrt{\frac{\kappa_\phi}{\phi_0^2}}. \tag{2.6}$$

Taking the unit of distance to be l_ϕ, we can recast the above free energy in a more transparent form as follows,

$$\begin{aligned} \mathcal{F} &= \frac{1}{2l^2}(\tilde{\nabla}\tilde{\psi}^*)(\tilde{\nabla}\tilde{\psi}) - \frac{1}{2}|\tilde{\psi}|^2 + \frac{1}{4}|\tilde{\psi}|^4 \\ &+ \left(\frac{\gamma}{\gamma_s}\right)^2\left[\frac{1}{2}(\tilde{\nabla}\tilde{\phi})^2 - \frac{1}{2}\tilde{\phi}^2 + \frac{1}{4}\tilde{\phi}^4\right] + \frac{\gamma^2}{2\gamma_s}|\tilde{\psi}|^2\tilde{\phi}^2 \\ &+ \lambda\tilde{\phi}[(\partial_{\tilde{x}}\tilde{\psi}^*)(\partial_{\tilde{x}}\tilde{\psi}) - (\partial_{\tilde{y}}\tilde{\psi}^*)(\partial_{\tilde{y}}\tilde{\psi})], \end{aligned} \tag{2.7}$$

where $l = l_\phi/l_\psi, \gamma_s = \gamma\psi_0^2/\phi_0^2, \lambda = \lambda_1/2l_\phi^2\psi_0^2$, $\tilde{x}, \tilde{y} = x/l_\phi, y/l_\phi$, $\tilde{\psi} = \Psi/\psi_0$, and $\tilde{\phi} = \phi/\phi_0$. From now on, we will drop the tilde symbols.

For $\lambda \neq 0$, a short-distance cutoff has to be imposed on Eq. 2.7. Otherwise, the system is unstable towards developing modulations of ψ with sufficiently short wavelength. We discuss the instability in Appendix A.1. In practice, we will mostly ignore this issue, assuming that there is a short-distance cutoff (which is provided by the finite grid used in our numerical calculations).

Before we begin our analysis, let us comment about the choice of parametrization in this problem. We would like to think of this problem in terms of a fixed $\gamma \leq 1$. Then on choosing a particular ratio of the length scales of ϕ and ψ, we still have one degree of freedom left in terms of the masses or the stiffnesses of the two order

parameters, which is fixed by tuning γ_s.

If we assume that $\gamma_s > 1$, then the uniform ground state is given by $\psi = 1$ and $\phi = 0$. This also constrains ϕ to be localized around the vortex cores, by making the mass term for ϕ positive deep inside the superconducting region. If we further assume that the nematic order is small, such that $\frac{\gamma}{2}\phi^2 \ll \psi_0^2$, then we can essentially ignore the feedback of ϕ on ψ. Therefore, we will first find the full profile of $\psi = \Psi_0$, the isolated vortex solution, in the absence of the nematic order and use that to find the form of the nematic order. Then Ψ_0 satisfies the following asymptotic relations:

$$\Psi_0(\rho) \approx \left[1 - \frac{1}{2}\left(\frac{1}{l\rho}\right)^2\right] e^{i\theta}, \qquad \rho \gg l^{-1} \tag{2.8}$$

$$\Psi_0(\rho) \sim Cl\rho e^{i\theta}, \qquad \rho \ll l^{-1} \tag{2.9}$$

where $\rho = r/l_\phi$, r being the radius in the original coordinate system, and C is a dimensionless constant. In general, it is difficult to find the solution of the full LG equation for Ψ_0 for all ρ analytically. Therefore we obtain the vortex solution $\Psi_0 = f(l\rho)e^{i\theta}$ for all ρ by minimizing the functional in Eqn. 2.7 numerically in the absence of ϕ.

The numerical solution conforms to the two asymptotic expressions above. It is interesting to note that Ψ_0 does not recover from the vortex core to its bulk value exponentially, but rather as a power law [124, 62]. The behavior of $\phi(\rho)$ in the vicinity of a vortex with $\lambda = 0$ was studied by Ref. [124].

2.3 Results

We present all of our results, obtained using a combination of numerical and analytical techniques, in the following subsections.

2.3.1 Phase diagram

We will now describe the mean-field phase diagram of a single vortex in the presence of a competing nematic order. There are three possible phases: in phase I, $\phi = 0$ everywhere; in phase II, ϕ vanishes at large distance from the vortex core but becomes non-zero near the vortex core due to the suppression of the competing ψ field to zero at the core; and in phase III, $\phi \neq 0$ even far away from the core. A non-zero solution for ϕ is favored whenever the smallest eigenvalue ϵ of the following eigenvalue problem [124]:

$$\left[-\nabla_\rho^2 - 1 + \gamma_s [f(l\rho)]^2 \right] \phi(x) = \epsilon \phi(x), \tag{2.10}$$

satisfies $\epsilon < 0$. In order to find the phase diagram, we solve this eigenvalue problem numerically on a discrete grid. The boundary between phases I and II is the locus of points at which the smallest eigenvalue satisfies $\epsilon = 0$. For $\gamma_s < 1$, ϕ becomes long-ranged, corresponding to phase III. The resulting phase diagram is shown in Fig. 2.1. This phase diagram is strictly valid as long as $\gamma_s > \gamma$. If this is not the case, then the state with uniform nematic background and no superconductivity is energetically favorable over any other state.

The physics behind the phase diagram can be understood as follows. When $l_\phi \gg l_\psi$ we are forcing the nematic order to coexist with superconductivity in a large region. This is unfavorable energetically due to the competition term $\gamma\phi^2|\Psi|^2$. Therefore,

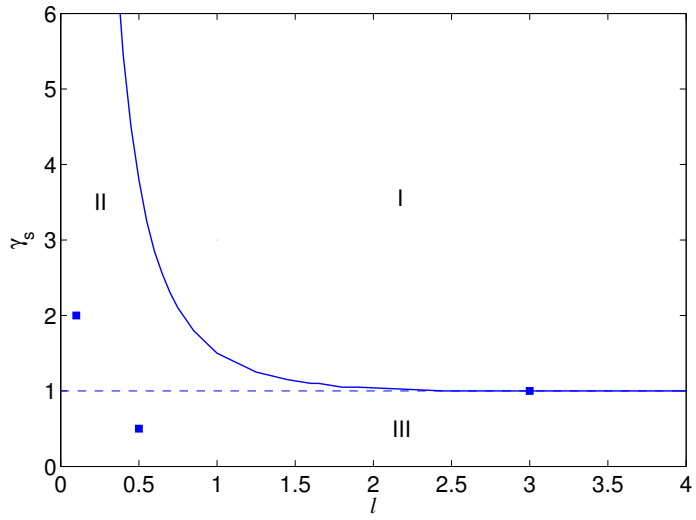

Figure 2.1: The phase diagram in the (γ_s, l) plane obtained by solving Eqn. 2.10 numerically on a grid with $n = 100$ and $\Delta x = 1$. The regions with qualitatively different solutions for ϕ are marked. Phase I has no nematic order with $\phi = 0$ everywhere, phase II has nematic order localized in the vortex core, and phase III has long-range nematic order away from the core. The blue squares correspond to points which we explore in more detail later. The dashed line $\gamma_s = 1$ represents the boundary between phases II and III.

when $\gamma_s > 1$, there is no $\phi \neq 0$ solution. If $\gamma_s < 1$, ϕ becomes non-zero even far away from the vortex core. In the opposite limit of $l_\phi \ll l_\psi$, the nematic order exists deep within the superconducting vortex. Since there is very little overlap between the two order parameters, the system can afford to have a higher value of critical γ_s below which there is a nontrivial nematic order. This explains the increasing trend of the critical γ_s for decreasing l.

In the $l_\phi \ll l_\psi$ case, it is possible to give an analytical expression for the phase boundary between regions I and II. The equation for this curve is given by,

$$\gamma_s = \frac{1}{4(Cl)^2}, \tag{2.11}$$

where C is the constant which appears in Eqn. 2.9. The details of this computation are discussed in Section 2.3.3.

We are now in a position to include the effect of the anisotropy and investigate the structure of the vortex cores in different regions of the phase diagram described above.

2.3.2 Vortex profile in the different regimes

We now turn to discuss the characteristics of the vortex profile in the different regimes shown in Fig. 2.1. To solve for the vortex profile, we minimize the free energy (2.7) with respect to ψ and ϕ numerically on a disk geometry. This is equivalent to solving the coupled Landau-Ginzburg equations with Neumann boundary conditions, as we discuss in Appendix A.2. Many of the features found in the numerical solution can be understood analytically, as we discuss in the next section.

We can expand both ψ and ϕ in terms of the different angular momentum channels ($\sim e^{in\theta}$). The term proportional to λ only couples angular momentum channels that differ by 2 units of angular momentum in ψ. Therefore, in the presence of ϕ, the bare vortex solution ($\sim e^{i\theta}$) gives rise to components of the form $e^{3i\theta}$, $e^{-i\theta}$, etc. Similarly, the feedback of the superconducting order on ϕ gives rise to the generation of the even harmonics, i.e. Φ_0 gives rise to terms proportional to $e^{2i\theta}$ and $e^{-2i\theta}$. It is also possible to have a solution with only the even harmonics of ψ, in which case, the vortex is absent. These two solutions do not mix with each other and therefore we shall focus on the solution in the presence of the vortex.

In light of this, we expand the order parameters as

$$\psi(\rho,\theta)=\sum_n \Psi_n(\rho)e^{i(2n+1)\theta}, \qquad \phi(\rho,\theta)=\sum_n \Phi_n(\rho)e^{i2n\theta}, \qquad n\in \text{integers} \tag{2.12}$$

In terms of the expansions in Eqn. 2.12, the free energy density can be written as,

$$\begin{aligned}
F_\rho &= \int d\theta \mathcal{F} = \sum_n \frac{1}{2l^2}\left[\left(\frac{\partial\Psi_n}{\partial\rho}\right)^2+\frac{(2n+1)^2\Psi_n^2}{\rho^2}\right]-\frac{\Psi_n^2}{2}+\frac{1}{4}\sum_{n,p,q}\Psi_n\Psi_{n+p-q}\Psi_p\Psi_q \\
&+ \left(\frac{\gamma}{\gamma_s}\right)^2\left[\frac{1}{2}\left(\sum_n\left(\frac{\partial\Phi_n}{\partial\rho}\right)^2+\frac{(2n)^2}{\rho^2}\Phi_n^2-\Phi_n^2\right)+\frac{1}{4}\sum_{n,p,q}\Phi_n\Phi_{n+p-q}\Phi_p\Phi_q\right] \\
&+ \frac{\lambda}{2}\sum_{m,p}\phi_p\left[\left(\frac{\partial\Psi_m}{\partial\rho}-(2m+1)\frac{\Psi_m}{\rho}\right)\left(\frac{\partial\Psi_{m+p+1}}{\partial\rho}+(2(m+p+1)+1)\frac{\Psi_{m+p+1}}{\rho}\right)\right. \\
&+ \left.\left(\frac{\partial\Psi_m}{\partial\rho}+(2m+1)\frac{\Psi_m}{\rho}\right)\left(\frac{\partial\Psi_{m+p-1}}{\partial\rho}-(2(m+p-1)+1)\frac{\Psi_{m+p-1}}{\rho}\right)\right] \\
&+ \frac{\gamma^2}{2\gamma_s}\sum_{n,p,q}\Psi_n\Psi_{n+p-q}\Phi_p\Phi_q,
\end{aligned} \tag{2.13}$$

and we are interested in minimizing $\int \rho d\rho F_\rho$. We shall minimize the above free energy for a given system size and for only a fixed number of harmonics at a time. We have kept n harmonics for ψ and ϕ, where for any given n (odd) we take all the harmonics Ψ_{-i} to Ψ_i, $i=(n-1)/2$, and similarly for ϕ. We have tried $n=3,5$ and found no substantial qualitative change in the results that we shall quote here, indicating that the results converge even with only 3 harmonics. We consider a system on a disk of radius $\rho=100$.

Below, we describe the results in regions II and III of the phase diagram, and on the critical line dividing them (In region I, where there is no nematic order, we get the regular circularly symmetric vortex). The specific values of γ_s, l which were used are marked by blue squares in the phase diagram in Fig. 2.1.

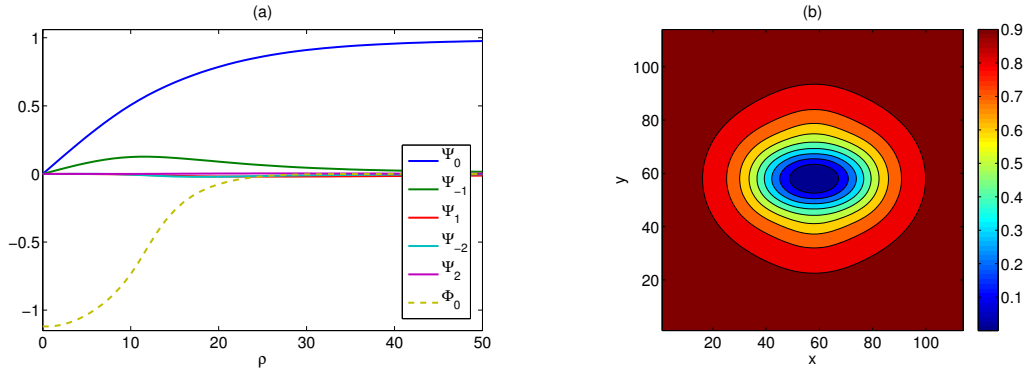

Figure 2.2: Nematic order in phase II. The profiles for the different order parameters for $\gamma_s = 2.0, l = 0.1, \gamma = 1.0, \lambda = 20.0$ for a system size of 100 ($N = 100, \Delta x = 1$). (a) Harmonics of ψ (solid) and Φ_0 (dashed) (b) Contour plot of $|\psi|^2$. The superconducting coherence length l_ψ is 10, in units of l_ϕ.

Region II

In this region, we expect to obtain a solution with a non-zero uniform $|\psi|$ away from the vortex core and a non-zero ϕ localized near the vortex core, decaying exponentially away from the core (given that $\gamma < \gamma_s$ and $\gamma_s > 1$). The contour plot for $|\psi|^2$ is shown in Fig. 2.2. The parameters used here are $\gamma_s = 2.0, l = 0.1, \gamma = 1.0, \lambda = 20.0$.

As can be seen in the figure, the core has an elliptical shape because of the interaction with the nematic order which coexists with superconductivity in the core region. As we go away from the core, the contours of equal $|\psi|^2$ become more and more isotropic, due to the rapid decay of the nematic order away from the core.

Region III

This region in the phase diagram corresponds to the case where there is a uniform nematic background coexisting with superconductivity, even away from the vortex core. In this regime, as we move away from the core, ϕ goes to a constant and ψ

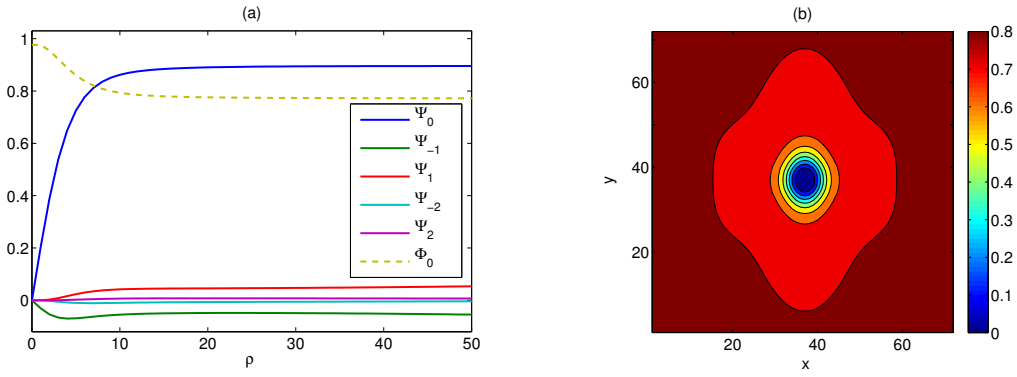

Figure 2.3: Nematic order in phase III. The profiles for the different order parameters for $\gamma_s = 0.5, l = 0.5, \gamma = 0.4, \lambda = 0.5$ for a system size of 100 ($N = 100, \Delta x = 1$). (a) Harmonics of ψ (solid) and Φ_0 (dashed) (b) Contour plot of $|\psi|^2$. The superconducting coherence length is 2, in units of l_ϕ.

remains anisotropic. In Fig. 2.3, the harmonics Ψ_1 and Ψ_{-1} are almost constant for large ρ. Moreover, $\Psi_1 = -\Psi_{-1}$ for large ρ. The contour plot of $|\psi|^2$ reveals a large anisotropic "halo" around the core, with a non-elliptical shape.

Far away from the core, where ϕ is constant, the Landau-Ginzburg equations can be solved analytically, showing that the anisotropy in $|\psi|^2$ decays as a power law in this case. We discuss this solution in the next section.

Critical case

Finally, we discuss the critical line separating regions II and III in Fig. 2.1, in which the ϕ field is critical far away from the core. Naively, one would expect ϕ to go as $1/\rho$ asymptotically in this regime. However, depending on the details of the solution at small ρ, there may be an intermediate regime in which $\phi \sim \ln \rho$, eventually crossing over to $1/\rho$ at a larger distance. This feature is discussed in more detail in the next section. Fig. 2.4a shows ψ and ϕ in the critical regime, with $\gamma_s = 1.0, l = 3.0, \gamma = 0.9$

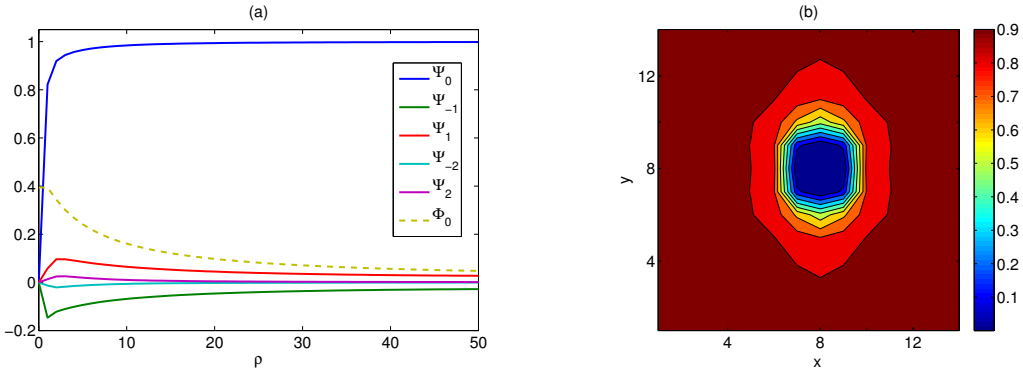

Figure 2.4: Nematic order at the critical point between phase III and phase I. The profiles for the different order parameters for $\gamma_s = 1.0, l = 3.0, \gamma = 0.9, \lambda = 0.07$ for a system size of 100 ($N = 100, \Delta x = 1$). (a) Harmonics of ψ (solid) and Φ_0 (dashed) (b) Contour plot of $|\psi|^2$. The superconducting coherence length is 1/3, in units of l_ϕ.

and $\lambda = 0.07$. Indeed, we observe that ϕ decays slowly away from the core. $\Psi_{\pm 1}$ also have long tails. The contour plot for $|\psi|^2$ shares features that are similar to the behavior in region III, namely a long-range, non-elliptical anisotropic halo. It is shown in Fig. 2.4b.

In the next section, we analyze the asymptotic behavior of the solution in the critical case, showing that the anisotropic component of $|\psi|^2$ falls off as $\sim (\lambda \ln \rho/\rho^2)\cos(2\theta)$ at intermediate ρ, crossing over to $\sim (\lambda/\rho^3)\cos(2\theta)$ at sufficiently large ρ.

2.3.3 Analytical Treatment

In this section, we propose various analytical arguments to explain the different features that were observed above by carrying out the minimization numerically. We first discuss the solution for the nematic order in the presence of superconductivity. Then, we analyze region III of the phase diagram (Fig. 2.1). Finally, we study the linearized GL equations in order to explain some of the other interesting features that

were observed earlier.

Phases of the nematic order

Here we will briefly review the solution for ϕ, and supplement it with some further details. The LG-equation for $\phi(\rho)$, assuming that $\lambda = 0$, is given by,

$$\Big[-\nabla_\rho^2 - 1 + \gamma_s[f(l\rho)]^2 + \phi^2 \Big]\phi = 0, \tag{2.14}$$

We shall now be interested in solving the linearized version of the above equation, which is justified for $\gamma_s > 1$. For $\rho \ll l^{-1}$, this becomes equivalent to solving the problem

$$\Big[-\nabla_\rho^2 - 1 + \gamma_s \left(Cl\rho\right)^2 \Big]\phi = 0. \tag{2.15}$$

This is identical to solving the Schrödinger equation for the 2D quantum harmonic oscillator. We know that $\phi'(\rho = 0) = 0$. The solution for this equation is given by

$$\phi(\rho) = e^{-\sqrt{\gamma_s C^2 l^2}\rho^2/2} \frac{\mathcal{L}_a(\sqrt{\gamma_s C^2 l^2}\rho^2)}{\mathcal{L}_a(0)}, \quad a = \frac{1 - 2\sqrt{\gamma_s C^2 l^2}}{4\sqrt{\gamma_s C^2 l^2}}, \tag{2.16}$$

where $\mathcal{L}_n(x)$ are the Laguerre polynomials. The profiles of $\phi(\rho)$ for a few different values of $\gamma_s C^2 l^2$ are shown in Fig.2.5.

At this point, we can also describe how we obtained the equation for the phase boundary between regions I and II in the phase diagram (Fig. 2.1). In this case, ϕ is non-zero only very close to the center of the core. We can therefore expand ψ around $\rho = 0$ and keep only the leading order term (Eq. 2.9). Eqn.2.15 can be re-written as,

$$\Big[-\frac{\nabla_\rho^2}{2} + \frac{\gamma_s C^2 l^2}{2}\rho^2 \Big]\phi = (\frac{1}{2} + \epsilon)\phi. \tag{2.17}$$

Non-trivial solutions exist for $\epsilon \leq 0$. The above equation is the Schrödinger equation for a quantum harmonic oscillator in two dimensions with $m = 1, \omega^2 = \gamma_s(Cl)^2$. Then

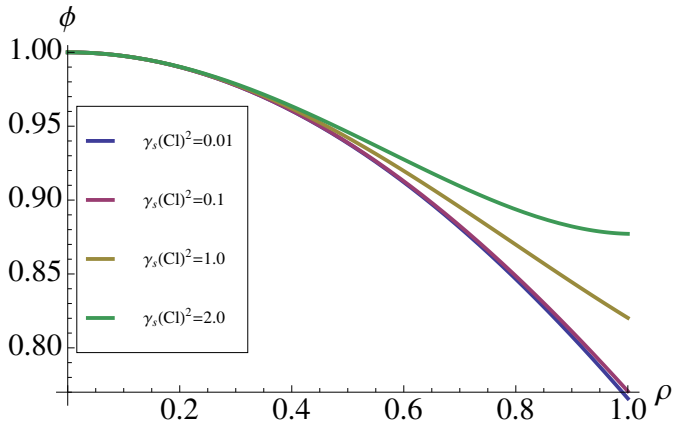

Figure 2.5: The profiles of ϕ as a function of ρ for different values of $\gamma_s C^2 l^2$ over a distance of one correlation length of ϕ, l_ϕ.

.

the smallest eigenvalue which corresponds to the zero point energy of the oscillator leads to the following equation for the curve

$$\gamma_s = \frac{1}{4(Cl)^2} \tag{2.18}$$

in the limit of small l.

On the other hand, for $\rho \gg l^{-1}$, we have to solve

$$\left[-\nabla_\rho^2 - 1 + \gamma_s \left(1 - \frac{1}{(\rho l)^2} \right) \right] \phi = 0, \tag{2.19}$$

from which we see that $\phi(\rho) \sim \rho^{-1/2} \exp(-\sqrt{\gamma_s - 1}\rho)$. However, there is a *fine-tuned* point at $\gamma_s = 1$, at which the field ϕ is critical far away from the vortex core. The full equation for ϕ becomes

$$\left[-\nabla_\rho^2 - \frac{1}{(\rho l)^2} + \phi^2 \right] \phi = 0, \tag{2.20}$$

$\phi(\rho) = \sqrt{1 + l^2}/(l\rho)$. Note that the $1/\rho$ solution can be obtained only for specific boundary conditions. For generic boundary conditions, with $\phi \to 0$ as $\rho \to \infty$,

the solution is nevertheless asymptotic to $\sqrt{1+l^2}/(l\rho)$ at large ρ. If $\phi(1) \ll 1$, for instance, then $\phi(\rho) \sim A \ln(\rho_0/\rho)$ at intermediate values of ρ, where A and ρ_0 are constants. $\phi(\rho)$ crosses over to $\phi(\rho) \sim 1/\rho$ at radii of the order of $\rho^\star \sim 1/A$ (see Appendix A.3). This behavior reflects itself in the asymptotic decay of the anisotropy of the field ψ away from the vortex core, as we saw in Sec. 2.3.2.

Coexistence of superconductivity and nematic order

In this subsection, we are interested in analyzing region III of the phase diagram, in which superconductivity and nematicity coexist even far away from the core. Let us assume, for simplicity, that far away from the core ϕ can be replaced by a constant. The effect of a constant ϕ is to render the effective masses in the two directions different. Therefore, if we re-scale the coordinates as

$$\begin{aligned} x' &= \frac{x}{\sqrt{1+\alpha}} \\ y' &= \frac{y}{\sqrt{1-\alpha}}, \end{aligned} \tag{2.21}$$

where $\alpha = 2\lambda\phi l^2$, then this problem now becomes identical to the isotropic problem we had solved in the beginning of section 2.2. The solution for Ψ_0 can then be written in terms of the new coordinates as,

$$\begin{aligned} \Psi_0 &= \frac{f(r')}{r'}(x' + iy'), \\ f(r') = c\left(1 \right. &- \left. \frac{1}{2l^2c^2r'^2}\right), \quad c = \sqrt{1 - \frac{\gamma^2\phi^2}{\gamma_s}} \end{aligned} \tag{2.22}$$

Note that due to the presence of the background nematic order, Ψ_0 does not tend to 1 asymptotically. We now go back to our original coordinate system x, y by expanding

the above result to linear order in α. Then we get,

$$\psi = c\left(1 - \frac{1}{2l^2c^2r^2}\right)e^{i\theta} - \frac{\alpha c}{4}\left(1 + \frac{1}{2l^2c^2r^2}\right)e^{-i\theta} + \frac{\alpha c}{4}\left(1 - \frac{3}{2l^2c^2r^2}\right)e^{3i\theta} \tag{2.23}$$

In the above expression, the first bracket corresponds to Ψ_0, the second bracket corresponds to Ψ_{-1} while the last one represents Ψ_1. It is interesting to observe that asymptotically, Ψ_1 and $-\Psi_{-1}$ approach the same constant value. We observe this feature in Fig.(2.3a). However, the harmonics do not recover to their asymptotic value as a power law, which is a result of the boundary conditions that were imposed while minimizing the free energy in the disk geometry (see Appendix A.2).

From Eqn. 2.23, we can evaluate the form of $|\psi|^2$ and find that,

$$|\psi|^2 = c^2\left(1 - \frac{1}{l^2c^2r^2}\right) - \frac{\alpha}{l^2r^2}\cos(2\theta) + O(\alpha^2) \tag{2.24}$$

Therefore, asymptotically, $|\psi|^2$ is isotropic and the anisotropy decays as $\sim \alpha\cos(2\theta)/r^2$.

Linearized GL analysis

In this section, we shall carry out an analysis of the linearized LG equations, to give an analytical explanation for some of the features that we have observed by carrying out the full minimization. For the sake of simplicity, let us ignore the feedback on ϕ resulting in the generation of the higher harmonics and assume that ϕ is isotropic (i.e. $\phi(\rho, \theta) = \phi(\rho)$). Then, the linearized LG equations for the harmonics

of ψ can be written as,

$$\begin{aligned}
\frac{1}{l^2}\left(\partial_\rho^2+\frac{\partial_\rho}{\rho}-\frac{(2n+1)^2}{\rho^2}\right)\Psi_n(\rho) &+ \left(1-\frac{\gamma^2}{\gamma_s}\phi^2\right)\Psi_n(\rho)-2\Psi_0^2(\rho)\Psi_n(\rho)-\Psi_0^2(\rho)\Psi_{-n}(\rho) \\
= -\lambda\phi(\rho)\Bigg[\left(\partial_\rho^2-(4n-1)\frac{\partial_\rho}{\rho}\right. &+ \left.\frac{(4n^2-1)}{\rho^2}\right)\Psi_{n-1}(\rho)+ \\
\left(\partial_\rho^2+(4n+5)\frac{\partial_\rho}{\rho}\right. &+ \left.\frac{(2n+3)(2n+1)}{\rho^2}\right)\Psi_{n+1}(\rho)\Bigg] \\
+\lambda\partial_\rho\phi(\rho)\left[\left(\partial_\rho-\frac{2n-1}{\rho}\right)\Psi_{n-1}(\rho)\right. &+ \left.\left(\partial_\rho+\frac{2n+3}{\rho}\right)\Psi_{n+1}(\rho)\right] \qquad (2.25)
\end{aligned}$$

There are some features of the problem that cannot be deduced from a study of the linearized version of the problem, which include the overall scale and sign of ϕ and the signs of the different harmonics of ψ.

In the limit of $\rho \ll l^{-1}$, i.e. inside the vortex core, at leading order $\Psi_n(\rho) \sim \rho^a$, where $a = |2n+1|$. This is a necessary condition for the harmonics to be well behaved in the limit of $\rho \to 0$.

On the other hand, in the limit of $\rho \gg l^{-1}$, i.e deep inside the superconducting region, the homogenous solution for the above equation gives exponentially damped solutions for all the $\Psi_{n\neq 0}$, i.e. the anisotropy is short ranged. Moreover, the source term, which is proportional to $\lambda\phi$ and is itself exponentially damped (Region II), is also not strong enough to give rise to any long ranged solution.

However, when ϕ is critical (i.e. $\gamma_s = 1$), the source term leads to the presence of long tails in the harmonics. In the regime where ϕ falls off logarithmically while Ψ_0 is a constant, at leading order $\Psi_{\pm 1}$ just follow ϕ, i.e. they also fall off logarithmically (with prefactors of equal magnitude but opposite sign) and have a correction of the form $\ln\rho/\rho^2$. On the other hand, when ϕ crosses over to the power law form, at leading order $\Psi_{\pm 1}$ also fall off as $\pm 1/\rho$ with a correction of order $1/\rho^3$.

2.4 Discussion

We have studied the interplay between nematic order and superconductivity in the presence of a vortex. If the nematic order coexists with superconductivity in the vicinity of a vortex core, the coupling between the two order parameters leads to an elongated shape of the core. We discuss two distinct scenarios: in one the nematic order coexists with superconductivity everywhere (i.e., even far away from the vortex core), whereas in the other the competition between the two order parameter suppresses the nematic order in the bulk, and nematicity only exists close to the core where the superconducting order parameter is diminished. Both scenarios lead to an anisotropic core. However, we show that they can, in principle, be distinguished by the way the anisotropy of the superconducting gap decays away from the core. If the nematicity exists only near the core, the anisotropy in the superconducting gap decays exponentially; if it exists throughout the sample, we expect the gap anisotropy to decay as $1/r^2$, where r is the distance from the core. Moreover, there are qualitative differences in the shape of the core in the two cases. In the former case, in which only the core region is nematic, the contours of equal gap tend to be more or less elliptical. In the latter case, the contours of equal gap tend to develop non-elliptical shapes with a four-petal pattern. Therefore, analyzing the gap profiles measured by STM around a vortex could reveal the nature of the nematic ordering - whether it is localized at the vortex core, or coexists with superconductivity in the bulk.

So far, we have discussed the structure of an isolated vortex at the mean-field level. However, if the nematic ordering is favored only within a vortex core, an isolated vortex cannot have static nematic order, since either thermal or quantum fluctuations

would destroy such order. Static nematic order is only possible when the density of vortices is finite. The coupling between the nematic halos of different vortices scales as $J_{\text{eff}} \sim \exp[-d/(\sqrt{1-\gamma_s} l_\phi)]$, where $d \sim 1/\sqrt{B}$ is the inter-vortex distance (B is the applied magnetic field). The system can be described by an effective two-dimensional transverse field Ising model with a spin-spin interaction J_{eff} and a B-independent transverse field. (Note that, unlike Ref. [124], we are considering a thin film, rather than a three-dimensional system.) This model has a nematic transition at a certain critical B, which should be seen, e.g., by measuring the anisotropy of the vortex cores as a function of B. If an external rotational symmetry breaking field exists, as is presumably the case in FeSe due to the small orthorhombic lattice distortion[146], the electronic nematic transition is smoothed out. However, one still expects a sharp crossover as a function of magnetic field if the orthorhombic distortion is sufficiently weak.

The microscopic origin of the anisotropic vortex cores observed in FeSe[224] remains to be understood. It is likely that it originates from electronic nematicity rather than from the lattice distortion, since the experimentally reported orthorhombic distortion seems too small to produce such a large effect. The electronic nematic order could have an orbital character[223, 128, 41, 255]. Alternatively, it could arise from a field-induced magnetic ordering[129] [1] at a wavevector $(\pi, 0)$ or $(0, \pi)$ in the one iron unit cell, which is necessarily accompanied by a nematic component (similar to the ordering in the iron arsenides). Although static ordering of this type has not been observed in the iron selenides[147], it remains to be seen if they develop a static

[1] Similar to the magnetic field induced antiferromagnetic order seen in certain cuprate superconductors.

ordering in the presence of an applied magnetic field. Neutron scattering experiments revealed a magnetic resonance at this wavevector in the superconducting state of FeTeSe[185, 160]. Moreover, ordering at such wavevectors nearly nests the electron and hole pockets, and therefore it is expected to couple strongly to superconductivity, explaining why the resulting anisotropy of the vortex cores is so large.

Chapter 3

Quantum Phase Transitions beneath the superconducting dome

"Once you eliminate the impossible, whatever remains, no matter how improbable, must be the truth." - Sir Arthur Conan Doyle

3.1 Introduction

An important focus of the study of the high temperature superconductors has been the quantum criticality of the onset of spin density wave (SDW) order within the superconducting phase. There is clear evidence across many different families of compounds that SC appears in close proximity to an AFM phase (see fig. 1.5 and ref. [200]); these families include the iron-pnictides, the electron-doped cuprates and the heavy-fermion superconductors. Moreover, the optimal transition temperature (T_c) of the SC is often situated where the normal state AFM quantum critical point (QCP)

would have been located, in the absence of superconductivity. The experimental detection of the QCP is often challenging in the normal state, and more so in the superconducting state.

A number of neutron scattering experiments have observed critical spin fluctuations in hole-doped LSCO [118, 6, 120, 40] and YBCO [95], and in electron-doped NCCO [164]. The phase diagrams of the iron-based superconductors show a clear overlap between the SDW and superconducting phases [57].

As reviewed in section 1.2.2, a number of measurements (fig.1.8a) were reported in a member of the pnictide family, $BaFe_2(As_{1-x}P_x)_2$, as a function of the isovalent P-doping, x. The experiments show a phase transition involving onset of spin-density wave (SDW) order in the normal state above T_c, which extrapolates to a $T = 0$ SDW QCP (see [218] and references therein). These experiments include: (i) a sharp enhancement in the effective mass, m^*, upon approaching a critical doping from the overdoped side, as obtained from de Haas-van Alphen oscillations [220] and from the jump in the specific-heat at T_c [242] , and, (ii) a vanishing Curie-Weiss temperature (θ_{CW}), extracted from the $1/T_1T$ measurements using NMR.

A number of puzzling results have appeared from experiments investigating whether the SDW QCP actually survives "under the SC dome." A novel feature of these observations is that the influence of the magnetic critical point appears to have been observed in a property of the superconducting phase, the London penetration depth. As discussed in section 1.2.2, the penetration depth has a sharp peak around $x = x_c$ (fig.1.8b). Such an observation supports the proposal that the 'same' electrons are involved in both the SDW order and superconductivity, and that these two orders are

strongly coupled [195].

This chapter is organized into two parts. In the first part in section 3.2, we provide a general theory of the singularity in the superfluid stiffness and the London penetration depth near a wide class of symmetry-breaking or topological transitions within superconductors in two spatial dimensions. A careful analysis will demonstrate that the singularities associated with the critical fluctuations of an order parameter in a clean system are unable to account for the experimental observations. This will lead us to the second part in section 3.3, where we propose a possible mechanism for the strong suppression of the superfluid density in the vicinity of the putative QCP.

3.2 Singularity of the penetration depth at quantum critical points

We shall begin in section 3.2.1 by describing the field-theory for the transitions of interest in the presence of an external probe gauge-field. For the benefit of the reader, our results for the singular structure of the penetration depth, which is related to the superfluid stiffness, are summarized in Fig. 3.1 for 3 cases labelled A, B, C; they will be derived in section 3.2.2. Case A (B) refers to the onset of SDW (nematic) order, leading to a transition from SC to SC+SDW (SC+nematic SC). Case C corresponds to a more exotic deconfinement transition to a fractionalized SC phase.

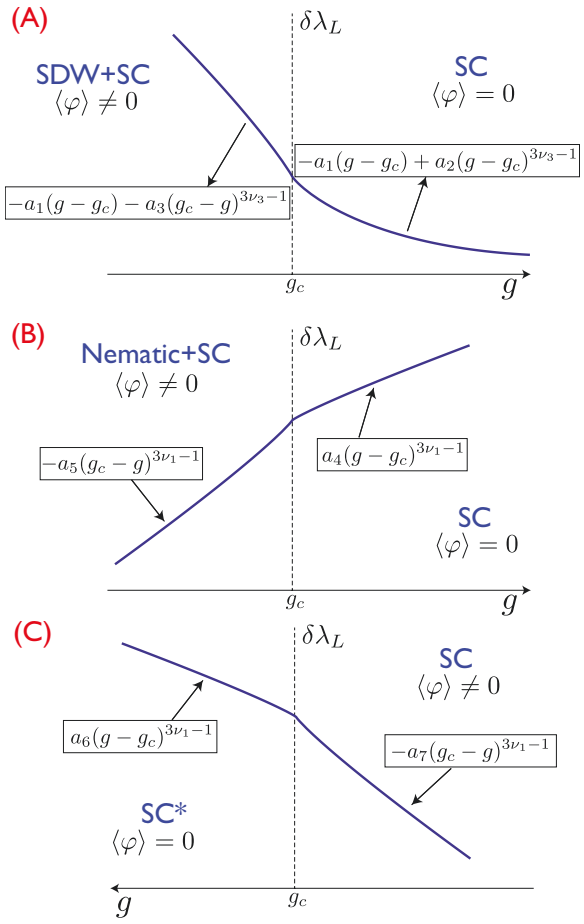

Figure 3.1: Main results for the singular behavior of the London penetration depth, λ_L in (A) onset of spin density wave order leading to transition from SC to SDW+SC, (B) onset of nematic order, and (C) a deconfinement transition to a fractionalized SC* phase. These transitions are tuned by a generic zero temperature parameter g, and the quantum critical point is at $g = g_c$. The coupling C_2 in Eq. (3.2) has values which are (A) negative, (B) positive (or negative, depending on the underlying details of the band-structure), (C) positive. *All* the prefactors a_{1-7} are *positive*, and some of their ratios are universal: $a_2/a_3 = 1.52$ and $a_4/a_5 = a_6/a_7 = 0.52$. The correlation length exponents are $\nu_1 = 0.631$ and $\nu_3 = 0.710$. For case A, we have included a non-singular term $-a_1(g - g_c)$ because it is larger than the singular terms; cases B,C can also have such non-singular terms, but here they are subdominant to the singular terms.

3.2.1 Model

All three cases, labelled A, B, C are described by the familiar φ^4 field theory of a N-component field φ with imaginary time (τ) action:

$$\mathcal{S}_\varphi = \frac{1}{2}\int d^2x d\tau \left[(\partial_\tau \varphi)^2 + c^2(\nabla_x \varphi)^2 + (g - g_c^0)\varphi^2 + \frac{u}{2}(\varphi^2)^2\right], \tag{3.1}$$

where c is a velocity of the collective mode excitations of the ordered phase, g_c^0 is the bare critical point, and u is a strongly-relevant self-interaction between φ fluctuations. The transition is taking place within the superconducting phase, but we can ignore the fluctuations of the phase of the superconducting order because these are suppressed by the long-range Coulomb interactions.

As written, the theory $\mathcal{S}_\varphi$ has no direct coupling to the external magnetic field for cases A and B [1], and so cannot influence the superfluid stiffness and the London penetration depth. In these two cases, the vector potential $\mathbf{A}$ of the external field couples to the underlying electrons, as does the order parameter φ. We will describe below the theory of the electrons coupled to both φ and $\mathbf{A}$, and obtain an effective Lagrangian by integrating out the electronic degrees of freedom. While performing this integration we assume that wavevectors, q, of φ obey $q\xi_{sc} \ll 1$ where ξ_{sc} is the coherence length of the superconductor. At the same time, q is of order the correlation length, ξ^{-1}, of fluctuations of the bosonic mode φ; consequently, the validity of our theory is limited to the critical region where $\xi \gg \xi_{sc}$. With $q\xi_{sc} \ll 1$, we can safely evaluate all gapped fermion loops at $q = 0$, and this leads to a simple and local effective Lagrangian after the fermions have been accounted for. Moreover, in case C

[1] Since the order parameters characterizing the broken symmetry are gauge neutral under the external vector potential.

the external magnetic field couples to the "dual" Ising field φ directly so that in all the three cases, one ends up with,

$$\mathcal{L}_{\text{eff}}[\mathbf{A}, \varphi] = C_1 \mathbf{A}^2 + C_2 \mathbf{A}^2 \varphi^2, \tag{3.2}$$

where $C_{1,2}$ are constants to be evaluated in section 3.2.2 below.

Case A & B: SDW and Nematic criticality

We now describe the microscopic model and low-energy field theory for the computation of C_2 for case A & B with SDW and nematic order respectively. We consider models appropriate for the cuprates and pnictides, and also the model in Ref. [30], of electrons $c_{i,a\alpha}$ on sites i with orbital index a and spin index α in a SC state described by

$$H = -\sum_{\substack{ij \\ ab}} t_{ab,ij} c^\dagger_{i,a\alpha} c_{j,b\alpha} + \sum_{\mathbf{k},a} \Delta^a_{\mathbf{k}} c_{\mathbf{k},a\uparrow} c_{-\mathbf{k},a\downarrow} + \text{H.c.} \tag{3.3}$$

where $t_{ab,ij}$ are the hopping matrix elements, and $\Delta^a_{\mathbf{k}}$ is the pairing amplitude. These electrons are coupled to the 3-component SDW order parameter φ_m via a Yukawa-coupling

$$H_{sdw} = w \sum_i \varphi_m(i)\, c^\dagger_{i,a\alpha} \sigma^m_{\alpha\beta} c_{i,b\beta}\, e^{i\mathbf{K}\cdot\mathbf{r}_i} \tag{3.4}$$

where σ^m are the Pauli matrices and $\mathbf{K}$ is the SDW ordering wavevector. We choose the superconducting pairing function $\Delta^a_{\mathbf{k}}$ so that points on the Fermi surface connected by $\mathbf{K}$ always have pairing amplitudes with opposite sign: this is the type of spin-singlet superconductivity found in both the cuprates and the pnictides. Finally, we introduce an external magnetic field by a vector potential $\mathbf{A}$ in the gauge $\nabla \cdot \mathbf{A} = 0$

via a Peierls substitution in the hopping matrix elements t_{ij}. Then conventional many-body perturbation theory in the coupling w leads to the Feynman diagrams in Fig 3.2, generating terms $\sim C_2\mathbf{A}^2\varphi^2$. It is worth noting that a three-point coupling, $\sim C_3\mathbf{A}_\perp\varphi^2$, where $\mathbf{A}_\perp$ is the transverse component of $\mathbf{A}$, is also generated upon integrating out the fermions, but $C_3 = 0$ within the critical region $\xi \gg \xi_{sc}$.

A similar analysis applies to the nematic ordering transition in case B. The order parameter φ has only one component, and its coupling to the electrons in the pairing channel is

$$H_{\text{nematic}} = w\varphi \sum_{\mathbf{k},a} c_{\mathbf{k},a\uparrow} c_{-\mathbf{k},a\downarrow} + \text{H.c.} \tag{3.5}$$

In order to proceed with the diagrammatic perturbation theory, it is more convenient to re-write the bands as $c_{\mathbf{k},1} \to \psi_{\mathbf{k},1}$ and $c_{\mathbf{k},2} \to \psi_{\mathbf{k}+\mathbf{K},2}$ [30]. We have therefore shifted the ψ_2 fermions by $\mathbf{K}$, the ordering wave-vector; expressing the Yukawa term in terms of $\psi_{1,2}$ is more convenient. The action on a lattice with sites i, j for the SDW problem ($N = 3$ component order parameter, φ) is then given by, $\mathcal{S} = \int_0^\beta d\tau(\mathcal{L}_F + \mathcal{L}_\varphi + \mathcal{L}_{F\varphi})$, where

$$\mathcal{L}_F = \sum_{\substack{i,j \\ \alpha,a}} \psi^\dagger_{i,a\alpha}\left[(\partial_\tau - \mu)\delta_{ij} - t_{a,ij}e^{ie\mathbf{A}_{ij}.(\mathbf{r}_i - \mathbf{r}_j)}\right]\psi_{j,a\alpha}, \tag{3.6}$$

$$\mathcal{L}_\varphi = \frac{1}{2}\sum_i \frac{1}{c^2}\left(\frac{d\varphi_i}{d\tau}\right)^2 + \frac{1}{2}\sum_{\langle i,j\rangle}(\varphi_i - \varphi_j)^2 + \sum_i\left(\frac{g - g_c^0}{2}\varphi_i^2 + \frac{u_0}{4}\varphi_i^4\right), \tag{3.7}$$

$$\mathcal{L}_{F\varphi} = w\sum_i \psi^\dagger_{i,1\alpha}(\boldsymbol{\sigma}_{\alpha\beta}.\varphi_i)\psi_{i,2\beta} + \text{h.c.} \tag{3.8}$$

In the above action, μ is the chemical potential, $t_{a,ij}$ represent the hopping parameters, w is an $O(1)$ Yukawa coupling, $\boldsymbol{\sigma}$ are the Pauli matrices acting in spin-space and $(g - g_c^0), u_0$ are the bare mass and non-linear self-coupling of the φ field, respectively.

As before, $a(=1,2)$ represents the orbital label and α, β represent the spin labels. We have introduced an external gauge field, $\mathbf{A}_{ij} = \sum_{\mathbf{q}} \mathbf{A}_{\mathbf{q}}\, e^{i\mathbf{q}.(\boldsymbol{r}_i+\boldsymbol{r}_j)/2}$, defined at the center of each bond i, j. We only need terms up to $O(\mathbf{A}^2)$ in order to compute ρ_S.

Upon expanding $\mathcal{L}_F$ (in the normal state) in powers of $\mathbf{A}_{ij}$ till second order, we obtain,

$$\begin{aligned}
\mathcal{L}_F &= \sum_{\mathbf{k},a,\alpha} [i\omega - \xi_a(\mathbf{k})] \psi^\dagger_{\mathbf{k},a\alpha} \psi_{\mathbf{k},a\alpha} \\
&+ \sum_{\substack{\mathbf{k},\mathbf{q} \\ a,\alpha}} \mathbf{v}_a(\mathbf{k},\mathbf{q}).\mathbf{A}_{\mathbf{q}}\; \psi^\dagger_{\mathbf{k}+\mathbf{q},a\alpha} \psi_{\mathbf{k},a\alpha} \\
&+ \sum_{\substack{\mathbf{q},\mathbf{q}',\mathbf{k} \\ a,\alpha,i}} K^i_a(\mathbf{q},\mathbf{q}',\mathbf{k}) A^i_{\mathbf{q}} A^i_{\mathbf{q}'} \psi^\dagger_{\mathbf{q}+\mathbf{q}'+\mathbf{k},a\alpha} \psi_{\mathbf{k},\alpha a} + \text{h.c.},
\end{aligned} \tag{3.9}$$

where $\xi_a(\mathbf{k}) = \varepsilon_a(\mathbf{k}) - \mu$ and $\varepsilon_a(\mathbf{k}) = -\sum_{i,j} t_{a,ij} e^{i\mathbf{k}.(\mathbf{r}_i - \mathbf{r}_j)}$ are the dispersions of the orbitals. The paramagnetic current density is given by $\mathbf{v}_a(\mathbf{k},\mathbf{q}) = e\nabla_k \xi_a(\mathbf{k}+\mathbf{q}/2)$ and $K^i_a(\mathbf{q},\mathbf{q}',\mathbf{k}) = e^2 \partial^2_{k_i} \xi_a(\mathbf{k}+\mathbf{q}/2+\mathbf{q}'/2)/2$ is the kinetic-energy density along direction i.

We shall work in the superconducting state and introduce pairing gaps Δ_a on the different orbitals by hand, instead of solving for the gaps self-consistently. There is reason to believe that there are accidental (loop-like) nodes on the electron-pockets in the $s^{\pm}$ state in this particular material (see refs. [86, 219, 261, 159]). However the nodal excitations don't quantitatively affect our conclusions provided they don't coincide with the hot-spots and couple to the low energy order parameter modes.

In order to carry out a diagramatic analysis, we work with the Nambu (i.e. normal and anomalous) Green's functions, which can be written in the following 2×2 matrix

notation,

$$\begin{aligned}
\hat{G}_a(\boldsymbol{p}, i\omega_n) &= \begin{pmatrix} \mathcal{G}_a^0(\boldsymbol{p}, i\omega_n) & -\mathcal{F}_a^0(\boldsymbol{p}, i\omega_n) \\ -\mathcal{F}_a^0(\boldsymbol{p}, i\omega_n) & -\mathcal{G}_a^0(-\boldsymbol{p}, -i\omega_n) \end{pmatrix}, \text{where} \\
\mathcal{G}_a^0(\mathbf{p}, i\omega_n) &= -\frac{i\omega_n + \xi_a(\mathbf{p})}{\omega_n^2 + E_a^2(\mathbf{p})}, \text{ and, } \mathcal{F}_a^0(\mathbf{p}, i\omega_n) = -\frac{\Delta_a}{\omega_n^2 + E_a^2(\mathbf{p})}. \qquad (3.10)
\end{aligned}$$

In the above, $E_a(\boldsymbol{p}) = \sqrt{\xi_a^2(\boldsymbol{p}) + \Delta_a^2}$, $\Delta_1 = \Delta$, $\Delta_2 = -\Delta$ (for the $s_\pm$ state) and $\mathcal{G}^0, \mathcal{F}^0$ are the normal and anomalous Green's functions. For the special case of the problem with only one-band, see appendix B.

The superfluid density, ρ_s, can be inferred from the current-current correlation function by taking the limits of the external frequency and momentum to zero in the correct order [193, 200]. When we take $\mathbf{A} = (A^x, 0)$, then the superfluid density is given by,

$$\begin{aligned}
\frac{\rho_s}{\pi e^2} &= \mathcal{K}_{xx}(q_x = 0, q_y \to 0, i\omega_n = 0), \qquad (3.11) \\
\mathcal{K}_{xx}(\mathbf{q}, 0) &= \left. \frac{\delta^2 \ln \mathcal{Z}}{\delta A^x_{\mathbf{q}} \delta A^x_{-\mathbf{q}}} \right|_{\mathbf{A}=0}, \qquad (3.12)
\end{aligned}$$

where $\mathcal{Z} = \int \mathcal{D}\varphi \; e^{-\mathcal{S}_{\text{eff}}}$ is the partition function of the theory corresponding to $\mathcal{L}_{\text{eff}}(\mathbf{A}, \varphi)$ in Eqn.3.2. Let us analyze case (A) first, since case (B) proceeds in an almost identical fashion. Upon integrating out the fermions and retaining terms up to second order in $\mathbf{A}$, one generates couplings between the vector potential and the SDW field.

The bare BCS contribution, ρ_{BCS} is given by C_1 and can be computed in a standard fashion. The leading singular contribution to the superfluid density at the QCP comes from the other terms above (see fig. 3.2). The term corresponding to $C_3 \mathbf{A}_\perp \varphi^2$ consists of a "triangle" graph, but with the paramagnetic current vertex. When the external

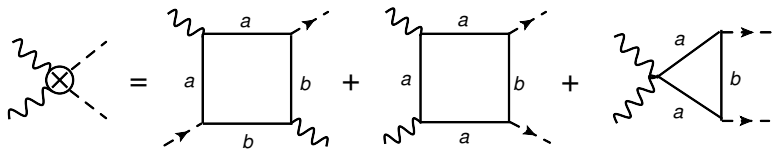

Figure 3.2: The four-point coupling (crossed circle) between $\mathbf{A}$ and φ after integrating out the Fermions. The wavy and the dashed lines represent the gauge field and the φ fields respectively. The solid lines represent Fermions having a Nambu structure, with $a \neq b$ for case (A), while $a = b$ for case (B).

momentum of the gauge field is zero, these diagrams only depend on the momentum of the SDW fluctuation. However, the fermions are all gapped with a typical energy scale Δ that is much larger than the SDW energy scale in the vicinity of the QCP. When the SDW mode goes soft at the critical point, it can't exchange energy/momentum with the massive fermions, which leads the two degrees of freedom to decouple. The couplings then reduce to contact interaction, independent of the momentum (and is only determined by the details of the band-structure, gap magnitudes etc.) Therefore, the two sets of diagrams reduce to three- and four-point momentum independent couplings between $\mathbf{A}$ and φ.

Now the generality of framework can be employed. For the nematic problem, φ corresponds to an $N = 1$ (Ising) field. When evaluating ρ_S for the nematic problem, we can compute C_2, the $4-$point coupling between $\mathbf{A}$ and φ, from the same diagrams as in fig.3.2, with a few additional differences; one of these includes the fact that the internal b fermion lines are the same as a (there's an overall sum over the different orbitals).

Case C: Deconfinement transition

Turning to case C, we consider the computation of C_2 for the case of the SC*-SC topological transition, where a rather different treatment is required. We consider models appropriate for heavy-fermion materials consisting of itinerant conduction electrons and localized spins. Let us start by considering a Kondo-lattice model of conduction electrons (c) interacting with localized spins ($\boldsymbol{S}$), described by the following Hamiltonian,

$$\begin{aligned} H &= H_c + H_K + H_H, \text{ where} \qquad (3.13) \\ H_c &= \sum_{\substack{\langle ij \rangle \\ \alpha}} (-t_{ij} e^{ie\mathbf{A}_{ij}.(\mathbf{r}_i - \mathbf{r}_j)} - \mu) c^\dagger_{i\alpha} c_{j\alpha} + \sum_{\mathbf{k}} (\Delta^c_{\mathbf{k}} c^\dagger_{\mathbf{k}\uparrow} c^\dagger_{-\mathbf{k}\downarrow} + \text{h.c.}) \\ H_K &= \frac{J_K}{2} \sum_i \boldsymbol{S}_i . c^\dagger_{i\alpha} \boldsymbol{\sigma}^i_{\alpha\beta} c_{i\beta} \ , \quad H_H = J_H \sum_{\langle ij \rangle} \boldsymbol{S}_i . \boldsymbol{S}_j . \qquad (3.14) \end{aligned}$$

H_c represents the Hamiltonian of the dispersing conduction electrons that exhibit a superconducting instability with pairing amplitude Δ^c at low temperatures. H_K represents the Kondo coupling between the conduction electrons and the localized spins. We have included an explicit interaction between the localized spins, H_H, which includes effects due to Heisenberg super-exchange and RKKY interactions. $\mathbf{A}_{ij}$ represents the physical external gauge field.

We shall use the fermionic spinon representation of the localized spins, $\boldsymbol{S}_i = f^\dagger_{i\alpha} \boldsymbol{\sigma}_{\alpha\beta} f_{i\beta}/2$. Let us now reformulate the above Hamiltonian in terms of a functional integral for the c and f fermions and a slave boson $\Phi \sim \langle c^\dagger f \rangle$. By decoupling H_K

and H_H above in terms of Hubbard-Stratanovich fields, we get

$$\begin{aligned} H'_K &= \sum_i (\Phi_i^* c_{i\alpha}^\dagger f_{i\alpha} + \Phi_i f_{i\alpha}^\dagger c_{i\alpha}) + |\Phi_i|^2/J_K, && (3.15) \\ H'_H &= \sum_{\langle ij \rangle} (|\chi_{ij}| e^{i\mathbf{a}_{ij}\cdot(\boldsymbol{r}_i - \boldsymbol{r}_j)} f_{i\alpha}^\dagger f_{j\alpha} + \text{h.c.}) + |\chi_{ij}|^2/J_H \\ &\quad + \sum_{\mathbf{k}} (\Delta_{\mathbf{k}}^f f_{\mathbf{k}\uparrow}^\dagger f_{-\mathbf{k}\downarrow}^\dagger + \text{h.c.}) + |\Delta_{\mathbf{k}}^f|^2/J_H, && (3.16) \end{aligned}$$

where $\mathbf{a}_{ij}$ is an emergent gauge-field, $|\chi_{ij}|$ is the hopping amplitude for the spinons and we also consider the spinons to be paired with amplitude Δ^f. The complete Hamiltonian of the system is now given by, $H = H_c + H'_K + H'_H + \sum_j \lambda_j (f_{j\alpha}^\dagger f_{j\alpha} - 1)$, where λ_j is a Lagrange multiplier that restricts the number density of the localized electrons to $n_f = 1$ on average. Φ_i is a complex field, which carries gauge charge $(-1_{\mathbf{A}}, 1_{\mathbf{a}})$ and whose condensation leads to confinement. The condensation of $\langle cc \rangle$ and $\langle ff \rangle$ break the $U(1)_{\mathbf{A}}$ and $U(1)_{\mathbf{a}}$ to $Z_{2\mathbf{A}}$ and $Z_{2\mathbf{a}}$ respectively. The operator Φ^2 is neutral under both $\mathbb{Z}_2$ gauge fields. However, once Φ condenses the gauge invariance $\mathbb{Z}_{2A} \times \mathbb{Z}_{2a}$ is broken to its diagonal $\mathbb{Z}_{2(A-a)}$. We can now write the following low-energy theory in terms of the gauge-fields $A_\perp, a_\perp$ (transverse components of $\mathbf{A}, \mathbf{a}$) and the scalar field Φ after having integrated out the fermions (both species of fermions remain gapped on either side of the transition),

$$\begin{aligned} S_{\text{eff}} &= S_0[\mathbf{A}, \mathbf{a}] + S[\Phi, \tilde{\mathbf{A}}], && (3.17) \\ S_0[\mathbf{A}_\perp, \mathbf{a}_\perp] &= \int d^2x d\tau \left(\frac{\mathbf{A}_\perp \Pi^c \mathbf{A}_\perp}{2} + \frac{\mathbf{a}_\perp \Pi^f \mathbf{a}_\perp}{2} \right) && (3.18) \\ S[\Phi, \tilde{\mathbf{A}}] &= \int d^2x d\tau \left(\frac{1}{2} \left| \left(\partial - i\tilde{\mathbf{A}} \right) \Phi \right|^2 + \frac{U_{\text{eff}}}{2} \right), && (3.19) \\ U_{\text{eff}} &= b_1 \Phi^2 + b_1^* (\Phi^\dagger)^2 + b_2 \Phi^\dagger \Phi + c_1 \Phi^4 + c_1^* (\Phi^\dagger)^4 \\ &+ c_2 (\Phi^\dagger \Phi)^2 + \Phi^\dagger \Phi [c_3 \Phi^2 + c_3^* (\Phi^\dagger)^2], && (3.20) \end{aligned}$$

where $\Pi^{c,f}$ denote the bare BCS contribution to the mass for $\mathbf{A}, \mathbf{a}$ due to the c, f Fermions and $\tilde{\mathbf{A}} = \mathbf{A}_\perp - \mathbf{a}_\perp$. By making a particular choice of gauge, we can set b_1 to be real (b_2 and c_2 are also real). Expressing Φ as $\varphi_0 + i\varphi$, with φ_0, φ as real fields, the most general form of $S[\varphi_0, \varphi, \tilde{\mathbf{A}}]$ is given by,

$$\begin{aligned} S[\varphi_0, \varphi, \tilde{A}] &= \int d^2x d\tau \Bigg(\frac{1}{2}\Big[(\partial\varphi)^2 + (\partial\varphi_0)^2 \Big] + U_{\text{eff}} \\ &\qquad + \tilde{A}(\varphi\partial\varphi_0 - \varphi_0\partial\varphi) + \frac{1}{2}\tilde{A}^2(\varphi_0^2 + \varphi^2) \Bigg), \qquad (3.21) \\ U_{\text{eff}} &= \frac{r_1}{2}\varphi^2 + \frac{r_2}{2}\varphi_0^2 + \frac{g_1}{4}\varphi_0^4 + \frac{g_2}{4}\varphi^4 \\ &+ \frac{g_3}{2}\varphi_0^2\varphi^2 + g_4\varphi_0^3\varphi + g_5\varphi_0\varphi^3, \qquad (3.22) \end{aligned}$$

where $r_1 = 2(b_2 - 2b_1)$, $r_2 = 2(b_2 + 2b_1)$ and all the g_i's are real. We can access the QCP by tuning r_1 to zero, where the φ mode goes gapless while the φ_0 mode remains gapped. We can therefore safely integrate φ_0 out, which leads to a critical theory that is governed by $\mathcal{S}_\varphi$ with $N = 1$, albeit with renormalized coupling constants. The coupling between φ and the gauge-fields is given by,

$$\mathcal{S}[\varphi, \mathbf{A}, \mathbf{a}] = \mathcal{S}_\varphi + \int d^2x d\tau \frac{1}{2}(\mathbf{A}_\perp - \mathbf{a}_\perp)^2\varphi^2. \qquad (3.23)$$

As we tune across the QCP, there will be a smooth background superfluid density governed by the variation of $\Pi^{c,f}$. However, in this study, we are interested in the singular corrections that arise from the critical fluctuations of φ and are dictated by the form of $\langle\varphi^2\rangle$.

3.2.2 Results

Case A & B: SDW and Nematic criticality

Let us now look at the diagrams in Fig.3.2—these diagrams effectively give rise to a 4-point coupling between the gauge field and the SDW/nematic order parameter. At zero external momentum and frequency, C_2 for case A is given by

$$C_2 = w^2[I_V + I_\Sigma + I_T], \quad \text{where} \tag{3.24}$$

$$I_V = \sum_{\mathbf{p}, ip_n, a\neq b} v_a^x(\boldsymbol{p}) v_b^x(\boldsymbol{p}) \mathrm{Tr}[\hat{G}_a(\boldsymbol{p}, ip_n)\hat{G}_a(\boldsymbol{p}, ip_n)\hat{G}_b(\boldsymbol{p}, ip_n)\hat{G}_b(\boldsymbol{p}, ip_n)], \tag{3.25}$$

$$I_\Sigma = 2\sum_{\mathbf{p}, ip_n, a\neq b} [v_a^x(\boldsymbol{p})]^2 \mathrm{Tr}[\hat{G}_a(\boldsymbol{p}, ip_n)\hat{G}_a(\boldsymbol{p}, ip_n)\hat{G}_b(\boldsymbol{p}, ip_n)\hat{G}_a(\boldsymbol{p}, ip_n)], \tag{3.26}$$

$$I_T = 2\sum_{\mathbf{p}, ip_n, a\neq b} K_a^x(\boldsymbol{p}) \mathrm{Tr}[\hat{G}_a(\boldsymbol{p}, ip_n)\hat{G}_b(\boldsymbol{p}, ip_n)\hat{G}_a(\boldsymbol{p}, ip_n)\hat{\tau}_z]. \tag{3.27}$$

"Tr" stands for trace over the Nambu indices. Upon integrating out the fermions, we also generate a three-point coupling between $\mathbf{A}$ and φ. Two of these diagrams combine to give an $O(\mathbf{A}^2)$ term and is referred to as the *Aslamazov-Larkin* diagram. The expression for C_3 is given by,

$$C_3 = w^2 \sum_{\mathbf{p}, ip_n, a\neq b} v_a^x(\boldsymbol{p}) \mathrm{Tr}[\hat{G}_a(\boldsymbol{p}, ip_n)\hat{G}_b(\boldsymbol{p}, ip_n)\hat{G}_a(\boldsymbol{p}, ip_n)\hat{\tau}_z]. \tag{3.28}$$

As mentioned above, it turns out that C_3 is identically zero when evaluated at zero external momentum as it is an odd function of p_x and so we can ignore the three-point coupling between the gauge-fields and φ. We can compute the traces and carry out the Matsubara sums analytically, leading to expressions that are a function of the lattice momenta. Finally we choose a specific band-structure and evaluate the momentum integrals on a lattice, which gives us a numerical value for C_2.

Similarly, for case B, the expressions are given by,

$$C_2 = w^2[I_V + I_\Sigma + I_T], \quad \text{where} \tag{3.29}$$

$$I_V = \sum_{\mathbf{p},ip_n,a} [v_a^x(\boldsymbol{p})]^2 \mathrm{Tr}[\hat{G}_a(\boldsymbol{p},ip_n)\hat{G}_a(\boldsymbol{p},ip_n)\hat{\tau}_x\hat{G}_a(\boldsymbol{p},ip_n)\hat{G}_a(\boldsymbol{p},ip_n)\hat{\tau}_x], \tag{3.30}$$

$$I_\Sigma = 2\sum_{\mathbf{p},ip_n,a} [v_a^x(\boldsymbol{p})]^2 \mathrm{Tr}[\hat{G}_a(\boldsymbol{p},ip_n)\hat{G}_a(\boldsymbol{p},ip_n)\hat{\tau}_x\hat{G}_a(\boldsymbol{p},ip_n)\hat{\tau}_x\hat{G}_a(\boldsymbol{p},ip_n)], \tag{3.31}$$

$$I_T = 2\sum_{\mathbf{p},ip_n,a} K_a^x(\boldsymbol{p}) \mathrm{Tr}[\hat{G}_a(\boldsymbol{p},ip_n)\hat{\tau}_x\hat{G}_a(\boldsymbol{p},ip_n)\hat{\tau}_x\hat{G}_a(\boldsymbol{p},ip_n)\hat{\tau}_z]. \tag{3.32}$$

C_3 for this problem continues to be zero as long as the external momentum/frequency is zero.

We have evaluated C_2 numerically for different band-structures that resemble the pnictide and cuprate Fermi surfaces. As discussed below, we find that $C_2 < 0$ for the SDW problem in all the cases that we have considered here. Note that for the nematic problem, the sign of C_2 depends on the underlying microscopic details of the band-structure.

Case C: Deconfinement transition

For case C, it is now a simple matter to integrate $\mathbf{a}$ out from $\mathcal{S}_0[\mathbf{A},\mathbf{a}] + \mathcal{S}[\varphi,\mathbf{A},\mathbf{a}]$ in Eqns.3.20, 3.23, which yields the action in Eq. (3.2) with

$$C_1 = \frac{\Pi^c}{2}, \text{ and, } C_2 = \frac{\Pi^f}{2(\Pi^f + \varphi^2)} > 0. \tag{3.33}$$

In the limit of large Π^f and sufficiently close to the critical point, $C_2 \approx 1/2$.

Penetration depth across the QCP

Returning now to Eqn.3.2, we obtain the superfluid stiffness as

$$\frac{\hbar^2 c^2}{4e^2}\rho_s = C_1 + C_2 \left\langle \varphi^2 \right\rangle_{\mathcal{S}_\varphi} \tag{3.34}$$

where our notation indicates that the expectation value of φ^2 is to be computed in the field theory $\mathcal{S}_\varphi$. So our final results depend upon two distinct computations. The first is the computation of C_2: we have shown how its magnitude and sign depend upon the structure of the underlying fermionic excitations. The second is the computation of $\langle\varphi^2\rangle$ for which numerous precise results are readily available [262]. Specifically we have $\langle\varphi^2\rangle \sim A_\pm|g-g_c|^{3\nu-1} + \ldots$ as $g - g_c \to \pm 0$, where ν is the exponent of the correlation length $\xi \sim |g-g_c|^{-\nu}$, the ratio A_+/A_- is universal, and the ellipses indicate non-universal terms analytic in $g-g_c$. Crucial constraints on the signs of the various coefficients arise from the fact that $-\partial\langle\varphi^2\rangle/\partial g$ is proportional to the "specific heat", C_V, of the classical statistical system described by the Euclidean field theory $\mathcal{S}_\varphi$, and so must be positive (note that C_V is unrelated to the specific heat of the quantum model we are studying). If $\nu > 2/3$, C_V has only a cusp-like singularity at $g = g_c$, and we assume for this case that C_V is a local maximum at $g = g_c$. After assembling these constraints with the values of C_2 computed for a specific choice of the Fermi-surface, it is a simple matter to obtain the results in Fig. 3.1 .

For the sake of completeness, we also present a specific example of a Fermi-surface, with the corresponding numerically evaluated $\delta\lambda_L$ in Figs. 3.3 and 3.4. In the numerical computations, $\langle\varphi^2\rangle$ has been computed at the Gaussian level on the disordered side of the critical point. We also note that our present methods, which focus only on the longest wavelength fluctuations of φ, cannot accurately account for the *analytic* dependence of λ_L on $g-g_c$ contained in the a_1 term in Fig. 3.1A; Ref [137] accounts for the short wavelength fluctuations of φ more completely, and so their methods give a better estimate of a_1, and of the enhancement of λ_L upon approaching the critical

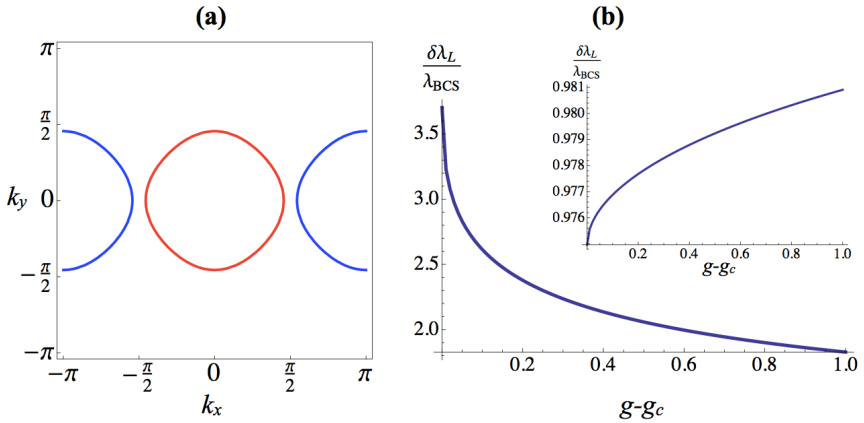

Figure 3.3: (a) A two-orbital band structure of the form $\varepsilon_1(\mathbf{k}) = -2t_1\cos(k_x) - 2t_2\cos(k_y) - \mu$, $\varepsilon_2(\mathbf{k}) = 2t_2\cos(k_x) - 2t_1\cos(k_y) - \mu$, with $t_1 = t_2 = 0.22$, $\mu = -0.5$, $w = 1.0$, $\Delta_1 = -\Delta_2 = 1.0$, $c = 1$. (b) The singular correction to $\delta\lambda_L/\lambda_{\rm BCS}$ as a function of $g > g_c$ for the SDW quantum critical point. Inset: $\delta\lambda_L/\lambda_{\rm BCS}$ for $g > g_c$ for the nematic quantum critical point.

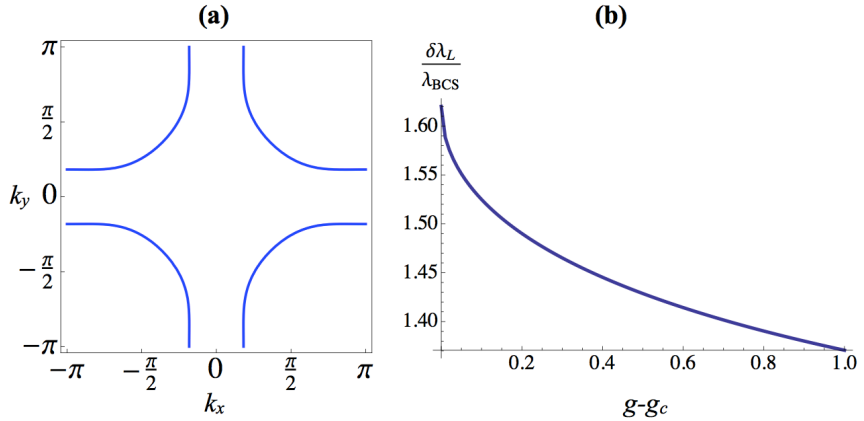

Figure 3.4: (a) Fermi surface for the one-band model, $\varepsilon(\mathbf{k}) = -2t_1(\cos(k_x) + \cos(k_y)) - 4t_2\cos(k_x)\cos(k_y) - 2t_3(\cos(2k_x) + \cos(2k_y)) - \mu$, with parameters $t_1 = 1.0, t_2 = -0.32, t_3 = 0.128, \mu = -1.11856$. The gap function is taken to be $\Delta(\mathbf{k}) = \Delta_0(\cos(k_x) - \cos(k_y))$ with $\Delta_0 = 1.0$. Other parameters are $w = 1.5, c = 1.0$. (b) $\delta\lambda_L/\lambda_{\rm BCS}$ is shown for $g > g_c$ for the $\mathbf{Q} = (\pi, \pi)$ SDW QCP.

point from the SC.

3.2.3 Discussion

Case A, the SDW transition, is the one best studied in experiments so far [85]. The critical theory is described by the fluctuations of a bosonic SDW order parameter φ with $N = 3$ real components, with an effective Lagrangian which has a relativistic form [180]; the coupling to the fermionic quasiparticle excitations of the superconductor only serves to renormalize the parameters of the Lagrangian. These features allow us to use the powerful critical phenomena technology [262] to make definitive statements on the singularity in the London penetration depth. We find that the London penetration depth λ_L *increases* as we approach the quantum critical point from the SC phase. This is in agreement with the observations [85], and an independent recent computation [2] which focused on quasiparticle renormalization effects within the SC phase [137].

The experiments [85] on the other hand have observe a sharp peak-like maximum in λ_L around the putative SDW QCP, and this is not present in our critical theory for the transition within the superconducting phase. One possible resolution is that the observed maximum does not appear at the quantum critical point, as has been previously suggested [85, 137, 171], and may appear *within* the SDW+SC phase. Within this scenario, explaining the maximum will require consideration of other physical properties of the SDW+SC phase and may involve physics at scales $\xi \sim \xi_c$ or smaller. In this regime, there are renormalizations of the spectrum and lifetime of the fermionic excitations, such as those that are crucial for the onset of the SDW

[2] Our results for $\delta\lambda_L$ agree with the results of Ref. [137] on the disordered side of the SDW QCP in case (A). However, they show a maximum in λ at the QCP in Fig. (1) of their paper: this was an assumption not supported by any computations on the ordered side. We show here that the actual situation is as in our Fig 1A.

order in a metal [2, 1, 154, 82]. Therefore, it is necessary to evaluate diagrams like those in Fig. 3.2 while including Fermi surface reconstruction and fermion self energy corrections. However, we shall propose an alternative explanation [43] for the observed phenomenon in the next section.

Case B applies to the Ising-nematic transition, that is also observed in $BaFe_2(As_{1-x}P_x)_2$ [111]. This transition has a bosonic order parameter φ with $N = 1$ real component, and the effective theory is otherwise the same as that for the SDW case. However, fermionic quasiparticles which are gapless lead to a distinct critical theory [121], and so our present results apply to the nematic transition only if nodal quasiparticles are absent. There isn't enough evidence yet from the experiments on the pnictides whether the penetration depth has any non-analytic features in the vicinity of the nematic critical point. However, nematic phases are ubiquitous in these systems and hence more careful experiments in the near future are likely to reveal interesting features close to such quantum critical points.

Finally, case C is a more exotic topological transition between a 'fractionalized' superconductor [213, 215, 50, 19] (often labeled SC* [211]) [3] and a conventional superconductor (SC). Roughly speaking, in a SC* state some of the electrons have localized into a spin liquid (we consider the case of a $\mathbb{Z}_2$ spin liquid [188, 244]), while the remaining electrons are in a paired BCS state; there can then be a confinement transition to a SC state which has all the electrons in the BCS state. Ultimately, the critical theory is the same as that considered above for the Ising-nematic case, with the important difference that it is now the SC phase which has $\langle\varphi\rangle \neq 0$. The heavy fermion

[3] Refs. [50, 19] also considered the interplay between spin liquids and superconductivity, but did not discuss a phase with the precise characteristics of SC*.

compounds with indications of fractionalized metallic states [33, 169, 75, 54] are good candidates for realizing a SC* superconductor. Moreover, in $CeCu_2(Si_{1-x}Ge_x)_2$, experiments have found two distinct superconducting domes as a function of pressure alongwith similar results in $Ce(Rh,Ir,Co)In_5$ as a function of doping [257, 174]. The nature of one of these SC states remains mysterious and is often attributed to valence fluctuations. It would be interesting to carry out penetration depth measurements in these materials and compare with the present study.

3.3 Effect of quenched disorder in the vicinity of putative quantum critical points

The experimental observation of a sharp peak in $\lambda_L^2(0)$ in $BaFe_2(As_{1-x}P_x)_2$ at $x = x_c$ was interpreted as evidence for a SDW QCP [137]. However, as discussed in the previous section, this interpretation is at odds with general theoretical considerations [47] concerning a QCP associated with the onset of SDW order in the presence of a superconductor with gapped quasiparticle excitations. Recent computations of the superfluid density [204] across the SDW QCP in a sign-problem free quantum monte carlo calculation [30] are also consistent with the theoretical considerations reported in the previous section.

Here we propose a resolution of the experimental puzzles by postulating a weakly first-order transition for the onset of SDW order in the presence of SC order (see Fig. 3.5a). Our results are independent of the specific microsopic mechanism responsible for rendering the transition weakly first-order [70, 247]. It is well known that 'random

bond' disorder has a strong effect on symmetry-breaking first-order transitions [107, 103], and ultimately replaces them with a disorder-induced second order transition in two dimensional systems. Our main claim is that the inhomogeneities associated with these highly relevant effects of disorder can resolve the experimental puzzles. A qualitative summary of the behavior of the penetration depth as a function of the tuning parameter is shown in Fig. 3.5b.

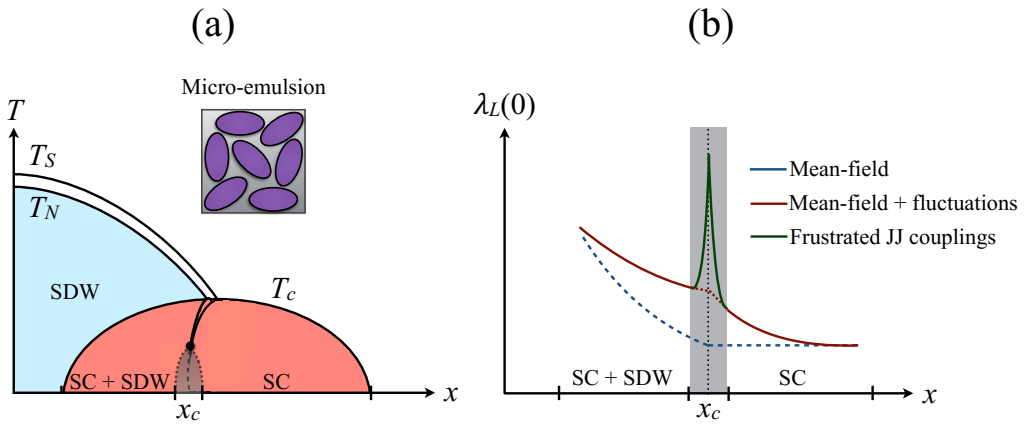

Figure 3.5: (a) A cartoon phase-diagram showing the interplay between SDW and SC phases. The T_N (Néel temperature) and T_S (structural/nematic transition) lines may survive as continuous transitions inside the SC phase up until the point marked '•', below which they become weakly first-order (shown as black dashed line). The grey region depicts the regime where the system develops spatial inhomogeneity due to the presence of disorder. Inset: Emulsion with SC grains (purple) and SDW(+SC) regions (grey). (b) The behavior of $\lambda_L(0)$ as a function of the tuning parameter, x, within different scenarios (see text for details).

3.3.1 Insights from optical sum-rules

As a first step toward resolving this discrepancy, it is useful to place measurements of ρ_s in the context of what is known about the normal state conductivity of the $BaFe_2(As_{1-x}P_x)_2$ system, as these quantities are intimately related through a

sum rule. The low temperature superfluid density of a spatially homogeneous superconductor can be estimated from the "missing area" relation,

$$\rho_s \approx \frac{2}{\pi}\Gamma \int_0^{2\Delta/\Gamma} \sigma(z)dz, \tag{3.35}$$

where Γ is the elastic scattering rate and $z \equiv \omega/\Gamma$. In the dirty limit where $\Delta/\Gamma \ll 1$, the above relation yields Homes' Law [98, 66], $\rho_s \approx \sigma(0)\Delta$, whereas in the clean limit $\rho_s = \rho_n$ where ρ_n is the conductivity spectral weight in the normal state. Eqn. 3.35 is particularly useful when the normal state resistivity data can reasonably be extrapolated to $T = 0$. By combining dc transport data as a function of x [112] and a measurement of 2Δ from optical conductivity [163], Eq. 3.35 provides a lower bound on $\lambda_L^2(0)$ (with the assumption that Δ is independent of x). Fig.3.6 shows $\lambda_L^2(0)$ as a function of x obtained under this assumption (details of the procedure are presented in Appendix B). The decrease of superfluid density on the underdoped side reflects the growth in residual resistivity that begins as x drops below about 0.33.

The values of $\lambda_L^2(0)$ estimated from Eq. 3.35 form a baseline for comparison with the experimental results presented in Ref. [85]. On the same graph in Fig. 3.6, we show the experimentally measured $\lambda_L^2(0)$ [85]. The data generally reflect the trend expected from the variation in the residual resistivity, with the exception of the sample with $x = 0.3$, in which the condensate spectral weight is suppressed by about 40% from the Homes' Law estimate. Given the constraints imposed by the sum rule, there are two possible sources of this discrepancy: (i) the quasiparticle mass could be renormalized at this value of x, corresponding to an intrinsic decrease in ρ_n, or, (ii) a considerable fraction of the (unrenormalized) ρ_n could fail to contribute to the low temperature superfluid density. The latter possibility is suggested within the scenario

that we develop here.

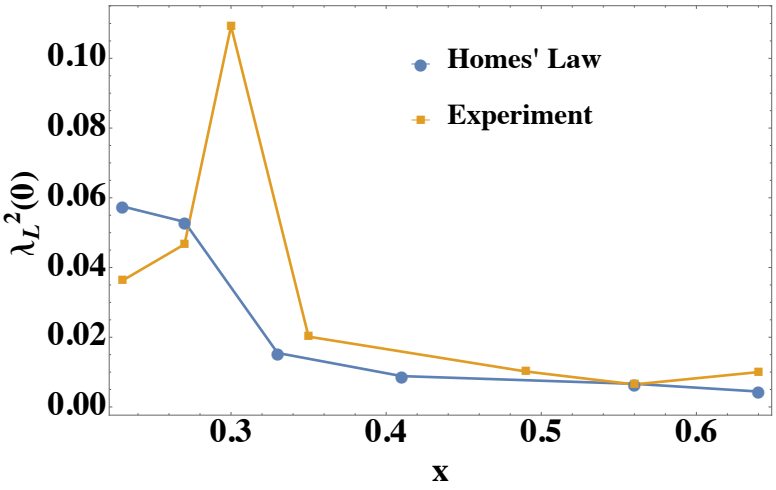

Figure 3.6: A comparison between the experimentally obtained values of $\lambda_L^2(0)$ [85] and those deduced from Homes' law. The value of 2Δ is taken to be 150cm^{-1} [163], independent of x.

3.3.2 Model

We analyze the above experiments by assuming a weakly first-order transition [70, 247], and argue that the presence of quenched disorder leads to formation of a *micro-emulsion* at small scales [107, 103]. The system consists of SC puddles, where some of the puddles additionally have SDW order (see Fig. 3.5a inset). The SDW(+SC) regions, which have a locally well-developed antiferromagnetic moment but no long-range orientational order, act as barriers between the different SC grains. Upon moving deeper into the ordered side of the transition, the SDW(+SC) regions start to percolate and crossover to a state with long-range SDW order; this is the regime with a microscopically coexistent SC+SDW. As a function of decreasing x, the micro-emulsion is therefore a transitional state (shown as grey region in Fig. 3.5a)

between a pure SC and a coexistent SC+SDW. Recent experiments in the vicinity of optimal doping using neutron-scattering and NMR have found results broadly consistent with our proposed phase diagram [102]. We note that the granular nature of superconductivity should have no effect on the bulk T_c in the presence of percolating SC channels.

When the system is well described in the vicinity of x_c by a micro-emulsion as explained above, the phase fluctuations associated with the SC grains (shown as purple regions in Fig. 3.5a inset), can be modeled by the following effective theory,

$$H_\theta = -\sum_{a,b} J_{ab} \cos(\theta_a - \theta_b), \tag{3.36}$$

where J_{ab} represent the Josephson junction (JJ) couplings between grains 'a' and 'b'. We have ignored the capacitive contributions.

The Josephson current across the junction will be given by $I_s = J_{ab} \sin(\theta_a - \theta_b)$, and J_{ab} may therefore be interpreted as the lattice version of the local superfluid density, $\rho_s(\boldsymbol{r})$, i.e. $\boldsymbol{J}_s(\boldsymbol{r}) = \rho_s(\boldsymbol{r})\ \boldsymbol{v}_s(\boldsymbol{r})$, with $\boldsymbol{J}_s(\boldsymbol{r})$, $\boldsymbol{v}_s(\boldsymbol{r})$ representing the superfluid-current and velocity respectively. Having a frustrated JJ (also known as a $\pi-$junction) with a negative value of J_{ab} leads to a local suppression in ρ_s. Similar ideas have been discussed in the past in a variety of contexts (see Refs. [225, 234] for a specific example), though the mechanism considered here will be different. We shall now propose an explicit scenario under which a suppression in ρ_s arises in the vicinity of putative magnetic QCPs, utilizing the SC gap structure in the material under question.

The basic idea is as follows: suppose that the tunneling of electrons between the two grains is mediated by the SDW moment in the intervening region [15], and is

accompanied by a transfer of finite momentum that scatters them from a hole-like to an electron-like pocket. Because the SC gaps on the two pockets have a relative phase-difference of π, the JJ coupling will be frustrated [13].

Let us first focus on a single grain. In order to capture the multi-band nature of the SCs, we introduce two superconducting order parameters, Δ_i with $i = \pm$ to model the $s^{\pm}$ state on the two pockets. Microscopically, these belong to regions in the grain having different momenta, $\mathbf{k}_\parallel$, parallel to the junction. The gaps are related to the microscopic degrees of freedom [28] via the following relation,

$$\Delta_i(z) = \frac{1}{A} \sum_{\mathbf{k}_\parallel \in \mathcal{R}_i} V_{\mathbf{k}_\parallel, \mathbf{k}'_\parallel} \langle \psi_{\mathbf{k}'_\parallel \uparrow} \psi_{-\mathbf{k}'_\parallel \downarrow} \rangle, \tag{3.37}$$

where $\psi^\dagger_{\mathbf{k}_\parallel \sigma}$ creates an electron at position z with momentum $\mathbf{k}_\parallel$ parallel to the junction and spin σ. $V_{\mathbf{k}_\parallel, \mathbf{k}'_\parallel}$ is the pairing interaction in the Cooper channel and z is the coordinate perpendicular to the junction with area A. The regions $\mathcal{R}_i$ are defined as, $\mathcal{R}_+ = \{\mathbf{k}_\parallel | k_0 > |\mathbf{k}_\parallel|\}$ and $\mathcal{R}_- = \{\mathbf{k}_\parallel | k_0 \leq |\mathbf{k}_\parallel|\}$, where k_0 is an arbitrary momentum scale chosen such that $\Delta_+ > 0,\ \Delta_- < 0$ (see Fig. 3.7 for an illustration). We'll assume that such a prescription is valid for each grain, with possibly different values of k_0.

Let us then write down a model for the two coupled SC grains with an intervening proximity coupled SDW that has a well developed moment, $\boldsymbol{n}$. Our notation is as follows: we use $\alpha = a, b$ to denote the grain index and $i = \pm$ to denote the band index within each grain. From now on, we relabel $\mathbf{k}_\parallel$ as $\mathbf{k}$. We introduce the Nambu spinor, $\Psi^{\alpha\dagger}_{i,\mathbf{k},\sigma} = (\psi^{\dagger\alpha}_{i,\mathbf{k},\sigma}\ \epsilon_{\sigma\sigma'}\psi^{\alpha}_{i,-\mathbf{k},\sigma'})$, where now $\psi^{\dagger\alpha}_{i,\mathbf{k},\sigma}$ creates an electron with momentum $\mathbf{k}$ parallel to the junction and at a position z (label suppressed), which belongs to a

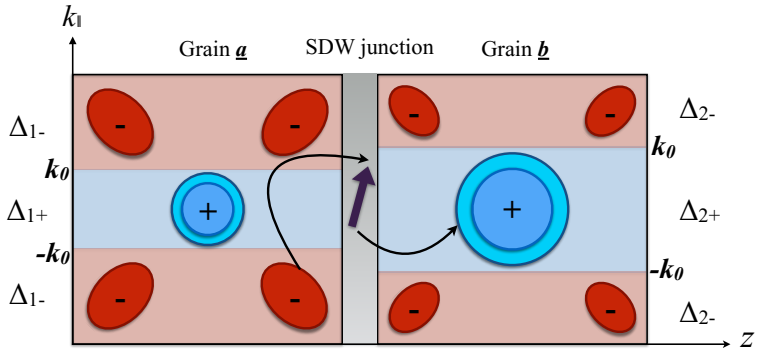

Figure 3.7: A cartoon of a frustrated $\pi-$junction between two superconducting grains with a SDW(+SC) barrier. The SDW moment imparts a finite momentum transfer along the direction of the interface while scattering electrons from the electron (hole) pocket on one grain to the hole (electron) pocket on the other grain.

region of band "i" within grain "α". The effective Hamiltonian is given by,

$$H_{\text{eff}} = H_\Delta + H_T, \tag{3.38}$$

$$H_\Delta = \sum_{\alpha,i,\mathbf{k}} \Psi^{\alpha\dagger}_{i,\mathbf{k},\sigma} \left[\varepsilon_{i\alpha,\mathbf{k}} \hat{\tau}^z + \Delta_{i\alpha,\mathbf{k}} \hat{\tau}^x \right] \Psi^{\alpha}_{i,\mathbf{k},\sigma}, \tag{3.39}$$

$$H_T = g \sum_k \boldsymbol{n} \cdot \Big(\Psi^{a\dagger}_{+,\mathbf{k},\sigma} [\boldsymbol{\sigma}_{\sigma\sigma'} \otimes \hat{\tau}^0] \Psi^{b}_{-,\mathbf{k},\sigma'} + \Psi^{a\dagger}_{-,\mathbf{k},\sigma} [\boldsymbol{\sigma}_{\sigma\sigma'} \otimes \hat{\tau}^0] \Psi^{b}_{+,\mathbf{k},\sigma'} \Big) + \text{H.c.}, \tag{3.40}$$

where g is the tunneling matrix element, $\hat{\tau}^i$ $(i = 0, x, y, z)$ act in Nambu space and $\hat{\sigma}^i$ $(i = 0, x, y, z)$ act in spin space.

In the above, H_Δ corresponds to the bare pairing Hamiltonian written for the $\pm$ bands within each of the two grains. H_T represents the SDW moment mediated hopping of electrons from one grain to the other (represented by the a, b superscripts) and simultaneously scattering from one band to the other (represented by the $\pm$ subscripts). Therefore, $\boldsymbol{n}$ imparts a finite momentum (along the interface) to the electrons when it scatters them from the electron (hole) pocket on one grain to the

hole (electron) pocket on the other grain (shown as the black arrows in Fig. 3.7).

3.3.3 Results

Using the Ambegaokar-Baratoff relation [13], we can write the Josephson coupling (at $T = 0$) between the two grains as,

$$J_{ab} = \frac{g^2 \langle \boldsymbol{n}^2 \rangle}{\pi^2} \Big[\sum_{\ell \in a, \ell' \in b} \Delta_\ell \Delta_{\ell'} \int_0^\infty \frac{d\varepsilon_\ell}{E_\ell} \int_0^\infty \frac{d\varepsilon_{\ell'}}{E_{\ell'}} \frac{1}{E_\ell + E_{\ell'}} \Big] \tag{3.41}$$

where $E_\ell^2 = \varepsilon_\ell^2 + \Delta_\ell^2$ and $\ell,\ \ell'$ represent the band indices on the different grains. Since $\Delta_\ell \Delta_{\ell'} < 0$, the coupling $J_{ab} < 0$. Note that the specific nature of the frustrated tunneling arises from the same spin-fluctuation mediated mechanism that is predominantly responsible for the $s^{\pm}-$ pairing symmetry [200]. However, there will also be a direct tunneling term (not included in Eqn. 3.38) in the Hamiltonian, which does not scatter the electrons from one pocket to the other, as they hop across the junction. The contribution to the JJ coupling from this term will be unfrustrated (i.e. $J_{ab} > 0$).

The ratio of the tunneling amplitudes in the two different channels is non-universal and depends on various microscopic details. In particular, the emulsion is associated with a distribution of Josephson-couplings, $\mathcal{P}(J)$, with a mean coupling strength, $\langle J \rangle = \bar{J}$. If a substantial fraction of the JJ couplings become negative due to the mechanism proposed above, $\bar{J}$ will be small, and the superfluid density will be suppressed (see green curve in Fig.3.5b).

We now propose a resolution as to the fate of the uncondensed spectral weight (highlighted in Fig. 3.6), which can potentially be tested by measurements of the low frequency optical conductivity. Frustrated $\pi-$junctions host gapless states at the interface between the two grains [108, 101, 230], giving rise to a finite density of

states around zero energy (see Fig 3.8 inset). As a result of the gapless 'normal'-fluid component at the interface, a fraction f of the spectral weight will be displaced from the superfluid-density to non-zero frequencies (shaded region in Fig. 3.8). Given that the weight of the condensate is proportional to $\bar{J}(1-f)$, the 40% suppression in ρ_s for $BaFe_2(As_{1-x}P_x)_2$ in the vicinity of the putative QCP corresponds to $f \sim 0.6$.

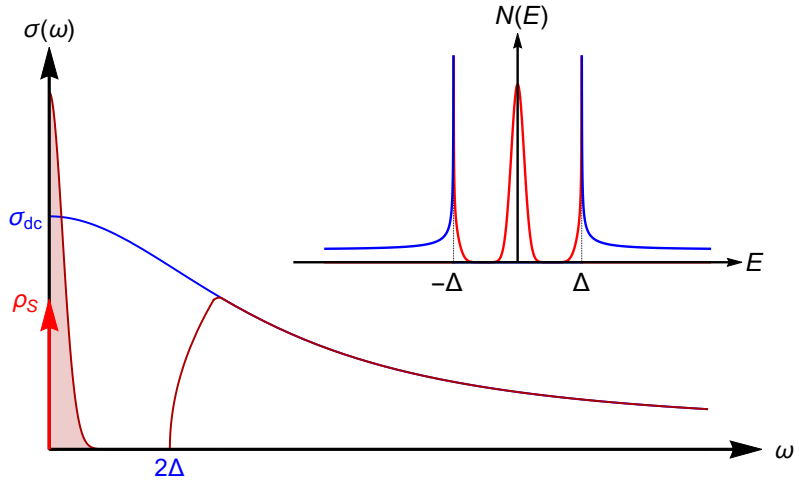

Figure 3.8: Plot of the optical conductivity, $\sigma(\omega)$, for a Drude metal (blue curve) and a superconductor with a large number of sub-gap excitations (red curve). The shaded region corresponds to the displaced spectral weight from the superfluid-density, ρ_s (red arrow). Inset: Density of states, $N(E)$ vs. E, for a conventional gapped superconductor (blue curve). A superconductor with a large number of subgap states has a finite $N(E)$ below Δ (red curve).

Our proposed optical conductivity, $\sigma(\omega)$, in the vicinity of penetration depth anomaly is shown in in Fig 3.8. The spectrum shows clearly that the connection between normal state conductivity and superfluid density implied by Eq. 3.6 will break down. In particular, $\sigma_{\rm dc}$ (which is a property of the normal state), could vary monotonically with isovalent-doping across x_c, while the abundance of low-energy excitations in the immediate vicinity of x_c would give rise to a non-monotonic variation

in the superfluid density. This allows for an unusual way of rearranging spectral weight in the *superconducting* state below the gap, without violating optical sum-rules.

The above scenario will give rise to a number of interesting low temperature thermodynamic and transport properties, as we now discuss. First of all, there should be a striking enhancement in the low-temperature thermal conductivity and specific-heat, as a function of x in the narrow vicinity of x_c, due to the 'normal'-component. It is important to recall that this material has loop-like nodes on the electron-pockets [86, 219, 261, 159]. However, the geometry of the electron-pockets and the magnitude of the gap do not change substantially in the vicinity of x_c, and therefore it is unlikely that the contribution to the above quantities from the nodal-quasiparticles will have a drastic modificiation. It should therefore be relatively straightforward to disentangle the contribution arising from the nodal versus the 'normal' quasiparticles. Studying the NMR-spectra as a function of decreasing temperature (across T_c) and down to sufficiently low temperatures in the vicinity of x_c should also reveal the spatial inhomogeneity associated with the SDW regions. A large residual density of states in the superconducting state has been detected at a particular P-doping via the power-law temperature dependence of $1/T_1 \sim T$ [167]. Within our scenario, there should be a striking enhancement in this quantity as a function of doping around x_c. Finally, we note that a promising direction for future studies would be to measure the magnetic-field distribution due to the propagating currents in the emulsion using NV-based magnetometers [99].

3.3.4 Discussion

Our primary objective in the second part of this chapter was to provide an explanation for the striking enhancement of the London penetration depth in the vicinity of a putative SDW QCP in the SC state of $BaFe_2(As_{1-x}P_x)_2$. We developed a scenario based on the idea that true SDW criticality is masked by a weak first-order phase transition in the superconducting state at $T = 0$. In this picture, quenched disorder naturally gives rise to an *emulsion* at small length scales with puddles of SC and SDW(+SC). It is then, in principle, possible for SDW moments at the interface of the SC grains to generate frustrated Josephson couplings, which deplete the local superfluid-density. Our proposed scenario naturally calls for a number of experimental tests that should be carried out in the near future, which should directly look for both the spatial inhomogeneities associated with the emulsion [53], and probe the gapless excitations using thermodynamic probes, as explained above.

In addition to experiments on $BaFe_2(As_{1-x}P_x)_2$, it should be important to further investigate the contrasting behavior of the electron-doped system, $Ba(Fe_{1-x}Co_x)_2As_2$, where $\lambda_L(0)$ behaves monotonically as a function of x across the putative QCP [79]. Electron-doping leads to significantly higher amounts of disorder compared to the isovalently-doped case, and would therefore lead to puddles with typically much smaller size [63]. Our proposed mechanism for the strong suppression of the superfluid-density in the isovalently-doped material relies on the existence of an emulsion with puddles of appreciable size, in the presence of an optimal amount of disorder. A comparison of the NMR spectra in the narrow vicinity of the putative QCP in the electron and isovalently doped materials would shed light on these microscopic

differences between the two families.

Finally, though we have hypothesized that the SDW onset transition *inside* the SC is, in the absence of disorder, a weak first order transition, we emphasize that the normal state properties are consistent with the presence of a "hidden" QCP around optimal doping [242, 220, 14]. It is plausible that in the normal state, different experimental techniques are probing the critical fluctuations associated with not one, but distinct QCPs as a function of x. For instance, m^* extracted from high-field quantum oscillations is dominated by the vicinity of 'hot-spots', where quasiparticles are strongly damped due to coupling to the SDW fluctuations [209]. On the other hand, strong critical fluctuations associated with the nematic order-parameter [69], that couple to the entire Fermi-surface, would dominate m^* extracted at zero-field from the jump in the specific heat at T_c.

Chapter 4

Precursor thermal fluctuations in underdoped cuprates

"Science cannot solve the ultimate mystery of nature.....And that is because, in the last analysis, we ourselves are part of nature and therefore part of the mystery that we are trying to solve." - Max Planck

4.1 Introduction

In the present and the following chapter, we shall investigate various aspects of the phenomenology in the underdoped cuprates, starting from a traditional 'weak-coupling' approach and invoking the effect of thermal fluctuations of various competing orders. From our discussion in section 1.2.3, we know that the suppression of the paramagnetic spin susceptibility of the cuprate superconductors at a high temperature [12] (denoted T^*) implies the growth of antiferromagnetic spin correlations, and

a gap-like decrease in the electronic density of states at the Fermi level. It is useful to separate existing theoretical models of the resulting pseudogap regime into two broad categories.

In the first category, the antiferromagnetic correlations signal the onset of a quantum spin liquid [254, 148, 22, 183, 44, 253], which in turn could be unstable to other symmetry-broken phases at lower temperatures. We shall defer the discussion of this point of view to later chapters.

In the second category [122, 194, 205, 109, 259], the antiferromagnetic correlations are precursors to the appearance of antiferromagnetism, superconductivity, charge density wave, and possibly other conventional orders at low temperatures. In the pseudogap regime, we then have primarily thermal and classical, rather than quantum, fluctuations of these orders. In the recent work of Hayward *et al.* [91], it was shown that the unusual temperature dependence of the X-ray scattering signal of the charge density wave order [248, 78, 5, 39, 249] is obtained naturally from an effective classical model of angular thermal fluctuations of the charge-density wave and superconducting orders alone. The same model has also been connected to diamagnetism measurements over the same temperature range [90]. Within this framework, in the intermediate temperature range over which the charge order correlations have been observed, antiferromagnetic correlations need not be included explicitly, but can be absorbed into the phenomenological parameters of the classical model of charge and superconducting orders. However, for the onset of the pseudogap at T^*, these can't be ignored.

In the underdoped regime, quantum oscillations have been observed in two differ-

ent families of the cuprates at high-fields and low temperatures [65, 131, 229, 81, 207, 25, 206]. The results seem to indicate that the phase at high-fields has Fermi-liquid like properties, albeit with a Fermi-surface that occupies only a tiny fraction of the Brillouin zone. Harrison and Sebastian propose [81] that these can be understood as a consequence of a bidirectional charge density wave order: they argue that with the Fermi surface topology of the hole-doped cuprates, such an order leads to oscillations from a single electron pocket, and that this is compatible with all important observed features. Their analysis is based upon a computation in zero field, followed by a semiclassical account of the influence of the magnetic field. However, since incommensurate charge order induces a complex Fermi surface reconstruction, it is not a priori evident that this particular electron pocket would dominate the oscillations.

In Ref. [11] we demonstrated that a model of charge-density wave and superconducting orders provides a unified description of the high-field, low-temperature quantum-oscillations, and of certain features of the zero-field photoemission results at intermediate temperatures. While this model fits naturally into the second category of theories of the pseudogap summarized above, it may also be accommodated by the symmetry breaking instabilities of the spin liquid models in the first category. We carried out a fully quantum mechanical analysis of the oscillations, carried out in a model which includes the lattice potential, charge order, and the magnetic field. We found signatures of the electron pocket in the quantum oscillations. We also found clear oscillations from smaller hole pockets, which should be detectable in experiments. Our analysis included a description of the crossover in the oscillations from bidirectional (checkerboard) to unidirectional (stripe-like) density wave order. How-

ever, we shall not discuss details of this computation in the present chapter, which is devoted to a discussion of the photoemission experiments in the pseudogap regime [58, 110, 252, 87, 238, 127, 189] at intermediate temperatures and in the absence of a magnetic field.

The rest of this chapter is organized as follows: in section 4.2, we define our model for the Fermi-surface, coupled to the charge-density wave and superconducting order parameters. Sections 4.2.1 and 4.2.2 describe the phenomenological theory used for describing the thermal fluctuations of these order parameters and the modifications brought about by coupling them to the Fermi-surface. In section 4.3, we present our results for the electronic spectral functions and compare them with experimentally observed trends.

4.2 Model

We base our analysis on the following model hamiltonian

$$\begin{aligned} H = \sum_{\boldsymbol{r},\boldsymbol{a}} \Big[& - t_a c^\dagger_{\boldsymbol{r}+\boldsymbol{a}} c_{\boldsymbol{r}} + \Delta_{\boldsymbol{a}} \Psi_{\boldsymbol{r}+\boldsymbol{a}/2} c^\dagger_{\boldsymbol{r}+\boldsymbol{a},\uparrow} c^\dagger_{\boldsymbol{r},\downarrow} + \text{h.c.} \\ & + \sum_i P^i_{\boldsymbol{a}} e^{\mathrm{i}\boldsymbol{Q}_i\cdot(\boldsymbol{r}+\boldsymbol{a}/2)} \Phi^i_{\boldsymbol{r}+\boldsymbol{a}/2} c^\dagger_{\boldsymbol{r}+\boldsymbol{a}} c_{\boldsymbol{r}} + \text{h.c.} \Big] . \end{aligned} \tag{4.1}$$

Here $\boldsymbol{r}$ labels the sites of a square lattice and the vector $\boldsymbol{a}$ runs over first, second and third neighbors, and also on-site ($\boldsymbol{a} = 0$). The first term is the usual kinetic term, with hopping parameters t_a.

The second term couples the electron to the superconducting order parameter. The coefficient $\Delta_{\boldsymbol{a}}$ specifies the superconducting form factor and the field Ψ is the superconducting order parameter: it can be short-ranged or acquire an expectation

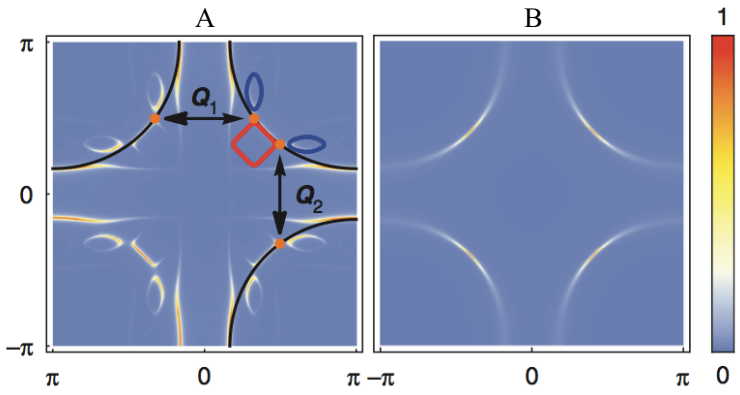

Figure 4.1: (a) The color density plot displays the electron spectral function in the presence of long-range bidirectional bond density wave (BDW) at zero magnetic field (in the unfolded Brillouin zone). Such long-ranged BDW is likely to be present only in a strong magnetic field and will not be seen in ARPES experiments. Annotations are superimposed to highlight aspects of the spectral density. In black, the Fermi surface used for our computation. Dashed arrows mark the wavevectors of the BDW. The BDW causes reconstruction of the Fermi surface and the formation of an electron-like pocket, marked in red, and two hole-like pockets, marked in blue. The pocket contours are obtained by semiclassical analysis as described in Ref. [11]. The parameters are $t_1 = 1.0$, $t_2 = -0.33$, $t_3 = 0.03$, $\mu = -0.9604$, $p = 10\%$, $P_0^x = P_0^y = 0.15$, $\delta = 0.317$. (b) Electron spectral function in the presence of fluctuating superconducting and bond density wave correlations. The parameters are $p = 11\%$, $\Delta_0 = P_0^x = P_0^y = 1$, $T/t_1 = 0.06$, $g/\Lambda^2 = 0.2$, $\rho_S = 0.05$, $\Lambda = 2$. The details are discussed in sec. 4.2.2

value.

The third term couples the fermion to the bond order. The index i labels different wavevectors $\boldsymbol{Q}_i$, the coefficients $P_{\boldsymbol{a}}^i$ specify the corresponding form factors and the fields Φ^i are the order parameters, which can also be long-ranged or fluctuating. Throughout this work we consider a specific form of a density wave which resides primarily upon the bonds of the lattice: this is not crucial for the quantum oscillations, but is important for the electron spectral function at intermediate temperatures. Building on recent experimental and theoretical work [154, 196, 67, 97, 105, 27, 117,

20, 60, 199, 10, 9, 149, 52, 77] we use a bond density wave (BDW) with a d-form factor.

Both interaction terms can be obtained by appropriate decoupling of the Heisenberg interaction in the particle-hole and particle-particle channels [196].

We use a d-wave superconducting form factor $\Delta_{\pm\hat{\boldsymbol{x}}} = +\Delta_0/2, \Delta_{\pm\hat{\boldsymbol{y}}} = -\Delta_0/2$ and a bond order with the same form factor $P^i_{\pm\hat{\boldsymbol{x}}} = +P^i_0/2, P^i_{\pm\hat{\boldsymbol{y}}} = -P^i_0/2$ [154, 196] which is supported by recent experimental evidence [52, 77] although a small s-wave component may also be present [45]. We consider a set of two wavevectors $\mathbf{Q}_1 = 2\pi(\delta, 0)$ and $\mathbf{Q}_2 = 2\pi(0, \delta)$, with $\delta \sim 0.3$, also based on experimental evidence.

A summary of the main results from Ref. [11] appears in fig.4.1, which shows the electronic spectral functions in the presence of long-range incommensurate BDW (fig.4.1a) and in the presence of fluctuating BDW and superconductivity (fig.4.1b). The computations leading to the latter will be discussed in much more details in the remainder of this chapter.

4.2.1 Onset of charge-order and superconductivity

As mentioned previously, a peculiar feature associated with charge-order in the underdoped cuprates, is the highly *non mean-field-like* nature of the onset, at a temperature that is typically lower than the pseudogap temperature, T^*. In fact this behavior is reminiscent of the onset of antiferromagnetism in the parent insulating antiferromagnetic state of La_2CuO_4 [118]. We now understand this gradual onset of intensity[1] in the structure factor over a broad range of temperatures in terms of the

[1]The finite transition temperature arises solely due to the non-zero interlayer coupling.

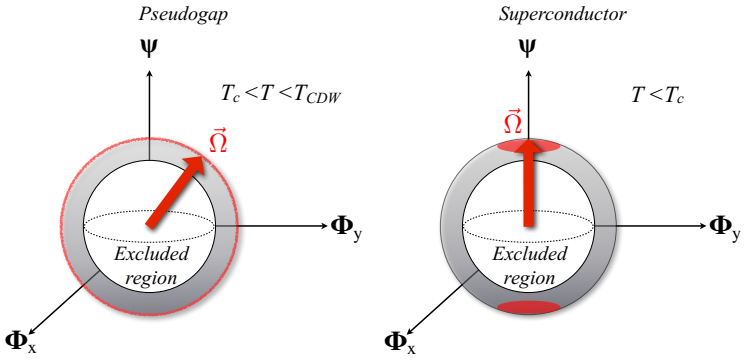

Figure 4.2: The angular fluctuations of the six-component order-parameter, $\mathbf{\Omega}$, describe the non-mean field onset of charge density wave correlations below $T_{\rm CDW}$. Due to a finite $g > 0$, $\mathbf{\Omega}$ fluctuates only along the superconducting directions for $T < T_c$, the Kosterlitz-Thouless transition temperature corresponding to the $O(2)$ component associated with Ψ. For $w < 0$, the Z_2 invariance associated with $x \leftrightarrow y$ can be broken spontanteously.

angular fluctuations of an O(3) field (corresponding to the Néel order) in two spatial dimensions [35].

The above observation then begets the question if the onset of charge-order can be understood in terms of the angular-fluctuations of an order-parameter [67], and if so, can one write down an effective field theory that describes these fluctuations. Let us first note the symmetries associated with the above problem: $\mathrm{O}(2)\times\mathrm{O}(2)\times\mathrm{O}(2)\times\mathbb{Z}_2$. These correspond to, charge-conservation, $x-$translations, $y-$translations and the $x \leftrightarrow y$ symmetries. In addition, we use the fact that the system also preserves time-reversal and inversion symmetries.

The onset can then be best understood in terms of the angular fluctuations associated with a six-component order parameter [91]:

$$\mathbf{\Omega} = (\mathrm{Re}\Psi, \mathrm{Im}\Psi, \mathrm{Re}\Phi_x, \mathrm{Im}\Phi_x, \mathrm{Re}\Phi_y, \mathrm{Re}\Phi_y), \tag{4.2}$$

where Ψ represents the superconducting component and $\Phi_{x,y}$ represent the incom-

mensurate charge density wave order parameters along x and y directions[2]. The fluctuations are assumed to be of a purely classical and thermal nature and are postulated to be described by the following non-linear σ-model (NLσM),

$$Z = \int \mathcal{D}\mathbf{\Omega}(\boldsymbol{r})\delta(\mathbf{\Omega}^2 - 1)\, \exp\Big(- \frac{\mathcal{S}_{\rm cl}}{T}\Big), \tag{4.3}$$

$$\mathcal{S}_{\rm cl} = \frac{\rho_{\rm S}}{2}\int d^2r \Big[|\nabla\Psi|^2 + \lambda(|\nabla\Phi_x|^2 + |\nabla\Phi_y|^2) + g(|\Phi_x|^2 + |\Phi_y|^2) + w(|\Phi_x|^4 + |\Phi_y|^4)\Big]. \tag{4.4}$$

In the above, $\rho_{\rm S}$ and $\rho_{\rm S}\lambda$ control the helicity moduli of the superconducting and of the density wave order respectively. The coupling g breaks the symmetry explicitly between the Ψ and Φ_x, Φ_y directions. It sets the relative energetic cost of ordering between the superconducting and density wave directions. We take $g > 0$, so that superconductivity is preferred at low temperatures (figure 4.2). The coupling w imposes the square lattice point group symmetry on the density wave order.

It is possible to add higher-order terms to the above action, without significant qualitative differences in the results. The above action was studied using (classical) Monte-Carlo simulations and within a '$1/N$' expansion (where N corresponds to the number of components of $\mathbf{\Omega}$; $N = 6$ for the theory in Eq.4.4) [91]. The results for the structure factor and comparison to experiments on YBCO are shown in Fig. 4.3. The agreement with experimental data is very good, except at low and high temperatures. In the absence of impurities, that would otherwise pin the charge-order and give rise to a finite intensity at low temperatures, the structure-factor goes to zero. On the other hand, at higher temperatures, the onset of amplitude fluctuations, which are

[2]Note that the region in the vicinity of $\mathbf{\Omega} = 0$ is forbidden, i.e. the amplitude fluctuations of $|\mathbf{\Omega}|$ are completely forbidden below $T_{\rm CDW}$ and probably onset at an even higher temperature.

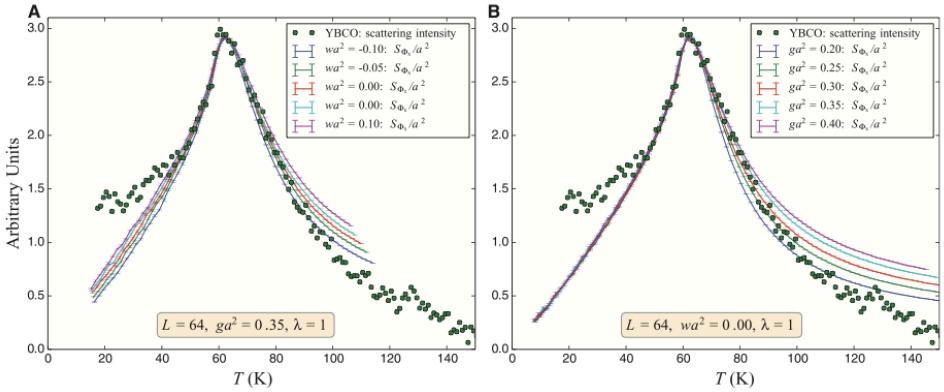

Figure 4.3: Comparison of X-ray data for the CDW scattering intensity to the structure-factor calculated in Monte Carlo simulations of $\mathcal{Z}$ for different parameter sets. Adapted from Ref.[91].

ignored in the above setup, would also decrease the intensity.

The theory in Eq. (4.4) has also been applied to measurements of the diamagnetic susceptibility [139, 126] in YBCO. This measures the superconducting Ψ component of the O(6) order parameter, complementing the X-ray measurements of the charge order represented by Φ_x, Φ_y. It was found [90] that the same set of parameters can provide a reasonable simultaneous fit to both the X-ray and diamagnetism measurements. Thus the O(6) theory provides a surprising quantitative connection between two very different classes of experiments, and this supports its validity as a theory of fluctuating orders in the low temperature pseudogap regime.

4.2.2 Order parameter fluctuations coupled to Fermi-surface

In this section, we couple the O(6) order, $\boldsymbol{n}$, to the electrons and compute the electronic self energies. Similar computations of photoemission spectrum have been carried out earlier for the case of superconducting fluctuations [29, 212, 23, 24, 155];

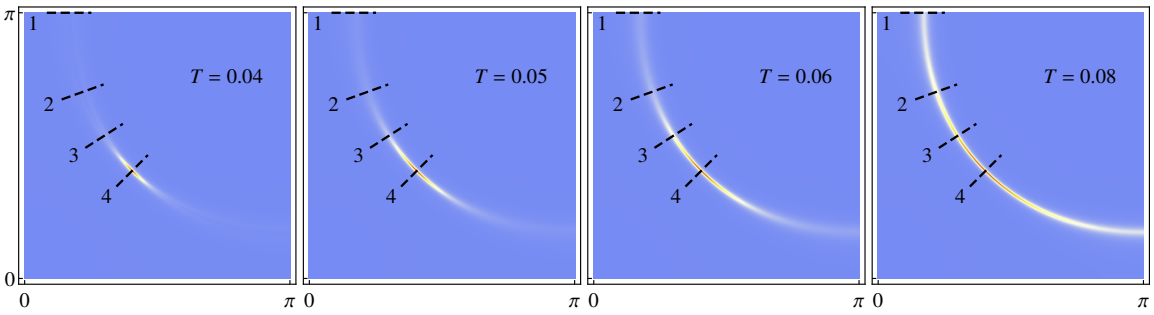

Figure 4.4: Electron spectral function in the presence of superconducting and bond order fluctuations, at four different temperatures. Dashed lines mark the cuts shown in Fig. 4.7. At sufficiently low temperatures superconducting fluctuations gap out the antinodal region. Bond order fluctuations are very short-ranged and do not have observable effects. $p = 11\%$, $\Delta_0 = P_0^x = P_0^y = 1$, $\rho_S = 0.05$, $\Lambda = 2$.

our analysis below shows that a combined model agrees well with many of the observed trends as a function of temperature, angle around the Fermi surface, and energy.

In the large N limit (N being the number of components of $\boldsymbol{n}$), the propagators of Ψ and $\Phi_{x,y}$ have a massive form of the type (we ignore here the possibility of having a $C_4 \to C_2$, Ising symmetry breaking),

$$D^{\rm s}_{\rm cl}(\boldsymbol{q}) = \frac{1}{\boldsymbol{q}^2 + \overline{\sigma}}, \qquad\qquad D^{\rm b}_{\rm cl}(\boldsymbol{q}) = \frac{1}{\lambda \boldsymbol{q}^2 + \overline{\sigma} + g + \overline{\phi}}, \tag{4.5}$$

where the parameters $\bar{\sigma}$ and $\bar{\phi}$ are to be determined in terms of the couplings in (4.4) by solving the large N saddle point equations,

$$\begin{aligned} \frac{\rho_S}{T} &= \int \frac{{\rm d}^2\boldsymbol{q}}{(2\pi)^2} \left[\frac{1}{\boldsymbol{q}^2 + \overline{\sigma}} + \frac{2}{\lambda \boldsymbol{q}^2 + \overline{\sigma} + g + \overline{\phi}} \right], \\ \overline{\phi} &= \frac{2wT}{\rho_S} \int \frac{{\rm d}^2\boldsymbol{q}}{(2\pi)^2} \frac{1}{\lambda \boldsymbol{q}^2 + \overline{\sigma} + g + \overline{\phi}}, \end{aligned} \tag{4.6}$$

which we regulate with a hard momentum cutoff $\boldsymbol{q}^2 < \Lambda^2$.

The mass $\overline{\sigma}$ of the superconducting order parameter is strongly temperature de-

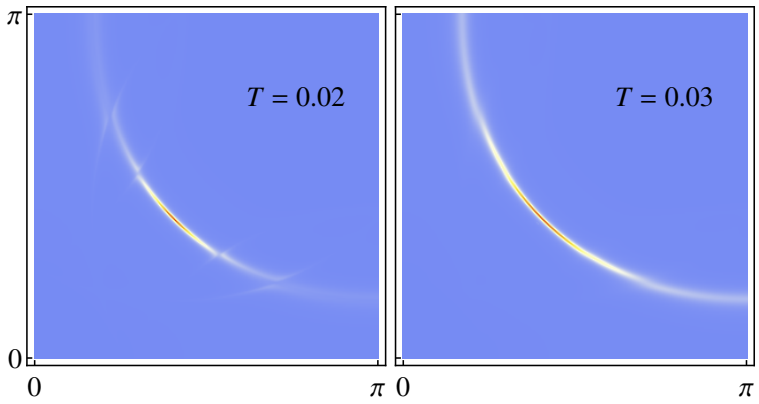

Figure 4.5: Electron spectral function in the presence of superconducting and bond order fluctuations for a fully isotropic O(6) model ($g/\Lambda^2 = 0$). At sufficiently low temperatures bond order fluctuations lead to incipient Fermi surface reconstruction. $p = 11\%$, $\Delta_0 = P_0^x = P_0^y = 1$, $\rho_S = 0.05$, $\Lambda = 2$.

pendent, and it is exponentially suppressed if $T \ll \rho_S$:

$$\frac{\overline{\sigma}(T)}{\Lambda^2} \sim e^{-4\pi\rho_S/T} . \tag{4.7}$$

This is how the large N sigma model approximates long-range superconductivity. On the other hand, for $T \gg \rho_S$

$$\frac{\overline{\sigma}(T)}{\Lambda^2} \sim \frac{3}{4\pi}\frac{T}{\rho_S} - \frac{2}{3}\frac{g}{\Lambda^2} - \frac{1}{2} + \mathcal{O}\left(\frac{\rho_S}{T}\right) . \tag{4.8}$$

The mass of the bond order parameter is $\bar{\sigma} + g$ (when $w = 0$), and hence the parameter g determines the correlation length of the bond order at low temperatures. We take the universal number $g/\Lambda^2 \sim 0.2$, based on the results in ref. [91], but we still have to fix Λ. We choose it in such a way that the correlation length of the density wave order at low temperature is a few lattice spacings. We also verify explicitly that our conclusions are not affected as the correlation length of the bond order varies from 2 to 10 lattice spacings, which is the range in which the experimental value lies.

The NLσM (Eqn. 4.4) is a completely classical model, and neglects the fact that superconducting and bond order parameters are coupled to the gapless fermionic degrees of freedom along the Fermi surface. We include this contribution at RPA level, computing the one-loop self-energy of the bosons due to the interaction with the fermions (see appendix C.2). The sole effect of these bubbles is to give rise to damping terms at low energies. The improved form of the propagators is,

$$\begin{aligned} D_{\mathrm{s}}(\boldsymbol{q},\, \mathrm{i}\Omega_n) &= \frac{1}{\alpha_{\mathrm{s}}|\Omega_n| + \boldsymbol{q}^2 + \bar{\sigma}}\,, \\ D_{\mathrm{b}}(\boldsymbol{q},\, \mathrm{i}\Omega_n) &= \frac{1}{\alpha_{\mathrm{b}}|\Omega_n| + \lambda\boldsymbol{q}^2 + \bar{\sigma} + g + \bar{\phi}}\,, \end{aligned} \tag{4.9}$$

where $\alpha_{\mathrm{s,b}}$ parametrizes the strength of damping (we will take $\alpha_{\mathrm{s}} = \alpha_{\mathrm{b}} = 1$ in the rest of the computation).

The electron spectral function due to the retarded self-energy $\Sigma(\boldsymbol{k}, \omega)$ of the electrons in the presence of fluctuating superconducting and bond order parameters is given by,

$$A(\boldsymbol{k}, \omega) = -\frac{1}{\pi}\mathrm{Im}\,\frac{1}{\omega - \epsilon_{\boldsymbol{k}} - \Sigma(\boldsymbol{k}, \omega)}\,. \tag{4.10}$$

The self-energy has two contributions, from the particle-particle and particle-hole channel. We have

$$\begin{aligned} \Sigma_{\mathrm{s}}(\boldsymbol{k}, i\omega_m) &= -\frac{1}{\beta}\sum_n \int_{\boldsymbol{q}} \Delta^2_{\boldsymbol{k}-\frac{\boldsymbol{q}}{2}} \frac{1}{-\mathrm{i}\omega_m + \mathrm{i}\Omega_n - \epsilon_{\boldsymbol{q}-\boldsymbol{k}}} \frac{1}{|\Omega_n| + \varepsilon^{\mathrm{s}}_{\boldsymbol{q}}}\,, \\ \Sigma_{\mathrm{b}}(\boldsymbol{k}, i\omega_m) &= +\frac{1}{\beta}\sum_{n,i} \int_{\boldsymbol{q}} P^{i\ 2}_{\boldsymbol{k}+\frac{\boldsymbol{q}}{2}} \frac{1}{+\mathrm{i}\omega_m + \mathrm{i}\Omega_n - \epsilon_{\boldsymbol{q}+\boldsymbol{k}}} \frac{1}{|\Omega_n| + \varepsilon^{\mathrm{b}}_{\boldsymbol{q}-\boldsymbol{Q}_i}}\,, \end{aligned} \tag{4.11}$$

where Ω_n are bosonic Matsubara frequencies, ω_n are fermionic Matsubara frequenices and

$$\begin{aligned} \varepsilon^{\mathrm{s}}_{\boldsymbol{q}} &= \boldsymbol{q}^2 + \bar{\sigma}\,, \\ \varepsilon^{\mathrm{b}}_{\boldsymbol{q}} &= \lambda\boldsymbol{q}^2 + \bar{\sigma} + g + \bar{\phi}\,. \end{aligned} \tag{4.12}$$

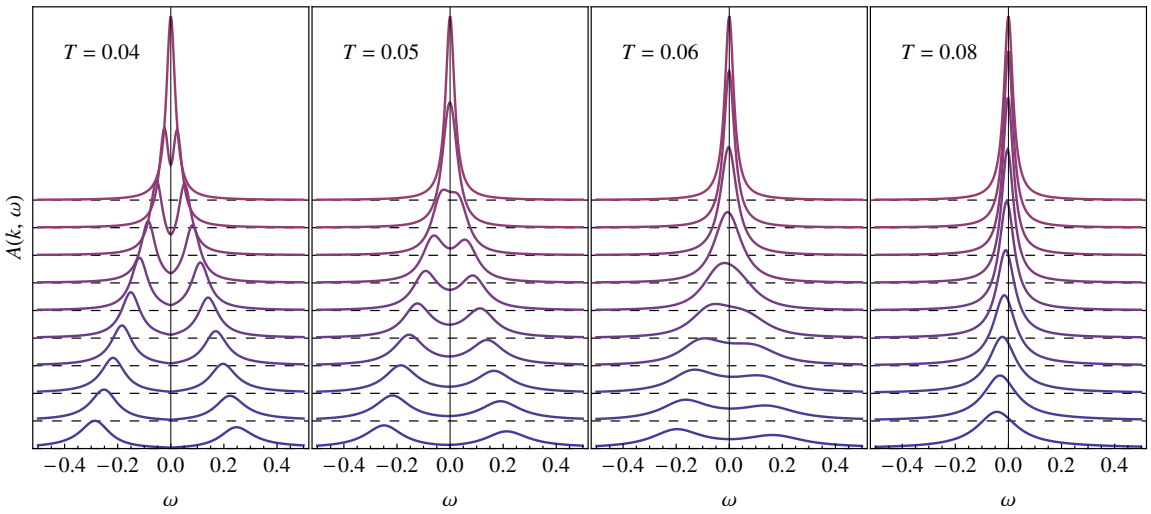

Figure 4.6: $A(\mathbf{k},\omega)$ at several $\boldsymbol{k}$-points on the bare Fermi surface $\epsilon_{\boldsymbol{k}} = 0$: from the node in red at the top to the antinode in blue at the bottom. $p = 11\%$, $\Delta_0 = P_0^x = P_0^y = 1$, $\rho_{\rm S} = 0.05$, $g/\Lambda^2 = 0.2$, $\Lambda = 2$.

The self energies are identical for up and down spin.

We carry out the Matsubara sum analytically and carry out the integral over $\boldsymbol{q}$ numerically using an adaptive integration routine as described below. The naive Matsubara sum

$$H_0(\omega - \epsilon, \varepsilon) \equiv \frac{1}{\beta} \sum_n \frac{1}{\omega + i\Omega_n - \epsilon} \frac{1}{|\Omega_n| + \varepsilon}\,, \tag{4.13}$$

although convergent, has poles for both $\mathrm{Im}\,\omega > 0$ and $\mathrm{Im}\,\omega < 0$. We are however free to add to H_0 the function

$$H_1(\omega, \epsilon, \varepsilon) \equiv \frac{n_{\rm F}(\epsilon) + n_{\rm B}(\epsilon - \omega)}{i(\epsilon - \omega) + \varepsilon}\,, \tag{4.14}$$

because $H_1(\mathrm{i}\omega_n, \epsilon, \varepsilon) = 0$. It is easy to verify that the function

$$H(\omega, \epsilon, \varepsilon) \equiv H_0(\omega - \epsilon, \varepsilon) + H_1(\omega, \epsilon, \varepsilon) \tag{4.15}$$

is analytic for $\mathrm{Im}\,\omega > 0$, and hence yields the retarded self-energy. Note that H_0 is a

real function of ω whereas H_1 has both a real and an imaginary part. Moreover, as a consequence of unitarity,

$$\mathrm{Im}\, H(\omega, \epsilon, \varepsilon) = \mathrm{Im}\, H_1(\omega, \epsilon, \varepsilon) \leq 0\,. \tag{4.16}$$

An explicit expression for H_0 exists in terms of the digamma function (see appendix C.3).

In terms of H we have

$$\begin{aligned} \Sigma_{\mathrm{s}}(\boldsymbol{k}, \omega) &= -\int_{\boldsymbol{q}} \Delta^2_{\boldsymbol{k}-\frac{\boldsymbol{q}}{2}}\; H^{\star}(-\omega, \epsilon_{\boldsymbol{q}-\boldsymbol{k}}, \varepsilon^{\mathrm{s}}_{\boldsymbol{q}})\,, \\ \Sigma_{\mathrm{b}}(\boldsymbol{k}, \omega) &= \sum_i \int_{\boldsymbol{q}} P^{i\;2}_{\boldsymbol{k}+\frac{\boldsymbol{q}}{2}}\; H(\omega, \epsilon_{\boldsymbol{k}+\boldsymbol{q}}, \varepsilon^{\mathrm{b}}_{\boldsymbol{q}-\boldsymbol{Q}_i}). \end{aligned} \tag{4.17}$$

4.3 Results

There are two energy scales in the system: the bandwidth, set by the hopping $t_1 \approx$ 3000 K, and the bare helicity modulus $\rho_{\mathrm{S}} \approx 150$K, which controls the temperature at which there is an onset of phase fluctuations of $\boldsymbol{n}$ in the O(6) model, and hence the temperature dependence of the correlation length of superconducting and bond order fluctuations. In the following, we explore a range of temperature $\rho_{\mathrm{S}} \lesssim T \lesssim 2\rho_{\mathrm{S}}$, with $\rho_{\mathrm{S}} = 0.05\, t_1$. We express temperature in units of t_1.

In Fig. 4.4 we display a section of the spectral function $A(\boldsymbol{k}, \omega)$ at constant frequency equal to the Fermi energy ($\omega = 0$), at four different temperatures. Even at the lowest temperature, a portion of the Fermi surface close to the node, a Fermi arc, survives as a contour of well-defined excitations in the presence of bond order and superconducting fluctuations. As the temperature increases, there is a gradual build up of spectral weight in the antinodal regions, and around $T \approx 0.08$, the full Fermi surface is recovered.

Let us now give an intuitive picture for what is causing the arcs. The damping of the superconducting order, combined with the $d-$wave form factor, leads to enhanced scattering of the fermionic excitations close to the anti-nodes. What is left in the form of an arc are essentially the nodal quasiparticles which have survived as sharp excitations. As temperature increases, a larger region around the nodes survives the effect of scattering by superconducting fluctuations. This is consistent with the observations of Kanigel et al. [110], who also observed an increase in the arc length as a function of increasing temperature.

It is reasonable to expect that $d-$wave bond order fluctuations would also cause enhanced scattering around points of the Fermi surface that are nested by the BDW wavevector. However, the correlation length of the bond order is much shorter than the superconducting one, by merit of our choice of the parameters g and Λ, and hence this phenomenon is not visible in Fig. 4.4. In general, for correlation lengths of order a few lattice spacings, as seen in experiment, the effect of bond order fluctuations on the spectral function is negligible.

If, however, the correlation length is enhanced, for example by setting $g = 0$, such that we have a fully isotropic O(6) model, then bond order fluctuations have a distinct effect, as shown in Fig. 4.5. At the lowest temperature the original Fermi surface breaks up into an arc-like feature close to the nodes and a number of shadow-like features similar to those discussed earlier in connection to long-range bond order. In spite of the bond order correlations being short-ranged and fluctuating, the shadows arise purely from the real part of the self-energy.

In addition to the observations made above, here we have the additional effect that

superconducting fluctuations somewhat suppress the shadows near the antinodes. It would be interesting to look for signatures of these features in future experiments in high quality samples.

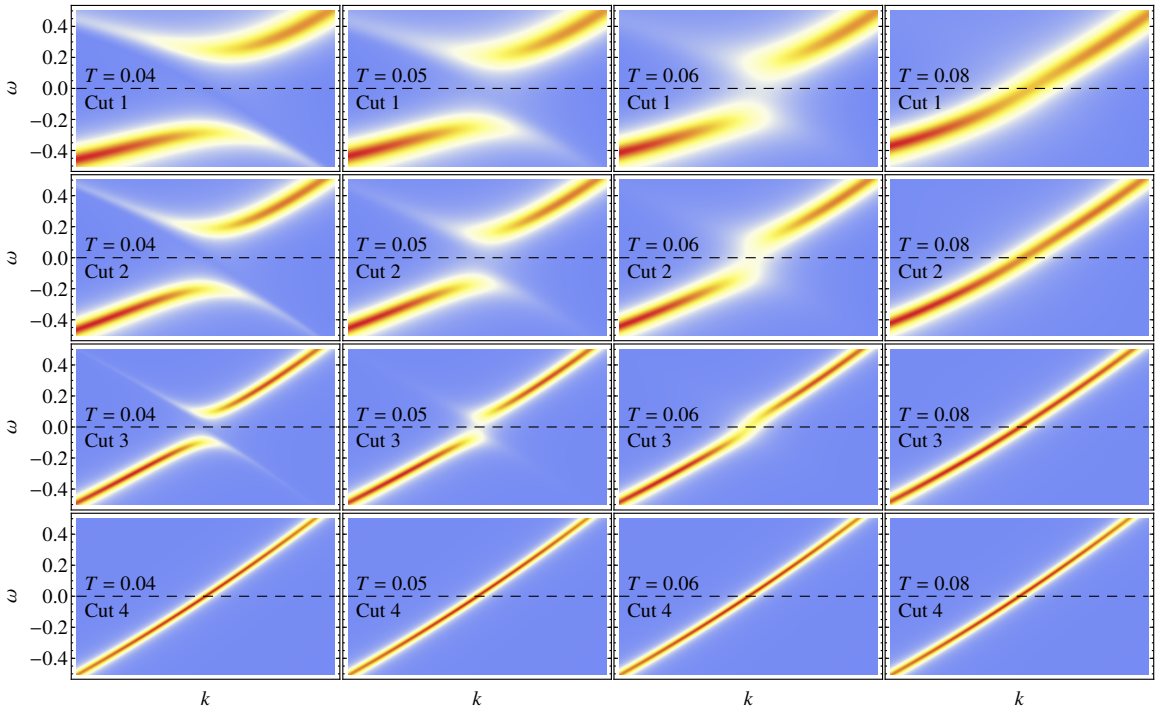

Figure 4.7: Frequency scans of the electron spectral function along the dashed lines in Fig. 4.5, at four different temperatures. $p = 11\%$, $\Delta_0 = P_0^x = P_0^y = 1$, $\rho_S = 0.05$, $g/\Lambda^2 = 0.2$, $\Lambda = 2$.

Interestingly, more recent experiments carried out using a different protocol seem to suggest that the arc length stays constant over a wide range of temperature and eventually undergoes a collapse at low temperatures [127]. This was presented as evidence for the BDW fluctuations playing a more prominent role in giving rise to the arcs. However, within our setup, the density wave fluctuations with a correlation length of even up to 10 lattice spacings don't play any significant role in the arc phenomenology. Furthermore, in the presence of purely density wave fluctuations,

the energy gap is centered above the Fermi energy for points situated between the antinodes and regions that are nested by the density wave wavevector [243]. This has been confirmed in ARPES experiments [252, 238].

Let us now discuss the properties of $A(\boldsymbol{k}, \omega)$ as a function of frequency for $\boldsymbol{k}$ points on the bare Fermi surface $\epsilon_{\boldsymbol{k}} = 0$. As shown in Fig. 4.6, at the lowest temperature $T = 0.04$, a well-defined gap is present at the antinodes. Moving towards the node (from the blue to the red scans), the gap closes at a $\boldsymbol{k}$ point which we identify with the tip of the arc. As temperature increases the gap closes and the full Fermi surface is recovered at sufficiently high temperatures. We note in passing that the location of the peak at the antinode at $T = 0.08$ is shifted away from $\omega = 0$ due to a renormalization of the bare dispersion by $\mathrm{Re}\,\Sigma(\boldsymbol{k}, \omega = 0)$.

Fig. 4.7 displays the quasiparticle dispersion along the black dashed lines labelled 1-4 in Fig.4.4 as a function of temperature. For the first cut, at the antinode, there is a well-defined gap in the quasiparticle spectrum at the Fermi surface, which closes as temperature increases. The overall scale of the gap is set by the magnitudes of Δ_0 and P_0^i. A similar behavior is seen for the second and third cut, albeit with a smaller gap that closes at a lower temperature. The fourth cut is a scan across the nodes and the dispersion remains gapless since neither the SC nor the BDW fluctuations affect the nodal quasiparticles.

As noted above, for our specific choice of parameters, the BDW fluctuations are subdominant to the SC fluctuations in the photoemission spectrum. In particular, the dispersions and the gap structure in the normal state obtained from this analysis are approximately particle-hole symmetric (as evident from Figs. 4.6 and 4.7). However,

recent experiments have seen evidence for particle-hole asymmetry at the tips of the Fermi-arcs and in the antinodes [252, 87]. Such an asymmetry arises naturally in the presence of more pronounced BDW fluctuations (as compared to the superconducting fluctuations). Our formalism can reproduce some of these features in the presence of fluctuating BDW with longer correlation lengths and stronger coupling to the fermions.

Finally, we reiterate the statement in the introduction that the present computation is expected to apply at the intermediate temperatures where charge order fluctuations are appreciable. A more complex model also including antiferromagnetism is likely needed at higher temperatures, which we do not discuss in this chapter.

4.4 Discussion

In this chapter, we have analyzed the combined effect of pairing and density wave fluctuations on photoemission at intermediate temperatures in the underdoped cuprates. In ref.[11], we also studied the influence of the same incommensurate density wave order on quantum oscillations in the high-field limit. In combination with other recent results [91], such a model appears to provide a satisfactory description of the underdoped cuprates in current high-field [65, 131, 229, 81, 207, 25, 206], photoemission [110, 238, 127], NMR [248, 249], STM [77, 125, 130, 96, 100, 235, 51, 55], and X-ray [78, 5, 39, 52, 51, 55] experiments. It can also be subjected to further tests by experiments at higher fields, in cleaner samples, or with higher precision. However, our analysis does not strongly constrain the nature of the high temperature pseudogap, where we need sharper experimental tests of the distinction between the

two categories of models described in the introduction.

On this issue, a recent work by the present author [44] has argued that the wavevector of the d-form factor BDW supports the spin liquid models in the first category. Some of the subsequent chapters shall take this alternative point of view. We suggest that unravelling the nature of the quantum-critical point apparent in recent experiments near optimal doping [92, 76, 187], and deciphering the nature of the strange metal, may be the route to resolving some of these long-standing and difficult questions.

Chapter 5

Feedback of pairing fluctuations on charge-order

"A wise man will make more opportunities than he finds." - Francis Bacon

5.1 Introduction

Based on our discussion so far, it is evident that the pseudogap (PG) regime of the hole-doped cuprates is possibly one of the most enigmatic phases of matter. It is identified by the onset of a large gap (~ 50 meV) below a temperature, T^*, as observed in a number of different probes. The gap persists down to the superconducting transition temperature, T_c, below which of course the system develops the usual superconducting gap.

A huge leap in our understanding came about with the discovery of quantum oscillations caused by a small electron-like pocket at very large magnetic fields [65].

This was the first clear evidence of the "normal" state in the pseudogap phase under large magnetic fields having some resemblance to a metallic state. More recently, in a series of remarkable experiments, it has become clear that the reconstructed electron-like pocket is caused by an incommensurate charge-density wave (CDW), competing with superconductivity [78, 5, 39, 51, 3, 248, 249, 132, 96, 235, 130, 151, 52, 77, 144]. The wavevector of this charge-density wave, which is of the type $(\pm Q_0, 0)$, $(0, \pm Q_0)$, appears to be linked to the Fermi surface in the anti-nodal regions. Furthermore, diamagnetism measurements in YBCO show significant fluctuation diamagnetism over approximately the same range of temperatures where X-ray experiments measure charge order fluctuations, indicating that there are significant superconducting fluctuations in this phase [139, 126]. A natural question that needs to be addressed is if both SC and CDW arise out of the same physics.

In the underdoped cuprates, due to the proximity to an antiferromagnet (AF) close to half-filling, the susceptibility, $\chi(\mathbf{q})$, is peaked around $\mathbf{K} = \pm(\pi, \pi(1-\delta))$, $\pm(\pi(1-\delta), \pi)$, ($\delta \neq 0$ when the fluctuations are peaked around an incommensurate wavevector) [89]. It is now well-understood that a metal interacting via such antiferromagnetic exchange interactions is unstable to $d-$wave superconductivity at low temperatures [201, 158, 186]. However, as was already discussed in section 1.3.2, an interesting consequence of the AF exchange interactions is that they also give rise to a secondary instability to a charge-density wave with a predominantly d-wave form factor [154, 196]. Significant recent developments have been the evidence for the predicted d-wave form factor in X-ray observations [52], and a direct phase-sensitive measurement of the d-wave form factor in scanning tunneling microscopy (STM) ex-

periments [77]. In the present chapter we will turn our attention to the wavevector of this CDW, and in particular, its connection to the SC fluctuations.

A number of recent works have addressed such issues [154, 196, 199, 60, 67, 149, 61, 10, 9, 243, 150, 233, 20]. In Refs. [154, 196], the wavevector of the leading CDW instability has been found to be of the form $\pm(Q_0, Q_0)$, $\pm\,(Q_0, -Q_0)$, while the experimentally observed wavevector was a subleading instability. At this point it is useful to introduce some new notation. From now on, we shall often refer to the experimentally observed CDW with wavevectors $(Q_0, 0)$ and $(0, Q_0)$ as "CDW-a" and the one with wavevectors $(Q_0, \pm Q_0)$ as "CDW-b" (see fig.5.1). More recently, it has been pointed out that in the presence of strong correlations arising from on-site and nearest-neighbor Coulomb repulsion, it is possible to obtain a stable CDW-a phase, with the wavevectors seen in experiments, in a certain window of parameter space [10]. Wang and Chubukov [243] have recently also examined retardation effects linked to the damping of spin fluctuations with a long correlation length, and argued for an extension of CDW-a with time-reversal symmetry breaking.

In this chapter, we will show that upon accounting for the interplay between superconductivity and charge-order in the underdoped cuprates, the CDW state with the correct wavevector (*i.e.* CDW-a) appears to be preferred over CDW-b over at least a small temperature window, as long as the antinodal regions of the fermi-surface are reasonably nested with a small curvature (a criterion to be made more precise later) [1]. In fig.5.1, Q_0 represents the separation between two neighboring "hot-spots". However, our computations in this paper are applicable for a range of different values

[1]However, we do not address here the issue of how the onset temperature for CDW-a compares to the bare superconducting T_c.

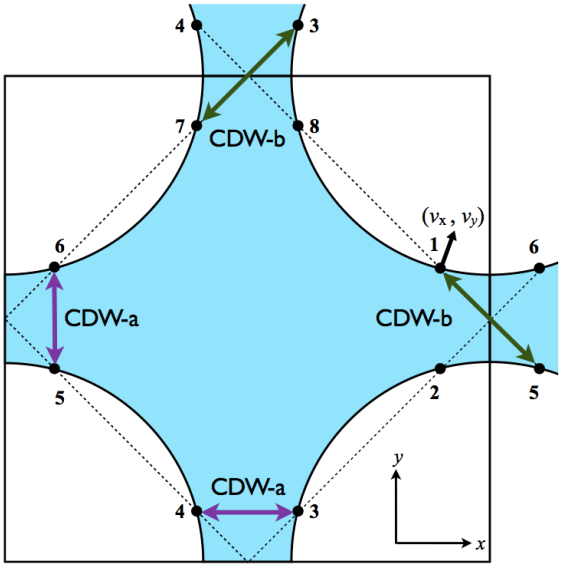

Figure 5.1: Generic Fermi-surface for hole-doped cuprates, with the filled states shaded in blue. Solid circles, numbered $1, .., 8$, represent hot-spots where the Fermi-surface intersects the magnetic Brillouin zone for a (π, π) SDW. The purple arrows represent the CDW-a wavevectors, which closely resemble the experimentally observed wavevector, while the green arrows represent the CDW-b wavevectors, which arise as the leading instability in a HF calculation . The fermi-velocity, (v_x, v_y), is shown at the hot-spot 1. The wavevectors of CDW-a are $(\pm Q_0, 0)$ and $(0, \pm Q_0)$, while those of CDW-b are $(Q_0, \pm Q_0)$. The computation in the present paper applies for a range of values of Q_0, and not just when it is equal to the separation between hot-spots as shown above; for different Q_0 we have to consider a corresponding set of 8 points around the Fermi surface, and our computations proceed unchanged.

of Q_0 that connect points in the antinodal regions and can be different from the hot-spot wavevector. Meier *et al.* [149] have also recently looked at the effect of superconducting fluctuations on charge-order in a different setup.

We also note our recent work [44], which employs a 'quantum disordered' model of the pseudogap as a topological metal, and proposes an alternative mechanism for charge ordering at the $(Q_0, 0)$, $(0, Q_0)$ wavevectors. This will be the topic of discussion in the next chapter.

The remainder of this chapter is organized as follows: In section 5.2.1, we introduce the theory of a metal interacting via antiferromagnetic exchange interactions (henceforth referred to as t-J model, but without any on-site Coulomb repulsion) and review a Hartree-Fock analysis for various charge-ordering and pair-density wave instabilities. Based on the leading instabilities that occur in a metal, we construct the minimal model in section 5.2.2 for a metal with pairing and charge-order fluctuations. In section 5.2.3, we take the low-energy limit of this theory and present the effective theory for the Fermions coupled to the order-parameters in the vicinity of special points—the "hot-spots"—where the magnetic Brillouin-zone corresponding to $\mathbf{K}$ intersects the fermi-surface. We present the results of our computation, describing the mutual feedback of superconductivity and charge-order on each other, in sections 5.3.1 and 5.3.2. Finally in section 5.4, we summarize the main results emerging from this analysis. Some of the technical details are summarized in appendices D.1 and D.2.

5.2 Model

5.2.1 Instabilities of metal with antiferromagnetic exchange interaction

In this section, we briefly review some of the earlier results [196] obtained by carrying out a Hartree-Fock (HF) analysis of the t-J model (without any Gutzwiller projection). Consider the following model for fermions, $c_{i\alpha}$, interacting via short-

range antiferromagnetic exchange interactions,

$$H_{tJ} = \sum_{i,j} \left[(-t_{ij} - \mu\delta_{ij}) c^\dagger_{i\alpha} c_{j\alpha} + \frac{1}{2} J_{ij} \boldsymbol{S}_i \cdot \boldsymbol{S}_j \right], \tag{5.1}$$

where t_{ij} are the hopping amplitudes, μ denotes the chemical potential, J_{ij} are the AF exchange couplings and $\boldsymbol{S}_i = c^\dagger_{i\alpha} \boldsymbol{\sigma}_{\alpha\beta} c_{i\beta}/2$.

We are interested in looking at the various instabilities that can arise in this model in the particle-particle as well as particle-hole channel. We shall restrict our attention to pair-density wave (PDW), where the SC condensate carries a finite momentum, and charge-density wave states. We ignore the possibility of having spin-order, partly motivated by most experiments on the non-La-based cuprates (e.g. YBCO and BSCCO), where the region of charge-order has hardly any overlap with that of spin-order [248]. For the Hartree-Fock analysis, we need the best variational estimate for the following mean-field Hamiltonian,

$$\begin{aligned} H_{MF} = \sum_{\mathbf{k}} \Bigg[\varepsilon(\mathbf{k}) c^\dagger_{\mathbf{k},\alpha} c_{\mathbf{k},\alpha} \quad &+ \quad \sum_{\mathbf{Q}} \Delta_Q(\mathbf{k}) \epsilon_{\alpha\beta} c_{-\mathbf{k}+\mathbf{Q}/2,\alpha} c_{\mathbf{k}+\mathbf{Q}/2,\beta} \\ &+ \quad \sum_{\mathbf{Q}} P_Q(\mathbf{k}) c^\dagger_{\mathbf{k}+\mathbf{Q}/2,\alpha} c_{\mathbf{k}-\mathbf{Q}/2,\alpha} + \text{H.c.} \Bigg]. \end{aligned} \tag{5.2}$$

In the above, $\varepsilon(\mathbf{k})$ represents the electronic dispersion. All the functions, $\Delta_Q(\mathbf{k}), P_Q(\mathbf{k})$ are variational parameters which will be optimized by minimizing the free energy, $F \leq F_{MF} + \langle H - H_{MF} \rangle_{MF}$. As mentioned earlier, we have allowed for a spin-singlet pair-density wave along with a charge density wave at a finite wavevector, $\mathbf{Q}$. The pair-density wave at $\mathbf{Q} \to 0$ reduces to the standard BCS state where particles with opposite spins are paired at $\pm\mathbf{k}$.

Expanding the right-hand side of F in powers of $\Delta_Q(\mathbf{k})$ and $P_Q(\mathbf{k})$, we get,

$$\begin{aligned} F &= 2\sum_{\mathbf{k},\mathbf{k}',\mathbf{Q}} \Delta_Q^*(\mathbf{k})\sqrt{\Pi_S(\mathbf{k})}\mathcal{M}_S(\mathbf{k},\mathbf{k}')\sqrt{\Pi_S(\mathbf{k}')}\Delta_Q(\mathbf{k}') \\ &+ \sum_{\mathbf{k},\mathbf{k}',\mathbf{Q}} P_Q^*(\mathbf{k})\sqrt{\Pi_C(\mathbf{k})}\mathcal{M}_C(\mathbf{k},\mathbf{k}')\sqrt{\Pi_C(\mathbf{k}')}P_Q(\mathbf{k}'), \end{aligned} \tag{5.3}$$

where the kernels $\mathcal{M}_{S,C}(\mathbf{k},\mathbf{k}')$ are given by,

$$\mathcal{M}_{S,C}(\mathbf{k},\mathbf{k}') = \delta_{\mathbf{k},\mathbf{k}'} + \frac{3}{V}\,\chi(\mathbf{k}-\mathbf{k}')\sqrt{\Pi_{S,C}(\mathbf{k})\Pi_{S,C}(\mathbf{k}')}, \tag{5.4}$$

and the polarizabilities are,

$$\Pi_S(\mathbf{k}) = \frac{1-f(\varepsilon(\mathbf{k}+\mathbf{Q}/2))-f(\varepsilon(-\mathbf{k}+\mathbf{Q}/2))}{\varepsilon(\mathbf{k}+\mathbf{Q}/2)+\varepsilon(-\mathbf{k}+\mathbf{Q}/2)}, \tag{5.5}$$

$$\Pi_C(\mathbf{k}) = \frac{f(\varepsilon(\mathbf{k}+\mathbf{Q}/2))-f(\varepsilon(\mathbf{k}-\mathbf{Q}/2))}{\varepsilon(\mathbf{k}-\mathbf{Q}/2)-\varepsilon(\mathbf{k}+\mathbf{Q}/2)}, \tag{5.6}$$

with $f(...)$ the Fermi-function and $\chi(\mathbf{k})(=\sum_{i,j} J_{ij}e^{i\mathbf{q}.(\mathbf{r}_i-\mathbf{r}_j)}/4)$, the AF susceptibility. Note that for dispersions that satisfy $\varepsilon(\mathbf{k}+\mathbf{Q}) = -\varepsilon(\mathbf{k})$, $\Pi_S(\mathbf{k}) = \Pi_C(\mathbf{k})$. This holds in the vicinity of the hot-spots for certain values of $\mathbf{Q}$ and will have important consequences, which we shall revisit later.

Pair-density wave and charge-ordering in the metal occurs via condensation in the eigenmodes of the operators $\mathcal{M}_{S,C}$ with the lowest eigenvalues. In order to find the leading instability in the pairing and charge-ordering channel, we need to solve the following eigenvalue problem,

$$\frac{3}{V}\sum_{\mathbf{k}'}\sqrt{\Pi_S(\mathbf{k})}\;\chi(\mathbf{k}-\mathbf{k}')\sqrt{\Pi_S(\mathbf{k}')}\phi_S(\mathbf{k}') = \lambda_S\phi_S(\mathbf{k}'), \tag{5.7}$$

$$\frac{3}{V}\sum_{\mathbf{k}'}\sqrt{\Pi_C(\mathbf{k})}\;\chi(\mathbf{k}-\mathbf{k}')\sqrt{\Pi_C(\mathbf{k}')}\phi_C(\mathbf{k}') = \lambda_C\phi_C(\mathbf{k}'). \tag{5.8}$$

Instead of working with the form of $\chi(\mathbf{k})$ introduced above, we assume that the

AF susceptibility, $\chi(\mathbf{q})$, has the form,

$$\chi(\mathbf{q}) = \sum_{\mathbf{K}} \frac{\chi_0}{4(\xi^{-2} + 2(2 - \cos(q_x - K_x) - \cos(q_y - K_y)))}, \tag{5.9}$$

which is peaked near the antiferromagnetic wavevector, $\mathbf{K}$ (as introduced earlier), with ξ representing the AF correlation length and χ_0 the overall strength of the spin-fluctuations. There is little difference between the results for $\delta = 0$ and $\delta \neq 0$.

In figs. 5.2 (a) and (b) we plot the lowest eigenvalues $\lambda_{S,C}/\chi_0$, obtained after diagonalizing eqns.5.8 on a discrete Brillouin zone with L^2 points. We use the following electronic dispersion: $\varepsilon(\mathbf{k}) = -2t_1(\cos(k_x) + \cos(k_y)) - 4t_2\cos(k_x)\cos(k_y) - 2t_3(\cos(2k_x) + \cos(2k_y)) - \mu$. Let us start with a discussion of the pair-density wave state (fig.5.2a). Not surprisingly, the state with $\mathbf{Q} = 0$ is the leading instability and in particular, $-\lambda_S$ for $\mathbf{Q} = 0$ has a logarithmic divergence as $T \to 0$. We do not find any other local-minima in phase-space; the BCS-log for $\mathbf{Q} = 0$ simply overwhelms any other PDW state that might have otherwise arisen within this weak-coupling approach. Comparing the numerical values of the eigenvalues λ_S and λ_C in figs.5.2 (a) and (b), it is clear that $-\lambda_S$ (at $\mathbf{Q} = 0$) is the smallest. Therefore, in the presence of short-range AF interactions, the leading weak-coupling quadratic instability indeed turns out to be to a SC (with $d-$wave symmetry; this information is contained in the structure of ϕ_S).

For the charge-ordering instability (fig.5.2b), the global minimum is located at the diagonal wavevector (Q_0, Q_0). This corresponds to the CDW-b state introduced earlier. However notice the "valleys" of local minima extending from this wavevector to $(Q_0, 0)$ and $(0, Q_0)$, the CDW-a. It is also worth pointing out that the form factors associated with these CDWs, ϕ_C, primarily have a $d-$wave component. In real space,

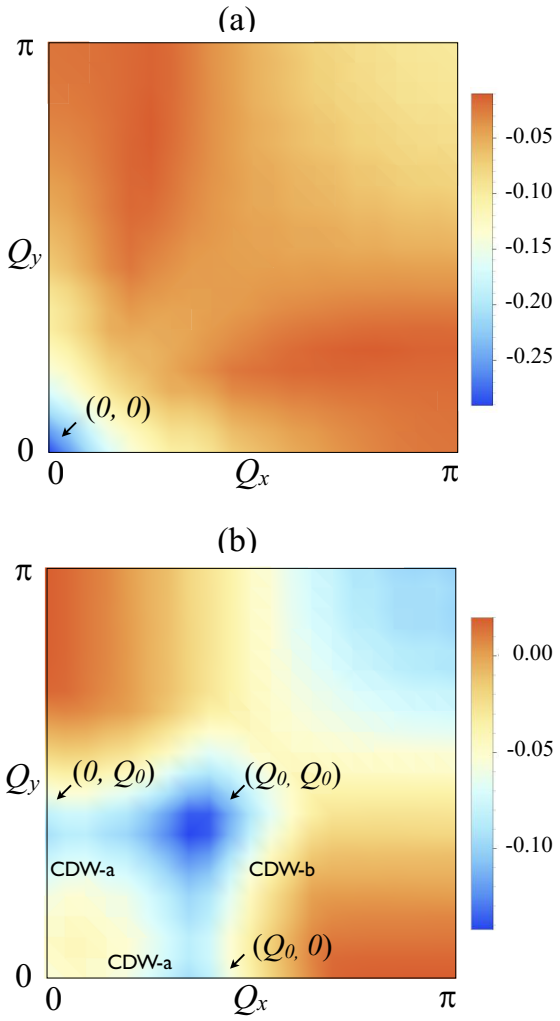

Figure 5.2: Plot of the smallest eigenvalue (a) λ_S/χ_0 and (b) λ_C/χ_0 as a function of Q_x and Q_y. We use a band-structure with $t_1 = 1.0$, $t_2 = -0.32$, $t_3 = 0.128$, $\mu = -1.11856$ (corresponding to the same fermi-surface used in Ref.[196]). The other parameters are $\xi = 2$, $T = 0.1$, $\delta = 1/4$ and $L = 20$. For the pair-density wave, the global minimum is located at $\mathbf{Q} = 0$ while for the charge-order, it is located at $\mathbf{Q} = (Q_0, Q_0)$ (CDW-b). In (b), note the valleys extending from (Q_0, Q_0) to $(Q_0, 0)$ and $(0, Q_0)$ (CDW-a)—the latter are local, but not global, minima.

this implies that the charge-density modulation is mostly on the Cu-Cu links (bonds) rather than on the sites. Hence they are also referred to as bond-density wave (BDW).

The reason why CDW-b turned out to be the leading CDW instability is actu-

ally related to two features in our problem above: (i) the absence of a gap in the spectrum at the antinodes, and, (ii) an *emergent* particle-hole symmetry associated with the exchange interactions, $J_{ij}\boldsymbol{S}_i \cdot \boldsymbol{S}_j$. This exchange interaction is invariant under independent SU(2) rotations on each lattice site that map particles to holes and vice-versa. These rotations therefore naturally map SC to CDW-b. In the absence of any fermi-surface curvature or other interaction terms that break this symmetry, both of these instabilites would be exactly degenerate. However, once it is broken, CDW-b becomes a sub-leading instability (SC is always guaranteed to remain the leading instability even in the presence of a curvature since the points $\pm\mathbf{k}$ are always "nested". However, a very large nearest neighbor Coulomb interaction term, Vn_in_j, can suppress superconductivity, for instance). We also note in passing that CDW-a is mapped to the PDW [134] at the same wave-vector under these rotations; we do not consider this PDW [2] here because it does not appear as a preferred eigenvalue of λ_S in fig. 5.2a.

The above analysis was carried out in the limit where the different orders were decoupled from each other, i.e. we did not look at the feedback of one over the other and analyzed the free-energy F to only quadratic order. Let us therefore now construct a minimal model for SC and CDW fluctuations in a metal and analyze the effective theory beyond quadratic order in the next section.

[2]Ref. [134] argued that a pair-density wave state might arise due to interactions mediated by transverse components of gauge-fields (that remain unscreened) in an RVB scenario by an effect analogous to the Ampere effect. We considered possible PDW states in fig. 5.2a, but they were not preferred in our computation.

5.2.2 Metal with SC and CDW fluctuations

Consider now a model for the fermions with a generic fermi-surface as shown in fig.5.1. Based on our HF analysis in the previous section, we know the (sub-)leading instabilities were to a (i) $d-$wave superconductor, (ii) CDW-b with wavevectors $(Q_0, \pm Q_0)$, and, (iii) CDW-a with wavevectors $(Q_0, 0)$ and $(0, Q_0)$. We can use this information to construct a model for a metal with strong pairing and CDW fluctuations. Therefore, we consider the theory for the fermions coupled to superconducting (Ψ) and CDW (Φ) fluctuations (which are in their uncondensed phase, as is the case in the PG regime). The Hamiltonian is then given by,

$$
\begin{aligned}
H &= H_0 + H_S + H_B, \text{ where} && (5.10)\\
H_0 &= \sum_{\mathbf{k}} (\varepsilon_{\mathbf{k}} - \mu)\ c^{\dagger}_{\mathbf{k},\alpha} c_{\mathbf{k},\alpha}, && (5.11)\\
H_S &= \sum_{\mathbf{k}} (\Delta_s(\mathbf{k})\ c^{\dagger}_{\mathbf{k}+\mathbf{q}/2,\uparrow} c^{\dagger}_{-\mathbf{k}+\mathbf{q}/2,\downarrow} \Psi_{\mathbf{q}} + \text{H.c.}), && (5.12)\\
H_B &= \sum_{\mathbf{k},\mathbf{q}} \left[\left(\sum_{\mathbf{Q}} P_Q(\mathbf{k})\ \Phi_{\mathbf{q}-\mathbf{Q}} \right) c^{\dagger}_{\mathbf{k}+\mathbf{q}/2,\alpha} c_{\mathbf{k}-\mathbf{q}/2,\alpha} + \text{H.c.} \right]. && (5.13)
\end{aligned}
$$

In the above, $\Delta_s(\mathbf{k})$ is the usual form factor associated with $d-$wave superconductivity and $P_Q(\mathbf{k})$ is the form-factor for CDW with wave-vector $\mathbf{Q}$. We would now like to obtain an effective action in terms of Ψ and Φ (both CDW-a and b) after integrating out the fermions. The aim of this work is to study the effect of SC fluctuations on these two different CDW states and to analyze if the competition between the different order parameters can preferentially select a particular state. It will be particularly interesting if this state corresponds to the one that has been seen experimentally.

5.2.3 Low-energy theory

Instead of carrying out the above task with the full Fermi-surface, let us analyze the theory in the vicinity of the hot-spots labelled $j = 1, .., 8$ in fig.5.1. We expand the dispersion close to the hot-spots so that

$$\varepsilon_{\mathbf{k},j} = v_{F,\mathbf{k}_j} k_\perp + \kappa k_\parallel^2, \tag{5.14}$$

with $k_\perp (k_\parallel)$ being the momentum normal (parallel) to the Fermi surface. The Fermi-velocities are given by, $\mathbf{v}_{F,\mathbf{k}_1} = (v_x, v_y)$, $\mathbf{v}_{F,\mathbf{k}_2} = (v_x, -v_y)$, $\mathbf{v}_{F,\mathbf{k}_4} = (-v_y, -v_x)$ and $\mathbf{v}_{F,\mathbf{k}_7} = (-v_y, v_x)$. The other velocities can be obtained similarly by symmetry. The parameter κ is related to the Fermi surface curvature.

The bare Lagrangian for the fermions in the vicinity of the hot-spots, ψ_j ($j = 1, .., 8$), is then given by,

$$\mathcal{L}_0 \;=\; \sum_{j=1}^{8} \Big[\psi_j^\dagger (i\omega - \varepsilon_{\mathbf{k},j}) \psi_j \Big]. \tag{5.15}$$

The same expansion can be carried out for a set of any eight points in the antinodal regions, that are not necessarily connected by the hot-spot wavevectors.

Form-factor of the CDW

There are two fundamental properties associated with the CDW orders — the wavevector and the structure of the form factor. We have explored the wavevectors that can arise in our HF computation in section 5.2.1, while the form factors associated with the different CDW orders for the full underlying fermi-surface were already computed in Ref.[196]. In this section, we shall revisit this issue within our low-energy formulation.

If we go back to eqn.5.3 and focus only on the terms involving charge-order, we obtain

$$F_C = \sum_{\mathbf{Q}} \left[\sum_{\mathbf{k}} |P_Q(\mathbf{k})|^2 \Pi_C(\mathbf{k}) + \frac{3}{V} \sum_{\mathbf{k},\mathbf{k}'} \chi(\mathbf{k}-\mathbf{k}') \Pi_C(\mathbf{k}) \Pi_C(\mathbf{k}') P_Q^*(\mathbf{k}) P_Q(\mathbf{k}') \right]. \quad (5.16)$$

We now assume that $\chi(\mathbf{k}-\mathbf{k}')$ is peaked at $\mathbf{k}-\mathbf{k}' = \mathbf{K} = (\pi,\pi)$ and perform the integrations over $\mathbf{k}$ and $\mathbf{k}'$ in patches in the neighborhoods of the hot-spots that satisfy the above constraint. Furthermore, we assume that $P_Q(\mathbf{k})$ can be treated as piecewise constant in the patches and treat χ as static and non-critical, i.e. $\chi \approx \chi_0/\xi^{-2}$. For CDW-b, let us focus on the hot-spot pairs $\{2,6\}$ and $\{7,3\}$ where $P_Q(\mathbf{k})$ takes the values Υ_1^b and Υ_2^b. Similarly, for CDW-a, we choose to focus on the pairs $\{1,2\}$ and $\{4,7\}$ where $P_Q(\mathbf{k})$ takes the values Υ_1^a and Υ_2^a.

It is straightforward to see that for CDW-b, $\Pi_C(\mathbf{k})$ evaluated in the patches $\{2,6\}$ and $\{7,3\}$ are equal to each other due to purely geometric reasons, i.e. $\Pi_1^b = \Pi_2^b = \Pi^b$, so that,

$$F_C\Big|_b = \Pi^b \left[|\Upsilon_1^b|^2 + |\Upsilon_2^b|^2 \right] + \frac{3\chi_0}{\xi^{-2}} (\Pi^b)^2 \left[\Upsilon_1^{b*}\Upsilon_2^b + \Upsilon_2^{b*}\Upsilon_1^b \right]. \quad (5.17)$$

It is simple to diagonalize the above quadratic form and obtain the optimum linear combination of Υ_1^b and Υ_2^b. For CDW-b, the eigenvector corresponding to the lower eigenvalue has a purely $d-$wave form.

We can now do the same computation for CDW-a and we immediately find that $\Pi_1^a \neq \Pi_2^a$ (once again, for purely geometric reasons), so that,

$$F_C\Big|_a = \Pi_1^a |\Upsilon_1^a|^2 + \Pi_2^a |\Upsilon_2^a|^2 + \frac{3\chi_0}{\xi^{-2}} \Pi_1^a \Pi_2^a \left[\Upsilon_1^{a*}\Upsilon_2^a + \Upsilon_2^{a*}\Upsilon_1^a \right]. \quad (5.18)$$

We can diagonalize the above quadratic form and find that the eigenvector corresponding to the lower eigenvalue contains a mixture of $d-$ and $s-$wave forms. It

is important to note that there is an ambiguity in choosing the eigenvector of the quadratic form [196, 9]: we can rescale $\Upsilon_1^a, \Upsilon_2^a$ by different factors (*i.e.* perform a similarity transform) before diagonalizing the quadratic form, and then undo the similarity transform after the diagonalization. This modifies the eigenvectors except when the lowest eigenvalue is zero. It was argued [196, 9] that the appropriate similarity transform is determined by looking at the structure of the particle-hole T-matrix, which leads to the requirement that the diagonal terms in the quadratic form have equal values. In this manner, we find that the eigenvector with lower eigenvalue has $(\Upsilon_1^a, \Upsilon_2^a) \propto (1/\sqrt{\Pi_1^a}, -1/\sqrt{\Pi_2^a})$.

In order to estimate the difference between Π_1^a and Π_2^a, we can do an explicit computation at $T = 0$ and in the absence of a fermi-surface curvature, so that

$$\Pi_1^a = \frac{2}{4\pi^2 v_x v_y} \int_{-\Lambda_x}^{\Lambda_x} dx \int_0^{\Lambda_y} dy \, \frac{\theta(y-x) - \theta(-y-x)}{2y}, \tag{5.19}$$

where $\Lambda_{x,y} = v_{x,y}\Lambda$, $\theta(...)$ represents the heaviside-step function and we are integrating near the hot-spots in a momentum window $|\mathbf{k}| < \Lambda$, with Λ a UV regulator. We are interested in the limit $\Lambda_y > \Lambda_x$ (since $v_y > v_x$ in the antinodal regions) and obtain,

$$\Pi_1^a = \frac{\Lambda}{2\pi^2 v_y} \left[1 + \log\left(\frac{v_y}{v_x}\right) \right]. \tag{5.20}$$

On the other hand,

$$\Pi_2^a = \frac{2}{4\pi^2 v_x v_y} \int_0^{\Lambda_x} dx \int_{-\Lambda_y}^{\Lambda_y} dy \, \frac{\theta(y+x) - \theta(y-x)}{2x}, \tag{5.21}$$

$$\Pi_2^a = \frac{\Lambda}{2\pi^2 v_y}. \tag{5.22}$$

Therefore, we see that,

$$\Pi_1^a = \eta \Pi_2^a > 0, \text{ where} \tag{5.23}$$

$$\eta = 1 + \log(v_y/v_x). \tag{5.24}$$

We then conclude from the discussion below Eq. (5.18) that the ratio of the s to the remaining bond components in the form factor of CDW-a is

$$\left|\frac{\Upsilon_1^a + \Upsilon_2^a}{\Upsilon_1^a - \Upsilon_2^a}\right| = \frac{\sqrt{\eta}-1}{\sqrt{\eta}+1}, \tag{5.25}$$

which can be quite small. We expect the aforementioned remaining component of the CDW to be d. (Although the present hot-spot computation does not, strictly speaking, distinguish between s' and d, demanding smooth variation of the form factor in the anti-nodal region strongly prefers d).

Wang and Chubukov [243] also analyzed the form-factor of CDW-a by looking at the set of coupled CDW vertices, retaining the Landau damping terms in the Bosonic propagator. (In particular our $\eta \to 1$ limit corresponds to $\varphi \to \pi/4$ in their notation.)

Interplay of charge-order and superconductivity

In section 5.2.1, we saw that at quadratic order one doesn't obtain the CDW with the experimentally measured wavevector. Therefore, it is necessary to go to quartic order; our real interest in this section is to compute these terms and, in particular, their temperature dependencies.

Let us now write the full low-energy theory in terms of the (a) fermions, ψ_j, (b) CDW -a (Φ_x^a, Φ_y^a) with wave-vectors $\mathbf{Q}_x^a = (Q_0, 0)$ and $\mathbf{Q}_y^a = (0, Q_0)$, (c) CDW-b ($\Phi_x^b$,

Φ_y^b) with wave-vectors $\mathbf{Q}_x^b = (Q_0, Q_0)$ and $\mathbf{Q}_y^b = (Q_0, -Q_0)$, and, (d) SC ($\Psi$):

$$\begin{aligned}
\mathcal{L} &= \mathcal{L}_0 + \mathcal{L}_S + \mathcal{L}_B, && (5.26)\\
\mathcal{L}_S &= \Psi(\psi_1^\dagger \psi_5^\dagger + \psi_2^\dagger \psi_6^\dagger) - \Psi(\psi_7^\dagger \psi_3^\dagger + \psi_4^\dagger \psi_8^\dagger) + \text{H.c.}, && (5.27)\\
\mathcal{L}_B &= \Phi_x^a(\psi_6^\dagger \psi_1 + \psi_5^\dagger \psi_2 - \psi_3^\dagger \psi_4 - \psi_8^\dagger \psi_7) \\
&- \Phi_y^a(\psi_1^\dagger \psi_2 + \psi_6^\dagger \psi_5 - \psi_3^\dagger \psi_8 - \psi_4^\dagger \psi_7) \\
&+ \Phi_x^b(\psi_6^\dagger \psi_2 - \psi_3^\dagger \psi_7) - \Phi_y^b(\psi_5^\dagger \psi_1 - \psi_8^\dagger \psi_4) + \text{H.c.}, && (5.28)
\end{aligned}$$

where we have suppressed the momentum and spin-index structure above and $\mathcal{L}_0$ was already expressed in eqn.5.15. While writing $\mathcal{L}_B$, we have ignored the possibility of having a small $s-$wave component in the form factors of $\Phi_{x,y}^a$ *i.e.* we have assumed $P_Q(\mathbf{k}) = \cos k_x - \cos k_y$. We also choose not to write any explicit coupling constants as they can be absorbed into the fields by a redefinition. In the low-energy limit, the patches 1-2-5-6 and 3-4-7-8 are decoupled from each other.

Once again, we integrate out the fermions in the vicinity of the hot-spots (in a momentum window $|\mathbf{k}| < \Lambda$) and compute the action upto fourth order in Φ^a, Φ^b and Ψ. All the four-point diagrams contributing to these terms are shown in fig. 5.3. There is also a three-point diagram, as shown in fig.5.4, contributing to the effective action, which takes the form,

$$
\begin{aligned}
S_{\text{eff}}[\Phi^a, \Phi^b, \Psi] = \int d^2\mathbf{r}\; d\tau \quad & \Bigg[\quad r_a\Big(|\Phi^a_x|^2 + |\Phi^a_y|^2\Big) + r_b\Big(|\Phi^b_x|^2 + |\Phi^b_y|^2\Big) + r_b|\Psi|^2 \\
& + \quad u_a\Big(|\Phi^a_x|^4 + |\Phi^a_y|^4\Big) + u_b\Big(|\Phi^b_x|^4 + |\Phi^b_y|^4\Big) + u_b|\Psi|^4 \\
& + \quad u_{ab}\Big(|\Phi^a_x|^2 + |\Phi^a_y|^2\Big)\Big(|\Phi^b_x|^2 + |\Phi^b_y|^2\Big) + w_a|\Phi^a_x|^2|\Phi^a_y|^2 \\
& + \quad \overline{u}_{ab}\Big((\Phi^a_x)^2\Phi^{b*}_x\Phi^{b*}_y + (\Phi^a_y)^2\Phi^{b*}_x\Phi^b_y + \text{H.c.}\Big) \\
& + \quad t_{ab}\Big(\Phi^a_x\Phi^a_y\Phi^{b*}_x + \Phi^a_x\Phi^{a*}_y\Phi^{b*}_y + \text{H.c.}\Big) \\
& + \quad s_a|\Psi|^2\Big(|\Phi^a_x|^2 + |\Phi^a_y|^2\Big) + s_b|\Psi|^2\Big(|\Phi^b_x|^2 + |\Phi^b_y|^2\Big)\Bigg],
\end{aligned}
\tag{5.29}
$$

where $r_a = a(T - T^a_{c,0})$ and $r_b = b(T - T^b_{c,0})$ with $a, b > 0$ and the bare transition temperatures, $T^b_{c,0} > T^a_{c,0}$. Note that we have already utilized the emergent symmetry of the linearized hot-spot theory to equate the transition temperatures for SC and CDW-b, and also equated the coefficients of $|\Psi|^4$ and $|\Phi^b_x|^4,\ |\Phi^b_y|^4$. In the presence of terms that break this symmetry, $T^b_{c,0} < T^{\text{SC}}_{c,0}$; the exact details are beyond the scope of this work.

It is important to note that the above action is invariant under all the underlying symmetries (including under rotations, e.g. $\mathcal{R}_{\pi/2} : \Phi^a_x \to \Phi^a_y; \Phi^a_y \to \Phi^{a*}_x; \Phi^b_x \to \Phi^{b*}_y; \Phi^b_y \to \Phi^b_x$). The terms in the third and fourth lines arise naturally due to the existence of two types of CDW correlations in the system with wavevectors that satisfy the following geometric constraints: $\mathbf{Q}^b_x = \mathbf{Q}^a_x + \mathbf{Q}^a_y$ and $\mathbf{Q}^b_y = \mathbf{Q}^a_x - \mathbf{Q}^a_y$. Some of these coefficients were computed for the full fermi-surface in Ref.[150]. Note the absence of a term of the form $|\Phi^b_x|^2|\Phi^b_y|^2$ above, which is allowed by symmetry but missing due to lack of available phase-space for this kind of a scattering process. The

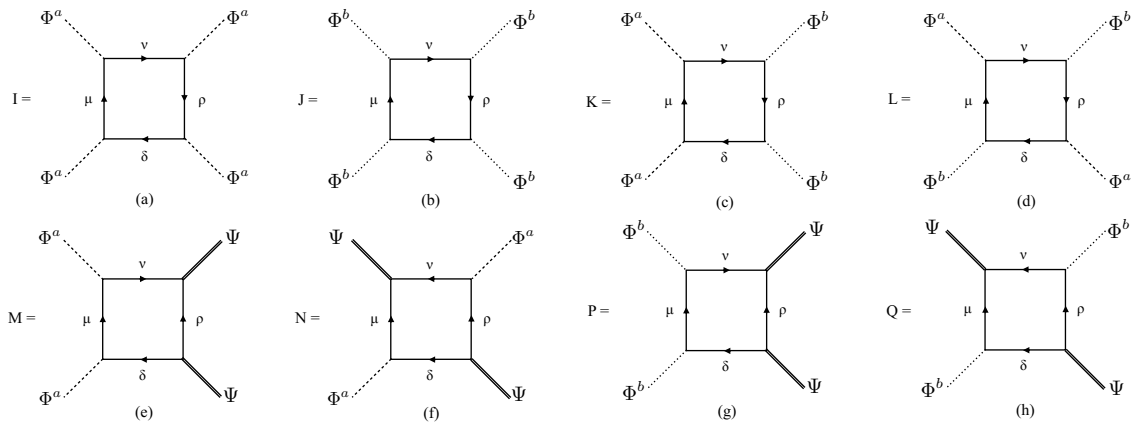

Figure 5.3: Feynman diagrams representing the various 4-point functions that contribute to different terms in S_{eff}. The solid internal lines carry different hot-spot indices (μ, ν, ρ, δ) depending upon the term being evaluated. The dashed, dotted and double lines represent Φ^a, Φ^b and Ψ respectively. The individual diagrams are labelled (a) $I_{\mu\nu\rho\delta}$, (b) $J_{\mu\nu\rho\delta}$, (c) $K_{\mu\nu\rho\delta}$, (d) $L_{\mu\nu\rho\delta}$, (e) $M_{\mu\nu\rho\delta}$, (f) $N_{\mu\nu\rho\delta}$, (g) $P_{\mu\nu\rho\delta}$, (h) $Q_{\mu\nu\rho\delta}$.

terms that are of particular interest to us appear in the last line ($\sim s_a, s_b$), as will become clear in the next section.

Let us now present the results for the different coefficients that appear above.

5.3 Results

We start by presenting the results for the linearized theory (i.e. set $\kappa = 0$) in the vicinity of the hot-spots.

5.3.1 Linearized hot-spot theory

In this section, we shall list the expressions for the coefficients in terms of the loop integrals. The details of the computation are presented in appendix D.1. At

the outset, we note the regime that we are working in here — we assume that $T \ll v_x\Lambda \ll v_y\Lambda$, i.e. the temperature is much lower than any other ultraviolet energy scale in the problem and futhermore, the regions in the vicinity of the hot-spots (and in the antinodal regions) are almost nested. In the next section, we will show that the fermi-surface curvature, κ, introduces another temperature scale in the problem above which our analysis remains valid.

We start with u_a, representing the coefficient of the $|\Phi_x^a|^4, |\Phi_y^a|^4$ term (fig.5.3a). Evaluating the contributions arising from both the patches, we obtain,

$$u_a = -(I_{1616} + I_{2525} + I_{3434} + I_{7878}) \tag{5.30}$$

$$= -(I_{1212} + I_{3838} + I_{4747} + I_{5656}), \text{ where} \tag{5.31}$$

it is straightforward to see that $I_{1616} = I_{2525} = I_{3838} = I_{4747}$, and $I_{1212} = I_{3434} = I_{5656} = I_{7878}$. The loop integrals are given by,

$$I_{1212} = -\frac{1}{2}\int_{\mathbf{k}} G_1^2\, G_2^2 \approx -\frac{1}{16\pi^2 v_x^2 v_y \Lambda}\frac{1}{(1+(\frac{\pi T}{v_x\Lambda})^2)}, \tag{5.32}$$

$$I_{2525} = -\frac{1}{2}\int_{\mathbf{k}} G_2^2\, G_5^2 = 0, \tag{5.33}$$

where we use the notation $\int_{\mathbf{k}} \equiv T\sum_m \int\, dk_x\, dk_y/(2\pi)^2$ and all the internal Green's functions carry the same argument: $(i\omega_m, \mathbf{k})$, with $\omega_m = (2m+1)\pi T$. Note that in the limit of $T \ll v_x\Lambda$, $I_{1212} \to -1/(16\pi^2 v_x^2 v_y\Lambda)$, i.e. it is non-singular and approaches a constant independent of temperature.

The competition term between Φ_x^a and Φ_y^a, described by w_a (also, fig.5.3 a), is

given by,

$$w_a = -(2\mathrm{S} + \mathrm{V}), \text{ where} \tag{5.34}$$

$$\mathrm{S} = I_{2565} + I_{5212} + I_{2161} + I_{1656}, \tag{5.35}$$

$$\mathrm{V} = 4I_{1256}. \tag{5.36}$$

In the above, S, V represent the self-energy and vertex-correction type diagrams. Furthermore, it is straightforward to see that $I_{2565} = I_{5212} = I_{2161} = I_{1656}$. The explicit expressions are given by,

$$I_{2565} = -\int_{\mathbf{k}} G_2\, G_5^2\, G_6 \approx -\frac{1}{8\pi^2 v_x^2 v_y \Lambda} \log\left(\frac{v_x \Lambda}{\pi T}\right), \tag{5.37}$$

$$I_{1256} = -\int_{\mathbf{k}} G_1 G_2 G_5 G_6 = -\frac{1}{32 v_x v_y T}, \tag{5.38}$$

where the second integral has been evaluated in the limit $v_x\Lambda \to \infty$. Therefore, we see that the most singular contribution to w_a comes from I_{1256} and is $\sim 1/T$. This has interesting consequences, as will be discussed at the end of this section, and has also been pointed out by a recent work [243].

Similarly, the contributions to the $|\Phi^b|^4$ terms arise from (fig.5.3 b),

$$u_b = -(J_{2626} + J_{3737}) = -(J_{1515} + J_{4848}), \text{ where} \tag{5.39}$$

due to the underlying symmetries, all the diagrams turn out to be equal, i.e. $J_{1515} = J_{2626} = J_{3737} = J_{4848}$. The integral evaluates to,

$$J_{1515} = -\frac{1}{2}\int_{\mathbf{k}} G_1^2\, G_5^2 = -\frac{7\zeta(3)}{32\pi^4}\frac{\Lambda}{v_y T^2}, \tag{5.40}$$

where $\zeta(n)$ is the Riemann-zeta function. The singularity here is much stronger than what we encountered before in the case of the $|\Phi^a|^4$ terms. However, the T^{-2} behavior

is not at all surprising— recall that there is a perfect SU(2) symmetry between CDW-b and SC within our linearized theory and the coefficient of $|\Phi^b|^4$ term should therefore be identical to that of $|\Psi|^4$, which is known to be of the same T^{-2} form. In the presence of a finite curvature, this symmetry will be broken below some temperature scale set by κ, as we shall see in the next section.

Let us now shift our focus to terms that describe the competition between the different components of the charge-orders, Φ^a and Φ^b. There are two types of four-point functions between these orders, denoted u_{ab} and $\overline{u}_{ab}$. Let us focus on u_{ab} first (fig.5.3c). If we focus only on the coefficient of, let us say, the $|\Phi^a_x|^2|\Phi^b_x|^2$ term (the overall form in which the different order-parameters appear is strongly constrained by various symmetries), we get,

$$u_{ab} \;=\; -2(K_{1626} + K_{4373}), \tag{5.41}$$

where $K_{4373} = K_{6515}$ by symmetry under $\mathcal{R}_{\pi/2}$ (and the latter appears in the coefficient of $|\Phi^a_y|^2|\Phi^b_y|^2$). Evaluating these loop integrals gives,

$$K_{1626} \;=\; -\int_{\mathbf{k}} G_1\; G_2\; G_6^2 = -\frac{1}{64 v_x v_y T}, \tag{5.42}$$

$$K_{6515} \;=\; -\int_{\mathbf{k}} G_1\; G_5^2\; G_6 = -\frac{1}{64 v_x v_y T}. \tag{5.43}$$

Similarly, while evaluating $\overline{u}_{ab}$ (fig.5.3d), if we focus only on the coefficient of $(\Phi^a_x)^2 \Phi^{b*}_x \Phi^{b*}_y$ (the overall form of the terms is once again constrained by symmetry),

$$\overline{u}_{ab} = -(L_{2516} + L_{3784}), \tag{5.44}$$

where $L_{3784} = L_{2516}$ and the explicit form is given by,

$$L_{2516} = -\int_{\mathbf{k}} G_1 G_2 G_5 G_6 = -\frac{1}{32 v_x v_y T}. \tag{5.45}$$

It is interesting to note that the leading singularities in all of the above diagrams (with the exception of $u_a,\ u_b$) is of the form $\sim 1/T$. This is something that we can understand by applying standard power-counting arguments. In $(2+1)-$dimensions for such 4-point functions, the singular structure in the IR (with a cutoff, $k_0 \sim T$) will be obtained as $\int d^3k/k^4 \sim 1/k_0$, where $k \equiv (i\omega, \mathbf{k})$. However, there are obviously exceptions to this naive argument, which arise due to the interesting pole structure of the propagators involved in the different diagrams.

We now move over to the terms that actually describe the competition between CDW and SC—these will be responsible for some of the interesting results to come out of our analysis. We start by evaluating the diagrams contributing to s_a, which describes competition between Φ^a and Ψ (fig.5.3 e, f),

$$\begin{aligned} s_a &= 2\overline{S} + \overline{V}, \text{ where} && (5.46) \\ \overline{S} &= M_{2515} + M_{6151} + M_{7848} + M_{4373}, \\ &= M_{1262} + M_{6515} + M_{8373} + M_{4737}, && (5.47) \\ \overline{V} &= N_{2615} + N_{8437} = N_{2651} + N_{8473}. && (5.48) \end{aligned}$$

In the above, $\overline{S}$ and $\overline{V}$ represent the self-energy and vertex correction contributions respectively. We have written the coefficients of both $|\Phi^a_x|^2|\Psi|^2$ and $|\Phi^a_y|^2|\Psi|^2$ above, which are of course equal. Moreover, some of the symmetry related diagrams are individually equal as well, such as $M_{1262} = M_{7848} = M_{6515} = M_{4373}$ and $M_{2515} = M_{8373} = M_{4737} = M_{6151}$. Similarly, $N_{2651} = N_{2615} = N_{8437} = N_{8473}$. The explicit

expressions for the (distinct) diagrams are given by,

$$M_{2515} = -\int_{\mathbf{k}} G_2\ G_5^2\ G_1' = \frac{1}{64 v_x v_y T} \tag{5.49}$$

$$M_{1262} = -\int_{\mathbf{k}} G_1\ G_2^2\ G_6' = \frac{1}{64 v_x v_y T}, \tag{5.50}$$

$$N_{2651} = -\int_{\mathbf{k}} G_1 G_2 G_5' G_6' = -\frac{1}{32 v_x v_y T}. \tag{5.51}$$

The "primed" Green's functions have arguments $(-i\omega_m, -\mathbf{k})$. Once again, the leading singularity is of the form $1/T$.

Finally, the coefficent s_b, which describes the competition between Φ^b and Ψ (figs.5.3 g and h) is given by,

$$s_b = 2(P_{2626} + P_{3737}) + (Q_{2626} + Q_{3737}) \tag{5.52}$$

$$= 2(P_{1515} + P_{4848}) + (Q_{1515} + Q_{4848}),\ \text{where} \tag{5.53}$$

all the self-energy type diagrams, $P_{1515} = P_{2626} = P_{3737} = P_{4848}$, are equal and the vertex-correction type diagrams are equal and opposite in sign to the self-energy type ones, i.e. $Q_{1515} = Q_{2626} = Q_{3737} = Q_{4848} = -P_{1515}$. We therefore only need to evaluate one such integral—the corresponding expression is given by,

$$P_{2626} = -\int_{\mathbf{k}} G_2\ G_6^2\ G_2' = \frac{7\zeta(3)}{16\pi^4}\frac{\Lambda}{v_y T^2}. \tag{5.54}$$

The $1/T^2$ behavior is to be expected by the same reasoning that was presented earlier — the coefficients of $|\Psi|^4$, $|\Phi^b|^4$ and $|\Phi^b|^2|\Psi|^2$ should have an identical (singular-) structure arising from the emergent SU(2) symmetry.

Now that we have evaluated all the four-point functions allowed by symmetry, let us also evaluate the three-point functions between Φ^a, Φ^b that contribute to t_{ab}

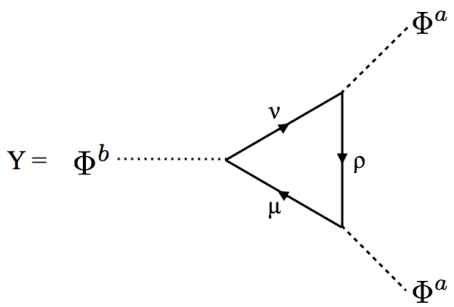

Figure 5.4: Feynman diagram representing the 3-point function, $Y_{\mu\nu\rho}$, between Φ^a (dashed lines) and Φ^b (dotted line). The solid internal lines carry different hot-spot indices (μ, ν, ρ).

(fig.5.4). Once again, we remind the reader that such a term is allowed because of purely geometric reasons associated with the wavevectors of the various CDWs: $\mathbf{Q}^b_x = \mathbf{Q}^a_x + \mathbf{Q}^a_y$ and $\mathbf{Q}^b_y = \mathbf{Q}^a_x - \mathbf{Q}^a_y$. If we focus on the coefficient of the $\sim \Phi^a_x \Phi^a_y \Phi^{b*}_x$ term (and the rest just follows by symmetry), we get,

$$t_{ab} = (Y_{261} + Y_{265} + Y_{374} + Y_{378}), \text{where} \tag{5.55}$$

it is easy to see that $Y_{265} = Y_{261} = Y_{374} = Y_{378}$. If we choose to evaluate just one of these,

$$Y_{261} = -\int_{\mathbf{k}} G_1 \; G_2 \; G_6 = 0. \tag{5.56}$$

It is very interesting to see that within our linearized theory, the integral evaluates exactly to 0. However, in the presence of a finite curvature, this term assumes a non-zero value, as will be shown in the next section.

Assembling all the expressions that we have computed above, the leading (singular-

) behavior of the coefficients in the effective action, $S_{\text{eff}}[\Phi^a, \Phi^b, \Psi]$ are given by,

$$u_a = \frac{1}{8\pi^2 v_x^2 v_y \Lambda},\ w_a = \frac{1}{8 v_x v_y T},\ u_b = \frac{7\zeta(3)\Lambda}{16\pi^4 v_y T^2}, \tag{5.57}$$

$$u_{ab} = \frac{1}{16 v_x v_y T},\ \overline{u}_{ab} = \frac{1}{16 v_x v_y T},\ t_{ab} = 0 \tag{5.58}$$

$$s_a = \frac{1}{16 v_x v_y T},\ s_b = \frac{7\zeta(3)\Lambda}{8\pi^4 v_y T^2}. \tag{5.59}$$

At this point, it is worth pointing out some of the interesting features associated with the above terms. First of all, notice that depending on the nature of the term, we have obtained two different types of singularities—there are terms that go as $1/T$, and others that go as $1/T^2$— in addition to the non-singular term. This has two interesting consequences. In the presence of only the terms involving CDW-a, the competition between the $x, y-$ components, w_a, far exceeds u_a, i.e. $w_a/u_a \sim \Lambda v_x/T \gg 1$. The implication is that at low enough temperatures, CDW-a would necessarily have a tendency to form stripe-like, instead of checkerboard, order [243] which would spontaneously break the underlying C_4 symmetry of the lattice. On the other hand, with only CDW-b order, due to the absence of any competition between its $x, y-$ components, there won't be any tendency to break the C_4 symmetry. There is indication for the CDW being unidirectional and stripe-like in the absence of a magnetic field in various experiments.

Let us now discuss an important feature of our analysis, involving the s_a, s_b terms that describe the competition of the different CDWs with SC. We find that $s_b/s_a \sim \Lambda v_x/T \gg 1$, implying that at low enough temperatures, SC competes with CDW-b much more strongly than with CDW-a. However, this is not surprising for the following reason: In our linearized hot-spot theory, there is no fundamental difference

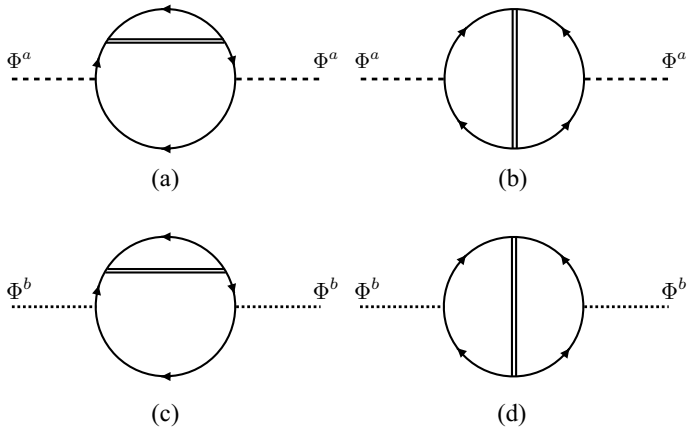

Figure 5.5: Contracting the $\Psi-$ fields (solid-double lines) in (a) $M_{\mu\nu\rho\delta}$, (b) $N_{\mu\nu\rho\delta}$ renormalize the $|\Phi^a|^2$ term, and, (c) $P_{\mu\nu\rho\delta}$, (d) $Q_{\mu\nu\rho\delta}$ renormalize the $|\Phi^b|^2$ term.

between CDW-b and SC due to the SU(2) symmetry. In fact both of these orders are strongly coupled to each other and compete for density of states on the fermi-surface in the vicinity of the same hot-spots. Therefore, it is natural for them to compete with each other more strongly. The same is not true about CDW-a and SC, which compete for density of states along different portions of the Fermi-surface. Note that CDW-a and CDW-b also compete mutually, so suppressing one naturally makes it favorable for the other one to emerge.

To summarize, the results of this section indicate that at very high temperatures, there is an almost perfect symmetry between CDW-b and SC (in fact, this symmetry persists even in the presence of a finite curvature, as we shall show in the next section) which makes it unfavorable for CDW-a to appear in the scene. However, as a function of decreasing temperature, as the strength of superconducting fluctuations increase, the CDW-b fluctuations are preferentially suppressed compared to CDW-a, which could possibly allow CDW-a to emerge. The exact crossovers, if any,

are beyond the scope of this work. The net effect of the SC fluctuations is to effectively renormalize the quadratic terms in the action for Φ^a and Φ^b, as shown in fig.5.5. At low temperatures, the coefficient of $|\Phi^b|^2$ is renormalized more strongly compared to the coefficient of $|\Phi^a|^2$. In order to extract an estimate of the relative renormalizations, let us compute Δr_a and Δr_b for CDW-a,b due to purely thermal and Gaussian fluctuations associated with superconductivity, $\langle |\Psi_{\mathbf{q}}|^2 \rangle \sim (\mathbf{q}^2 + \sigma^2)^{-1}$. This approximation is valid sufficiently far away from the superconducting T_c. The renormalizations are then given by,

$$\Delta r_a \approx s_a \int \frac{d^2q}{(2\pi)^2} \frac{1}{q^2+\sigma^2} \approx -\frac{s_a}{2\pi} \log\left(\frac{\sigma}{\Lambda}\right) = -\frac{1}{32\pi v_x v_y T} \log\left(\frac{\sigma}{\Lambda}\right), \quad (5.60)$$

$$\Delta r_b \approx s_b \int \frac{d^2q}{(2\pi)^2} \frac{1}{q^2+\sigma^2} \approx -\frac{s_b}{2\pi} \log\left(\frac{\sigma}{\Lambda}\right) = -\frac{7\zeta(3)\Lambda}{16\pi^5 v_y T^2} \log\left(\frac{\sigma}{\Lambda}\right). \quad (5.61)$$

Hence, the relative renormalizations $\Delta r_b / \Delta r_a \sim \Lambda v_x / T \gg 1$, which indicates that within our simplified theory, there exists an intermediate range of temperatures where the transition temperature for CDW-b gets suppressed more than the one for CDW-a.

The only caveat in the calculations presented in this section is that all of them were performed in the limit of $\kappa \to 0$. Of course, in the actual problem, the curvature is finite (albeit small, in the anti-nodal region). Therefore, we revisit the whole problem with a non-zero curvature in the next section and analyze the consequences numerically.

We would like to remind the reader, that at the level of approximation that we have used in this section, the CDW-a state is degenerate with the corresponding PDW state and the two compete strongly with each other. However, in the presence of a curvature or other features that break the SU(2) symmetry, the PDW state is destroyed completely, at least within the weak-coupling picture (unlike the other

states, as we saw in fig.5.2). Moreover, as we shall see in the next section, the competition effects between CDW-a,b and SC discussed above survive even in the presence of curvature as long as the temperature is higher than a scale set by κ.

5.3.2 Effect of fermi-surface curvature

In the previous section we ignored the effect of the fermi-surface curvature completely and analyzed the linearized theory in the vicinity of the hot-spots. Most of the graphs that we evaluated were singular in the limit of $T \to 0$ (though we intend to apply our results to the metallic state at strictly $T > 0$). The question we would now like to address is to what extent do these results remain valid and what is the regime of validity, in the presence of a finite curvature. In fact, it is possible that the curvature sets a temperature scale above which our analytical results for the linearized theory continue to hold. We shall denote all the previously evaluated integrals by $\tilde{I}, \tilde{J}, ..., \tilde{Q}, \tilde{Y}$, to distinguish them from the symbols used earlier. This time around, we shall perform the Matsubara sums first and then evaluate the momentum-integrals numerically as a function of temperature for various fixed values of curvature, κ, and $\alpha = v_y/v_x$.

The aim of this computation is two-fold. First of all, in the limit of $\kappa \to 0$, we should recover the temperature dependencies of the different terms obtained earlier. Secondly, we would like to have an approximate estimate of the functional form of $T_0(\kappa, \alpha)$, the temperature scale above which our analytical results for the $\kappa = 0$ problem continue to hold, assuming such a scale exists.

In the presence of a finite curvature, the modified dispersions are now given by,

$$\varepsilon_1(\mathbf{k}) = v_x k_x + v_y k_y + \kappa(k_x^2 + k_y^2), \tag{5.62}$$

$$\varepsilon_2(\mathbf{k}) = v_x k_x - v_y k_y + \kappa(k_x^2 + k_y^2), \tag{5.63}$$

with $\varepsilon_5(\mathbf{k}) = \varepsilon_1(-\mathbf{k})$, $\varepsilon_6(\mathbf{k}) = \varepsilon_2(-\mathbf{k})$ and so on.

We only present the main findings of this analysis in the present section. The technical details of the computations alongwith plots of the numerical results are provided in Appendix D.2.

Let us start by analyzing the temperature dependence of diagrams ($\tilde{I}_{1212}$) contributing to u_a. We found that (i) at a fixed value of α, but for $\kappa \neq 0$, $\tilde{I}_{1212}$ goes to a constant value in the limit of $T \to 0$. Moreover, in the limit of $\kappa \to 0$, this constant is nearly identical to what we had computed earlier for I_{1212} (eqn.5.33). (ii) On the other hand, for $T \to v_x\Lambda$, there is a power-law fall off going as $\sim 1/T^2$ for all considered values of κ, which again matches with our analytical result for I_{1212} (eqn.5.33). (iii) Finally, $\tilde{I}_{1212}$ scales as $\sim 1/\alpha$, which was apparent from the perfect scaling collapse that we observed for $\alpha\tilde{I}_{1212}$ (not shown). This agrees with our analytical results from earlier, even though they were computed with $\kappa = 0$. The numerically evaluated results for $\tilde{I}_{1212}$ are shown in fig.D.1(a).

We next computed the leading diagrams contributing to w_a, giving rise to competition between $x-$ and $y-$ components of CDW-a. We came across the following interesting results: (i) irrespective of the value of the curvature, the diagrams all asymptote to a $1/T$ behavior at low temperatures (upto $T/v_x\Lambda \sim 10^{-4}$). (ii) There were however deviations at higher temperatures. (iii) Finally, this particular diagram also scales as $1/\alpha$ (not shown). The plots as a function of temperature are shown in

fig.D.1(b).

It is especially interesting to see that even in the presence of a small curvature, w_a continues to scale as $1/T$ down to very low temperatures. However, as a function of decreasing temperature, there will be a preemptive instability to superconductivity, which in turn will cut-off the $1/T$ behavior to $1/\Delta$, where Δ is the superconducting gap.

Let us now revisit the terms that turned out to be the most singular in our earlier analysis, which includes u_b (J_{1515}) and s_b ($P_{2626},\ Q_{2626}$), and went as $\sim 1/T^2$. As a reminder, in the linearized theory, we obtained $2J_{1515} = -P_{2626} = Q_{2626}$. However, a finite curvature breaks this symmetry. We first focussed on the temperature-dependence of these diagrams at a fixed α but different values of κ and noticed the following common features: (i) The limit of $\kappa \to 0$ computation agrees perfectly with the analytical computation from the previous section. (ii) With an increasing κ, we note that the results for the different computations (i.e. with and without κ) only agree with each other above a characteristic temperature, $T_0 = \mathrm{C}\kappa$, with C different for each diagram (This is determined by noting the temperature, T_0, at which the deviation starts; these are marked by the dotted vertical lines in fig.D.2). To investigate whether C is $\alpha-$dependent, we computed the same diagrams as a function of temperature at a fixed $\kappa \neq 0$ and v_x, but for different values of α. Remarkably, the value of T_0 remains unaffected by changing α, which shows that C is independent of α. (iii) We also observed them to scale as $\sim 1/\alpha$, just like in all the previous cases. Therefore, to summarize, u_b and s_b continue to behave as $1/T^2$ above a temperature scale that is set by curvature, $T_0 \sim \kappa$. Therefore, at high enough temperatures com-

pared to this scale, the degeneracy between CDW-b and SC is maintained and the competition is sufficiently weak that it is unlikely that CDW-a will be a preferred state, based on our arguments from the previous section. It is however important to remind ourselves that the coefficient of $|\Psi|^4$, which also goes as $\sim 1/T^2$, survives even in the presence of a finite curvature but is eventually cut-off by Δ. The numerically evaluated results are shown as a function of temperature in fig.D.2 (a)-(f).

Finally, we also evaluated the term responsible for competition between SC and CDW-a. Recall that in the linearized theory, $2M_{2515} = -N_{2651} = -N_{2615}$ and where the leading singularities were all $\sim 1/T$. However, in the presence of a finite κ these degeneracies are lifted. However, all the diagrams continue to behave as $\sim 1/T$ down to temperatures of $T/v_x\Lambda \sim 10^{-4}$, even in the presence of a reasonably large κ. However, as a function of decreasing temperature, the system will go superconducting thereby cuting-off the singularity. We have also checked that just like all the other diagrams considered so far, these diagrams also scale as $\sim 1/\alpha$. The results are shown in fig.D.3 (a)-(c).

Towards the end of section 5.3.1, we saw that the three-point functions between CDW-a and b turned out to be identically zero. However, when we evaluated the same diagrams in the presence of a finite curvature, they turned out to be non-zero. In fact, based on the numerically evaluated results, we were able to guess an analytical functional form for $\tilde{Y}_{261}$, which is as follows,

$$\mathcal{Y}(T,\kappa,\alpha) \approx \frac{\kappa\Lambda}{\pi^2\alpha v_x}\frac{1}{\pi^2T^2 + v_x^2\Lambda^2}. \tag{5.64}$$

Note that it indeed reproduces the $\kappa \to 0$ limit correctly and approaches a constant in the limit of $T \to 0$ otherwise. The numerically evaluated results and a comparison

with $\mathcal{Y}$ is shown in fig.D.4(a), (b).

To conclude this section, we found that at sufficiently high temperatures, our results from the previous section continue to hold even in the presence of a finite, but small, curvature. The terms that we found to be most singular in our earlier computation ($\sim 1/T^2$), continue to have the same form as long as $T > T_0 \sim \mathrm{C}\kappa$. On the other hand, the terms that went as $\sim 1/T$, continue to be so down to very low temperatures compared to the scales set by the fermi-velocities. However, as a function of decreasing temperature, these singularities are cut-off eventually by the preemptive instability to superconductivity. It is therefore safe to conclude that our computations in section 5.3.1 are applicable in the window $\max\{T_c, T_0\} < T < v_x\Lambda \ll v_y\Lambda$.

5.4 Discussion

Over the past few years, we have learnt a great deal about the nature of the various symmetry-broken states that arise in the pseudogap regime of the underdoped cuprates. This has largely been possible due to the enormous number of remarkable experiments performed on these materials. Most of these experiments point toward the existence of a fluctuating and short-ranged charge-density wave in a metallic state; the onset of the CDW happens below a characteristic scale $T_{\mathrm{cdw}} \lesssim T^*$, as deduced from X-ray scattering measurements [91]. There is a considerable amount of evidence suggesting that the CDW competes with superconductivity. It is therefore essential to understand the true nature of the CDW and its relation to superconductivity, as this might be the key to gaining a complete understanding of the pseudogap phase

out of which both orders emerge [11].

Theoretically, we have now started to realize that the cuprates are a model system where the Fermi surface geometry, the strong interactions between the constituent electrons and the quasi-two dimensional structure conspire to give rise to some remarkable consequences. One of these is the universal feature that in the presence of strong antiferromagnetic interactions, superconductivity and charge-order are tied to each other; this has been highlighted by the observation [52, 77] of the predicted [154, 196] d-wave form factor of the CDW. While SC and CDW necessarily arise as dual instabilites of the same normal state, they also compete with each other. One of the puzzling features, on the theoretical side, has been the discrepancy between the wavevector of the CDW seen experimentally and the one obtained from the leading CDW instabilities in various models. The primary purpose of this paper has been to address one interesting ingredient that could be partly responsible for resolving this discrepancy over at least an intermediate window of temperature. The primary motivation for invoking the effect of $d-$wave superconducting fluctuations was to suppress density of states in the antinodal regions.

In this chapter, we studied the interplay of fluctuating charge-order and superconductivity. Our starting point was the t-J model (without Gutzwiller projection) for a metal interacting via short range antiferromagnetic exchange interactions, where the various instabilities at the Hartree-Fock level are to SC and CDWs with different sets of wavevectors (a t-J-V model with an infinite on-site Hubbard U also leads to similar instabilites, in addition to a staggered flux state [10]). The leading CDW-b state was found to have a wavevector of the form $\pm(Q_0, \pm Q_0)$, while there was a

sub-leading instability to the CDW-a with wavevectors $(\pm Q_0, 0)$ and $(0, \pm Q_0)$. It is the latter that is closely related to the state seen in the experiments. In order to study the minimal model with all the necessary ingredients, we then considered the theory of a metal with pairing fluctuations and both types of CDW correlations and computed the effective Ginzburg-Landau (GL) theory upto the quartic order in in the low-energy limit.

We obtained a number of interesting results for the temperature dependencies of the coefficients in the GL theory. In particular, one of the central results of this paper is the nature of the competition between CDW-a and b with SC. We observed that SC competes with CDW-b much more strongly than with CDW-a at low enough, but non-zero temperatures. In the low-energy limit, we attributed this to the emergent SU(2) symmetry between SC and CDW-b, which really doesn't distinguish between the two different phases, and the absence of a gap in the spectrum at the antinodes. At low temperatures, we presented hints that the SC fluctuations might make it more favorable for CDW-a to arise and CDW-b to be suppressed preferentially. In fact, we showed that even in the presence of a finite fermi-surface curvature, the results for the mutual competition between CDW-a,b and SC continue to hold above a temperature scale that is set by the curvature ($T_0 \sim \kappa$). However at the same time, it is important to note that in the $\kappa \to 0$ limit, CDW-a is related by SU(2) symmetry to the PDW state with the same wavevectors and these two orders would therefore compete strongly with each other. However when the SU(2) symmetry is broken explicitly by a finite fermi-surface curvature (or by a nearest-neighbor Coulomb repulsion term), the fragile PDW state disappears completely, as witnessed in our HF computation

for the t-J model. It would be interesting to explore the interplay between SC, CDW and PDW orders beyond weak-coupling, starting from a microscopic model in the near future.

Finally, if it is indeed the superconducting flucutations that are responsible for giving rise to the experimentally observed wavevector, then it is possible that the CDW-b state would show up in experiments if one were to suppress these SC fluctuations completely. Furthermore, the CDW-b order should have tendency to form checkerboard order, unlike CDW-a which has a tendency to form stripe-like order [243]. This is a direction worth exploring in STM experiments at really high magnetic fields, for instance, and repeating phase-resolved analysis similar to what has been carried out recently to look for signatures of the CDW-a state [77]. However, if the CDW-b state continues to be absent, then it is likely that there are other factors at play here in addition to the SC fluctuations. One such factor has already been considered recently, which arises from strong correlation effects due to Coulomb repulsion [10].

Chapter 6

Fractionalized Fermi-liquids

"Do not fear to be eccentric in opinion, for every opinion now accepted was once eccentric." - Bertrand Russell

6.1 Introduction

We hope that the reader is convinced by now that one of the central puzzles related to the hole-doped cuprates at low doping is the origin of the "pseudogap" — a suppression in the density of states at the Fermi-level below a temperature, T^*— and its relation to other symmetry-broken states found at lower temperatures. Most notably, recent experiments on a number of different families of the hole-doped cuprates have detected the onset of an incommensurate charge density wave (CDW) state at a temperature, $T_c < T_{\rm cdw} < T^*$ which competes with superconductivity below the superconducting T_c [78, 5, 39, 51, 55, 3, 248, 249, 132, 96, 235, 130, 151, 52, 77]. One of the primary motivations behind investigating the nature of the CDW is the

hope that a better understanding of this state would lead to a better understanding of the "normal" state above T_c out of which it emerges.

A number of recent theoretical works [154, 97, 105, 27, 196, 117, 199, 60, 67, 149, 61, 10, 9, 45, 243, 150, 233, 34, 20, 73] , including the previous chapter, have tried to approach this problem from a weak-coupling approach, where the CDW is interpreted as an instability of a large Fermi surface in the presence of strong antiferromagnetic (AFM) exchange interactions. The experiments on certain families of the cuprates, such as YBCO, BSCCO and Na-CCOC, have found strong evidence for the wavevector $\boldsymbol{Q}$ to be of the form: $(\pm Q_0, 0)$ and $(0, \pm Q_0)$, where Q_0 decreases with increasing hole-doping and is believed to nest portions of a putative large Fermi surface in the vicinity of, but away from, $(\pi, 0)$ and $(0, \pi)$. Moreover, recent phase-sensitive STM experiments [77] and other X-ray measurements [52] have unveiled the form factor $P_{\boldsymbol{Q}}(\boldsymbol{k})$ to be predominantly of a $d-$wave nature, *i.e.* $P_{\boldsymbol{Q}}(\boldsymbol{k}) \sim (\cos k_x - \cos k_y)$. Fig.1.13 in chapter 1 provides an illustration of unidirectional "bond density" waves (BDW) of different types in real space for both commensurate as well as incommensurate wavevectors.

We note in passing that recent X-ray observations [4] in the La-based cuprates indicate a dominant s'-form factor (where $P_{\boldsymbol{Q}}(\boldsymbol{k}) \sim (\cos k_x + \cos k_y)$), and this has been ascribed to the presence of magnetic 'stripe' order in these compounds, and is in agreement with computations in such states [73]. Further, computations [231] of density wave instabilities in the presence of commensurate antiferromagnetism show suppression of the d-form factor with increasing magnetic order.

Without magnetic ordering, the form factor does indeed come out to be predomi-

nantly $d-$wave within all the weak-coupling approaches [154, 196, 199, 10, 9, 45, 243]. However, the wavevector of the leading density-wave instability within all of these approaches is always of the diagonal type, $(\pm Q_0, \pm Q_0)$. This feature can be traced back to the absence of a pre-existing gap in the anti-nodal region of the large Fermi surface normal state. It is also related to the remnant of an emergent SU(2) symmetry associated with AFM exchange interactions, that maps particles to holes and vice versa [154, 198]; therefore $d-$wave superconductivity, which is the leading instability in the problem, gets mapped to $d-$form factor BDW with the diagonal wavevectors. While the diagonal wavevector is a serious drawback of the weak-coupling approaches, various scenarios have been proposed under which the experimentally observed state might be favored over the diagonal state [10, 45, 149, 243].

Here we shall explore the consequences of gapping out the anti-nodal region by examining the density wave instabilities of a metallic state denoted [213, 215] the fractionalized Fermi liquid (FL*). An independent related analysis has been carried recently by Zhang and Mei [258] using the Yang-Rice-Zhang (YRZ) ansatz [254] for the fractionalized metal. The FL* has similarities to the YRZ ansatz [184], but as we shall review below, can be derived systematically from microscopic models while keeping careful track of its 'topological' order [213, 215] (see also Ref. [148]). These density wave instabilities were also discussed in Refs. [51, 240, 241], but without allowance for non-trivial form factors for the density wave.

FL* phases are most conveniently described within multi-band models, such as in Kondo lattice models for heavy-Fermion systems [213, 215] or Emery-type models suited for the cuprates, where the spins in only one of the bands go into a quantum-

disordered (spin-liquid) state. In this work, we shall take a different route that has been adopted earlier in Refs.[113, 115, 197, 184]. This approach is best understood as follows [198]: Imagine that we start from a metal with long-range AFM order, so that the Fermi surface has been reconstructed into hole-pockets.[1] If we now want to describe the loss of antiferromagnetism, then the transitions where the long-range order is lost and the entire Fermi surface is recovered need not be coincident. In particular, it is possible to have two separate transitions, where at the first transition the *orientational* order of the AFM is lost over long distances, while the magnitude of the AFM order remains fixed; the large Fermi surface is recovered at the second transition. Therefore, it is possible to have an intermediate phase with a locally well-defined AFM order (over distances of the order of a short correlation length, ξ). As we will review below, this intermediate phase can have hole pockets. Because there is no broken symmetry, the Luttinger theorem on the Fermi surface volume is violated, but this is permitted because of the presence of topological order [213, 215].

In the context of one-band models linked to the physics of the cuprates, our realization of the FL* state is linked to the analysis presented in Ref. [113]. We used their and subsequent results [115, 197, 184, 162, 183] to obtain the global phase diagram presented in Fig. 6.1. The starting point of this phase diagram is a deconfined quantum critical point [214, 210] in the antiferromagnet at zero doping, while tuning a coupling constant g, which measures the degree of "frustration" in the antiferromagnet. This critical point is described by a deconfined gauge theory involving a U(1) gauge field A_μ and relativistic, bosonic $S = 1/2$ spinons z_α which carry the

[1] In general, electron pockets could also appear, but let us assume that the parameters are such that only the hole-pockets are present.

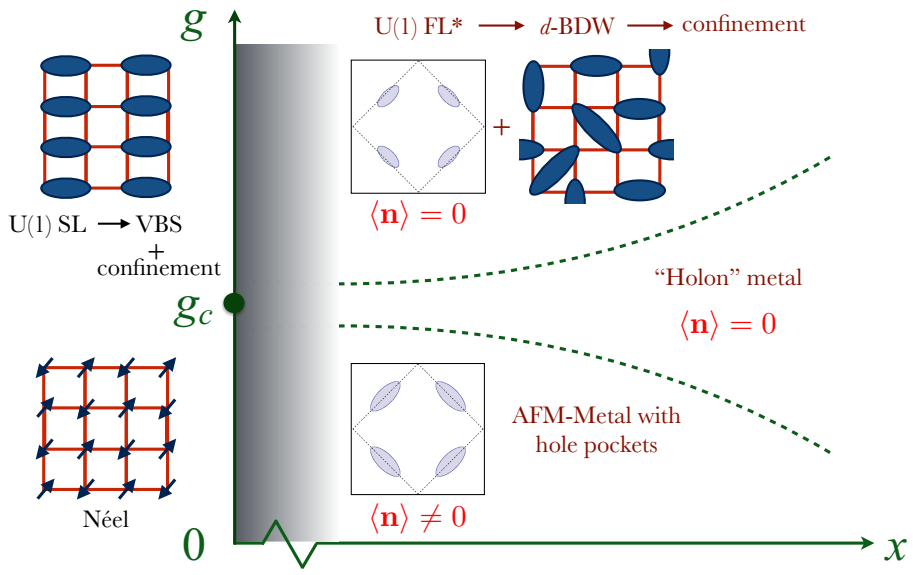

Figure 6.1: Phase diagram of a quantum antiferromagnet as a function of the parameter, g, which controls the strength of quantum fluctuations and the carrier density, x. The $x = 0$ phases are insulators, and we assume that the insulator has a deconfined quantum critical point [214, 210] at a $g = g_c$. The arrows on the labels of the phases indicate crossovers upon going to lower energies and longer distances. For $x = 0$ and $g < g_c$, the ground state is an ordered antiferromagnetic insulator, while for $x = 0$ and $g > g_c$ the ground state is a valence bond solid (VBS), which arises as an instability at long confinement scale of a U(1) spin-liquid (SL). The $g = g_c$, deconfined quantum critical point, broadens into a "holon" metal phase above a small, finite x. Binding of the emergent spinon and holon excitations in the holon metal phase leads to the FL* phase shown for $g > g_c$ and non-zero x. We do not discuss the small x (shaded grey) region in this paper [113]. The BDW instabilities of the U(1) FL* have a $d-$form factor and could be relevant for the observations in the non La-based cuprates. The physical trajectory in the phase diagram (for the non-La cuprates) corresponds to not only changing x, but also g, *i.e.* the trajectory runs diagonally. The eventual confinement transition out of the $d-$BDW state must occur, and its description remains an important topic for future work.

U(1) gauge charge. Upon doping the antiferromagnet in the vicinity of this deconfined critical point with charge carriers of density x, we have to include a density x of spinless fermions ('holons'), ψ_p, which carry gauge charge ($p = \pm 1$) under the same $U(1)$ gauge field. The resulting gauge theory for z_α and ψ_p has a complicated

phase diagram as a function of g and the hole density, which is sketched in Fig. 6.1 and will be partly reviewed in Section 6.2. Our attention here will focus on the FL* region of Fig. 6.1: here the z_α and ψ_p bind to form gauge-neutral fermions of density x, which then form Fermi pockets in the Brillouin-zone near, but not centered at, $(\pm\pi/2, \pm\pi/2)$. The total area enclosed by these pockets is x, and hence the Luttinger volume of $1 + x$ is not obeyed, and a FL* phase is realized.

In this chapter, we carry out a generalized RPA analysis of a model of this FL* phase interacting via short-range interactions. In most of the parameter space that we have explored, the leading instability in the particle-hole channel is a bond density wave with predominantly $d-$form factor whose wavevector nests the tips of the hole-pockets.[2] This result is a promising step in the direction of identifying essential characteristics of the normal state which are responsible for giving rise to the BDW instability that is observed experimentally in the underdoped cuprates.

The rest of this chapter is arranged as follows: we describe and review a particular route towards constructing an FL* state, starting from a one-band model of electrons coupled to the fluctuations of an AFM order-parameter in section 6.2.1. We then setup our computation for determining the charge-ordering instabilities in an FL* interacting via short-range interactions in section 6.2.2. Finally, we describe our results for the nature of the BDW instabilities, with special emphasis on its wavevector and form factor, in section 6.3 and conclude with a future outlook in section 6.4. We review some of the previous analysis of density-wave instabilities in metals with large Fermi surfaces interacting via short-range interactions ([196, 9]) in appendix E.1 in

[2]The density of states, $n(E) = \oint_{E_{\boldsymbol{k}}=E} \frac{1}{|\nabla_{\boldsymbol{k}} E_{\boldsymbol{k}}|} d^2\boldsymbol{k}$ is high at the tips of the pockets, $E_{\boldsymbol{k}} = 0$.

order to highlight the differences with the main results presented in this paper. The analysis here will be similar to section 5.2.1. Appendix E.2 contains a brief discussion of density-wave instabilities in the presence of large Coulomb repulsion.

6.2 Model

We begin by summarizing the arguments [113, 184] that lead to the phase diagram in Fig. 6.1. The starting point is the theory for the electrons, $c_{i\alpha}$ ($\alpha =\uparrow,\downarrow$), hopping on the sites of a square lattice. The electrons are coupled to the fluctuations of an O(3) field, $\mathbf{n}_i$, which describes the local orientation of the antiferromagnetic Néel order at $\boldsymbol{K} = (\pi, \pi)$. We shall focus on the long-wavelength fluctuations of $\mathbf{n}_i$ while retaining the full lattice dispersions for the fermions. The imaginary time Lagrangian, $\mathcal{L} = \mathcal{L}_f + \mathcal{L}_n + \mathcal{L}_{fn}$, is given by,

$$\mathcal{L}_f = \sum_{i,j} c^\dagger_{i\alpha}\Big[(\partial_\tau - \mu)\delta_{ij} - t_{ij}\Big]c_{j\alpha} + \text{h.c.}, \tag{6.1}$$

$$\mathcal{L}_n = \frac{1}{2g}\int d^2\boldsymbol{r}\ [(\partial_\tau \mathbf{n})^2 + \mathrm{v}^2(\nabla \mathbf{n})^2], \tag{6.2}$$

$$\mathcal{L}_{fn} = \lambda \sum_i e^{i\boldsymbol{K}\cdot\boldsymbol{r}_i}\ \mathbf{n}_i \cdot c^\dagger_{i\alpha}\boldsymbol{\sigma}_{\alpha\beta}c_{i\beta}. \tag{6.3}$$

In the above, t_{ij} represent the hopping matrix elements that give rise to a large Fermi surface, μ represents the chemical potential, λ is an $O(1)$ coupling, v represents a characteristic spin-wave velocity and g is used to tune the strength of quantum fluctuations associated with the AFM order parameter. The vector $\mathbf{n}$ satisfies the local constraint $\mathbf{n}_i^2 = 1$.

When $g < g_c$, the above model has long-range antiferromagnetic order, $\langle \mathbf{n} \rangle \neq 0$ (with a correlation length, $\xi \to \infty$). In the presence of such long-range order (LRO),

the large Fermi surface breaKS10 up into electron and hole pockets. The resulting state in the presence of short-range fermionic interactions could be unstable to other symmetry-broken states; the nature of these instabilities in the particle-hole channel, starting from a reconstructed Fermi surface, have been analyzed [20, 231]. As we noted in Section 6.1, this approach leads to density waves with the d-form factor suppressed [20], consistent with recent observations on the La-based cuprates [4] which do have magnetic order at low temperatures.

Our interest in the present paper is on the $g \geq g_c$ portion of the phase diagram in Fig. 6.1, which we argue is relevant to the physics of the non-La-based cuprates. The deconfined critical point $g = g_c$ and $x = 0$ is expressed not in terms of the $\mathbf{n}$ fields, but in terms of the spinor z_α, with

$$\mathbf{n}_i = z^*_{i\alpha} \boldsymbol{\sigma}_{\alpha\beta} z_{i\beta} \tag{6.4}$$

and a U(1) gauge field A_μ. At the same time [184], one tranforms the underlying electrons, $c_{i\alpha}$, to a new set of spinless Fermions, ψ_{ip},

$$c_{i\alpha} = R^i_{\alpha p} \psi_{ip}, \quad \text{where} \tag{6.5}$$

$$R^i_{\alpha p} = \begin{pmatrix} z_{i\uparrow} & -z^*_{i\downarrow} \\ z_{i\downarrow} & z^*_{i\uparrow} \end{pmatrix}, \tag{6.6}$$

is a spacetime dependent SU(2) matrix ($\sum_\alpha |z_{i\alpha}|^2 = 1$) and the fermions ψ_{ip} carry opposite charges $p = \pm 1$ under the same emergent U(1) gauge transformation.

We begin our discussion of the complex dynamics of z_α and ψ_p by first considering the effect of non-zero x at the critical coupling $g = g_c$. At very low hole density, each ψ_p fermion can be treated independently of all the others, while interacting with the

deconfined gauge theory described by z_α and A_μ. As shown in Ref. [113], there is an 'orthogonality catastrophe' and each ψ_p fermion is effectively localized by the critical fluctuations. We are not interested here in the very small values of x at which this localization happens, and so will not discuss it further; it is also excluded from Fig. 6.1 (shown as the grey-shaded region). Moving to higher hole densities, we can assume the holons form a Fermi surface, and this can then quench the A_μ fluctuations via Landau damping [114, 208]; the holon Fermi surface is then stable,[3] and we obtain the holon metal shown in Fig. 6.1.

Let us now turn to $g > g_c$. Now there is at least one additional length scale, the spin correlation length, ξ. This length should be compared with the spacing between the holons $\sim 1/\sqrt{x}$. There is actually another significant scale, the length scale at which Landau-damping of the photon sets in; this also diverges as $x \to 0$, and for simplicity we will ignore its difference from the spacing between the holons. When $1/\sqrt{x} \ll \xi$, we revert to the $g = g_c$ situation described in the previous paragraph. However, for $\xi \ll 1/\sqrt{x}$, we have to first consider the influence of a non-zero ξ on the gauge theory of the deconfined critical point. As described in Refs. [214, 210], here we crossover to a Coulomb phase in which the A_μ field mediates a logarithmic Coulomb force. This Coulomb force binds the z_α and ψ_p quanta into gauge-neutral fermions [113, 115, 184] (an additional attractive force is also provided by the "Shraiman-Siggia term" [113, 184, 221]). At longer scales, these gauge-neutral fermions start to notice each other via the Pauli principle, and so they form Fermi surfaces leading to the FL*

[3] At low temperatures, the holons can pair to form a composite Boson that is neutral under the A_μ field, condensation of which leads to the holon superconductor [115].

state of interest here.[4]

At even longer length scales we have to consider confinement effects from monopoles in the A_μ gauge field, which are not suppressed in the FL* regime (but monopoles are suppressed in the holon metal). This we will not do here, leaving it as a difficult but important problem for future study.

6.2.1 Fractionalized Fermi liquid (FL*)

As discussed in section 6.1 and in Refs. [184, 162], the emergent photon gives rise to binding of the ψ_p fermions and the z_α spinons into gauge-neutral objects. However, there are two such combinations,

$$F_{i\alpha} \sim z_{i\alpha}\psi_{i+}, \quad G_{i\alpha} \sim \varepsilon_{\alpha\beta} z^*_{i\beta}\psi_{i-}, \tag{6.7}$$

where $\varepsilon_{\alpha\beta}$ is the unit antisymmetric tensor. The physical electronic operator has a non-zero overlap with both of these,

$$c_{i\alpha} \equiv Z(F_{i\alpha} + G_{i\alpha}), \tag{6.8}$$

where Z is a quasiparticle renormalization factor that is nonlocal over ξ; this expression differs from the bare relationship in Eq. (6.6) because we are now dealing with fully renormalized quasiparticles [184]. Over distances that are larger than ξ, where there is no net AFM order, the F_α and G_α fermions preferentially, but not exclusively, reside on the different sublattice sites.

[4] The FL* phase considered here is a descendant of the "holon-hole" metal phase of ref.[115], in the extreme limit where all of the holon states have been depleted into forming gauge-neutral fermions.

Based on symmetry considerations alone, we can write the following effective Hamiltonian for $F_{i\alpha}$ and $G_{i\alpha}$,

$$\begin{aligned} H_{\text{eff}} = & - \sum_{i,j} t_{ij}(F^\dagger_{i\alpha}F_{j\alpha} + G^\dagger_{i\alpha}G_{j\alpha}) + \lambda \sum_i e^{i\boldsymbol{K}\cdot\boldsymbol{r}_i}(F^\dagger_{i\alpha}F_{i\alpha} - G^\dagger_{i\alpha}G_{i\alpha}) \\ & - \sum_{i,j} \tilde{t}_{ij}(F^\dagger_{i\alpha}G_{j\alpha} + G^\dagger_{i\alpha}F_{j\alpha}). \end{aligned} \tag{6.9}$$

Once again, the t_{ij} represent the hopping matrices corresponding to a large Fermi surface, λ represents the potential due to the local AFM order (at distances shorter than ξ). The terms proportional to $\tilde{t}_{ij}$ represent the analogs of the "Shraiman-Siggia" (SS) terms [221] which couple the F and G particles. In the absence of these terms, but with $\lambda \neq 0$, one obtains hole-like pockets centered at $(\pi/2, \pi/2)$. However, when the SS terms are finite, the pockets can be shifted away from these special points.

It is more convenient now to change basis to a new set of fermionic operators,

$$C_{\boldsymbol{k}\alpha} = \frac{1}{\sqrt{2}}(F_{\boldsymbol{k}\alpha} + G_{\boldsymbol{k}\alpha}), \quad D_{\boldsymbol{k}\alpha} = \frac{1}{\sqrt{2}}(F_{\boldsymbol{k}+\boldsymbol{K}\alpha} - G_{\boldsymbol{k}+\boldsymbol{K}\alpha}), \tag{6.10}$$

so that the physical electronic operator $c_{\boldsymbol{k}\alpha} \simeq (Z/\sqrt{2})C_{\boldsymbol{k}\alpha}$. The revised Hamiltonian then reads,

$$\begin{aligned} H_{\text{eff}} = \sum_{\boldsymbol{k}} \Big[& \xi^+_{\boldsymbol{k}} C^\dagger_{\boldsymbol{k}\alpha} C_{\boldsymbol{k}\alpha} \quad + \quad \xi^-_{\boldsymbol{k}+\boldsymbol{K}} D^\dagger_{\boldsymbol{k}\alpha} D_{\boldsymbol{k}\alpha} \\ & -\lambda (C^\dagger_{\boldsymbol{k}\alpha} D_{\boldsymbol{k}\alpha} \quad + \quad D^\dagger_{\boldsymbol{k}\alpha} C_{\boldsymbol{k}\alpha}) \Big], \end{aligned} \tag{6.11}$$

where the dispersions, $\xi^+_{\boldsymbol{k}}$, $\xi^-_{\boldsymbol{k}}$ are given by,

$$\xi^+_{\boldsymbol{k}} = \varepsilon_{\boldsymbol{k}} + \tilde{\varepsilon}_{\boldsymbol{k}}, \quad \xi^-_{\boldsymbol{k}} = \varepsilon_{\boldsymbol{k}} - \tilde{\varepsilon}_{\boldsymbol{k}}, \tag{6.12}$$

$$\begin{aligned} \varepsilon_{\boldsymbol{k}} = & -2t_1(\cos(k_x) + \cos(k_y)) - 4t_2\cos(k_x)\cos(k_y) \\ & -2t_3(\cos(2k_x) + \cos(2k_y)) - \mu, \end{aligned} \tag{6.13}$$

$$\tilde{\varepsilon}_{\boldsymbol{k}} = -\tilde{t}_0 - \tilde{t}_1(\cos(k_x) + \cos(k_y)). \tag{6.14}$$

The Green's function for the electronic operator can be obtained from the Hamiltonian in eqn.6.11 and is given by [184],

$$G^c(\boldsymbol{k},\omega) = \frac{Z^2}{\omega - \xi^+_{\boldsymbol{k}} - \lambda^2/[\omega - \xi^-_{\boldsymbol{k}+\boldsymbol{K}}]}. \tag{6.15}$$

It is more transparent to rewrite the above Green's function in the following form,

$$G^c(\boldsymbol{k},\omega) = \sum_{\alpha=\pm} \frac{Z^\alpha_{\boldsymbol{k}}}{\omega - E^\alpha_{\boldsymbol{k}}}, \text{ where} \tag{6.16}$$

$$\left(\frac{Z^\pm_{\boldsymbol{k}}}{Z^2}\right)^{-1} = 1 + \frac{\lambda^2}{(E^\pm_{\boldsymbol{k}} - \xi^-_{\boldsymbol{k}+\boldsymbol{K}})^2}, \tag{6.17}$$

$$E^\pm_{\boldsymbol{k}} = \frac{\xi^+_{\boldsymbol{k}} + \xi^-_{\boldsymbol{k}+\boldsymbol{K}}}{2} \pm \sqrt{\left(\frac{\xi^+_{\boldsymbol{k}} - \xi^-_{\boldsymbol{k}+\boldsymbol{K}}}{2}\right)^2 + \lambda^2}. \tag{6.18}$$

In the limit where $\lambda = \tilde{t}_{ij} = 0$, one recovers the original large Fermi surface, $\xi_{\boldsymbol{k}}$.

6.2.2 Charge-order instabilities via T-matrix

Based on the analysis above, we have arrived at a description of the electronic excitations which have been renormalized by the quantum fluctuations of the antiferromagnet. A natural question that we need to address now is whether the resulting state is unstable to other symmetry-broken phases in the presence of short-range interactions. We shall address this question by studying the effect of short-range Coulomb repulsion and AF exchange interaction acting on top of the FL* phase, described by,

$$H_C = U \sum_i c^\dagger_{i\uparrow} c_{i\uparrow} c^\dagger_{i\downarrow} c_{i\downarrow} + \sum_{i<j} V_{ij} c^\dagger_{i\alpha} c_{i\alpha} c^\dagger_{j\beta} c_{j\beta}, \tag{6.19}$$

$$H_J = \sum_{i<j} \frac{J_{ij}}{4} \boldsymbol{\sigma}_{\alpha\beta} \cdot \boldsymbol{\sigma}_{\gamma\delta}\ c^\dagger_{i\alpha} c_{i\beta} c^\dagger_{j\gamma} c_{j\delta}. \tag{6.20}$$

The notation that we shall use to define the interaction parameters from now on is as follows: $J_{ij} \equiv J_a,\ V_{ij} \equiv V_a$, where $a(= 1, 2, 3)$ denotes whether $i,\ j$ are 1^{st}, 2^{nd}, or, 3^{rd} nearest neighbors.

Let us now look for the possible charge-ordering instabilities. We will consider the effect of first, second and third neighbor Coulomb and exchange interactions (*i.e.* $V_\ell,\ J_\ell$ with $\ell = 1, 2, 3$). Our generalized order parameter in the particle-hole channel, $P_{\boldsymbol{Q}}(\boldsymbol{k})$, at a wavevector $\boldsymbol{Q}$ can be defined as follows:

$$\langle c^\dagger_{i\alpha} c_{j\alpha} \rangle = \sum_{\boldsymbol{Q}} \left[\int_{\boldsymbol{k}} P_{\boldsymbol{Q}}(\boldsymbol{k}) e^{i\boldsymbol{k}\cdot(\boldsymbol{r}_i - \boldsymbol{r}_j)} \right] e^{i\boldsymbol{Q}\cdot(\boldsymbol{r}_i + \boldsymbol{r}_j)/2}. \tag{6.21}$$

It is useful to expand $P_{\boldsymbol{Q}}(\boldsymbol{k})$ in terms of a set of orthonormal basis functions $\phi_\ell(\boldsymbol{k})$ as,

$$P_{\boldsymbol{Q}}(\boldsymbol{k}) = \sum_\ell \mathcal{P}_\ell(\boldsymbol{Q}) \phi_\ell(\boldsymbol{k}), \tag{6.22}$$

where we choose a set of 13 orthonormal basis functions, as described in table 6.1.

The basis functions from $\ell = 0, .., 6$ preserve time-reversal symmetry, while the ones from $\ell = 7, .., 12$ spontaneously break time-reversal symmetry. The remainder of our analysis will be carried out using the T-matrix formalism developed in ref.[9] to determine the structure of the charge-ordering instability.

The first step in this procedure involves expressing the interaction terms in eqn.6.20 as,

$$H_J + H_C = \sum_{\boldsymbol{k},\boldsymbol{k}',\boldsymbol{q}} \sum_{\ell=0}^{12} \phi_\ell(\boldsymbol{k}) \phi_{\ell'}(\boldsymbol{k}') \Bigg[\frac{\overline{J}_\ell}{8} \boldsymbol{\sigma}_{\alpha\beta} \cdot \boldsymbol{\sigma}_{\gamma\delta} c^\dagger_{\boldsymbol{k}'-\boldsymbol{q}/2,\alpha} c_{\boldsymbol{k}-\boldsymbol{q}/2,\beta} c^\dagger_{\boldsymbol{k}+\boldsymbol{q}/2,\gamma} c_{\boldsymbol{k}'+\boldsymbol{q}/2,\delta} + \frac{\overline{V}_\ell}{2} c^\dagger_{\boldsymbol{k}'-\boldsymbol{q}/2,\alpha} c_{\boldsymbol{k}-\boldsymbol{q}/2,\alpha} c^\dagger_{\boldsymbol{k}+\boldsymbol{q}/2,\beta} c_{\boldsymbol{k}'+\boldsymbol{q}/2,\beta} \Bigg], \tag{6.23}$$

ℓ	$\phi_\ell(\boldsymbol{k})$	$\overline{J}_\ell$	$\overline{V}_\ell$	ℓ	$\phi_\ell(\boldsymbol{k})$	$\overline{J}_\ell$	$\overline{V}_\ell$
0	1	0	U				
1	$\cos k_x - \cos k_y$	J_1	V_1	7	$\sin k_x - \sin k_y$	J_1	V_1
2	$\cos k_x + \cos k_y$	J_1	V_1	8	$\sin k_x + \sin k_y$	J_1	V_1
3	$2\sin k_x \sin k_y$	J_2	V_2	9	$2\cos k_x \sin k_y$	J_2	V_2
4	$2\cos k_x \cos k_y$	J_2	V_2	10	$2\sin k_x \cos k_y$	J_2	V_2
5	$\cos 2k_x - \cos 2k_y$	J_3	V_3	11	$\sin 2k_x - \sin 2k_y$	J_3	V_3
6	$\cos 2k_x + \cos 2k_y$	J_3	V_3	12	$\sin 2k_x + \sin 2k_y$	J_3	V_3

Table 6.1: Basis functions, $\phi_\ell(\boldsymbol{k})$, used for determining the symmetry of the charge-ordering instability.

where $\overline{J}_\ell$, $\overline{V}_\ell-$ represent various interaction parameters, as summarised in table 6.1.

After summing all the ladder diagrams in the particle-hole channel, we obtain (see fig.6.2),

$$\begin{aligned} T_{\ell m}(\boldsymbol{Q}) &= \left(\frac{3}{4}\overline{J}_\ell + \overline{V}_\ell\right)\delta_{\ell m} - 2\delta_{\ell,0}\delta_{m,0}W(\boldsymbol{Q}) \\ &+ \frac{1}{2}\sum_{n=0}^{12}\left(\frac{3}{4}\overline{J}_\ell + \overline{V}_\ell\right)\Pi_{\ell n}(\boldsymbol{Q})T_{nm}(\boldsymbol{Q}) - \delta_{\ell,0}\sum_{n=0}^{12}W(\boldsymbol{Q})\Pi_{0,n}(\boldsymbol{Q})T_{nm}(\boldsymbol{Q}), \end{aligned} \tag{6.24}$$

where,

$$W(\boldsymbol{Q}) \equiv \sum_{\ell=0}^{12}\overline{V}_\ell\phi_\ell(0)\phi_\ell(\boldsymbol{Q}) \tag{6.25}$$

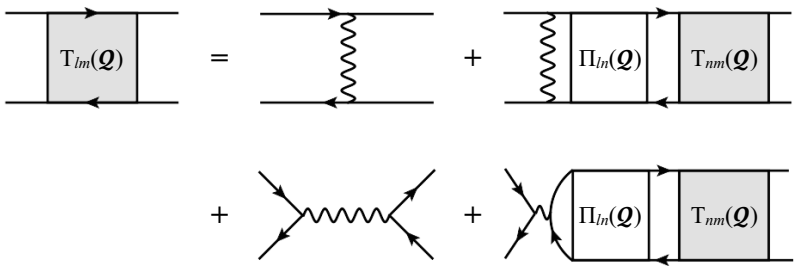

Figure 6.2: The equation for the T-matrix in the particle-hole channel with total momentum $\boldsymbol{Q}$.

arises from the direct interaction, and the polarizabilities are given by,

$$\Pi_{\ell m}(\boldsymbol{Q}) = 2\sum_{\boldsymbol{k}} \phi_\ell(\boldsymbol{k})\phi_m(\boldsymbol{k})\Pi_{\boldsymbol{Q}}(\boldsymbol{k}), \tag{6.26}$$

$$\Pi_{\boldsymbol{Q}}(\boldsymbol{k}) = \sum_{\alpha,\beta=\pm} Z^\alpha_{\boldsymbol{k}+\boldsymbol{Q}/2} Z^\beta_{\boldsymbol{k}-\boldsymbol{Q}/2} \frac{f(E^\alpha_{\boldsymbol{k}+\boldsymbol{Q}/2}) - f(E^\beta_{\boldsymbol{k}-\boldsymbol{Q}/2})}{E^\beta_{\boldsymbol{k}-\boldsymbol{Q}/2} - E^\alpha_{\boldsymbol{k}+\boldsymbol{Q}/2}}. \tag{6.27}$$

In the above, $f(...)$ represents the Fermi-Dirac distribution function.

From eqn.6.24, it is straightforward to see that the charge-ordering instability is determined by the lowest eigenvalues, $\lambda_{\boldsymbol{Q}}$, of the matrix $\mathcal{M}_{\ell,\ell'}(\boldsymbol{Q})$,

$$\mathcal{M}_{\ell,\ell'}(\boldsymbol{Q}) = \delta_{\ell\ell'} - \frac{1}{2}\left(\frac{3}{4}\overline{J}_\ell + \overline{V}_\ell\right)\Pi_{\ell\ell'}(\boldsymbol{Q}) + \delta_{\ell,0} W(\boldsymbol{Q})\Pi_{0\ell'}(\boldsymbol{Q}), \tag{6.28}$$

and the $\mathcal{P}_{\ell'}(\boldsymbol{Q})$ are determined by the corresponding right eigenvector.

In the remainder of the paper, we shall investigate the nature of these instabilities by studying the eigenvalues and eigenvectors corresponding to the matrix $\mathcal{M}(\boldsymbol{Q})$ as a function of $\boldsymbol{Q}$.

6.3 Results

We have analyzed the lowest eigenvalues, $\lambda_{\boldsymbol{Q}}$, as a function of $\boldsymbol{Q}$ for a variety of interaction and FL* parameters (see figs. 6.3, 6.4). These results should be contrasted with the eigenvalues obtained for instabilities of metals with a large Fermi surface, interacting via short-ranged interactions, as shown in appendix E.1 and earlier works [196, 9].

Let us now start by exploring the nature of these instabilities in the presence of purely exchange interactions, *i.e.* set $U = V_1 = V_2 = V_3 = 0$. We plot $\lambda_{\boldsymbol{Q}}$ as a function of $\boldsymbol{Q}$ in fig.6.3 for two different choice of FL* and exchange-interaction parameters, $\{J_1,\ J_2,\ J_3\}$. For the FL* state shown in fig.6.3(a), the charge-ordering eigenvalues are displayed in fig.6.3(b). Note that the global-minimum at $\boldsymbol{Q} = (\pm Q_0, \pm Q_0)$, which is a robust feature of an instability arising out of a large FS (with $\tilde{t}_0 = \tilde{t}_1 = \lambda = 0$), has disappeared (see fig. E.1(a) in appendix E.1; Refs. [196, 9]). Instead, there are now ridges of instability that extend starting from wavevectors of the type $(Q_0, 0)$ and $(0, Q_0)$. Interestingly, the lowest eigenvalue is shifted slightly away from the axis and corresponds to $\boldsymbol{Q}^* = (\pm 11\pi/25, \pm 3\pi/50),\ (\pm 3\pi/50, \pm 11\pi/25)$. However, the eigenvalue, $\lambda_{\boldsymbol{Q}^{**}}$, for the state on the axis with $\boldsymbol{Q}^{**} = (\pm 11\pi/25, 0),\ (0, \pm 11\pi/25)$, is infinitesimally close to the lowest eigenvalue.[5] The charge-ordering eigenvectors for

[5] where the difference, $|\lambda_{\boldsymbol{Q}^{**}} - \lambda_{\boldsymbol{Q}^{*}}| \simeq 10^{-4}$.

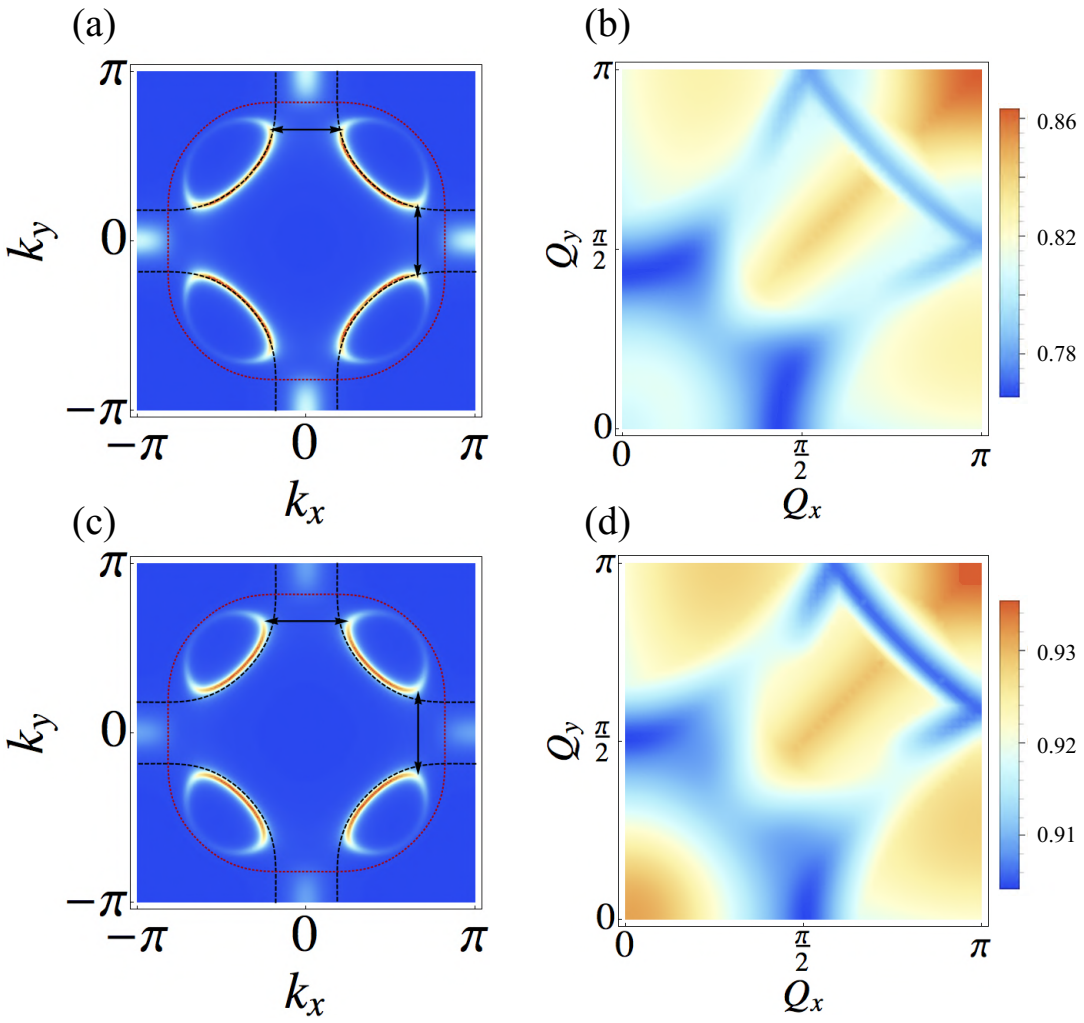

Figure 6.3: The spectral function, $A^c(\boldsymbol{k}, \omega = 0)$, for bare hopping parameters $t_1 = 1.0$, $t_2 = -0.32$, $t_3 = 0.128$, $\mu = -1.11856$ and FL* parameters: (a) $\tilde{t}_0 = -0.5t_1$, $\tilde{t}_1 = 0.4t_1$, $\lambda = 0.6t_1$, and, (c) $\tilde{t}_0 = -0.5t_1$, $\tilde{t}_1 = 0.6t_1$, $\lambda = 0.75t_1$. The black dashed lines represent, $\epsilon_{\boldsymbol{k}} = 0$, and the red dotted lines represent, $\epsilon_{\boldsymbol{k}+\boldsymbol{K}} = 0$. The lowest eigenvalue, $\lambda_{\boldsymbol{Q}}$ as a function of $\boldsymbol{Q}$ at a temperature $T = 0.06$ are shown in (b), (d) for the FL* states in (a), (c) respectively. The wavevectors corresponding to the minimum eigenvalues are shown as the black arrows. The exchange interaction parameters are given by (b) $J_1 = 1.0$, $J_2 = J_3 = 0.05$, and, (d) $J_1 = 0.5$, $J_2 = J_3 = 0.05$. $U = V_1 = V_2 = V_3 = 0$ for both cases. We have put in a finite imaginary part $(= 0.1t_1)$ in the Green's function for visualization purpose.

these states are given by,

$$\begin{aligned} P_{\boldsymbol{Q}^*}(\boldsymbol{k}) = & - 0.996[\cos k_x - \cos k_y] + 0.079[\cos k_x + \cos k_y] \\ & + 0.017[2\cos k_x \cos k_y] \\ & - 0.027[\cos 2k_x - \cos 2k_y] - 0.014[\cos 2k_x + \cos 2k_y], \qquad (6.29) \\ P_{\boldsymbol{Q}^{**}}(\boldsymbol{k}) = & + 0.996[\cos k_x - \cos k_y] - 0.084[\cos k_x + \cos k_y] \\ & - 0.017[2\cos k_x \cos k_y] \\ & + 0.027[\cos 2k_x - \cos 2k_y] + 0.014[\cos 2k_x + \cos 2k_y], \qquad (6.30) \end{aligned}$$

both of which predominantly have a $d-$wave component (and a tiny $s'-$ component).

While the eigenvalue analysis doesn't directly tell us how the wavevector of the leading instability relates to the underlying Fermi surface geometry, it is reasonable to associate it with points in the Brillouin-zone which have a high joint density of states. It is then straightforward to see that $\boldsymbol{Q}^{**}$ connects the tips of the pockets (shown as the black arrows in fig.6.3a). There is also a secondary ridge of instability, which corresponds to a set of local but not global minima, extending from approximately $\boldsymbol{Q} \approx (\pi/2, \pi)$ to $\boldsymbol{Q} \approx (\pi, \pi/2)$. Upon close inspection, we realize that such a ridge exists even for the large Fermi surface computation (fig.E.1a), though the eigenvalues there were significantly larger than the one corresponding to the global minimum. These BDW states contain an admixture of $d-$ and $s'-$ form factors. However, the states marked in yellow in the vicinity of $\boldsymbol{Q} = (\pi, \pi)$ and $\boldsymbol{Q} = (\pi, 0),\ (0, \pi)$ break time-reversal symmetry and correspond to states that have spontaneous currents.

We can repeat a similar analysis for other FL* and interaction parameters, as shown in fig.6.3(c), (d). For the FL* state shown in fig.6.3(c), the lowest eigenvalue

corresponds to $\boldsymbol{Q}^* = (\pm\pi/2, 0),\ (0, \pm\pi/2)$. Though the particular wavevector in this case corresponds to a period-4 CDW, this is entirely a coincidence; $\boldsymbol{Q}^*$ happens to connect the tips of the pockets (shown as black arrows in fig.6.3c). The charge-ordering eigenvector for this state is given by,

$$\begin{aligned} P_{\boldsymbol{Q}^*}(\boldsymbol{k}) = &+ 0.993[\cos k_x - \cos k_y] - 0.095[\cos k_x + \cos k_y] \\ &- 0.032[2\cos k_x \cos k_y] \\ &+ 0.050[\cos 2k_x - \cos 2k_y] + 0.027[\cos 2k_x + \cos 2k_y], \end{aligned} \tag{6.31}$$

which, once again, predominantly has a $d-$wave component. The secondary ridge of instability appears here as well, extending from approximately $\boldsymbol{Q} \approx (29\pi/50, \pi)$ to $\boldsymbol{Q} \approx (\pi, 29\pi/50)$, and contains an admixture of $d-$ and $s'-$ form factors. The states marked in yellow in the vicinity of $\boldsymbol{Q} = (\pi, \pi)$ and $\boldsymbol{Q} = (\pi, 0),\ (0, \pi)$ continue to break time-reversal symmetry.

The results for both of these cases above are very similar, with one major qualitative difference. In the first case, the region around $\boldsymbol{Q} = 0$ has a local "valley" of instability, where the state at $\boldsymbol{Q} = 0$ corresponds to a nematic instability with a purely $d-$form factor. This is no longer true for the second case considered here.

Let us now study the problem in the presence of Coulomb repulsion — the results are displayed in fig.6.4. Interestingly, in this case for the particular choice of parameters, the leading instability in the particle-hole channel for the FL* state in fig.6.4(a) corresponds to $\boldsymbol{Q}^* = (\pm 13\pi/25, \pm\pi),\ (\pm\pi, \pm 13\pi/25)$. The charge-ordering

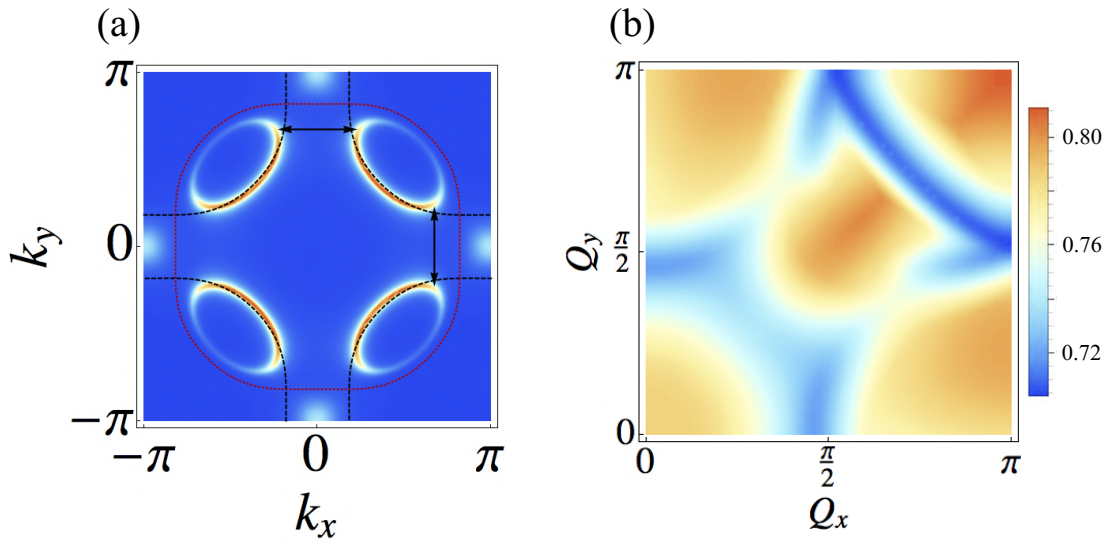

Figure 6.4: (a) The spectral function, $A^c(\boldsymbol{k}, \omega = 0)$, for bare hopping parameters $t_1 = 1.0,\ t_2 = -0.32,\ t_3 = 0.128,\ \mu = -1.11856$ and FL* parameters: $\tilde{t}_0 = -0.2t_1,\ \tilde{t}_1 = -0.1t_1,\ \lambda = 0.75t_1$. The black dashed lines represent, $\epsilon_{\boldsymbol{k}} = 0$, and the red dotted lines represent, $\epsilon_{\boldsymbol{k}+\boldsymbol{K}} = 0$. The lowest eigenvalue, $\lambda_{\boldsymbol{Q}}$ as a function of $\boldsymbol{Q}$ at a temperature $T = 0.06$ is shown in (b). The wavevectors corresponding to the minimum eigenvalue are shown as the black arrows. The interaction parameters are given by $J_1 = 1.0,\ J_2 = 0.1,\ J_3 = 0.05$, and, $U = 0,\ V_1 = 0.05,\ V_2 = V_3 = 0.01$. We have put in a finite imaginary part ($= 0.1t_1$) in the Green's function for visualization purpose.

eigenvector for this state is given by,

$$\begin{aligned} P_{\boldsymbol{Q}^*}(\boldsymbol{k}) = \ & - \ 0.184 - 0.694[\cos k_x - \cos k_y] - 0.694[\cos k_x + \cos k_y] \\ & + \ 0.021[2 \sin k_x \sin k_y] \\ & - \ 0.006[\cos 2k_x - \cos 2k_y] - 0.033[\cos 2k_x + \cos 2k_y]. \end{aligned} \tag{6.32}$$

However, as can be seen from fig.6.4(b), there is a subleading instability to a BDW with $\boldsymbol{Q}^{**} = (\pm 23\pi/50, 0), (0, \pm 23\pi/50)$, whose eigenvalue, $\lambda_{\boldsymbol{Q}^{**}}$, is in fact very close

to $\lambda_{\boldsymbol{Q}^*}$. The corresponding eigenvector is given by,

$$\begin{aligned} P_{\boldsymbol{Q}^{**}}(\boldsymbol{k}) = & - 0.012 - 0.986[\cos k_x - \cos k_y] + 0.162[\cos k_x + \cos k_y] \\ & + 0.024[2\cos k_x \cos k_y] \\ & - 0.032[\cos 2k_x - \cos 2k_y] - 0.012[\cos 2k_x + \cos 2k_y], \end{aligned} \tag{6.33}$$

which, not surprisingly, has a predominantly $d-$form factor.

The remaining features in the $\lambda_{\boldsymbol{Q}}-\boldsymbol{Q}$ phase diagram remain identical to the earlier results shown in fig.6.3(b).

We investigate the nature of the instabilities for two more cases in appendix E.2, when $U = 2J_1 \gg V_1$ and $U \sim J_1 \sim V_1$. The nature of the leading instabilities in these two cases is different; in the first case it is a "staggered-flux" state (though away from (π, π)) that breaks time reversal symmetry, while in the second case it leads to a conventional charge-density wave at (π, π). However, within the region of small $|\boldsymbol{Q}|$ of interest to us here, there remains a local instability to a d-form factor density wave with wavevectors of the form $(0, Q_0)$ and $(Q_0, 0)$, similar to those found above.

6.4 Discussion

We have argued here that the incommensurate charge density wave state in the underdoped cuprates acts as a window into the exotic "normal" phase out of which it emerges. The traditional weak-coupling computations that start with a large Fermi surface give rise to a density wave instability with diagonal wavevectors of the form $(\pm Q_0, \pm Q_0)$, which is in disagreement with the experimental observations. A promising candidate for the normal state of the underdoped cuprates is a U(1)-FL*, where

the electrons are coupled to the fractionalized excitations of a quantum fluctuating antiferromagnet. In this paper, we have investigated the charge-ordering instabilities of such a FL* state, and have identified the leading instability of the FL* state in the particle-hole channel. In most of the cases considered here, this leads to a $d-$form factor bond density wave with wavevectors of the form $\boldsymbol{Q} = (\pm Q_0, 0),\ (0, \pm Q_0)$, where Q_0 is related to a geometric property of the Fermi surfaces of the FL* state. Moreover, as a function of increasing doping, as the size of the hole-pockets increase, the magnitude of the wavevector that nests the tips of the pockets decreases. This agrees with the trend that has been seen in experiments, where the BDW wavector is a decreasing function of the increasing hole-doping [31].

While the identification of the correct BDW starting from a more exotic normal state is an interesting result, there are other implications at low temperatures of having a parent FL*. The vanilla FL* state has hole pockets with non-zero (but small) photoemission intensity on the 'back side' *i.e.* outside the first antiferromagnetic Brillouin zone, and the photoemission observations of Ref. [253] have been argued to be consistent with this. However, the superconducting state descending from such a FL* metal has 8 nodal points [162], and no signs of such a feature have been experimentally detected. But, it should be noted that U(1)-FL* is ultimately unstable to confinement, because in the absence of fermions carrying the U(1) gauge charge, monopoles must proliferate at large enough scales. It is expected that this crossover to confinement will resolve the experimental conflicts of the FL* state. Moreover, with the presence of an incommensurate BDW, there are no issues with the conventional Luttinger theorem, and so the crossover to confinement can happen without the need

for further symmetry breaking.

Finally, we note implications for experiments on the cuprates in high magnetic fields. In the light of the above results, it would be interesting to investigate how the BDW derived from an FL* evolves as a function of magnetic field, and in particular, determine its relation to the observed quantum oscillations at intermediate and high fields [65, 131, 229, 81, 207, 25, 206, 64]. Computations starting from a large Fermi surface in the presence of long-range charge order show a nodal electron-pocket [81, 207, 206, 64, 11] and the more recently discovered hole-pockets [64, 11]; it is not implausible that similar results will also be obtained starting from U(1)-FL*, especially after the crossover to confinement has been accounted for. Moreover, in the FL* framework the full large Fermi surface is never recovered, because even in the absence of charge order the spin liquid suppresses much of the Fermi surface: this may be a way of reconciling with thermodynamic measurements of the specific-heat [190] and the spin-susceptibility [116].

Chapter 7

Quantum phase transitions in metals without broken symmetries

"There are more things in heaven and earth, Horatio, Than are dreamt of in your philosophy." - *William Shakespeare,* Hamlet

7.1 Introduction

Several recent experiments [92, 76, 88, 187] have provided strong evidence for a dramatic change in the nature of the low temperature electronic state of the hole-doped cuprate superconductors near optimal doping ($x = x_c$). Moreover, zero field photoemission experiments carried out in the normal state have seen evidence for a 'large' Fermi-surface for $x > x_c$, consistent with the overall Luttinger count [181, 178], and disconnected Fermi 'arcs' near the nodal regions for $x < x_c$ [110]. At high fields, quantum oscillations also reveal a 'large' Fermi-surface for $x > x_c$ [236], but a closed

electron-like Fermi-surface with an area that constitutes a tiny fraction of the entire Brillouin-zone for $x < x_c$ [65]. It is therefore quite natural to associate the transition with decreasing x at $x = x_c$ with the loss of a 'large' Fermi-surface and the simultaneous opening of a pseudogap. There has also been significant experimental progress [248, 78, 5, 39, 249, 228, 52, 77] in understanding the structure of the density-wave ordering at lower doping in the non-La-based superconductors, which is likely responsible for the reconstructed electron-like Fermi-surface seen in quantum oscillation experiments [207, 11].

In this chapter we will use these advances to motivate and develop a previously proposed model [197] for the physics of the strange metal near optimal doping. We argue that the rich phenomenology observed in the underdoped cuprates is primarily driven by a transition between metals with large and small Fermi surfaces which does not directly involve any broken global symmetry. All states with broken symmetry[1] observed at low temperatures and low doping are not part of the critical field theory [214, 22], but are either derived as low energy instabilities, or, perhaps driven by the confinement transition out of the parent small Fermi surface phase. This diminished role for broken symmetries is consistent with absence of any observed order with a significant correlation length at higher temperatures. We will also construct a global phase diagram to describe the many phases and crossovers around the strange metal.

A quantum phase transition which does not involve broken symmetries is necessarily associated with a *topological* change in the character of the ground state wavefunction. Emergent gauge fields are a powerful method of describing this topological

[1]We shall ignore the subtleties associated with the presence of quenched disorder, except when it acts as a source of momentum decay for DC transport, as discussed later.

structure, and they remain applicable also to the gapless metallic phases of interest to us here. Given the fundamental connection between emergent gauge fields and the size of the Fermi surface, which was established in Ref. [215, 175] using Oshikawa's method [173], we are naturally led to a quantum phase transition in which there is a change in the structure of the deconfined gauge excitations. Indeed, this describes a Higgs transition in a metal, such as that discussed in Ref. [197]. This argument is a general motivation for Higgs criticality near optimal doping in the cuprates, which applies beyond the specific model considered here.

We emphasize that we are using the traditional particle-physics terminology in which a "Higgs transition" describes the breaking of a local gauge 'symmetry'. We are not referring to the longitudinal mode of a broken global symmetry, which has also been labeled "Higgs" in condensed matter contexts [179].

The primary new motivation for the model of Ref. [197] arises from our recent work [44] analyzing the d-form factor density waves observed in scanning tunnelling microscopy [77] and X-ray experiments [52]. In this work [44], we argued that such density waves arise most naturally as an instability of a metallic higher temperature pseudogap state with small Fermi surfaces described as a [213] 'fractionalized Fermi liquid' (FL*); other works with related ideas on the pseudogap are Refs. [19, 245, 254, 71, 148, 258]. Specifically, we used a theory of the FL* involving a background U(1) spin liquid with bosonic spinons [113, 115, 184, 183]: it is therefore convenient to dub this metallic state for the pseudogap as[2] a U(1)-FL*. These results are also easily extended to a Z_2 spin liquid, and we will consider this case in Appendix F.1.

[2]However the Fermi surface excitations in this FL* phase carry the same quantum numbers as the electron, and do not couple minimally to the emergent (deconfined) gauge-fields.

The presence of a small Fermi surface without symmetry breaking requires topological order and emergent gauge fields [215], and so also a Higgs transition to the large Fermi surfaces at larger doping: here we provide a natural embedding of a FL* theory into such a transition, and we expect similar approaches are possible for other possible topological orders in the underdoped regime.

We now consider the evolution of the U(1)-FL*, and its small pocket Fermi surfaces, to the 'large' Fermi surface Fermi liquid state at large doping. There is an existing conventional theory of the transformation from small to large Fermi surfaces driven by the disappearance of antiferromagnetic order. This is a transition between two Fermi liquids, and the vicinity of the transition is described by the Hertz-Millis theory [93, 156] and its field-theoretic extensions [1, 154, 133, 227], as shown in Fig. 7.1.

Here, we describe a detour from this direct route [197] in which two new non-Fermi liquid phases appear between the conventional phases of Hertz-Millis theory. The detour is described by a SU(2) gauge theory, and the transition from small to large Fermi surfaces is now a Higgs transition without any local order parameter, in which the emergent gauge structure describing the topological order in the ground state changes from U(1) to SU(2). The Higgs field of this transition is a measure of the local antiferromagnetic correlations in a rotating reference frame to be introduced below in Eq. (7.1).

Note that the Higgs transition in Fig. 7.1 is between metallic states which we denote as 'algebraic charge liquids' (ACL). The small and large Fermi surfaces in the ACLs are those of spinless fermions which carry the electromagnetic charge of the

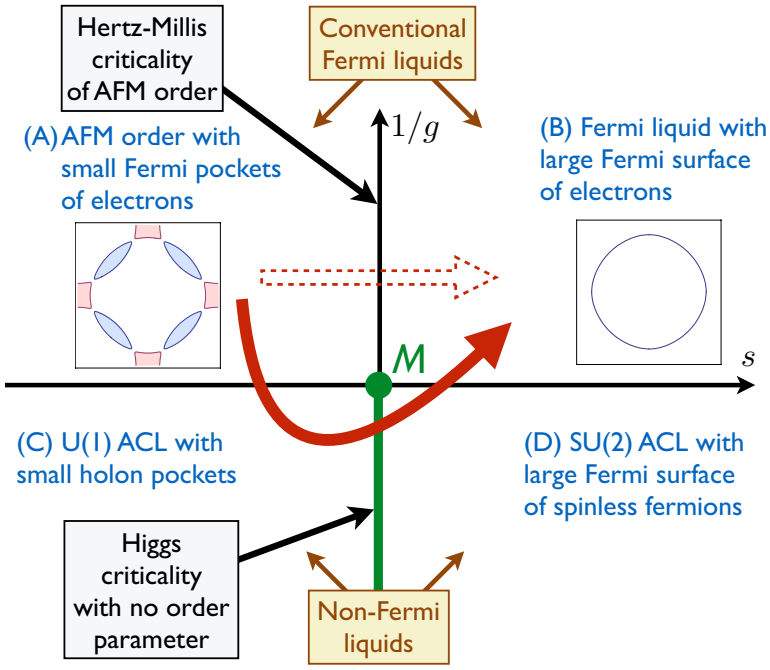

Figure 7.1: Sketch of the metallic phases of our theory. Only phase A has a broken global symmetry, associated with the presence of long-range antiferromagnetic (AFM) order. The conventional Fermi liquid phases at the top have a transition from small to large Fermi surfaces accompanied by the loss of AFM order. The dashed arrow represents a direct route between these phases, which could be a description of the electron-doped cuprates. The full arrow around the point M is our proposed route with increasing doping in the hole-doped cuprates. The U(1)-FL* descends from the U(1) ACL, as shown in Fig. 7.2. Note that the U(1)-FL* has a 'small' Fermi surface of electrons due to the presence of topological order, while phase A above has a 'small' Fermi surface of electrons because of translational symmetry breaking.

electron. For the U(1) ACL, a bound state forms between the spinless fermions and a spin $S = 1/2$ boson [113, 115, 184, 183], leading to small Fermi surfaces of fermionic quasiparticles carrying the same quantum numbers as the electron in the U(1)-FL*: so photoemission will detect a small Fermi surface of electrons in the U(1)-FL*. We anticipate that similar effects are also present in the SU(2) ACL metal: there is a large density of states of thermally excited $S = 1/2$ bosons at low energy, so that

the photoemission spectral function reflects the large Fermi surface of the spinless fermions.

We also note that although the Higgs field plays a central role in our phase diagram, its direct experimental detection will be difficult. It is overdamped via its coupling to the Fermi surfaces, and gauge invariance prohibits any experimental probe from coupling linearly to it. Nevertheless, we will see below that it has significant experimental consequences via its strong effect on the fermionic spectrum.

We will present details of this theory starting from a microscopic model in Section 7.2.3, but first, in Section 7.2, we shall describe some key aspects using our proposed phase diagram in Fig. 7.2.

The outline for the rest of our chapter is as follows. In section 7.2, we begin with a simplified picture of the critical point. In sections 7.2.1 and 7.2.2, we introduce key elements of the field theory for the Higgs critical point and describe how the Higgs field affects dc transport. In section 7.2.3, we arrive at the gauge-theoretic description starting from the theory of a metal with fluctuating antiferromagnetism and discuss the mean-field phase diagram as a function of the relevant tuning parameters. In Section 7.3.2, we describe the properties of the QCP using a low-energy description of the Fermi-surface coupled to a gauge-field and the critical fluctuations of the Higgs' field. Finally in Section 7.4, we discuss the relation of our proposed phase-diagram to the actual phase-diagram in the hole-doped cuprates. Appendix F.1 contains the extension to spiral order and $\mathbb{Z}_2$ gauge theory, while technical details are in Appendix F.2.

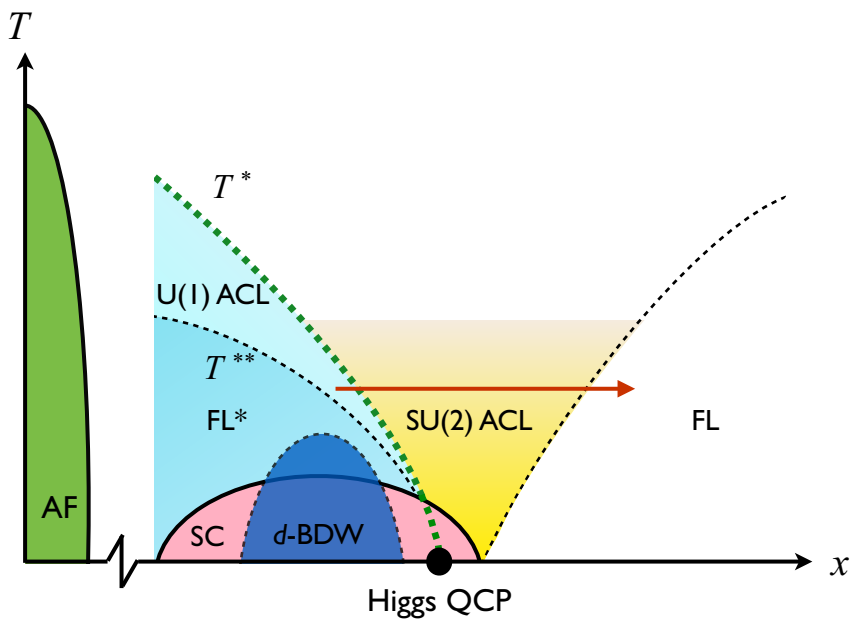

Figure 7.2: Our proposed phase diagram for the hole-doped cuprates, building on a theory for Higgs criticality for the optimal doping QCP. The green and red lines correspond to those in Fig. 7.1. The algebraic charge liquids (ACLs) have Fermi surfaces of spinless ψ fermions which carry the electromagnetic charge: in the SU(2) ACL the Fermi surface is 'large' and is coupled to an emergent SU(2) gauge field, while in the U(1) ACL the Fermi surface is 'small' and coupled to an emergent U(1) gauge field. The fractionalized Fermi liquid (FL*) descends from the U(1) ACL by the binding of ψ fermions to neutral spinons. The d-BDW is the d-form factor bond density wave, the SC is the d-wave superconductor, and the FL is the large Fermi surface Fermi liquid. We are not concerned here with the physics of the extremely underdoped region. Also, we expect that the crossovers within the superconducting phase will exhibit a 'back-bending' [161, 238, 88] which is not shown above, and which we do not discuss further here. The dashed lines at T^* and T^{**} are crossovers, while the Higgs QCP at $T = 0$ is a sharp phase transition.

7.2 Model

Let us begin with a simplified picture of the optimal doping strange metal with a large Fermi surface. We consider a model of electrons $c_{i\alpha}$ on the sites i of a square lattice, with $\alpha = \uparrow, \downarrow$ a SU(2) spin index. We transform the electrons to a rotating

reference frame[3] using a SU(2) rotation R_i and (spinless-)fermions $\psi_{i,p}$ with $p = \pm$,

$$\begin{pmatrix} c_{i\uparrow} \\ c_{i\downarrow} \end{pmatrix} = R_i \begin{pmatrix} \psi_{i,+} \\ \psi_{i,-} \end{pmatrix}, \tag{7.1}$$

where $R_i^\dagger R_i = R_i R_i^\dagger = 1$. Note that this representation immediately introduces a SU(2) gauge invariance (distinct from the global SU(2) spin rotation)

$$\begin{pmatrix} \psi_{i,+} \\ \psi_{i,-} \end{pmatrix} \to U_i \begin{pmatrix} \psi_{i,+} \\ \psi_{i,-} \end{pmatrix} \quad , \quad R_i \to R_i U_i^\dagger, \tag{7.2}$$

under which the original electronic operators remain invariant, $c_{i\alpha} \to c_{i\alpha}$; here U_i is a SU(2) gauge-transformation acting on the $p = \pm$ index. So the ψ_p fermions are SU(2) gauge fundamentals, they carry the physical electromagnetic global U(1) charge, but they do not carry the SU(2) spin of the electron. The density of the ψ_p is the same as that of the electrons. Such a rotating reference frame perspective was used in the early work by Shraiman and Siggia on lightly-doped antiferromagnets [221, 222], and the importance of its gauge structure was clarified in Ref. [197].

The strange metal is obtained by forming a large Fermi surface state of the ψ_p fermions, while R_i fluctuate isotropically over all SU(2) rotations with a moderate correlation length. This description suggests a simple trial wavefunction for this strange metal. Begin with a large Fermi surface (LFS) state of free ψ_p fermions:

$$\prod_{\boldsymbol{k} \text{ inside LFS, } p=\pm} \psi_p^\dagger(\boldsymbol{k}) \, |0\rangle \, . \tag{7.3}$$

Expand this out in position space, insert the inverse of Eq. (7.1) to write the wavefunction in terms of R and the physical electrons c_α, and finally average over R, to

[3]This allows us to describe phases without long-range antiferromagnetic order.

obtain

$$\int \prod_i dR_i \; W[\{R_j\}] \prod_{\boldsymbol{k} \text{ inside LFS}, \; p=\pm} \left[\sum_i e^{i\boldsymbol{k}\cdot\boldsymbol{r}_i} R_{i\alpha p} \, c^\dagger_{i\alpha} \right] |0\rangle \, , \tag{7.4}$$

where W is a variational weight-function of the R_i, invariant under global spin rotations. For $W = 1$, we have a zero correlation length for R_i, and we obtain a wavefunction for the c_α involving only empty and doubly-occupied sites. With non-trivial W, the correlation length of R increases, we also build in spin singlet pairs of c_α electrons on nearby sites. Comparing to the Gutzwiller-projected trial states commonly used for the underdoped cuprates [17], this wavefunction includes the possibility of doubly-occupied sites and assigns different complex weights to the off-site singlet pairs.

For a more precise and complete description of the strange metal, which accounts for the gauge structure in Eq. (7.1), we must turn to a quantum effective action for the ψ_p which necessarily includes an emergent SU(2) gauge field. In the terminology of Ref. [115], such a theory of spinless, gapless fermions coupled to an emergent gauge field is an 'algebraic charge liquid' (ACL), and hence we have labeled the strange metal as SU(2) ACL in Fig. 7.2. This name implies that the SU(2) gauge symmetry is unbroken (*i.e.* not 'Higgsed'), and in such a situation the ψ_p fermions have a large Fermi surface with a shape similar to that of the electron Fermi surface in Fermi liquid state at large doping.

Now let us consider the transition to the U(1) ACL in Fig. 7.2. This is described by the condensation of a real Higgs field H^a, where $a = 1, 2, 3$ indicates that the Higgs field transforms as a SU(2) adjoint. As we will see below in Eq. (7.15), this Higgs field is a measure of the local antiferromagnetic order in the rotating reference frame

defined by R (see also Ref. [145] for an illuminating analogy). The condensation of the Higgs breaks the gauge symmetry from SU(2) to U(1) and reconstructs the ψ_p Fermi surface from large to small. It is this Higgs transition which describes the optimal doping QCP in Fig. 7.2, and analyzing its structure is the main purpose of the present paper. In the case where H^a is complex, the Higgs phase can break the gauge symmetry down to Z_2, and we consider this case in Appendix F.1. The Shraiman-Siggia analyses [221, 222] of doped antiferromagnets were effectively within such a Higgs-condensed regime, and this obscured the gauge structure of their formulation [197].

Let us also note from Fig. 7.2 that the U(1) ACL is the parent of the U(1)-FL*. This was discussed in Refs. [115, 113], and will be reviewed below: the U(1)-FL* arises by the formation of bound states between the spinons, R, and ψ fermions around the small Fermi surface. We expect that a similar phenomenon also happens at low T in the SU(2) ACL at lower temperatures, so that the photoemission largely reflects the structure of the large Fermi surface of the SU(2) ACL.

The phase diagram in Fig. 7.2 is meant to be schematic; determining the exact nature of the various crossover and phase-transition lines is beyond the scope of this work. The Higgs transition is present only at $T = 0$, and there is only a crossover at $T > 0$ (shown as the dashed green line in Fig. 7.2).

7.2.1 Field theory

We now specify the imaginary time Lagrangian of the optimal doping QCP in Fig. 7.2, and its vicinity. For now, the Lagrangian will not include the R bosons:

we assume that R fluctuations are short-ranged, but the associated spin-gap in the SU(2) ACL phase of Fig. 7.2 is small because of proximity to the multi-critical point M in Fig. 7.1; we will include the R contributions in Section 7.2.3. Then we have

$$\mathcal{L}_{\rm QCP} = \mathcal{L}_\psi + \mathcal{L}_H + \mathcal{L}_Y. \tag{7.5}$$

The first term describes a large Fermi surface of ψ fermions minimally coupled to a SU(2) gauge field $A_\mu^a = (A_\tau^a, \boldsymbol{A}^a)$:

$$\mathcal{L}_\psi = \sum_i \psi_{i,p}^\dagger [(\partial_\tau - \mu)\delta_{pp'} + iA_\tau^a \sigma_{pp'}^a]\psi_{i,p'} + \sum_{i,j} t_{ij}\psi_{i,p}^\dagger \left[e^{i\sigma^a \boldsymbol{A}^a\cdot(\boldsymbol{r}_i - \boldsymbol{r}_j)}\right]_{pp'} \psi_{j,p'}, \tag{7.6}$$

where t_{ij} are the fermion hopping parameters, $\boldsymbol{r}_i$ are the spatial co-ordinates of the sites, μ is the chemical potential, and σ^a are Pauli matrices acting on the SU(2) gauge indices.

The Higgs Lagrangian is denoted $\mathcal{L}_H$, and it has a form familiar from its particle-physics incarnations,

$$\mathcal{L}_H = \frac{1}{2}(\partial_\tau H^a - 2i\epsilon_{abc}A_\tau^b H^c)^2 + \frac{\tilde{\rm v}^2}{2}(\nabla H^a - 2i\epsilon_{abc}\boldsymbol{A}^b H^c)^2 + \frac{s}{2}(H^a)^2 + \frac{u}{24}[(H^a)^2]^2. \tag{7.7}$$

The Higgs potential is determined by the parameters s and u, and transition across the QCP is controlled by the variation in s. As usual, for negative s, the Higgs field condenses, and this breaks the gauge symmetry from SU(2) to U(1); and for positive s, the Higgs field is gapped, and then the SU(2) gauge symmetry remains unbroken.

Finally, we have the Yukawa coupling in $\mathcal{L}_Y$. As in particle-physics, this is a trilinear coupling between the Higgs field and the fermions, but now it has a different spatial structure:

$$\mathcal{L}_Y = -\lambda\, H_i^a e^{i\boldsymbol{K}\cdot\boldsymbol{r}_i}\, \psi_{i,p}^\dagger \sigma_{pp'}^a \psi_{i,p'}, \tag{7.8}$$

where $\boldsymbol{K} = (\pi, \pi)$ is the antiferromagnetic wavevector. This spatial structure indicates that H^a transforms non-trivially under lattice translations:

$$H^a \to H^a e^{i\boldsymbol{K}\cdot\boldsymbol{a}} \text{ under translation by } \boldsymbol{a}; \tag{7.9}$$

note that this is permitted because $e^{i\boldsymbol{K}\cdot\boldsymbol{a}} = \pm 1$ is real for all spacings $\boldsymbol{a}$. The transformation in Eq. (7.9) arises from the role of the Higgs field as a measure of the antiferromagnetic correlations in a rotating reference frame. In the presence of the Higgs condensate, this Yukawa coupling reconstructs the ψ Fermi surface from large to small, and the $e^{i\boldsymbol{K}\cdot\boldsymbol{r}_i}$ factor is crucial in the structure of this reconstruction. While in the particle physics context the Higgs condensate gives the fermions a mass gap, here the fermions acquire a gap only on certain portions of the large Fermi surface, and a small Fermi surface of gapless fermions remains.

We note that the effective gauge theory will also acquire a Yang-Mills term for the SU(2) gauge field A^a when high energy degrees of freedom are integrated out. As is well known in theories of emergent gauge fields, such a term helps stabilize deconfined phases of the type considered here. We do not write this term out explicitly here, but will include its contributions in Section 7.3.2, and specifically in the L_A term in Eq. (7.21).

7.2.2 DC transport

The body of our paper will describe a field theoretic analysis of the non-Fermi liquid properties of $\mathcal{L}_{\rm QCP}$. This combines recent progress in the theories of Fermi surfaces coupled to order parameters [1, 154, 133, 227] and gauge fields [136, 153, 166]. Here we mention one notable result on the electrical resistivity in the quantum-critical

region of the Higgs transition. As in recent work [84, 177] on other quantum critical points of metals, we consider the situation in which there is a strong momentum bottleneck *i.e.* there is rapid exchange of momentum between the fermionic and bosonic degrees of freedom, and the resistivity is determined by the rate of loss of momentum. In particular, it is possible for the resistivity to be dominated by the scattering of neutral bosonic degrees of freedom, rather than that of charged fermionic excitations near the Fermi surface. In our model, we argue that an important source for momentum decay is the coupling of the Higgs field to disorder

$$\mathcal{L}_{\rm dis} = V(\boldsymbol{r}) \left[H^a(\boldsymbol{r})\right]^2, \tag{7.10}$$

where $V(\boldsymbol{r})$ is quenched Gaussian random variable with

$$\langle\langle V(\boldsymbol{r})\rangle\rangle = 0 \;\; ; \;\; \langle\langle V(\boldsymbol{r})V(\boldsymbol{r}')\rangle\rangle = V_0^2 \delta^2(\boldsymbol{r}-\boldsymbol{r}'), \tag{7.11}$$

where the double angular brackets indicate an average over quenched disorder. Comparing with Eq. (7.7), we see that $V(\boldsymbol{r})$ can be viewed as a random local variation in the value of s, the tuning parameter which determines the position of the QCP. We will show that the analysis of the contribution of $\mathcal{L}_{\rm dis}$ to the resistivity closely parallels the computation in Ref. [177] for the spin-density-wave quantum critical point. And as in Ref. [177], we find a resistivity for weak disorder which is proportional to V_0^2,

$$\rho(T) \sim V_0^2 \; T^{2(\Delta+1-z)/z}, \tag{7.12}$$

where $\Delta = d + z - \nu^{-1}$ is the scaling dimension of the $(H^a)^2$ operator, ν is the correlation length exponent and z is the dynamical exponent. As we will see in Section 7.3.2, this predicts a linear-in-T resistivity for the leading order values of the exponents.

7.2.3 SU(2) gauge theory of antiferromagnetic metals

We summarize the derivation in Ref. [197] of the SU(2) gauge theory, starting from a model of electrons on the square lattice coupled to the fluctuations of collinear antiferromagnetism at the wavevector $\boldsymbol{K} = (\pi, \pi)$. The case of collinear antiferromagnetism at other wavevectors was also considered in Ref. [197], and we treat spiral antiferromagnets at incommensurate wavevectors in Appendix F.1.

We begin with a model of electrons coupled to the quantum fluctuations of antiferromagnetism represented by the unit vector $n_{i\ell}$, with $\ell = x, y, z$ and $\sum_\ell n_{i\ell}^2 = 1$. The Lagrangian is given by

$$\begin{aligned} \mathcal{L} &= \mathcal{L}_f + \mathcal{L}_n + \mathcal{L}_{fn}, \\ \mathcal{L}_f &= \sum_i c_{i\alpha}^\dagger [(\partial_\tau - \mu)\delta_{ij} - t_{ij}] c_{j\alpha}, \\ \mathcal{L}_n &= \frac{1}{2g}\left[(\partial_\tau n_\ell)^2 + \mathrm{v}^2 (\nabla n_\ell)^2\right], \\ \mathcal{L}_{fn} &= -\lambda \sum_i e^{i\boldsymbol{K}\cdot\boldsymbol{r}_i}\ n_{i\ell} \cdot c_{i\alpha}^\dagger \sigma_{\alpha\beta}^\ell c_{i\beta}. \end{aligned} \tag{7.13}$$

In the above g measures the strength of quantum fluctuations associated with the orientation of n_ℓ, λ is an $\mathcal{O}(1)$ spin-fermion coupling and v is a characteristic spin-wave velocity.

Now we insert the parametrization in Eq. (7.1) into Eq. (7.13) and proceed to derive an effective theory for ψ_p and R. The formulation of the latter theory is aided by the introduction of a SU(2) gauge connection $A_\mu^a = (A_\tau^a, \boldsymbol{A}^a)$. As is familiar in many discussions of emergent gauge fields in correlated electron systems, this gauge field arises after decoupling hopping terms via an auxiliary field; here we skip these intermediate steps, and simply write down appropriate hopping terms for the ψ_p and

R which are made gauge-invariant by suitable insertions of the gauge connection.

With the parameterization in Eq. (7.1) we notice that the coupling $\mathcal{L}_{fn}$ in Eq. (7.13) maps precisely onto the Yukawa coupling in Eq. (7.8) with

$$H_i^a \sigma^a_{pp'} = n_{i\ell} R^*_{i\alpha p} \sigma^\ell_{\alpha\beta} R_{i\beta p'}, \tag{7.14}$$

and so we *define* the Higgs field H_i^a by

$$H_i^a \equiv \frac{1}{2} n_{i\ell} \ \mathrm{Tr}[\sigma^\ell R_i \sigma^a R_i^\dagger]. \tag{7.15}$$

This identifies H^a as the antiferromagnetic order in the rotating reference frame defined by Eq. (7.1). An important property of this definition is that the field H^a is *invariant* under a global SU(2) spin rotation V, which rotates the direction of the physical electron spin and of the antiferromagnetic order,

$$\begin{pmatrix} c_{i\uparrow} \\ c_{i\downarrow} \end{pmatrix} \to V \begin{pmatrix} c_{i\uparrow} \\ c_{i\downarrow} \end{pmatrix} \quad , \quad R_i \to V R_i. \tag{7.16}$$

Note that the SU(2) spin rotation is a left multiplication of R above, while the SU(2) gauge transformation in Eq. (7.2) is a right multiplication of R. With these properties, Eq. (7.15) implies that H^a transforms as a vector under the SU(2) gauge transformation in Eq. (7.2).

We have now assembled all the steps taken after substituting Eq. (7.1) into Eq. (7.13). The Lagrangian of the resulting gauge theory is then obtained as

$$\mathcal{L}_{\mathrm{SU(2)}} = \mathcal{L}_{\mathrm{QCP}} + \mathcal{L}_R, \tag{7.17}$$

where $\mathcal{L}_{\mathrm{QCP}}$ was described below Eq. (7.5) in Section 7.2.1, and $\mathcal{L}_R$ is the Lagrangian for R. The structure of the latter is determined by the transformations of R in

	$\mathrm{SU}(2)_{\mathrm{gauge}}$	$\mathrm{SU}(2)_{\mathrm{spin}}$	$\mathrm{U}(1)_{\mathrm{e.m.charge}}$
c	**1**	**2**	1
n	**1**	**3**	0
ψ	**2**	**1**	1
H	**3**	**1**	0
R	$\overline{\mathbf{2}}$	**2**	0

Table 7.1: Summary of the transformations of the fields under the various gauge-transformations. SU(2) representations of spin S are labelled by their dimension of $2S+1$. The U(1) column contains the charge under the U(1) gauge field.

Eqs. (7.2) and Eq. (7.16). So we have

$$\mathcal{L}_R = \frac{1}{2g}\mathrm{Tr}\left[(\partial_\tau R - iA_\tau^a R\sigma^a)(\partial_\tau R^\dagger + iA_\tau^a \sigma^a R^\dagger) + \mathrm{v}^2(\nabla R - i\boldsymbol{A}^a R\sigma^a)(\nabla R^\dagger + i\boldsymbol{A}^a\sigma^a R^\dagger)\right]. \tag{7.18}$$

This completes our derivation of the SU(2) gauge theory.

It is useful here to collect the transformations of the fields under the SU(2) gauge transformation, the global SU(2) spin rotation, and electromagnetic U(1) charge, as summarized in table 7.1.

Finally, we can make contact with other approaches by expressing R as

$$R_i = \begin{pmatrix} z_{i\uparrow} & -z_{i\downarrow}^* \\ z_{i\downarrow} & z_{i\uparrow}^* \end{pmatrix}, \tag{7.19}$$

with $|z_{i\uparrow}|^2 + |z_{i\downarrow}|^2 = 1$, but this parameterization will not be useful to us. Consider the situation in the Higgs phase, where the field H^a is condensed. Then we are free to choose a gauge in which the Higgs condensate is $H^a = (0, 0, 1)$. In such a condensate,

after inverting the relation in Eq. (7.15) we find

$$\begin{aligned} n_{i\ell} &= \frac{1}{2} H_i^a \ \mathrm{Tr}[\sigma^\ell R_i \sigma^a R_i^\dagger] \\ &= z_{i\alpha}^* \sigma_{\alpha\beta}^\ell z_{i\beta} \quad \text{for } H^a = (0,0,1). \end{aligned} \tag{7.20}$$

The last relationship is the familiar connection between the O(3) and CP^1 variables, but note that it holds here only within the phase where the Higgs field is condensed *i.e.* in the U(1) ACL.

7.3 Results

Let us now first describe the mean field phase diagram of the above theory in section 7.3.1. This will be followed by a discussion of the low-energy field theory for the Higgs transition in section 7.3.2.

7.3.1 Mean field phase diagram

We now describe the phases of $\mathcal{L}_{\mathrm{SU}(2)}$ obtained in a simple mean field theory [197] in which we allow condensates of the bosonic field R and H^a. These phases are obtained by varying the tuning parameters s and g,and were shown in Fig. 7.1; in Fig. 7.3, we label the phases by their condensates. The phases are:

- The Higgs phase, labelled as (A) in Fig. 7.3, where both $\mathrm{SU}(2)_{\mathrm{spin}}$ and $\mathrm{SU}(2)_{\mathrm{gauge}}$ are broken, leading to $\langle R \rangle \neq 0$, $\langle H^a \rangle \neq 0$. The gauge-excitations, $(A_\tau, \boldsymbol{A})$, are gapped here. This phase describes the *AFM-metal* where the large Fermi-surface gets reconstructed into hole (and electron) pockets due to condensation of $H^a \sim \boldsymbol{n}$, the Néel order parameter.

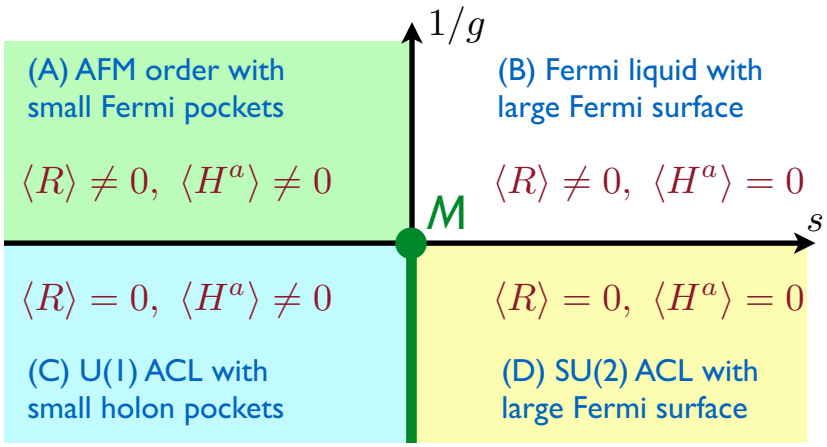

Figure 7.3: The phase diagram for the theory in Eq. (7.17) as a function of s and $1/g$ (also shown in Fig. 7.1). The color-coding of the phases corresponds to that in Fig. 7.2. The multicritical point, M, corresponds to $g = g_c$ and $s = 0$. This paper is concerned with the critical properties associated with the transition (C)↔(D).

- The SU(2) confining phase, labelled as (B) in Fig. 7.3. Note that the $\mathrm{SU}(2)_{\mathrm{spin}}$ here remains unbroken. We have $\langle R\rangle \neq 0$, $\langle H^a\rangle = 0$, which is necessary to preserve spin-rotation invariance since $\boldsymbol{n} = 0$ from Eq. (7.15). This is the usual *Fermi liquid* phase, with a large Fermi-surface.

- The Higgs phase, labelled as (C) in Fig. 7.3, where the $\mathrm{SU}(2)_{\mathrm{gauge}}$ is broken, but the $\mathrm{SU}(2)_{\mathrm{spin}}$ remains unbroken, leading to $\langle R\rangle = 0$, $\langle H^a\rangle \neq 0$. By recalling the physical interpretation of the fields, this amounts to a locally well developed amplitude of the AFM, without any long-range orientational order. We can choose $H^a \sim (0, 0, 1)$ by carrying out a gauge-transformation, which immediately implies that a U(1) subgroup of the $\mathrm{SU}(2)_{\mathrm{gauge}}$ remains unbroken, so that the A^z photon remains gapless. Thus this phase describes a *U(1) algebraic charge liquid*, or, the *holon-metal* [115]. However, due to the locally well developed AFM order, the Fermi-surface is reconstructed into ψ_p holon pockets

that are minimally coupled to a U(1) gauge-field.

As a function of temperature, there could be a continuous crossover from a U(1) ACL to a U(1) FL* (or a "holon-hole" metal), where some of the holons ($\psi_\pm$) start forming bound states with the gapped spinons (z_α) [115].

- The final phase (D) in Fig. 7.3 has the full symmetry, with none of the fields condensed: $\langle R \rangle = \langle H^a \rangle = 0$. Instead of the above U(1) ACL, where only A^z was gapless, in this phase there are a triplet of gapless SU(2) photons coupled to a large Fermi-surface. This phase can be described as a *SU(2) algebraic charge liquid*. Formally, this phase a spin gap, but we assume that T is greater than the gap in the metallic regions of Fig. 7.2 because of proximity to the point M in Fig. 7.1. At low enough T, this phase is unstable to superconductivity [152].

We should emphasize that the above mean-field analysis has been rudimentary; *e.g.* we cannot rule out the possibility that higher order couplings could induce first-order transitions, that could even eliminate an intermediate phase.

The next section shall present the theory for the interplay between the fluctuations of the gauge and Higgs' fields, within a low-energy field-theoretic formulation.

7.3.2 Low-energy field theory

We are interested in studying the properties of the QCP between the SU(2) ACL and the U(1) ACL. At the QCP, $s = 0$, the entire Fermi-surface is coupled to the transverse fluctuations of a SU(2) gauge field. There have been studies in the particle physics literature of Fermi surfaces coupled to non-Abelian gauge fields [202, 203]; however these have been restricted to spatial dimension $d = 3$, where a RPA analysis

gives almost the complete answer. In spatial dimension $d = 2$ of interest to us here, we shall follow the approach taken for Abelian gauge theories [136, 153, 166] which uses a patch decomposition of the Fermi surface. The same approach transfers easily to the non-Abelian case; indeed because of the Landau damping of the gauge bosons, there is little difference between the Abelian and non-Abelian cases [197, 202, 203], as will also be clear from our analysis in Section 7.3.2.

Apart from their coupling to a SU(2) gauge field, the fermionic ψ_p particles are also coupled to a quantum critical Higgs field. This coupling is strongest at 8 'hot spots' around the Fermi surface, and in Section 7.3.2 we shall be able to use the methods developed from the case of a spin-density-wave transition of Fermi liquids [1, 154, 133, 227]

Some of the details of the computations appear in Appendix F.2.

Fermi-surface coupled to gauge-field

Here we describe the low energy theory of the SU(2) ACL, away from the Higgs condensation at the QCP. We need only consider a SU(2) gauge field coupled to the large Fermi surface of the ψ_p fermions. As in the U(1) case [136, 153, 166], we can make a patch decomposition of the Fermi surface, and treat antipodal pairs of patches separately. For a single pair of antipodal patches, we have the fermions $\psi_{\pm p}$ (see Fig. 7.4), with $\pm$ the patch index, and p the usual SU(2) gauge index. This is coupled to the transverse components of the SU(2) gauge field, $\mathbf{A}^a$.

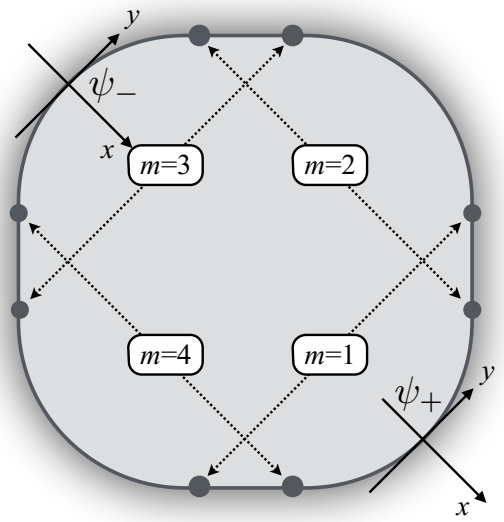

Figure 7.4: The shaded grey regions represent the occupied states. The transverse gauge-field fluctuations couple strongly to the flavor current arising from the $\psi_\pm$ patches and destroy the Landau quasiparticles all around the Fermi-surface. Across the Higgs transition, the fluctuations of the H^a field couple most strongly to the four-pairs ($m = 1, .., 4$) of "hot-spots", shown as the filled circles.

$$\begin{aligned} L &= L_f + L_{\mathbf{A}} + L_{\rm int}, \\ L_f &= \psi^\dagger_{+p}(\partial_\tau - i\partial_x - \partial_y^2)\psi_{+p} + \psi^\dagger_{-p}(\partial_\tau + i\partial_x - \partial_y^2)\psi_{-p}, \\ L_{\mathbf{A}} &= \frac{1}{2e^2}(\partial_y A^a_x)^2, \\ L_{\rm int} &= A^a_x(\psi^\dagger_{+p}\,\sigma^a_{pp'}\,\psi_{+p'} - \psi^\dagger_{-p}\,\sigma^a_{pp'}\,\psi_{-p'}) \end{aligned} \tag{7.21}$$

Let us review the one-loop renormalization of the gauge and fermionic matter fields. We start by looking at the self-energy of the gauge-field due to the particle-hole bubble (Fig. 7.5a). We have,

$$\Pi^{\mathbf{A}}_0(q) = 2\sum_s \int \frac{d\ell_\tau d^2\boldsymbol{\ell}}{(2\pi)^3}\; G^0_s(\ell)\; G^0_s(\ell+q), \tag{7.22}$$

where $\ell = (\ell_\tau, \boldsymbol{\ell})$ and the bare fermionic propagator is given by,

$$G_s^0(\ell) = \frac{1}{-i\ell_\tau + s\ell_x + \ell_y^2}. \tag{7.23}$$

The final result is of the form[4],

$$\Pi_0^{\mathbf{A}}(q) = c_b \frac{|q_\tau|}{|q_y|}, \quad \text{where } c_b = \frac{1}{2\pi}. \tag{7.24}$$

The computations are summarized in Appendix F.2.1.

Figure 7.5: One loop contributions to the (a) gauge-field, and, (b) Fermion self-energies. Curly lines represent the $\mathbf{A}$ propagators, $D(\ell)$, while solid lines represent the ψ propagators, $G(\ell)$.

Computing the fermionic self-energy due to the bosonic-propagator dressed with the RPA level polarization bubble (Fig. 7.5b) leads to,

$$\begin{aligned} \Sigma_{s,pp'}(k) &= -\sigma^a_{p\alpha}\sigma^a_{\alpha p'} \int \frac{d\ell_\tau d^2\boldsymbol{\ell}}{(2\pi)^3}\, D(\ell)\, G_s^0(k-\ell), & (7.25)\\ &= -3\, \delta_{pp'} \int \frac{d\ell_\tau d^2\boldsymbol{\ell}}{(2\pi)^3}\, D(\ell)\, G_s^0(k-\ell), & (7.26) \end{aligned}$$

where $D(\ell)$ is the gauge-field propagator,

$$D^{-1}(\ell) = \left(c_b \frac{|\ell_\tau|}{|\ell_y|} + \frac{1}{e^2}\ell_y^2 \right). \tag{7.27}$$

[4]We note that since the fermions are strictly in two-dimensions, the non-universal factor of Λ, the UV cutoff, drops out. The factor that appears in general is of the form Λ^{d-2}, where d is the number of space-dimensions.

We then obtain,

$$\Sigma_s(k) = -\frac{3i}{2}\int \frac{d\ell_\tau d\ell_y}{(2\pi)^2}\frac{\mathrm{sgn}(k_\tau-\ell_\tau)}{c_b|\ell_\tau|/|\ell_y|+\ell_y^2/e^2}, \tag{7.28}$$

$$\Sigma_s(k) = -ic_f\ \mathrm{sgn}(k_\tau)|k_\tau|^{2/3}, \quad \text{where } c_f = 2\sqrt{3}\left(\frac{e^2}{4\pi}\right)^{2/3}. \tag{7.29}$$

This self-energy contribution is more singular than the bare ∂_τ term. Therefore, upon including the RPA contribution into the fermionic propagator, we have,

$$G_s(\ell) = \frac{1}{-ic_f\mathrm{sgn}(\ell_\tau)\ |\ell_\tau|^{2/3}+s\ell_x+\ell_y^2}, \tag{7.30}$$

which is the well known result for the quasiparticles being damped all along the Fermi-surface.

Higgs criticality at the QCP

Now we consider the QCP at which the Higgs boson condensed from the non-Fermi liquid SU(2) ACL state described in the previous subsection. Across this Higgs transition from the SU(2) ACL to the U(1) ACL, the Fermi-surface gets reconstructed—this is controlled by the real Higgs field, H^a, which carries lattice momentum, $\boldsymbol{K} = (\pi, \pi)$. By the same arguments used for the onset of spin-density-wave order in a Fermi liquid [1, 154, 133, 227], the low energy physics of the QCP is dominated by the vicinity of the hot-spots: these are points on the Fermi surface which are connected by $\boldsymbol{K}$ (see Fig. 7.4). The computation for the present non-Fermi liquid Fermi surface proceeds just as for the Fermi liquid case, by linearizing the bare dispersion for the fermions

around the hot spots:

$$L = L_{hs} + L_H + L_{fH}, \tag{7.31}$$

$$L_{hs} = \psi_{1p}^{\dagger m}(\partial_\tau - i\boldsymbol{v}_1^m \cdot \nabla)\psi_{1p}^m + \psi_{2p}^{\dagger m}(\partial_\tau - i\boldsymbol{v}_2^m \cdot \nabla)\psi_{2p}^m, \tag{7.32}$$

$$L_{fH} = \frac{1}{\sqrt{N_f}} H^a \cdot (\psi_{1p}^{\dagger m}\sigma_{pp'}^a \psi_{2p'}^m + \psi_{2p}^{\dagger m}\sigma_{pp'}^a \psi_{1p'}^m), \tag{7.33}$$

where L_H already appeared in Eq. (7.7); m is the hot-spot pair index (Fig. 7.4).

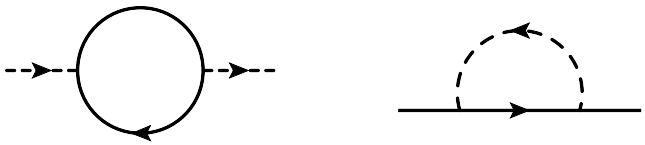

Figure 7.6: One loop contributions to the (a) Higgs-field, and, (b) Fermion self-energies. The dashed lines represent the Higgs' field propagator, χ.

Let us first look at the one-loop self energy of the H^a field (Fig. 7.6a). This is given by,

$$\Pi^H(q) = 2\sum_m \int \frac{d\ell_\tau d^2\boldsymbol{\ell}}{(2\pi)^3}\Big[G_1^m(\ell+q)G_2^m(\ell) + G_2^m(\ell+q)G_1^m(\ell)\Big], \tag{7.34}$$

where we now use the non-Fermi liquid fermion Green's function renormalized by the gauge field fluctuations, as discussed in earlier:

$$G_\alpha^m(\ell) = \frac{1}{-ic_f \mathrm{sgn}(\ell_\tau)|\ell_\tau|^{2/3} - \boldsymbol{v}_\alpha \cdot \boldsymbol{\ell}}. \tag{7.35}$$

Note the $z = 3/2$ scaling of the fermion self energy, which allows us to drop the bare frequency dependence from above ($\sim \partial_\tau$).

Upon including contributions from all pairs of hot-spots, we obtain (see Appendix F.2.2),

$$\Pi^H(q) = \Pi^H(q=0) + \gamma|q_\tau|, \quad \text{where } \gamma = \frac{n}{2\pi v_x v_y}, \tag{7.36}$$

where $n = 4$ is the number of pairs of hot spots. Note that the c_f dependence has completely dropped out and the above result is precisely the expression that we would have obtained if we had started with the bare fermion Green's functions (or, any anomalous power $\sim |\ell_\tau|^\beta$). This result is not surprising—it just reproduces the "Landau-damped" form of the propagator for H^a. As we know, the only requirement for the appearance of Landau-damping is the existence of particle-hole excitations around the Fermi-surface in the limit of $\omega \to 0$. In the general case, this always leads to $\sim |q_\tau|/|q_y|$ for a bosonic order-parameter coupled to a fermion-bilinear. When the order parameter itself carries a finite momentum $\boldsymbol{K}$, as is the case here, then the denominator in the damping term gets cut off and leads to $\sim |q_\tau|$.

Equipped with the above expression, let us now compute the self-energy of the fermions in the vicinity of the hot-spots (Fig. 7.6b),

$$\Sigma_{1,pp'}(p) = \sigma^a_{p\alpha}\sigma^a_{\alpha p'} \int \frac{d\ell_\tau d^2\boldsymbol{\ell}}{(2\pi)^3} G_2(p-\ell)\chi(\ell), \tag{7.37}$$

$$= 3\delta_{pp'} \int \frac{d\ell_\tau d^2\boldsymbol{\ell}}{(2\pi)^3} G_2(p-\ell)\chi(\ell), \tag{7.38}$$

where the propagator tuned to the critical point ($s = 0$) is given by : $\chi^{-1}(\ell) = (\gamma|\ell_\tau| + \boldsymbol{\ell}^2)$.

We are interested in the singular power law frequency dependence of the self-energy at the hot-spots. For future use, it is useful to express the Green's function in

Eq. (7.35) in the more general form

$$G^m_\alpha(\ell) = \frac{1}{-i\zeta_f \mathrm{sgn}(\ell_\tau)|\ell_\tau|^\beta - \boldsymbol{v}_\alpha \cdot \boldsymbol{\ell}}, \tag{7.39}$$

where the exponent $\beta = 2/3$ from the coupling to the SU(2) gauge field.

Upon evaluating the momentum integrals, the self-energy (for $\boldsymbol{p} = 0$) becomes (see Appendix F.2.3),

$$\Sigma_1(p_\tau) = 3i \int \frac{d\ell_\tau}{4\pi^2} \tan^{-1}\left(\frac{\sqrt{\gamma v_2^2|\ell_\tau| - \zeta_f^2|p_\tau - \ell_\tau|^{2\beta}}}{\zeta_f|p_\tau - \ell_\tau|^\beta}\right) \frac{\mathrm{sgn}(\ell_\tau - p_\tau)}{\sqrt{v_2^2\gamma|\ell_\tau| - \zeta_f^2|p_\tau - \ell_\tau|^{2\beta}}}, \tag{7.40}$$

which correctly reproduces $\Sigma_1(p_\tau = 0) = 0$. Furthermore, note that if $\zeta_f = 0$, i.e. if the anomalous self-energy contribution were to be absent, then the above reduces to the well known form [154]

$$\Sigma_1(p_\tau) = 3i \int \frac{d\ell_\tau}{8\pi} \frac{\mathrm{sgn}(\ell_\tau - p_\tau)}{\sqrt{v_2^2\gamma|\ell_\tau|}} = -\frac{3i}{2\pi\sqrt{\gamma v_2^2}} \mathrm{sgn}(p_\tau)\sqrt{|p_\tau|}, \tag{7.41}$$

reproducing the $z = 2$ result. Let us now proceed to evaluate the expression in the presence of a finite ζ_f. Rescaling $\ell_\tau = x p_\tau$ leads to,

$$\begin{aligned}\Sigma_1(p_\tau) = &\frac{3i}{2\pi\sqrt{\gamma v_2^2}} \mathrm{sgn}(p_\tau)|p_\tau|^{1-\beta} \\ &\times \int \frac{dx}{2\pi} \tan^{-1}\left(\frac{\sqrt{|p_\tau|^{1-2\beta}|x| - c|1-x|^{2\beta}}}{\sqrt{c}|1-x|^\beta}\right) \frac{\mathrm{sgn}(x-1)}{\sqrt{|p_\tau|^{1-2\beta}|x| - c|1-x|^{2\beta}}},\end{aligned} \tag{7.42}$$

where the dimensionless parameter, $c = \zeta_f^2/\gamma v_2^2$. An asymptotic analysis of Eq. (7.42) shows that

$$\Sigma_1(|p_\tau| \to 0) \sim -i\,\mathrm{sgn}(p_\tau)\,\sqrt{|p_\tau|} \quad , \quad \text{for } \beta \geq 1/2. \tag{7.43}$$

So the low energy singularity of the self-energy is *independent* of the non-Fermi liquid exponent β in the fermion Green's function, and has the same value as in the spin

density wave case without the gauge field. This is the key observation of the present subsection. To estimate the co-efficient, we can use a self-consistent approach in which we use a self energy in Eq. (7.39) with $\beta = 1/2$. This self-energy arises from the coupling to the Higgs field, and is always dominant over the one obtained from the gauge field with $\beta = 2/3$. Assembling all the constraints, the final expression takes the following $z = 2$ form

$$\Sigma_1(p_\tau) = \frac{3i}{2\pi\sqrt{\gamma v_2^2}}\, \mathcal{I}(c)\ \mathrm{sgn}(p_\tau)\sqrt{|p_\tau|}, \tag{7.44}$$

where the function $\mathcal{I}(c)$ is defined in Appendix F.2.4 and $\mathcal{I}(c \to 0) = -1$.

So we reach our main conclusion that, in both the fermionic and bosonic sectors, the low energy physics of the Higgs QCP is essentially identical to that of the spin-density-wave onset transition in a Fermi liquid. And the basic reason for this is simple. The hotspot theory has dynamic critical exponent $z = 2$, while the singularities arising from the SU(2) gauge field coupling around the Fermi surface have $z = 3/2$. At a given length scale, the contributions with the larger z dominate because they have a lower energy. Hence the Higgs criticality of a non-Fermi liquid maps onto the spin density wave criticality of a Fermi liquid.

With this conclusion in hand, we can now directly apply the results of Ref. [177] on the DC resistivity to the Higgs QCP. The approach of Ref. [177] requires that there is quasiparticle breakdown around the entire Fermi surface, and the fermionic excitations rapidly equilibriate with all the bosonic modes. While this was only marginally true for the spin-density-wave quantum critical point considered in Ref. [177], it is easily satisfied for the Higgs QCP being considered here: the SU(2) gauge field makes the entire Fermi surface "hot", while the Higgs field fluctuations induce additional

fermion damping at the hot spots on the Fermi surface. As in the previous case, it is possible for disorder to couple to the square of the Higgs field because such an operator is gauge-invariant, as we noted in Eq. (7.10). And the corresponding contribution to the resistivity is in Eq. (7.12). For the exponents $d = 2$, $z = 2$, and $\nu = 1/2$ presented above, this yields a linear-in-temperature results $\rho(T) \sim V_0^2 T$.

7.4 Discussion

The primary goal of this paper has been to propose a candidate theory for the quantum phase transition near optimal doping in the cuprates. We analyzed the QCP between metals with 'large' and 'small' Fermi-surfaces, which did not involve any broken global symmetries, but instead involved a Higgs' transition between metals with emergent SU(2) and U(1) gauge fields. The Higgs field acts as a measure of the local antiferromagnetic order in the rotating reference frame defined by Eq. (7.1). As we discussed in Sections 7.1 and 7.2, the symmetry broken phases observed in the underdoped cuprates arise as low temperature instabilities of the 'small' Fermi-surface metal.

The underlying QCP we studied was between two metals (the U(1) ACL and the SU(2) ACL) in which the Fermi surface excitations are coupled to emergent gauge fields, and so there are no Landau quasiparticles. However, electron-like quasiparticles do re-emerge around a small Fermi in the U(1)-FL*, and we will discuss similar features around the large Fermi surface in the SU(2) ACL below. The reconstruction to the 'small' Fermi-surface in the ACL phases is driven by the condensation of the Higgs field, and the Higgs critical point has additional singular structure in the vicinity

of the "hot-spots". The Higgs criticality has associated with it an interplay of both $z = 3/2$ physics on the whole Fermi-surface, and $z = 2$ physics in the vicinity of the hot-spots. We showed that near the Higgs QCP the $z = 2$ physics dominates, and hence many critical properties map onto the previously studied problem of the onset of spin density wave order in a Fermi liquid [1, 154, 133, 227, 177].

Let us now conclude with a discussion of the relationship of our proposed phase diagram in Fig. 7.2 to the experimentally obtained phase diagram in the non-La-based cuprates. The $d-$SC and $d-$BDW both arise as instabilities of the U(1) FL*, as has been discussed in Refs. [44, 162] (the SU(2) ACL is also unstable to superconductivity [152]). The high temperature pseudogap phase for $T^{**} < T < T^{*}$ is a U(1) ACL or more appropriately a *holon-hole* metal [115]. There is a crossover to the U(1) FL* phase at $T = T^{**}$, where all the holons have formed bound-states with the spinons. An important feature of the U(1) FL* phase is that its transport and photoemission signatures are mostly identical to those of a Fermi liquid. The primary difference from a Landau Fermi liquid is that the volume enclosed by the Fermi surface is proportional to the density of holes, x, and not to the Luttinger density $1 + x$. The U(1) FL* phase also has an emergent U(1) gauge field, as required by the topological arguments in Ref. [215], but the Fermi surface quasiparticles are gauge neutral. The recent remarkable observation of Fermi liquid transport properties in the pseudogap phase of Hg1201 [157, 38] below T^{**}, with some possibly non-Fermi liquid behavior between T^{**} and T^{*}, can therefore be viewed as strong support for the existence of a FL* derived out of a parent ACL. In particular, the alternative 'fluctuating order' picture of the pseudogap does not naturally lead to such temperature dependent

crossovers from non-Fermi liquid to Fermi liquid regimes.

For the La-based cuprates, there is a larger doping regime with magnetic order, overlapping with the regime of charge order. This can be accommodated in our phase diagram [44] by moving the full red arrow in Fig. 7.1 just to the other side of the point M, and allowing for incommensurate order as in Appendix F.1.

An important challenge for future experiments is to detect direct experimental signatures of the complete small Fermi surface of the proposed FL* phase. We presume that it is the small quasiparticle residue on the 'back side' of the small Fermi surface [184, 182] which is responsible for the arc-like features in the photoemission spectrum [253]. Therefore, we need a probe which does not involve adding or removing an electron from the sample, and so is not sensitive to the quasiparticle residue. Possibilities are Friedel oscillations, the Kohn anomaly, or ultrasonic attenuation.

Within our proposed phase diagram in Fig. 7.2, the strange metal phase is to be viewed as a SU(2) ACL at the Higgs critical point, and proximate to the multicritical point M to ensure the spin gap is smaller than T. The DC transport properties of this phase are controlled by the coupling of the gauge-invariant square of the Higgs field to *long* wavelength disorder, following an analysis of Ref. [177] for the spin density wave critical point. Such a coupling leads to a linear-in-temperature resistivity. Also, as emphasized in Ref. [177], the residual resistivity is proportional to *short* wavelength disorder which can scatter fermions across the Fermi surface. So there is no direct relationship between the residual resistivity and the slope of the linear resistivity. It would be interesting in future work to explore the role of intrinsic umklapp scattering events in the transport properties of such strange metals in the strong coupling regime.

The electron spectral function in the SU(2) ACL is a convolution of the spectra of the ψ fermions and the R bosons. As in the computation in Ref. [113], we assume the R spectrum is thermally overdamped, and the electron spectral function primarily reflects the ψ spectrum; we also expect precursors of the bound state formation between the ψ and the R to enhance the ψ features in the electron spectrum. Then the electron spectral functions should have an anisotropic structure around the Fermi surface, with the weaker gauge field-induced damping in the nodal region, and the stronger Higgs field-induced damping in the anti-nodal region. Also note that while the Higgs field coupling does show up in the resistivity as discussed above, the gauge fields coupling has a weaker effect on transport. This is because gauge-invariance prevents a non-derivative coupling between the gauge field and perturbations that violate momentum conversation. It would be interesting to explore in future work whether this rich theoretical structure can be made consistent with the complex experimental features of the conductivity and magnetotransport in the strange metal [106, 83, 32].

Our linear-T resistivity is proportional to disorder, as in the previous model in Ref. [177]. However, because the disorder couples to the Higgs field, the relevant disorder is long-wavelength. This is in contrast to short wavelength disorder, which can lead to efficient large momentum scattering of fermions around the Fermi surface. Modifying the coefficient of the resistivity therefore requires modifying long-wavelength disorder, and this may be difficult to do because of the intrinsic disorder from the dopant ions. Inducing short-wavelength disorder, by including *e.g.* Zn impurities, may not be effective in modifying the co-efficient of the linear-T resistivity.

These features can act as tests of our proposed mechanism for the resistivity of the strange metal [192].

Finally, we note from Figs. 7.2 and 7.3 that the SU(2) ACL survives for an extended region beyond the Higgs QCP. This implies strange metal behavior over a finite range of doping as $T \to 0$, and not only at a single QCP. Transport measurements [106] in magnetic fields which have suppressed superconductivity appear to be consistent with such a non-Fermi liquid phase.

Appendix A

Appendices for Chapter 2

A.1 Instabilities of the free energy

An interesting feature associated with the LG functional introduced in section 2.2 is that there is an instability to a state with modulated ψ. This arises due to a competition between two terms in the free energy, namely the ϕ and ϕ^2 terms. Let us suppose that ϕ does not vary spatially and $\psi = \beta e^{iqx}$. Then at leading order, the contribution to the free energy from ϕ is of the form

$$\mathcal{F}_\phi = \left(\frac{\gamma^2\beta^2}{2\gamma_s} - \frac{\gamma^2}{2\gamma_s^2}\right)\phi^2 + \lambda q^2\beta^2\phi. \tag{A.1}$$

From the above expression, we see that for a sufficiently large λq^2, it becomes energetically favorable to gain energy from the second term by condensing a large negative value of ϕ. By extremizing the above with respect to ϕ, we obtain $\phi_m = -\lambda\beta^2q^2/\left(\frac{\gamma^2\beta^2}{\gamma_s} - \frac{\gamma^2}{\gamma_s^2}\right)$. Hence, the contribution to free energy from ϕ_m is $\propto -\beta^2\lambda^2q^4$. This energy gain from a non-zero q always dominates over the energy cost of order q^2 for a sufficiently large q. In order to prevent this instability, we have to add a

term of the form $\zeta|\nabla^2\psi|^2/2l^4$ to the free energy, which is an allowed term from the underlying symmetry of the problem. We now want to obtain some restrictions on ζ. First of all, ζ should be such that it prevents the instability. This gives us a lower bound on the value of ζ. At the same time, ζ should be small enough so that it should not change the physics significantly. This gives us an upper bound on the value of ζ. Therefore, we obtain,

$$\frac{\lambda^2\gamma_s^2 l^4}{\gamma^2(\gamma_s-1)} < \zeta\ell 1 \tag{A.2}$$

The above expression is not valid when ϕ becomes critical, i.e. when $\gamma_s = 1, \beta = 1$. In this case, we have to compare ϕ with ϕ^4.

However, when we minimized the free energy in section 2.3.2, we did not have to include the above term with a finite ζ as for a sufficiently small λ, the cutoff in q arising from the discrete lattice prevented this instability from showing up.

A.2 Effect of boundary terms

In general, when we derive the GL equations from the free energy, there is a surface term arising from the gradient terms in the energy which can be ignored in the limit of an infinite system size. However, for a finite sized system, the boundary term does play an important role. Let us consider only the contribution of the gradient term of the superconducting order parameter in the free energy, in the absence of any nematic order. Then we have,

$$F_{grad} = \int d^2r|\nabla\psi|^2, \tag{A.3}$$

$$F_{tot} = F_{\text{grad}} + F_{\text{local}}, \tag{A.4}$$

where F_{local} contains the usual $|\psi|^2, |\psi|^4$ terms. On varying ψ^* by $\delta\psi^*$ in F_{tot}, we obtain for a finite system (up to other variations due to F_{local} denoted by ...),

$$-\int d^2r\delta\psi^*\nabla^2\psi + \int_{\text{surface}} \delta\psi^*(\nabla\psi)\cdot\hat{n}ds + ... = 0, \tag{A.5}$$

where $\hat{n}ds$ is the area element, normal to the boundary. When we solve for ψ in the interior of the region, only the first term contributes and the boundary term can be ignored. However, when we solve for ψ on the boundary, only the surface term plays a role, since it can be thought of as appearing with an infinite weight of the form $\int dr\delta(r-R)$ where R is the radius of the disk on which we are minimizing the free energy and $\delta(...)$ is the Dirac-delta function. Therefore, in order to solve for ψ, we have to solve for $-\nabla^2\psi + ... = 0$ in the interior of the region subject to the boundary condition $\nabla\psi\cdot\hat{n}|_{r=R} = 0$ (Neumann boundary conditions).

Now in the presence of a constant nematic background (ϕ_0), the gradient term in the free energy is,

$$F_{grad} = \int dxdy\Big[(1+\alpha)|\partial_x\psi|^2 + (1-\alpha)|\partial_y\psi|^2\Big], \tag{A.6}$$

where $\alpha = 2\lambda\phi_0 l^2$. As we did earlier, on carrying out the variation over ψ^* this amounts to solving for $-(1+\alpha)\partial_x^2\psi - (1-\alpha)\partial_y^2\psi + ... = 0$ subject to the boundary condition, $\tilde{D}\psi\cdot\hat{n} = 0$, where

$$\tilde{D}\psi = \Big((1+\alpha)\partial_x\psi, (1-\alpha)\partial_y\psi\Big), \quad \hat{n} = (\cos\theta, \sin\theta). \tag{A.7}$$

In polar coordinates, this condition can be written as,

$$\partial_r\psi + \alpha\Big[\cos 2\theta\partial_r\psi - \frac{\sin 2\theta}{r}\partial_\theta\psi\Big] = 0. \tag{A.8}$$

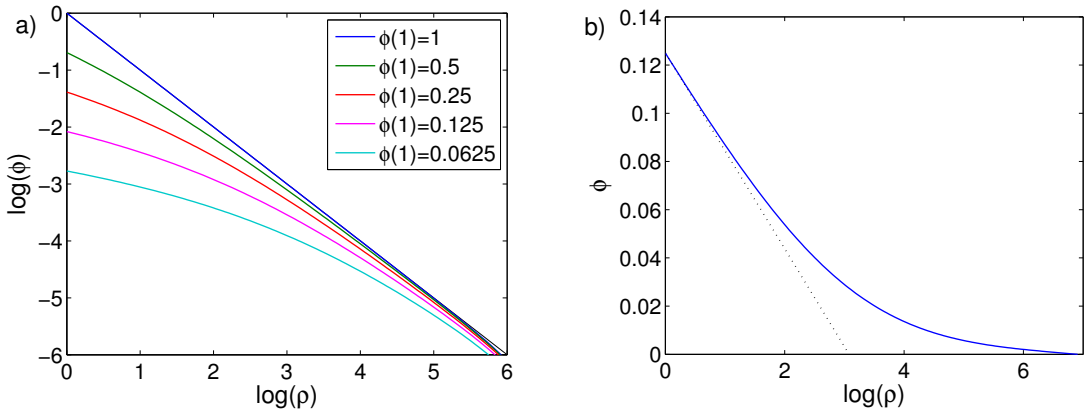

Figure A.1: Numerical solutions of Eq. A.9. a) Solutions with boundary conditions $\phi(1000) = 0$ and with various values of $\phi(1)$, on a log-log scale. b) Solution with boundary condition $\phi(1) = 0.125$, $\phi(1000) = 0$, on a semilog scale. The dashed line is a fit to the form $A + B\log(\rho)$ for small ρ.

These boundary conditions mean, in particular, that the current perpendicular to the boundary is zero. In our numerical calculations, we have used a disk geometry; therefore the boundaries are found to have a significant effect whenever we are considering a non-circularly symmetric solution, in particular in the regime where the nematic order is non-zero even far away from the core. We circumvent this problem, however, by taking a sufficiently large system and considering the solution only close to the vortex core, where the boundary effects are small.

A.3 Asymptotics of ϕ in the critical case

In this appendix, we analyze the asymptotics of the field ϕ far away from the vortex core in the case $\gamma_s = 1$, in which the nematic order is critical. In this case,

and for $\rho \gg 1$, the Landau-Ginzburg equation for ϕ (Eq. 2.14) becomes

$$\left[-\nabla_\rho^2 + \phi^2 \right] \phi = 0. \tag{A.9}$$

This non-linear equation admits the solution $\phi(\rho) = 1/\rho$ [124]. This solution is valid, however, for specific initial conditions, e.g., $\phi(1) = 1$, $\phi'(1) = -1$. Physically, the initial conditions for Eq. A.9 are determined by the details of the vortex profile at short distances, determined by Eq. 2.14. Nevertheless, one can make some general statements about the asymptotic behavior of the solution. If, for some arbitrary ρ_0 such that $\rho_0 \gg 1/l$ (far from the core), ϕ satisfies $\phi(\rho_0) \ell 1/\rho_0$, then it is justified to neglect the ϕ^2 term in Eq. A.9. Then, the solution close to ρ_0 behaves as $\phi(\rho) \approx A - B \ln(\rho/\rho_0)$, where A, B are determined by the initial conditions. This can only be valid, however, up to a point ρ_* at which $\phi(\rho_*) \approx 1/\rho_*$, i.e., at distances which are much smaller than the length scale set by the initial condition of Eq. A.9. At longer distances, we expect a crossover to $\phi(\rho) \approx 1/\rho$.

In Fig. A.1, we present a numerical solution of Eq. A.9 with boundary conditions $\phi(1000) = 0$ and various values for $\phi(1)$. When $\phi(1) = 1$, we get $\phi(\rho) \approx 1/\rho$ (where the deviations are due to the boundary condition at $\rho = 1000$). For smaller $\phi(1)$, there is an intermediate region where ϕ does not follow a power law, eventually crossing over to $1/\rho$ at larger ρ. $\phi(\rho)$ is approximately logarithmic in the intermediate region, as shown in Fig. A.1b.

Physically, we expect that $\phi < 1$ (since $\phi = 1$ corresponds to the equilibrium value of ϕ in the absence of superconductivity). Therefore, there is an intermediate logarithmic region, which becomes parametrically large in the limit of small ϕ.

Appendix B

Appendices for Chapter 3

B.1 Superfluid-density for one-band problem

In order to study the problem with just one-band with e.g. a cuprate-like Fermi surface, we can easily extend our formalism in chapter 3. Everything that we introduced for the two-orbital model goes through with the following modification, $f_2(\boldsymbol{k}) = f_1(\boldsymbol{k}+\boldsymbol{Q})$ (with $\boldsymbol{Q} = (\pi, \pi)$),where $f_a(...)$ denotes the momentum dependent functions such as the dispersions, velocities, gaps etc. of the orbitals. Moreover, $\Delta(\boldsymbol{k})$ is momentum dependent and has $d-$wave character.

B.2 Numerical computation of $\lambda_L^2(0)$

While computing $\lambda_L^2(0)$ numerically, we compute $\langle \boldsymbol{\varphi}^2 \rangle$ at the Gaussian level and on the lattice. The bare propagator for the SDW field is given by,

$$D^0(\mathbf{k}, i\omega_n) = \frac{1}{\omega_n^2/c^2 + [4 - 2\cos(k_x) - 2\cos(k_y)] + g - g_c^0}, \tag{B.1}$$

where we have set the lattice spacing to be unity. The bare propagator gets renormalized to $D(\boldsymbol{k}, i\omega_m) = 1/([D^0(\boldsymbol{k}, i\omega_m]^{-1} - \Pi(\boldsymbol{k}, i\omega_m))$, where $\Pi(\boldsymbol{k}, i\omega_m)$ is the polarization bubble due to the superconducting fermions. However the main effect of the gapped fermions is to shift the critical point, g_c^0, to a new location, $g_c = g_c^0 - \Pi(0,0)$, with some possible renormalization of the spin-wave velocity. Therefore, the functional form of the propagator of the SDW field remains identical to the bare propagator and we analyze the behavior of λ_L as a function of the distance away from the renormalized QCP, g_c.

B.3 Estimate of $\lambda_L^2(0)$ from Homes' law

As discussed in section 3.3.1, we compare the value of the penetration depth obtained from experiments [85] with the prediction from Homes' law; for the latter, we use a combination of the experimental data obtained from optical-conductivity and dc transport. For each value of the doping (x), we estimate the (approximate) dc resistivity (ρ_{xx}) by extrapolating the curves to $T = 0$, from the transport data in fig.1(b) of Ref.[112].

We estimate the value of 2Δ, where Δ is the superconducting gap, from the data for optical conductivity in the superconducting state, as shown in fig. 3(b) of Ref. [163]. Since T_c remains relatively unchanged as a function of x in the vicinity of optimal doping, we assume Δ to be independent of x such that $2\Delta \approx 150\text{cm}^{-1} (= 2.827 \times 10^{13}\text{s}^{-1})$. Then, in the dirty limit,

$$\rho_s = \frac{4}{\pi}\sigma_{\text{dc}}\Delta. \tag{B.2}$$

In order to obtain the penetration depth, we need to restore various dimensionful constants such that,

$$\lambda_L^2(0) = \frac{c^2 \varepsilon_0}{\rho_s}, \tag{B.3}$$

where $c(= 3 \times 10^8$ m/s) is the speed of light and $\varepsilon_0(= 8.85 \times 10^{-12}$ F/m; 1 F=1 Ω^{-1}s) is the permitivity of free space. The values obtained are shown in the table below and have been presented in fig. 3.6, along with a comparison to the experimental data [85].

x	ρ_{xx} (from Ref. [112]) ($\mu\Omega$ cm)	$\lambda_L^2(0)$ (μm^2)
0.23	130	0.057
0.27	120	0.053
0.33	35	0.015
0.41	20	0.009
0.56	15	0.007
0.64	10	0.004

Appendix C

Appendices for Chapter 4

C.1 Saddle point equations of the O(6) Model

In this section, we present some details associated with the saddle point equations of the O(6) model for fluctuating superconductivity and bond density wave, as introduced originally in Ref.[91] and in Eqn.4.4.

In order to solve for the temperature dependence of $\overline{\sigma}$, the saddle point equations must be regulated, and we employ a hard momentum cutoff $\boldsymbol{q}^2 < \Lambda^2$. We have

$$\begin{aligned} \frac{\rho_S}{T} &= \frac{1}{4\pi}\left[\log\left(\frac{\Lambda^2+\overline{\sigma}}{\overline{\sigma}}\right) + \frac{2}{\lambda}\log\left(\frac{\lambda\Lambda^2+\overline{\sigma}+g+\overline{\phi}}{\overline{\sigma}+g+\overline{\phi}}\right)\right], \\ \overline{\phi} &= \frac{wT}{2\pi\lambda\rho_S}\log\left(\frac{\lambda\Lambda^2+\overline{\sigma}+g+\overline{\phi}}{\overline{\sigma}+g+\overline{\phi}}\right). \end{aligned} \tag{C.1}$$

On dimensional grounds, the equations above are invariant under

$$\Lambda \mapsto b\,\Lambda \qquad\qquad (g,\bar{\sigma},\bar{\phi}) \mapsto b^2(g,\bar{\sigma},\bar{\phi})\,, \tag{C.2}$$

and $\overline{\phi}$ is non-zero only if $w \neq 0$. The universal function σ/Λ^2 for a few choice parameters and $w = 0$ is shown in supplementary fig. C.1.

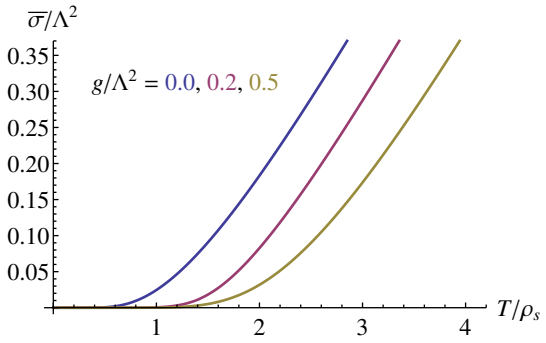

Figure C.1: Temperature dependence of $\overline{\sigma}/\Lambda^2$ obtained by solving (C.1) with $\lambda = 1.0$ and $w = 0$ for $g/\Lambda^2 = 0,\ 0.2,\ 0.5$.

C.2 Bosonic self-energy

Let us compute the frequency dependence that arises due to the coupling of Ψ and Φ to the underlying fermions. We want to evaluate the bubble diagrams of the type shown in supplementary fig. C.2.

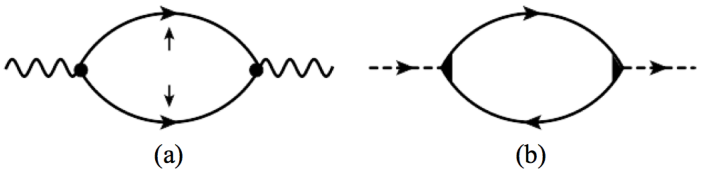

Figure C.2: The one-loop self-energy contribution to the (a) Cooper pair ($\Pi^{\rm s}$) and (b) Bond order ($\Pi^{\rm b}$) propagators after integrating out the fermions.

We start by evaluating the diagram in supplementary fig. C.2(a). It is given by,

$$\Pi^{\rm s}(\boldsymbol{q}, i\omega_n) = 2\int_{\boldsymbol{k}} \Delta_{\boldsymbol{k}}^2 \frac{1 - n_F(\epsilon_{\boldsymbol{k}+\boldsymbol{q}/2,\uparrow}) - n_F(\epsilon_{-\boldsymbol{k}+\boldsymbol{q}/2,\downarrow})}{i\omega_n - \epsilon_{\boldsymbol{k}+\boldsymbol{q}/2,\uparrow} - \epsilon_{-\boldsymbol{k}+\boldsymbol{q}/2,\downarrow}}, \tag{C.3}$$

where $i\omega_n$ is a bosonic Matsubara frequency. The leading contribution to this diagram comes from the quasiparticles in the vicinity of the antinodes, where $|\Delta_{\boldsymbol{k}}| \approx 2\Delta_0$ is maximum. Let us therefore analyze the behavior of $\Pi^{\rm s}$ at $\boldsymbol{q} = 0$ by expanding in the

vicinity of the antinodes. We can expand $\epsilon_{\boldsymbol{k}} = \boldsymbol{v}.\boldsymbol{k}$ where the Fermi velocities at the antipodal points are related by symmetry [45]. The imaginary part of the retarded bubble at real frequencies, ω ($i\omega_n \to \omega + i0^+$), then evaluates to,

$$\mathrm{Im}\Pi^{\mathrm{s}}_{\mathrm{R}}(\boldsymbol{q}=0,\omega) = \frac{8(2\Delta_0)^2}{4\pi v_x v_y}\int dxdy[1-2n_{\mathrm{F}}(x+y)]\delta(\omega-2(x+y)), \tag{C.4}$$

where $\boldsymbol{v}^2 = v_x^2 + v_y^2$ with $v_y > v_x$ and we have considered contributions from all the antinodal patches. By restricting ourselves to the region $|\boldsymbol{k}| < \Lambda$ and in the small frequency regime ($\omega < T << v\Lambda$),

$$\mathrm{Im}\Pi^{\mathrm{s}}_{\mathrm{R}}(\boldsymbol{q}=0,\omega) = \frac{32\Delta_0^2\Lambda}{4\pi v_y}\tanh\left(\frac{\omega}{4T}\right) \approx \frac{2\Delta_0\Lambda}{\pi v_y}\,\omega, \tag{C.5}$$

where we have used the fact that at low temperatures, the $1/T$ behavior gets cutoff by Δ_0. The linear dependence on ω implies a Landau damped form in the propagator, which gives rise to many of the interesting features at low energies.

Similarly, we can compute the diagram in supplementary figure C.2 (b). In the low energy limit, we would like to evaluate the bubble due to the fermions in the antinodal regions that are nested by the CDW wavevector, $\boldsymbol{Q}_i$. The Fermi velocities at two such points in the vicinity of $(\pi, 0)$ are given by $\boldsymbol{v}_1 = (v_x, v_y)$ and $\boldsymbol{v}_2 = (v_x, -v_y)$. The expression for the particle-hole bubble is given by the standard Lindhard-type form,

$$\Pi^{\mathrm{b}}(\boldsymbol{q}, i\omega_n) = -2\int_{\boldsymbol{k}} P^{i2}_{\boldsymbol{k}}\frac{n_{\mathrm{F}}(\epsilon_{\boldsymbol{k}-\boldsymbol{q}/2}|_1) - n_{\mathrm{F}}(\epsilon_{\boldsymbol{k}+\boldsymbol{q}/2,2}|_2)}{i\omega_n + \epsilon_{\boldsymbol{k}-\boldsymbol{q}/2}|_1 - \epsilon_{\boldsymbol{k}+\boldsymbol{q}/2}|_2}, \tag{C.6}$$

where $\epsilon_{\boldsymbol{k}}|_1 = v_x k_x + v_y k_y$ and, $\epsilon_{\boldsymbol{k}}|_2 = v_1 k_x - v_2 k_y$. In the antinodal region, $|P^i_{\boldsymbol{k}}| \approx 2P^i_0$ and ω_n is a bosonic Matsubara frequency. The imaginary part of the retarded bubble, $\mathrm{Im}\Pi^{\mathrm{b}}_{\mathrm{R}}(\boldsymbol{q}=0,\omega)$ at a real frequency ω and evaluated at $T=0$ is given by,

$$\mathrm{Im}\Pi^{\mathrm{b}}_{\mathrm{R}}(\boldsymbol{q}=0,\omega) = -\frac{2(2P^i_0)^2}{4\pi^2 v_x v_y}\int dxdy\ [\theta(-x-y)-\theta(y-x)]\delta(\omega+2y), \tag{C.7}$$

where $\theta(...)$ represents the Heaviside step function.

In the limit of small frequencies, $\omega < v_x\Lambda << v_y\Lambda$, the above evaluates to,

$$\mathrm{Im}\Pi^{\mathrm{b}}_{\mathrm{R}}(\boldsymbol{q}=0,\omega) = \frac{(2P^i_0)^2}{4\pi^2 v_x v_y}\,\omega, \tag{C.8}$$

which is once again a sign of the BDW propagator having a Landau damping term at low energies.

C.3 Real and imaginary part of Fermion self-energy

It is possible to evaluate the sum over n in the expression for $H_0(\omega,\epsilon)$ in Eqn.4.13 analytically. We obtain

$$H_0(\omega,\epsilon) = -\frac{T}{\omega\epsilon} - \frac{\omega\,\psi\left(\frac{\epsilon}{2\pi T}\right)}{\pi(\epsilon^2+\omega^2)} + \mathrm{Re}\left[\frac{\psi\left(\frac{\mathrm{i}\omega}{2\pi T}\right)}{\pi(\omega+\mathrm{i}\epsilon)}\right], \tag{C.9}$$

where $\psi(z) \equiv \Gamma'(z)/\Gamma(z)$ is the digamma function.

The real part and imaginary parts of the self energies have the explicit expression

$$\begin{aligned}
\mathrm{Re}\Sigma^{\mathrm{R}}_{\mathrm{s}}(\boldsymbol{k},\omega) &= \int_{\boldsymbol{q}} \Delta^2_{\boldsymbol{k}-\frac{\boldsymbol{q}}{2}}\Big[H_0(-\omega-\epsilon_{-\boldsymbol{k}+\boldsymbol{q}},\epsilon_{\mathrm{s}}(\boldsymbol{q})) \\
&\quad +[n_{\mathrm{F}}(\epsilon_{-\boldsymbol{k}+\boldsymbol{q}}) + n_{\mathrm{B}}(\epsilon_{-\boldsymbol{k}+\boldsymbol{q}}+\omega)]\;\frac{\epsilon_{\mathrm{s}}(\boldsymbol{q})}{(\omega+\epsilon_{-\boldsymbol{k}+\boldsymbol{q}})^2+(\epsilon_{\mathrm{s}}(\boldsymbol{q}))^2}\Big] \\
\mathrm{Re}\Sigma^{\mathrm{R}}_{\mathrm{b}}(\boldsymbol{k},\omega) &= \int_{\boldsymbol{q}} P^{i2}_{\boldsymbol{k}+\frac{\boldsymbol{q}}{2}}\Big[H_0(\omega-\epsilon_{\boldsymbol{k}+\boldsymbol{q}},\epsilon_{\mathrm{b}}(\boldsymbol{q})) \\
&\quad +[n_{\mathrm{F}}(\epsilon_{\boldsymbol{k}+\boldsymbol{q}}) + n_{\mathrm{B}}(\epsilon_{\boldsymbol{k}+\boldsymbol{q}}-\omega)]\;\frac{\epsilon_{\mathrm{b}}(\boldsymbol{q})}{(\omega-\epsilon_{\boldsymbol{k}+\boldsymbol{q}})^2+(\epsilon_{\mathrm{b}}(\boldsymbol{q}))^2}\Big],
\end{aligned} \tag{C.10}$$

$$\mathrm{Im}\Sigma^{\mathrm{R}}_{\mathrm{s}}(\boldsymbol{k},\omega) = \int_{\boldsymbol{q}} \Delta^2_{\boldsymbol{k}-\frac{\boldsymbol{q}}{2}}\;[n_{\mathrm{F}}(\epsilon_{-\boldsymbol{k}+\boldsymbol{q}}) + n_{\mathrm{B}}(\epsilon_{-\boldsymbol{k}+\boldsymbol{q}}+\omega)]\;\frac{\omega+\epsilon_{-\boldsymbol{k}+\boldsymbol{q}}}{(\omega+\epsilon_{-\boldsymbol{k}+\boldsymbol{q}})^2+(\epsilon_{\mathrm{s}}(\boldsymbol{q}))^2}, \tag{C.11}$$

$$\mathrm{Im}\Sigma^{\mathrm{R}}_{\mathrm{b}}(\boldsymbol{k},\omega) = \int_{\boldsymbol{q}} P^{i2}_{\boldsymbol{k}+\frac{\boldsymbol{q}}{2}}\;[n_{\mathrm{F}}(\epsilon_{\boldsymbol{k}+\boldsymbol{q}}) + n_{\mathrm{B}}(\epsilon_{\boldsymbol{q}+\boldsymbol{k}}-\omega)]\;\frac{\omega-\epsilon_{\boldsymbol{k}+\boldsymbol{q}}}{(\omega-\epsilon_{\boldsymbol{k}+\boldsymbol{q}})^2+(\epsilon_{\mathrm{b}}(\boldsymbol{q}))^2}. \tag{C.12}$$

Appendix D

Appendices for Chapter 5

D.1 Feynman diagrams for linearized hot-spot theory

In this appendix, we provide details of the calculations for some of the loop-integrals evaluated earlier. The momentum integrals will all be done with a cutoff Λ, since we only want to restrict ourselves to the neighborhood of the hot-spots. We start with the diagrams that contribute to u_a,

$$I_{2525} = -\frac{T}{2}\sum_m \int_{|\boldsymbol{k}|<\Lambda} \frac{1}{(i\omega_m - (v_x k_x - v_y k_y))^2}\frac{1}{(i\omega_m - (-v_x k_x - v_y k_y))^2}, \quad \text{(D.1)}$$

$$I_{1212} = -\frac{T}{2}\sum_m \int_{|\boldsymbol{k}|<\Lambda} \frac{1}{(i\omega_m - (v_x k_x + v_y k_y))^2}\frac{1}{(i\omega_m - (v_x k_x - v_y k_y))^2}. \quad \text{(D.2)}$$

It is useful to change the coordinates to $x = v_x k_x$, $y = v_y k_y$ so that $\Lambda_{x,y} = \Lambda v_{x,y}$. We are in the regime where $\Lambda_y \gg \Lambda_x \gg T$. The above integrals then become,

$$I_{2525} = -\frac{T}{8\pi^2 v_x v_y} \sum_m \int_{-\Lambda_x}^{\Lambda_x} dx \int_{-\Lambda_y}^{\Lambda_y} dy \, \frac{1}{(i\omega_m - x + y)^2} \frac{1}{(i\omega_m + x + y)^2}, \quad \text{(D.3)}$$

$$I_{1212} = -\frac{T}{8\pi^2 v_x v_y} \sum_m \int_{-\Lambda_x}^{\Lambda_x} dx \int_{-\Lambda_y}^{\Lambda_y} dy \, \frac{1}{(i\omega_m - x - y)^2} \frac{1}{(i\omega_m - x + y)^2}. \quad \text{(D.4)}$$

We shall always evaluate the k_y integral first and use $\int_{-\Lambda_y}^{\Lambda_y} dk_y = \int_{-\infty}^{\infty} dk_y - \int_{|k_y|>\Lambda_y} dk_y = \mathcal{I}_1 - \mathcal{I}_2$.

The contribution to I_{2525} from $\mathcal{I}_1$, i.e. $I_{2525}\Big|_1 = 0$ (poles on same side). From $\mathcal{I}_2$, we get,

$$I_{2525}\Big|_2 \approx \frac{T\Lambda_x}{4\pi^2 v_x v_y} \sum_m \int_{\Lambda_y}^{\infty} dy \left[\frac{1}{(y + i\omega_m)^4} + \frac{1}{(y - i\omega_m)^4} \right] = 0 \quad \text{(D.5)}$$

Therefore, we have $I_{2525} = 0$. For I_{1212}, we get,

$$\begin{aligned} I_{1212}\Big|_1 &= -\frac{iT}{16\pi v_x v_y} \sum_m \mathrm{sgn}(\omega_m) \int_{-\Lambda_x}^{\Lambda_x} \frac{dx}{(x - i\omega_m)^3} \\ &= -\frac{T}{8\pi v_x v_y} \int_{-\Lambda_x}^{\Lambda_x} dx \sum_{m>0} \frac{\omega_m^3 - 3x^2\omega_m}{(\omega_m^2 + x^2)^3} \\ &= -\frac{\Lambda_x T}{4\pi v_x v_y} \sum_{m>0} \frac{\omega_m}{(\omega_m^2 + \Lambda_x^2)^2} \approx -\frac{1}{16\pi^2 v_x v_y} \frac{\Lambda_x}{\Lambda_x^2 + \pi^2 T^2}. \quad \text{(D.6)} \end{aligned}$$

$$I_{1212}\Big|_2 \approx -\frac{T\Lambda_x}{2\pi^2 v_x v_y} \sum_m \int_{\Lambda_y}^{\infty} dy \, \frac{1}{(y^2 + \omega^2)^2} \approx -\frac{1}{16\pi^2 v_x v_y} \frac{\Lambda_x}{\Lambda_y^2}. \quad \text{(D.7)}$$

Since $\Lambda_y \gg \Lambda_x$, we can ignore the second contribution and $I_{1212} \approx I_{1212}\Big|_1$. Note that we have made the approximation, $T\sum_{m>0} F(\omega_m) \approx \int_{\pi T}^{\infty} \frac{d\omega}{2\pi} F(\omega)$.

Similarly, we have the following contributions to w_a,

$$I_{2565} = -T\sum_m \int_{|\boldsymbol{k}|<\Lambda} \frac{1}{(i\omega_m + v_x k_x + v_y k_y)^2}\frac{1}{(i\omega_m - v_x k_x + v_y k_y)}\frac{1}{(i\omega_m + v_x k_x - v_y k_y)}, \tag{D.8}$$

$$I_{1256} = -T\sum_m \int_{|\boldsymbol{k}|<\Lambda} \frac{1}{(i\omega_m - v_x k_x - v_y k_y)}\frac{1}{(i\omega_m - v_x k_x + v_y k_y)} \frac{1}{(i\omega_m + v_x k_x + v_y k_y)}\frac{1}{(i\omega_m + v_x k_x - v_y k_y)}. \tag{D.9}$$

Then,

$$I_{2565} = -\frac{T}{4\pi^2 v_x v_y}\sum_m \int_{-\Lambda_x}^{\Lambda_x} dx \int_{-\Lambda_y}^{\Lambda_y} dy \frac{1}{(i\omega_m + x + y)^2}\frac{1}{(i\omega_m - x + y)} \frac{1}{(i\omega_m + x - y)}, \tag{D.10}$$

$$I_{2565}\Big|_1 = \frac{T}{16\pi v_x v_y}\sum_m \int_{-\Lambda_x}^{\Lambda_x} dx \frac{\mathrm{sgn}(\omega_m)}{\omega_m}\frac{1}{(x+i\omega_m)^2} \approx -\frac{1}{8\pi^2 v_x v_y \Lambda_x}\log\left(\frac{\Lambda_x}{\pi T}\right), \tag{D.11}$$

$$I_{2565}\Big|_2 \approx \frac{\Lambda_x T}{2\pi^2 v_x v_y}\sum_m \int_{|y|>\Lambda_y} \frac{1}{(i\omega_m + y)^2}\frac{1}{y^2+\omega_m^2}$$

$$\approx \frac{\Lambda_x}{4\pi^3 v_x v_y}\int_{-\infty}^{\infty} d\omega \int_{\Lambda_y}^{\infty} dy \frac{2(y^2-\omega^2)}{(y^2+\omega^2)^3}, \tag{D.12}$$

$$I_{2565}\Big|_2 \approx \frac{1}{16\pi^2 v_x v_y}\frac{\Lambda_x}{\Lambda_y^2}. \tag{D.13}$$

Therefore, we can approximate $I_{2565} \approx I_{2565}\Big|_1$. Similarly, we have,

$$I_{1256} = -\frac{T}{4\pi^2 v_x v_y}\sum_m \int_{-\Lambda_x}^{\Lambda_x} dx \int_{-\Lambda_y}^{\Lambda_y} dy \frac{1}{(i\omega_m - x - y)}\frac{1}{(i\omega_m - x + y)} \frac{1}{(i\omega_m + x + y)}\frac{1}{(i\omega_m + x - y)}, \tag{D.14}$$

$$I_{1256}\Big|_1 = -\frac{T}{8\pi v_x v_y}\sum_m \int_{-\Lambda_x}^{\Lambda_x} dx \frac{\mathrm{sgn}(\omega_m)}{\omega_m}\frac{1}{\omega_m^2 + x^2}. \tag{D.15}$$

The above integral is convergent in the limit of $\Lambda_x \to \infty$ (and the singularity comes

from small momenta), so that,

$$I_{1256}\Big|_1 = -\frac{1}{4\pi^2 v_x v_y T}\sum_{m>0}\frac{1}{(2m+1)^2} = -\frac{1}{32 v_x v_y T}. \tag{D.16}$$

The other contribution is given by,

$$I_{1256}\Big|_2 = -\frac{T\Lambda_x}{2\pi^2 v_x v_y}\sum_m \int_{|y|>\Lambda_y} dy\ \frac{1}{(y^2+\omega_m^2)^2} = -\frac{\Lambda_x}{8\pi^2 v_x v_y \Lambda_y^2}. \tag{D.17}$$

Let us now compute the diagram(s) contributing to u_b. They are given by,

$$J_{1515} = -\frac{T}{2}\sum_m \int_{|\boldsymbol{k}|<\Lambda} \frac{1}{(i\omega_m - v_x k_x - v_y k_y)^2}\frac{1}{(i\omega_m + v_x k_x + v_y k_y)^2}. \tag{D.18}$$

This simplifies to,

$$J_{1515} = -\frac{T}{8\pi^2 v_x v_y}\sum_m \int_{-\Lambda_x}^{\Lambda_x} dx \int_{-\Lambda_y}^{\Lambda_y} dy \frac{1}{(i\omega_m - x - y)^2}\frac{1}{(i\omega_m + x + y)^2}, \tag{D.19}$$

$$J_{1515}\Big|_1 = -\frac{T\Lambda_x}{8\pi v_x v_y}\sum_m \frac{\mathrm{sgn}(\omega_m)}{\omega_m^3}, \tag{D.20}$$

$$J_{1515}\Big|_1 = -\frac{7\zeta(3)}{32\pi^4}\frac{\Lambda}{v_y T^2}, \tag{D.21}$$

The contribution from $\mathcal{I}_2$ turns out to be $J_{1515}\Big|_2 = I_{1212}\Big|_2$ and can therefore be ignored, compared to $J_{1515}\Big|_1$.

We now evaluate the contribution to the terms that lead to competition between

the different BO, via the 4-point couplings, u_{ab} and $\overline{u}_{ab}$.

$$K_{1626} = -T\sum_m \int_{|\boldsymbol{k}|<\Lambda} \frac{1}{(i\omega_m + v_x k_x - v_y k_y)^2}\frac{1}{(i\omega_m - v_x k_x + v_y k_y)} \frac{1}{(i\omega_m - v_x k_x - v_y k_y)}, \tag{D.22}$$

$$K_{6515} = -T\sum_m \int_{|\boldsymbol{k}|<\Lambda} \frac{1}{(i\omega_m + v_x k_x + v_y k_y)^2}\frac{1}{(i\omega_m - v_x k_x - v_y k_y)} \frac{1}{(i\omega_m + v_x k_x - v_y k_y)}, \tag{D.23}$$

$$L_{2516} = -T\sum_m \int_{|\boldsymbol{k}|<\Lambda} \frac{1}{(i\omega_m - v_x k_x - v_y k_y)}\frac{1}{(i\omega_m - v_x k_x + v_y k_y)}\frac{1}{(i\omega_m + v_x k_x + v_y k_y)} \frac{1}{(i\omega_m + v_x k_x - v_y k_y)}. \tag{D.24}$$

It is straightforward to see that $K_{1626} = -M_{2515}$, $K_{6515} = -M_{1262}$, and $L_{2516} = N_{2651}(= I_{1256})$ which we evaluate in detail below.

Let us now evaluate the terms contributing to the competition terms, s_a and s_b, between CDW and SC. We start with the distinct self-energy type diagrams contributing to s_a,

$$M_{2515} = -T\sum_m \int_{|\boldsymbol{k}|<\Lambda} \frac{1}{(i\omega_m + v_x k_x + v_y k_y)^2}\frac{1}{(i\omega_m - v_x k_x + v_y k_y)} \frac{1}{(-i\omega_m + v_x k_x + v_y k_y)}, \tag{D.25}$$

$$M_{1262} = -T\sum_m \int_{|\boldsymbol{k}|<\Lambda} \frac{1}{(i\omega_m - v_x k_x + v_y k_y)^2}\frac{1}{(i\omega_m - v_x k_x - v_y k_y)} \frac{1}{(-i\omega_m - v_x k_x + v_y k_y)}. \tag{D.26}$$

Transforming to the $x, y-$coordinates, this becomes,

$$M_{2515} = -\frac{T}{4\pi^2 v_x v_y}\sum_m \int_{-\Lambda_x}^{\Lambda_x} dx \int_{-\Lambda_x}^{\Lambda_x} dy \frac{1}{(i\omega_m + x + y)^2}\frac{1}{(i\omega_m - x + y)} \frac{1}{(-i\omega_m + x + y)}, \tag{D.27}$$

$$M_{1262} = -\frac{T}{4\pi^2 v_x v_y}\sum_m \int_{-\Lambda_x}^{\Lambda_x} dx \int_{-\Lambda_x}^{\Lambda_x} dy \frac{1}{(i\omega_m - x + y)^2}\frac{1}{(i\omega_m - x - y)} \frac{1}{(-i\omega_m - x + y)}. \tag{D.28}$$

By splitting the integral as earlier, we have from $\mathcal{I}_1$,

$$M_{2515}\Big|_1 = -\frac{iT}{16\pi v_x v_y}\sum_m \int_{-\Lambda_x}^{\Lambda_x} dx \frac{\mathrm{sgn}(\omega_m)}{\omega_m^2}\frac{1}{x - i\omega_m}$$

$$= \frac{T}{8\pi v_x v_y}\sum_{m>0}\int_{-\Lambda_x}^{\Lambda_x} dx \frac{1}{\omega_m(x^2+\omega_m^2)}, \tag{D.29}$$

$$M_{2515}\Big|_1 = \frac{1}{64 v_x v_y T}, \tag{D.30}$$

where we have used the fact that $2M_{2515}\Big|_1 = -I_{1256}\Big|_1$. Similarly from $\mathcal{I}_2$, we get,

$$M_{2515}\Big|_2 \approx -\frac{T\Lambda_x}{2\pi^2 v_x v_y}\sum_m \int_{|y|>\Lambda_y} dy \frac{1}{y^2+\omega_m^2}\frac{1}{(y+i\omega_m)^2}$$

$$\approx -\frac{\Lambda_x}{4\pi^3 v_x v_y}\int_{-\infty}^{\infty} d\omega \int_{\Lambda_y}^{\infty} dy \frac{2(y^2-\omega^2)}{(y^2+\omega^2)^3}, \tag{D.31}$$

$$M_{2515}\Big|_2 \approx -\frac{\Lambda_x}{16\pi^2 v_x v_y \Lambda_y^2}. \tag{D.32}$$

For M_{1262},

$$M_{1262}\Big|_1 = -\frac{iT}{16\pi v_x v_y}\sum_m \int_{-\Lambda_x}^{\Lambda_x} dx \frac{x - 2i\omega_m}{(x-i\omega_m)^2\omega_m^2}\mathrm{sgn}(\omega_m)$$

$$= -\frac{iT}{16\pi v_x v_y}\sum_{m>0}\int_{-\Lambda_x}^{\Lambda_x} dx \frac{4i\omega_m}{(x^2+\omega_m^2)^2}, \tag{D.33}$$

$$M_{1262}\Big|_1 = \frac{1}{64 v_x v_y T}. \tag{D.34}$$

$$M_{1262}\Big|_2 \approx \frac{T\Lambda_x}{2\pi^2 v_x v_y}\sum_m \int_{|y|>\Lambda_y} dy \frac{1}{(y^2+\omega_m^2)^2} = \frac{\Lambda_x}{8\pi^2 v_x v_y \Lambda_y^2}. \tag{D.35}$$

We can ignore $M_{2515}\Big|_2, M_{1262}\Big|_2$ compared to $M_{2515}\Big|_1, M_{1262}\Big|_1$.

Let us now evaluate the only distinct vertex-correction type diagram contributing to s_a,

$$\begin{aligned} N_{2651} &= -T\sum_m \int_{|\boldsymbol{k}|<\Lambda} \frac{1}{(i\omega_m - v_x k_x - v_y k_y)} \frac{1}{(i\omega_m - v_x k_x + v_y k_y)} \\ &\quad \frac{1}{(-i\omega_m - v_x k_x - v_y k_y)} \frac{1}{(-i\omega_m - v_x k_x + v_y k_y)}. \end{aligned} \tag{D.36}$$

Upon transforming coordinates, we have

$$\begin{aligned} N_{2651} &= -\frac{T}{4\pi^2 v_x v_y} \sum_m \int_{-\Lambda_x}^{\Lambda_x} dx \int_{-\Lambda_y}^{\Lambda_y} dy \; \frac{1}{(i\omega_m - x - y)} \frac{1}{(i\omega_m - x + y)} \\ &\quad \frac{1}{(-i\omega_m - x - y)} \frac{1}{(-i\omega_m - x + y)}, \end{aligned} \tag{D.37}$$

and we immediately see that $N_{2651} = I_{1256}$, as expected.

The diagrams contributing to s_b can also be evaluated analogously as follows:

$$\begin{aligned} P_{2626} &= -T\sum_m \int_{|\boldsymbol{k}|<\Lambda} \frac{1}{(i\omega_m - v_x k_x + v_y k_y)} \frac{1}{(i\omega_m + v_x k_x - v_y k_y)^2} \\ &\quad \frac{1}{(-i\omega_m + v_x k_x - v_y k_y)}. \end{aligned} \tag{D.38}$$

However, we immediately notice that $P_{2626} = -2J_{2626} = -2J_{1515}$ (which we have already evaluated above), due to the underlying SU(2) symmetry of the hot-spot theory.

Finally, let us compute the diagram contributing to the three-point function, $Y_{\mu\nu\rho}$.

The one we intend to compute is,

$$Y_{261} = -T\sum_m \int_{|\boldsymbol{k}|<\Lambda} \frac{1}{(i\omega_m - v_x k_x - v_y k_y)} \frac{1}{(i\omega_m - v_x k_x + v_y k_y)} \frac{1}{(i\omega_m + v_x k_x - v_y k_y)}, \tag{D.39}$$

$$Y_{261} = -\frac{T}{4\pi^2 v_x v_y}\sum_m \int_{-\Lambda_x}^{\Lambda_x} dx \int_{-\Lambda_y}^{\Lambda_y} dy \frac{1}{(i\omega_m - x - y)} \frac{1}{(i\omega_m - x + y)} \frac{1}{(i\omega_m + x - y)}. \tag{D.40}$$

It evaluates to,

$$\begin{aligned} Y_{261}\Big|_1 &= -\frac{T}{8\pi v_x v_y}\sum_m \int_{-\Lambda_x}^{\Lambda_x} dx \frac{\mathrm{sgn}(\omega_m)}{\omega_m(x - i\omega_m)} \\ &= -\frac{T}{8\pi v_x v_y}\sum_{m>0} \int_{-\Lambda_x}^{\Lambda_x} dx \frac{2x}{\omega_m(x^2 + \omega_m^2)} = 0, \qquad \text{(D.41)} \\ Y_{261}\Big|_2 &= -\frac{T\Lambda_x}{2\pi^2 v_x v_y}\sum_m \int_{|y|>\Lambda_y} dy \frac{1}{(y - i\omega_m)(y^2 + \omega_m^2)} \qquad \text{(D.42)} \\ &= -\frac{T\Lambda_x}{2\pi^2 v_x v_y}\sum_m \int_{\Lambda_y}^{\infty} dy \frac{2i\omega_m}{(y^2 + \omega_m^2)^2} = 0. \qquad \text{(D.43)} \end{aligned}$$

Therefore, we see that both pieces evaluate to zero, when working with the linearized dispersions.

D.2 Feynman diagrams for hot-spot theory with a finite curvature

In this appendix, we provide details for the computation of the same diagrams that were evaluated earlier, but now in the presence of a finite fermi-surface curvature, κ. We already summarized the results in section 5.3.2.

We start with the diagrams contributing to u_a. These were already well-behaved in the linearized theory in the $T \to 0$ limit, and hence should continue to be so in

the presence of a finite κ. Let us evaluate them nevertheless. The distinct diagrams contributing to u_a after performing the Matsubara summation are given by,

$$\begin{aligned}\tilde{I}_{1212} &= \frac{1}{8\pi^2 v_x v_y}\int_{-\Lambda_x}^{\Lambda_x} dx \int_{-\Lambda_y}^{\Lambda_y} dy \Bigg[2\frac{f(\epsilon_1(x,y)) - f(\epsilon_2(x,y))}{(\epsilon_1(x,y)-\epsilon_2(x,y))^3} \\ &\quad - \frac{f'(\epsilon_1(x,y)) + f'(\epsilon_2(x,y))}{(\epsilon_1(x,y)-\epsilon_2(x,y))^2}\Bigg]. \end{aligned} \tag{D.44}$$

In the above, $f[...]$ is the fermi-dirac distribution function and we have changed variables to $x = v_x k_x, y = v_y k_y$. $\tilde{I}_{2525}$ is identical in form to the above with $\epsilon_1 \to \epsilon_5$. We evaluate the above integrals numerically as a function of temperature for different values of κ at fixed α and vice versa. We find that $\tilde{I}_{2525}$ identically evaluates to 0 even in the presence of a finite (but small) curvature (recall that $I_{2525} = 0$). The results for $\tilde{I}_{1212}$ alongwith a comparison to the analytical predictions for I_{1212} are shown in fig.D.1(a).

Let us now move onto the diagrams contributing to w_a, which were singular ($\sim 1/T$) in our computation with the linearized dispersion. After carrying out the Matsubara summation, the distinct diagrams evaluate to,

$$\begin{aligned}\tilde{I}_{2565} &= -\frac{1}{4\pi^2 v_x v_y}\int_{-\Lambda_x}^{\Lambda_x} dx \int_{-\Lambda_y}^{\Lambda_y} dy \\ &\quad \Bigg[\frac{1}{(\epsilon_2(x,y)-\epsilon_5(x,y))^2}\left(\frac{f(\epsilon_2(x,y))}{\epsilon_2(x,y)-\epsilon_6(x,y)} - \frac{f(\epsilon_5(x,y))}{\epsilon_5(x,y)-\epsilon_6(x,y)}\right) \\ &+ \frac{1}{(\epsilon_6(x,y)-\epsilon_5(x,y))^2}\left(\frac{f(\epsilon_6(x,y))}{\epsilon_6(x,y)-\epsilon_2(x,y)} - \frac{f(\epsilon_5(x,y))}{\epsilon_5(x,y)-\epsilon_2(x,y)}\right) \\ &+ \frac{f'(\epsilon_5(x,y))}{(\epsilon_5(x,y)-\epsilon_2(x,y))(\epsilon_5(x,y)-\epsilon_6(x,y))}\Bigg], \end{aligned} \tag{D.45}$$

$$\begin{aligned}\tilde{I}_{1256} &= -\frac{1}{32\pi^2 v_x v_y}\int_{-\Lambda_x}^{\Lambda_x} dx \int_{-\Lambda_y}^{\Lambda_y} dy \left[\frac{f(\epsilon_1(x,y)) - f(\epsilon_5(x,y))}{xy(x+y)}\right. \\ &\quad \left. - \frac{f(\epsilon_2(x,y)) - f(\epsilon_6(x,y))}{xy(x-y)}\right], \end{aligned} \tag{D.46}$$

where we have used the explicit forms of the dispersions to simplify the expression for $\tilde{I}_{1256}$. We evaluate these diagrams numerically and find that both of them have a very similar behavior except at low temperatures, where $\tilde{I}_{2565}$ is always significantly smaller than $\tilde{I}_{1256}$ (this was the case even in our previous computation where the former went as $\sim \log(T)$ while the latter was $\sim 1/T$). We plot $\tilde{I}_{1256}$ in fig.D.1 (b).

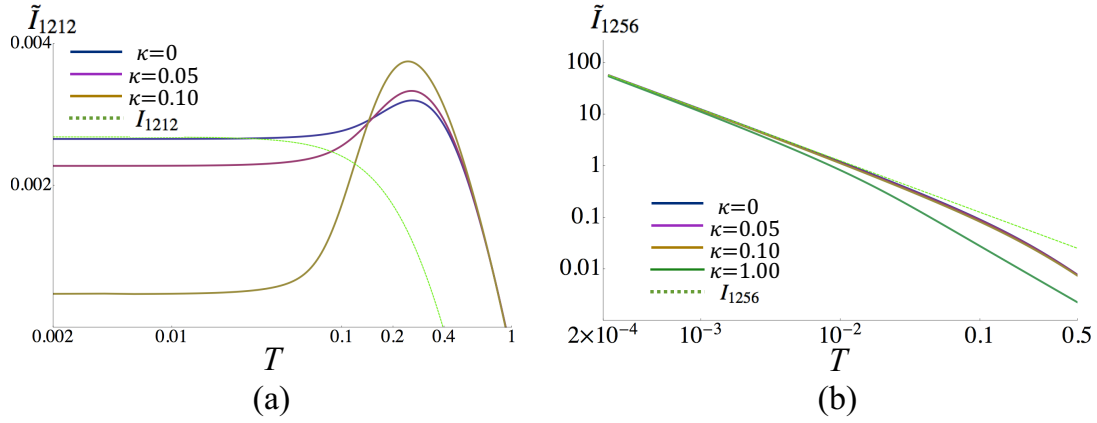

Figure D.1: Absolute values of diagrams contributing to u_a and w_a as a function of temperature, T for (a), (b), different values of κ but fixed $\alpha = 10.0$. Other parameters are $\Lambda = 2.0$ and $v_x = 0.5$. Note the almost perfect agreement of the analytical result for $\kappa = 0$ (dashed green line) with the numerical results for small curvature at low temperatures.

Let us now compute all the terms that turned out to be $\sim 1/T^2$ in our earlier computation, which included both u_b ($|\Phi^b|^4$) and s_b ($|\Psi|^2|\Phi^b|^2$), and study the effect of a finite κ. The diagrams that contribute to u_b are modified to,

$$\tilde{J}_{1515} = \frac{1}{8\pi^2 v_x v_y}\int_{-\Lambda_x}^{\Lambda_x} dx \int_{-\Lambda_y}^{\Lambda_y} dy \left[2\frac{f(\epsilon_1(x,y)) - f(\epsilon_5(x,y))}{(\epsilon_1(x,y) - \epsilon_5(x,y))^3} - \frac{f'(\epsilon_1(x,y)) + f'(\epsilon_5(x,y))}{(\epsilon_1(x,y) - \epsilon_5(x,y))^2}\right], \tag{D.47}$$

and $\tilde{J}_{2626} = \tilde{J}_{1515}$ even for $\kappa \neq 0$.

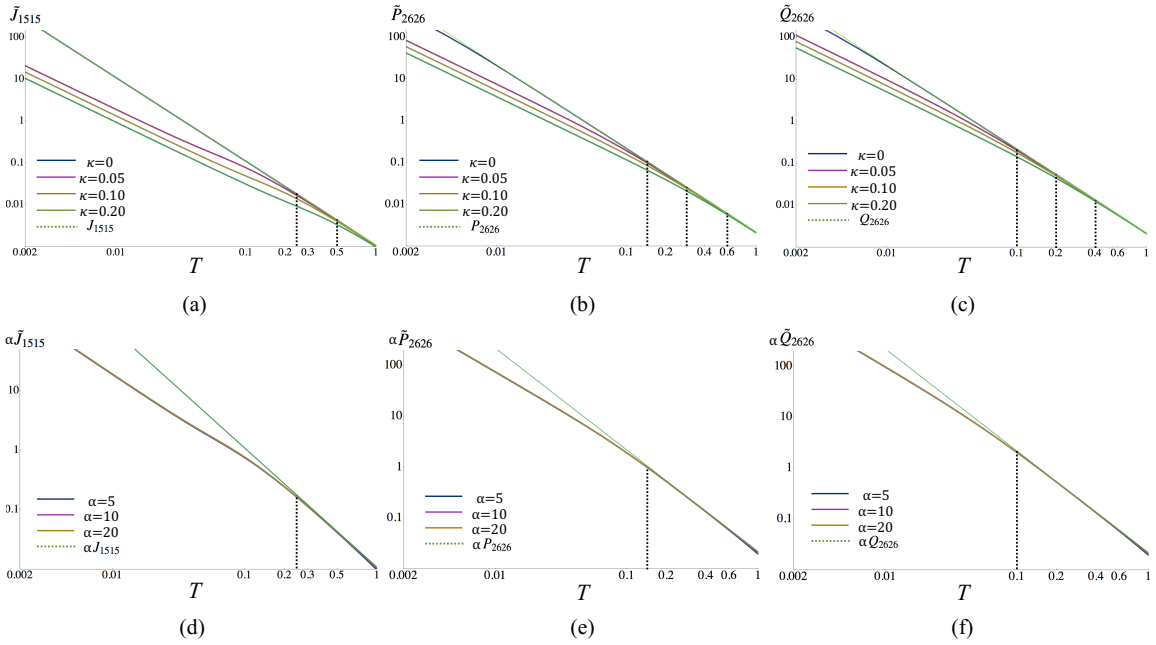

Figure D.2: Absolute values of diagrams contributing to u_b and s_b as a function of temperature, T for (a), (b), (c) different values of κ but fixed $\alpha = 10.0$ and (d), (e), (f) different values of α but fixed $\kappa = 0.05$. (a) $\tilde{J}_{1515}$, (b) $\tilde{P}_{2626}$, (c) $\tilde{Q}_{2626}$. (d)-(f) plot the same diagrams scaled with α. Other parameters are $\Lambda = 2.0$ and $v_x = 0.5$. The vertical black dotted lines represent the approximate temperature where the computation in the presence of a non-zero κ starts deviating from the one with $\kappa = 0$. Note that in figs. (a)-(c), the green dashed curves (representing the analytical results) overlap almost perfectly with the blue solid curves for $\kappa = 0$.

On the other hand, the self-energy type diagrams contributing to s_b are modified to,

$$\tilde{P}_{2626} = -\frac{1}{4\pi^2 v_x v_y}\int_{-\Lambda_x}^{\Lambda_x} dx \int_{-\Lambda_y}^{\Lambda_y} dy \Bigg[\frac{f(\epsilon_6(x,y)) - f(\epsilon_2(x,y))}{(\epsilon_6(x,y)-\epsilon_2(x,y))(\epsilon_6^2(x,y)-\epsilon_2^2(x,y))} + \frac{1-2f(\epsilon_6(x,y))}{4\epsilon_6^2(x,y)(\epsilon_2(x,y)+\epsilon_6(x,y))} - \frac{f'(\epsilon_6(x,y))}{2\epsilon_6(x,y)(\epsilon_6(x,y)-\epsilon_2(x,y))}\Bigg], \quad \text{(D.48)}$$

and $\tilde{P}_{1515} = \tilde{P}_{2626}$, even when $\kappa \neq 0$. Similarly, the vertex-correction diagrams are

modified to,

$$\tilde{Q}_{2626} = -\frac{1}{8\pi^2 v_x v_y}\int_{-\Lambda_x}^{\Lambda_x} dx \int_{-\Lambda_y}^{\Lambda_y} dy \left[\frac{1-2f(\epsilon_6(x,y))}{\epsilon_6(x,y)} - \frac{1-2f(\epsilon_2(x,y))}{\epsilon_2(x,y)}\right] \frac{1}{\epsilon_2^2(x,y)-\epsilon_6^2(x,y)}, \tag{D.49}$$

and $\tilde{Q}_{1515} = \tilde{Q}_{2626}$. The results for $\tilde{J}_{1515}$, $\tilde{P}_{2626}$ and $\tilde{Q}_{2626}$ are plotted in fig.D.2, alongwith a comparison to the respective diagrams evaluated with $\kappa = 0$. It is not surprising that the singular power-law agrees, but even the prefactor matches perfectly.

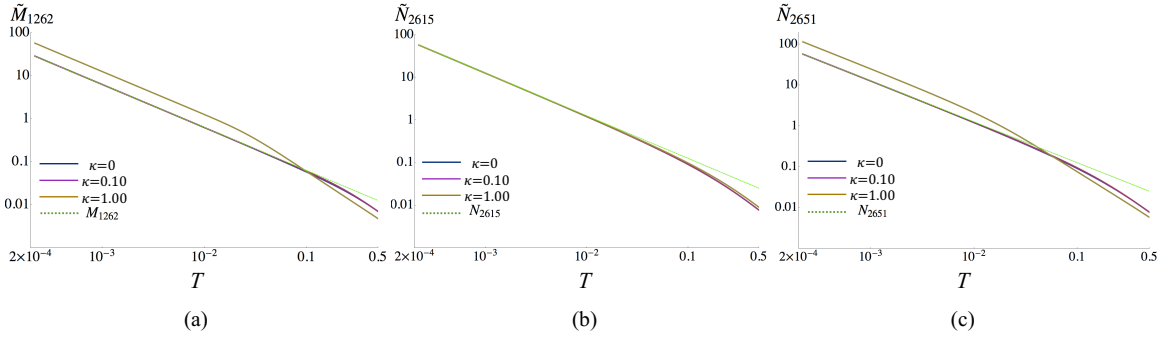

Figure D.3: Absolute values of diagrams contributing to s_a as a function of temperature, T for (a) $\tilde{M}_{1262}$, (b), $\tilde{N}_{2615}$, (c) $\tilde{N}_{2651}$ for different values of κ but fixed $\alpha = 10.0$. Other parameters are $\Lambda = 2.0$ and $v_x = 0.5$. Note the almost perfect agreement of the analytical result for $\kappa = 0$ (dashed green line) with the numerical results for small curvature at low temperatures.

Next, we compute the diagrams contributing to s_a ($|\Psi|^2|\Phi^a|^2$). The distinct self-energy type diagrams evaluate to,

$$\tilde{M}_{1262} = \frac{1}{4\pi^2 v_x v_y}\int_{-\Lambda_x}^{\Lambda_x} dx \int_{-\Lambda_y}^{\Lambda_y} dy \left[\frac{f(\epsilon_1(x,y))-f(\epsilon_2(x,y))}{(\epsilon_1(x,y)-\epsilon_2(x,y))(\epsilon_1^2(x,y)-\epsilon_2^2(x,y))} - \frac{1-2f(\epsilon_2(x,y))}{4\epsilon_2^2(x,y)(\epsilon_2(x,y)+\epsilon_1(x,y))} + \frac{f'(\epsilon_2(x,y))}{2\epsilon_2(x,y)(\epsilon_2(x,y)-\epsilon_1(x,y))}\right] \tag{D.50}$$

and $\tilde{M}_{2515}$ is identical in form to the above with the replacement, $\epsilon_1 \to \epsilon_2$ and $\epsilon_2 \to \epsilon_5$.

Similarly, the distinct vertex-correction type diagrams evaluate to,

$$\tilde{N}_{2615} = -\frac{1}{8\pi^2 v_x v_y}\int_{-\Lambda_x}^{\Lambda_x} dx \int_{-\Lambda_y}^{\Lambda_y} dy \left[\frac{1-2f(\epsilon_2(x,y))}{\epsilon_2(x,y)} - \frac{1-2f(\epsilon_5(x,y))}{\epsilon_5(x,y)}\right] \frac{1}{\epsilon_5^2(x,y)-\epsilon_2^2(x,y)}, \quad \text{(D.51)}$$

and where $\tilde{N}_{2651}$ can be obtained from the above by replacing $\epsilon_5 \to \epsilon_1$. The results are plotted in fig.D.3.

Finally, let us evaluate the three-point functions, t_{ab}. Recall that in the linearized theory, this was identically 0. In the presence of a curvature, it is modified to,

$$\tilde{Y}_{261} = -\frac{1}{4\pi^2 v_x v_y}\int_{-\Lambda_x}^{\Lambda_x} dx \int_{-\Lambda_y}^{\Lambda_y} dy \Bigg[\frac{f(\epsilon_1(x,y))}{(\epsilon_1(x,y)-\epsilon_2(x,y))(\epsilon_1(x,y)-\epsilon_6(x,y))} + \frac{1}{\epsilon_2(x,y)-\epsilon_6(x,y)}\left(\frac{f(\epsilon_2(x,y))}{\epsilon_2(x,y)-\epsilon_1(x,y)} - \frac{f(\epsilon_6(x,y))}{\epsilon_6(x,y)-\epsilon_1(x,y)}\right)\Bigg], \quad \text{(D.52)}$$

and where $\tilde{Y}_{261}$ is still equal to the other symmetry related diagrams. The results for $\tilde{Y}_{261}/\kappa$ and $\alpha\tilde{Y}_{261}$ are shown in figs.D.4 (a) and (b) respectively, alongwith a comparison to the particular form, $\mathcal{Y}$, that we guessed.

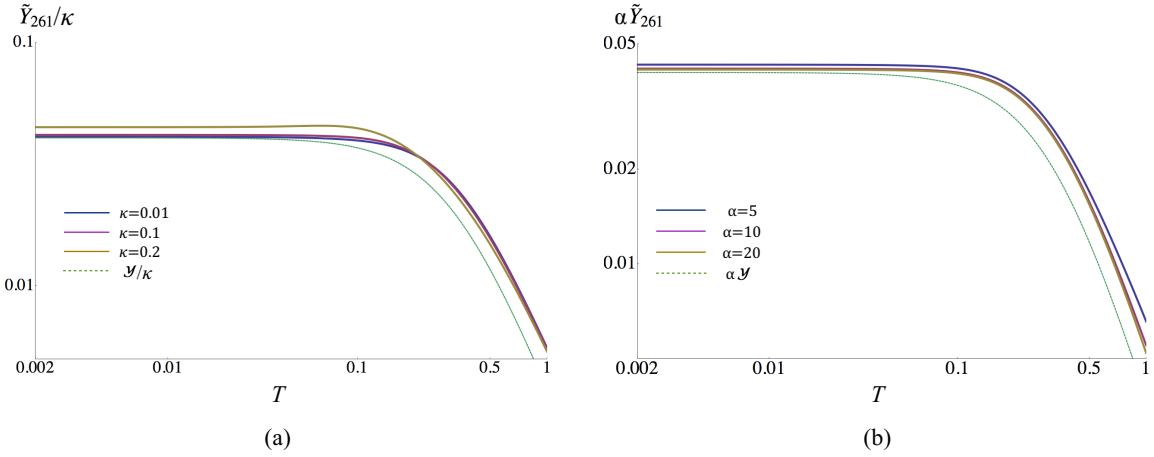

Figure D.4: Absolute value of $\tilde{Y}_{261}$ as a function of temperature and comparison with $\mathcal{Y}$ (a) at fixed $\alpha = 10$, (b) at fixed $\kappa = 0.1$

Appendix E

Appendices for Chapter 6

E.1 CDW instabilities of FL

We plot the lowest eigenvalues, $\lambda_{\boldsymbol{Q}}$, for the charge-ordering instabilities of the large FS corresponding to band-structure parameters of figs.6.3, 6.4 in fig.E.1 below. For the parameters in fig.E.1(a), the minimum eigenvalue occurs at $\boldsymbol{Q}^* = (\pm 19\pi/50, \pm 19\pi/50)$ and the corresponding eigenvector is given by,

$$P_{\boldsymbol{Q}^*} = -0.999[\cos k_x - \cos k_y] - 0.014[\cos(2k_x) - \cos(2k_y)]. \tag{E.1}$$

For the parameters in figs.E.1(b), (c), the minimum eigenvalue occurs at the same value of $\boldsymbol{Q}^*$ as above and the form of the eigenvector remains almost identical. This isn't surprising, since $\boldsymbol{Q}^*$ is determined by the separation between the "hot-spots".

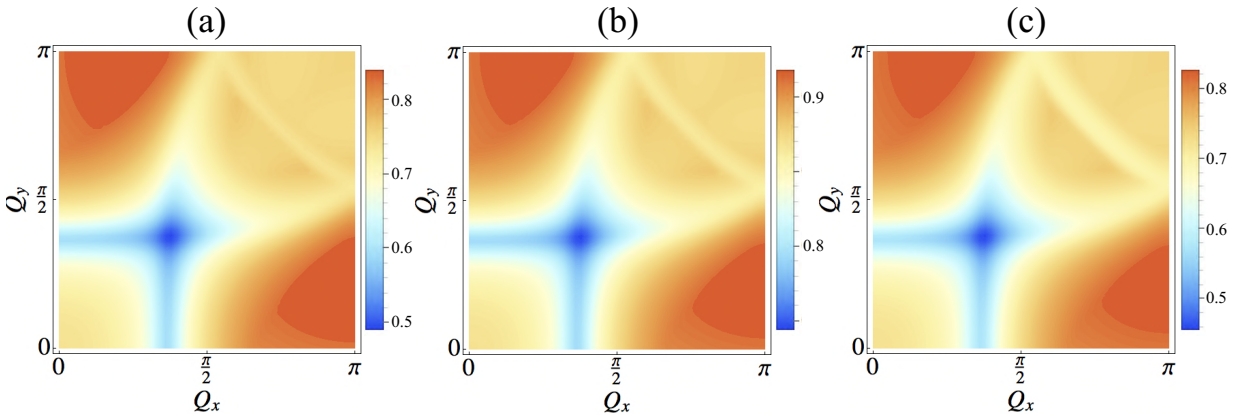

Figure E.1: The lowest eigenvalues, $\lambda_{\boldsymbol{Q}}$, as a function of $\boldsymbol{Q}$ at a temperature $T = 0.06$ for the large FS corresponding to $t_1 = 1.0,\ t_2 = -0.32,\ t_3 = 0.128,\ \mu = -1.11856$. These computations have been carried out as a limit of the FL* computation with $\tilde{t}_0 = 0,\ \tilde{t}_1 = 0,\ \lambda = 0$. The state with the diagonal wavevector is the leading instability in all the cases. The interaction parameters are given by: (a) $J_1 = 1.0,\ J_2 = J_3 = 0.05, U = V_1 = V_2 = V_3 = 0$, (b) $J_1 = 0.5,\ J_2 = J_3 = 0.05,\ U = V_1 = V_2 = V_3 = 0$, and, (c) $J_1 = 1.0,\ J_2 = 0.1,\ J_3 = 0.05,\ U = 0,\ V_1 = 0.05,\ V_2 = V_3 = 0.01$.

E.2 Instabilities in the presence of strong Coulomb repulsion

In this section, we present some additional results for the weak-coupling density-wave instabilities in the presence of strong Coulomb repulsion ($U \sim J_1$). The leading instabilities that we obtain are not bond-density waves of the type discussed in the main text. We explore the instabilities for the FL* state whose spectral function is shown in fig.6.4(a) for different combinations of the Coulomb repulsion parameters. The lowest eigenvalues, $\lambda_{\boldsymbol{Q}}$ as a function of $\boldsymbol{Q}$ are shown in fig.E.2.

We start with the case when $U = 2J_1 \gg V_1$ (fig.E.2a). We find that the leading instability corresponds to $\boldsymbol{Q}^* = (\pm 11\pi/20, \pm\pi),\ (\pm\pi, \pm 11\pi/20)$ and the eigenvector for this state is predominantly given by $P_{\boldsymbol{Q}}(\boldsymbol{k}) = \sin k_x - \sin k_y$. This state therefore

breaks time-reversal symmetry and is a generalized version of the "staggered-flux" state, but at a wavevector away from (π, π).

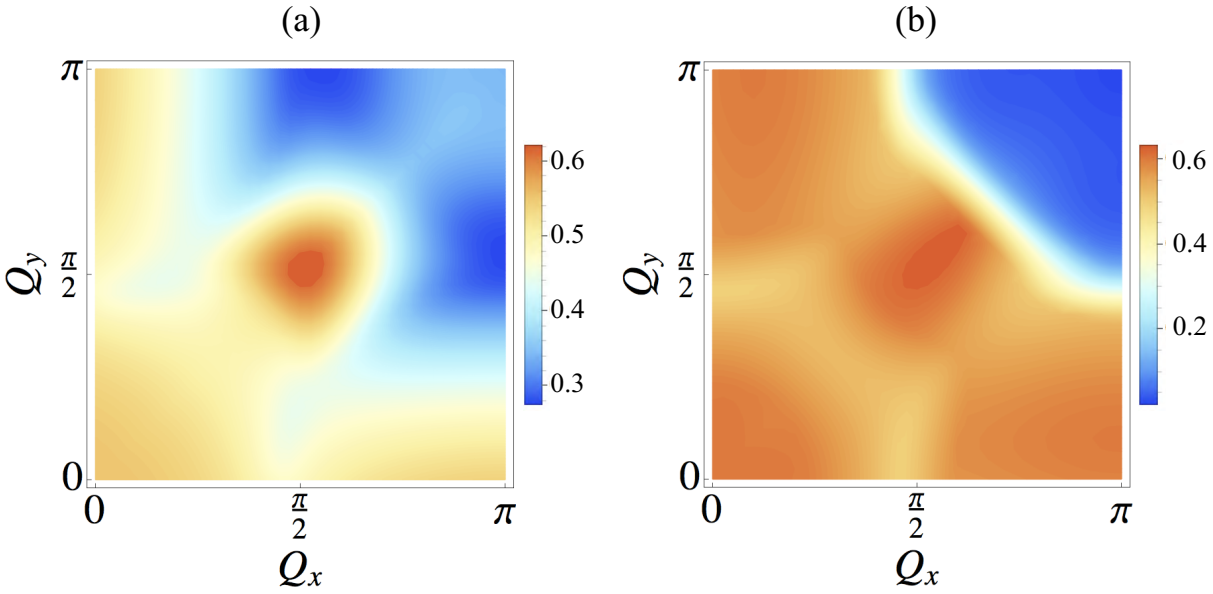

Figure E.2: The lowest eigenvalues, $\lambda_{\boldsymbol{Q}}$, as a function of $\boldsymbol{Q}$ at a temperature $T = 0.06$ for the FL* state shown in fig.6.4(a), corresponding to $t_1 = 1.0,\ t_2 = -0.32,\ t_3 = 0.128,\ \mu = -1.11856,\ \tilde{t}_0 = -0.2t_1,\ \tilde{t}_1 = -0.1t_1,\ \lambda = 0.75t_1$. The interaction parameters are given by: (a) $J_1 = 1.0,\ J_2 = 0.1,\ J_3 = 0.05,\ U = 2.0,\ V_1 = 0.1,\ V_2 = V_3 = 0.01$, (b) $J_1 = 1.0,\ J_2 = 0.1,\ J_3 = 0.05,\ U = 1.0,\ V_1 = 0.7,\ V_2 = V_3 = 0.01$.

We next consider the case when $U = J_1 \sim V_1$ (fig.E.2b). In this case, we find that the leading instability occurs at $\boldsymbol{Q}^* = (\pi, \pi)$ and the eigenvector for this state is given by $P_{\boldsymbol{Q}}(\boldsymbol{k}) = 1$. This state is therefore just a conventional (π, π) charge-density wave, that we should naively expect to arise due a large V_1.

However, we note that if we focus on the region of the Brillouin zone with smaller $|\boldsymbol{Q}|$, the d-form factor density waves found in the body of the paper with smaller Coulomb repulsion are present also in the cases considered in this appendix. Thus the Coulomb repulsion has little direct effect on the d-form factor density waves, but,

in the present simple RPA framework, it can induce other instabilities which are not of current experimental interest.

Appendix F

Appendices for Chapter 7

F.1 Spiral order and Z_2 gauge theory

Here we generalize the theory in Eq. (7.13) to the case of spiral spin order at an incommensurate wavevector $\boldsymbol{K}$. In this case the antiferromagnetic order is not characterized by a single unit vector n_ℓ, but by two orthogonal unit vectors $n_{1\ell}$ and $n_{2\ell}$ which obey

$$n_{1\ell}^2 = n_{2\ell}^2 = 1 \quad , \quad n_{1\ell}\, n_{2\ell} = 0. \tag{F.1}$$

The spin-fermion coupling to the electrons in Eq. (7.13) is replaced by

$$\mathcal{L}_{fn} = -\lambda \sum_i \left[n_{i1\ell} \cos\left(\boldsymbol{K}\cdot\boldsymbol{r}_i\right) + n_{i2\ell} \sin\left(\boldsymbol{K}\cdot\boldsymbol{r}_i\right)\right] \cdot c_{i\alpha}^\dagger \sigma_{\alpha\beta}^\ell c_{i\beta}, \tag{F.2}$$

After the change of variables in Eq. (7.1), this leads to the Yukawa coupling

$$\mathcal{L}_Y = -\lambda \frac{1}{2} \left(H_i^{a*} e^{i\boldsymbol{K}\cdot\boldsymbol{r}_i} + H_i^a e^{-i\boldsymbol{K}\cdot\boldsymbol{r}_i} \right) \psi_{i,p}^\dagger \sigma_{pp'}^a \psi_{i,p'}, \tag{F.3}$$

where, in contrast to Eq. (7.8), the Higgs field H^a is now *complex* and is defined by

$$H^a \equiv \frac{1}{2} \left(n_{1\ell} + i n_{2\ell} \right) \ \mathrm{Tr}[\sigma^\ell R_i \sigma^a R_i^\dagger], \tag{F.4}$$

generalizing Eq. (7.15). It is now also clear from Eq. (F.3) that under translation by a distance $\boldsymbol{a}$, the Higgs field transforms as in Eq. (7.9), where $e^{i\boldsymbol{K}\cdot\boldsymbol{a}}$ can now be complex.

The structure of SU(2) gauge theory with a complex Higgs field remains essentially the same as for the real Higgs discussed in the body of the paper, with one important distinction. The quartic term in Eq. (7.7) is replaced by two terms

$$u_1[H^{a*}H^a]^2 + u_2[H^a]^2[H^{b*}]^2, \tag{F.5}$$

and the presence of spiral order requires that $u_2 > 0$. Then in the Higgs phase, the minimum energy condensate can always be oriented so that

$$H^a = (1, i, 0). \tag{F.6}$$

Such a Higgs condensate breaks the SU(2) gauge symmetry all the way down to Z_2. And using Eq. (7.19), the analog of the relationship in Eq. (7.20) for the orientation of the spiral order is

$$\begin{aligned} n_{1\ell} + i n_{2\ell} &= \frac{1}{2} H^a \ \mathrm{Tr}[\sigma^\ell R \sigma^a R^\dagger] \\ &= -\varepsilon_{\alpha\gamma} z_\gamma \sigma^\ell_{\alpha\beta} z_\beta \quad \text{for } H^a = (1, i, 0). \end{aligned} \tag{F.7}$$

This co-incides with the conventional representation [193] of the spiral orientation in terms of spinons z_α, and it can verified that the values in Eq. (F.7) obey Eq. (F.1).

For the case with $u_2 < 0$ in Eq. (F.5), the Higgs condensate is instead a SU(2) rotation of

$$H^a = e^{i\theta}(1, 0, 0), \tag{F.8}$$

where θ is an arbitrary phase. This corresponds to incommensurate collinear spin order [197].

F.2 Feynman diagram computations

F.2.1 Self-energy: Gauge-field

Since we are interested in the singular structure of $\Pi_0^{\mathbf{A}}(q)$ in Eq. (7.22), we shall evaluate the integral over ℓ_x first, followed by ℓ_τ, ℓ_y. Therefore,

$$\begin{aligned}\Pi_0^{\mathbf{A}}(q) &= 2\int \frac{d\ell_\tau d\ell_y}{(2\pi)^2}\ \frac{i[\theta(\ell_\tau)-\theta(\ell_\tau+q_\tau)]}{-i\eta q_\tau + q_x + q_y^2 + 2\ell_y q_y} + \boldsymbol{q}\to -\boldsymbol{q}, &\text{(F.9)}\\ &= \frac{q_\tau}{\pi}\int \frac{d\ell_y}{(2\pi)}\frac{-i}{-i\eta q_\tau + q_x + q_y^2 + 2\ell_y q_y} + \boldsymbol{q}\to -\boldsymbol{q}, &\text{(F.10)}\\ &= \frac{|q_\tau|}{2\pi|q_y|}. &\text{(F.11)}\end{aligned}$$

This leads to the expression for $\Pi_0^{\mathbf{A}}(q)$ in Eq. (7.24).

F.2.2 Self-energy: Higgs' field

Focusing on just the $m=1$ contribution, Eq. (7.34) becomes,

$$\Pi^H_{m=1}(q) = 2\int \frac{d\ell_\tau d^2\boldsymbol{\ell}}{(2\pi)^3}\Bigg[\frac{1}{-ic_f \mathrm{sgn}(\ell_\tau+q_\tau)|\ell_\tau+q_\tau|^{2/3} - \boldsymbol{v}_1\cdot(\boldsymbol{\ell}+\boldsymbol{q})}\ \frac{1}{-ic_f\mathrm{sgn}(\ell_\tau)|\ell_\tau|^{2/3} - \boldsymbol{v}_2\cdot\boldsymbol{\ell}} + q\to -q\Bigg]. \quad \text{(F.12)}$$

Let us define $\ell_1 = \boldsymbol{v}_1\cdot(\boldsymbol{\ell}+\boldsymbol{q})$ and $\ell_2 = \boldsymbol{v}_2\cdot\boldsymbol{\ell}$, so that

$$\Pi^H_{m=1}(q) = \frac{1}{v_x v_y}\int \frac{d\ell_\tau d\ell_1 d\ell_2}{(2\pi)^3}\Bigg[\frac{1}{-ic_f \mathrm{sgn}(\ell_\tau+q_\tau)|\ell_\tau+q_\tau|^{2/3} - \ell_1}\ \frac{1}{-ic_f\mathrm{sgn}(\ell_\tau)|\ell_\tau|^{2/3} - \ell_2} + q\to -q\Bigg]. \quad \text{(F.13)}$$

It is not hard to see that the only non-zero contribution comes from the imaginary parts of both the terms. Then,

$$\Pi^H_{m=1}(q) = \frac{1}{v_x v_y}\int \frac{d\ell_\tau d\ell_1 d\ell_2}{(2\pi)^3}\left[\frac{ic_f\mathrm{sgn}(\ell_\tau+q_\tau)|\ell_\tau+q_\tau|^{2/3}}{c_f^2|\ell_\tau+q_\tau|^{4/3}+\ell_1^2}\ \frac{ic_f\mathrm{sgn}(\ell_\tau)|\ell_\tau|^{2/3}}{c_f^2|\ell_\tau|^{4/3}+\ell_2^2} + q\to -q\right]. \quad \text{(F.14)}$$

Upon carrying out the $\ell_1,\ \ell_2-$ integrals, this becomes,

$$\Pi^H_{m=1}(q) = -\frac{1}{4v_x v_y}\int \frac{d\ell_\tau}{2\pi}[\mathrm{sgn}(\ell_\tau + q_\tau)\ \mathrm{sgn}(\ell_\tau) + q \to -q]. \tag{F.15}$$

This directly leads to the expression for $\Pi^H(q)$ in Eq. (7.36).

F.2.3 Fermion self-energy at the hot-spot

The Fermionic self-energy due to the Higgs' field fluctuations (Eq. (7.38)) becomes,

$$\Sigma_1(p) = 3\int \frac{d\ell_\tau d^2\boldsymbol{\ell}}{(2\pi)^3}\frac{1}{-i\zeta_f \mathrm{sgn}(p_\tau - \ell_\tau)|p_\tau - \ell_\tau|^\beta - \boldsymbol{v}_2\cdot(\boldsymbol{p}-\boldsymbol{\ell})}\ \frac{1}{\gamma|\ell_\tau| + \boldsymbol{\ell}^2}. \tag{F.16}$$

Let us now change coordinates such that $\ell_\perp = \hat{v}_2\cdot\boldsymbol{\ell}$ and $\ell_\parallel$ is the component along the Fermi-surface of ψ_2. Then,

$$\Sigma_1(p) = -3\int \frac{d\ell_\tau d\ell_\perp d\ell_\parallel}{(2\pi)^3}\frac{1}{-i\zeta_f \mathrm{sgn}(p_\tau - \ell_\tau)|p_\tau - \ell_\tau|^\beta - \boldsymbol{v}_2\cdot\boldsymbol{p} + v_2\ell_\perp}\ \frac{1}{\gamma|\ell_\tau| + \ell_\perp^2 + \ell_\parallel^2}. \tag{F.17}$$

It is straightforward to carry out the integral over $\ell_\parallel$, which gives,

$$\Sigma_1(p) = -\frac{3}{2}\int \frac{d\ell_\tau d\ell_\perp}{(2\pi)^2}\frac{1}{-i\zeta_f \mathrm{sgn}(p_\tau - \ell_\tau)|p_\tau - \ell_\tau|^\beta - \boldsymbol{v}_2\cdot\boldsymbol{p} + v_2\ell_\perp}\ \frac{1}{\sqrt{\gamma|\ell_\tau| + \ell_\perp^2}}. \tag{F.18}$$

Let us now study the form of the self-energy at the hot-spot, $\boldsymbol{p} = 0$, and extract the p_τ dependence. We can symmetrize the above form then to give,

$$\Sigma_1(p_\tau) = 3i\int \frac{d\ell_\tau}{2\pi}\int_0^\infty \frac{d\ell_\perp}{2\pi}\frac{\zeta_f \mathrm{sgn}(\ell_\tau - p_\tau)|p_\tau - \ell_\tau|^\beta}{\zeta_f^2|p_\tau - \ell_\tau|^{2\beta} + v_2^2\ell_\perp^2}\ \frac{1}{\sqrt{\gamma|\ell_\tau| + \ell_\perp^2}}. \tag{F.19}$$

Carrying out the integral over $\ell_\perp$ (see Appendix F.2.4) leads to the expression in Eq. (7.40).

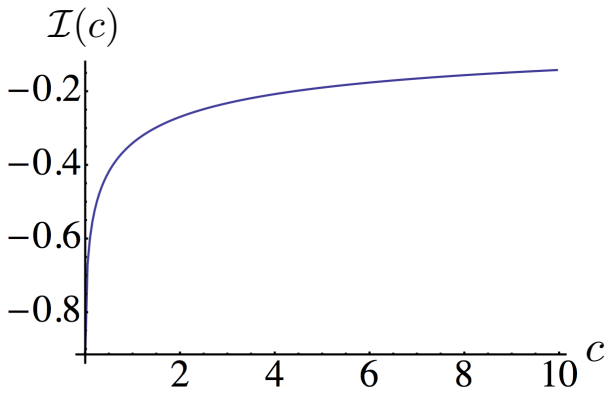

Figure F.1: $\mathcal{I}(c)$ evaluated numerically as a function of c. Note that $\mathcal{I}(c \to 0) = -1$, which reproduces Eq.7.41.

F.2.4 Integrals

We use the integral (for $a > 0, b > 0$):

$$\int_0^\infty dx \frac{1}{x^2 + a^2} \frac{1}{\sqrt{x^2 + b^2}} = \frac{1}{a\sqrt{b^2 - a^2}} \tan^{-1}\left(\frac{\sqrt{b^2 - a^2}}{a}\right). \tag{F.20}$$

The above is valid irrespective of whether $a > b$ or $a < b$.

The integral in Eq. (7.42) can be evaluated as a function of the dimensionless parameter, $c = \zeta_f^2/\gamma v_2^2$, when $\beta = 1/2$. The integral becomes,

$$\mathcal{I}(c) = \int_{-\infty}^{\infty} \frac{dx}{2\pi} \tan^{-1}\left(\frac{\sqrt{|x| - c|1 - x|}}{\sqrt{c|1 - x|}}\right) \frac{\mathrm{sgn}(x - 1)}{\sqrt{|x| - c|1 - x|}}. \tag{F.21}$$

We show the functional form of $\mathcal{I}(c)$ as a function of c in Fig. F.1.

Bibliography

[1] Ar. Abanov and A. Chubukov. Anomalous scaling at the quantum critical point in itinerant antiferromagnets. *Phys. Rev. Lett.*, 93:255702, Dec 2004.

[2] Ar. Abanov and Andrey V. Chubukov. Spin-fermion model near the quantum critical point: One-loop renormalization group results. *Phys. Rev. Lett.*, 84:5608–5611, Jun 2000.

[3] A. J. Achkar, F. He, R. Sutarto, J. Geck, H. Zhang, Y.-J. Kim, and D. G. Hawthorn. Resonant x-ray scattering measurements of a spatial modulation of the cu $3d$ and o $2p$ energies in stripe-ordered cuprate superconductors. *Phys. Rev. Lett.*, 110:017001, Jan 2013.

[4] A. J. Achkar, F. He, R. Sutarto, C. McMahon, M. Zwiebler, M. Hucker, G. D. Gu, R. Liang, D. A. Bonn, W. N. Hardy, J. Geck, and D. G. Hawthorn. Orbital symmetry of charge density wave order in $La_{1.875}Ba_{0.125}CuO_4$ and $YBa_2Cu_3O_{6.67}$. *ArXiv e-prints*, September 2014.

[5] A. J. Achkar, R. Sutarto, X. Mao, F. He, A. Frano, S. Blanco-Canosa, M. Le Tacon, G. Ghiringhelli, L. Braicovich, M. Minola, M. Moretti Sala, C. Mazzoli, Ruixing Liang, D. A. Bonn, W. N. Hardy, B. Keimer, G. A. Sawatzky, and D. G. Hawthorn. Distinct Charge Orders in the Planes and Chains of Ortho-III-Ordered $YBa_2Cu_3O_{6+\delta}$ Superconductors Identified by Resonant Elastic X-ray Scattering. *Phys. Rev. Lett.*, 109:167001, Oct 2012.

[6] G. Aeppli, T. E. Mason, S. M. Hayden, H. A. Mook, and J. Kulda. Nearly singular magnetic fluctuations in the normal state of a high-tc cuprate superconductor. *Science*, 278(5342):1432–1435, 1997.

[7] Ian Affleck, Z. Zou, T. Hsu, and P. Anderson. Su(2) gauge symmetry of the large-u limit of the hubbard model. *Phys. Rev. B*, 38:745–747, Jul 1988.

[8] A. Allais, J. Bauer, and S. Sachdev. Comment on "Symmetry classification of bond order parameters in cuprates". *ArXiv e-prints*, July 2014.

[9] Andrea Allais, Johannes Bauer, and Subir Sachdev. Auxiliary-boson and dmft studies of bond ordering instabilities of t-j-v models on the square lattice. *Indian Journal of Physics*, 88(9):905–913, 2014.

[10] Andrea Allais, Johannes Bauer, and Subir Sachdev. Density wave instabilities in a correlated two-dimensional metal. *Phys. Rev. B*, 90:155114, Oct 2014.

[11] Andrea Allais, Debanjan Chowdhury, and Subir Sachdev. Connecting high-field quantum oscillations to zero-field electron spectral functions in the underdoped cuprates. *Nat Commun*, 5, 12 2014.

[12] H. Alloul, P. Mendels, G. Collin, and P. Monod. ^{89}Y. *Phys. Rev. Lett.*, 61:746–749, Aug 1988.

[13] Vinay Ambegaokar and Alexis Baratoff. Tunneling between superconductors. *Phys. Rev. Lett.*, 10:486–489, Jun 1963.

[14] James G. Analytis, H-H. Kuo, Ross D. McDonald, Mark Wartenbe, P. M. C. Rourke, N. E. Hussey, and I. R. Fisher. Transport near a quantum critical point in $BaFe_2(As_{1-x}P_x)_2$. *Nat Phys*, 10(3):194–197, 03 2014.

[15] P. W. Anderson. Localized magnetic states and fermi-surface anomalies in tunneling. *Phys. Rev. Lett.*, 17:95–97, Jul 1966.

[16] P. W. Anderson. The Resonating Valence Bond State in La_2CuO_4 and Superconductivity. *Science*, 235(4793):1196–1198, 1987.

[17] P W Anderson, P A Lee, M Randeria, T M Rice, N Trivedi, and F C Zhang. The physics behind high-temperature superconducting cuprates: the 'plain vanilla' version of rvb. *Journal of Physics: Condensed Matter*, 16(24):R755, 2004.

[18] Yoichi Ando, Kouji Segawa, Seiki Komiya, and A. N. Lavrov. Electrical resistivity anisotropy from self-organized one dimensionality in high-temperature superconductors. *Phys. Rev. Lett.*, 88:137005, Mar 2002.

[19] N. Andrei and P. Coleman. Cooper instability in the presence of a spin liquid. *Phys. Rev. Lett.*, 62:595–598, Jan 1989.

[20] W. A. Atkinson, A. P. Kampf, and S. Bulut. Charge Order in the Pseudogap Phase of Cuprate Superconductors. *ArXiv e-prints*, April 2014.

[21] S. Badoux, W. Tabis, F. Laliberté, G. Grissonnanche, B. Vignolle, D. Vignolles, J. Béard, D. A. Bonn, W. N. Hardy, R. Liang, N. Doiron-Leyraud, Louis Taillefer, and Cyril Proust. Change of carrier density at the pseudogap critical point of a cuprate superconductor. *Nature*, 531(7593):210–214, 03 2016.

[22] Leon Balents, Lorenz Bartosch, Anton Burkov, Subir Sachdev, and Krishnendu Sengupta. Putting competing orders in their place near the mott transition. *Phys. Rev. B*, 71:144508, Apr 2005.

[23] Sumilan Banerjee, T. V. Ramakrishnan, and Chandan Dasgupta. Effect of pairing fluctuations on low-energy electronic spectra in cuprate superconductors. *Phys. Rev. B*, 84:144525, Oct 2011.

[24] Sumilan Banerjee, Shizhong Zhang, and Mohit Randeria. Theory of quantum oscillations in the vortex-liquid state of high-tc superconductors. *Nat Commun*, 4, 04 2013.

[25] Neven Barisic, Sven Badoux, Mun K. Chan, Chelsey Dorow, Wojciech Tabis, Baptiste Vignolle, Guichuan Yu, Jerome Beard, Xudong Zhao, Cyril Proust, and Martin Greven. Universal quantum oscillations in the underdoped cuprate superconductors. *Nat Phys*, 9(12):761–764, 12 2013.

[26] J.G. Bednorz and K.A. Muller. Possible highTc superconductivity in the Ba-La-Cu-O system. *Zeitschrift fur Physik B Condensed Matter*, 64(2):189–193, 1986.

[27] Matias Bejas, Andres Greco, and Hiroyuki Yamase. Possible charge instabilities in two-dimensional doped mott insulators. *Phys. Rev. B*, 86:224509, Dec 2012.

[28] E. Berg, N. H. Lindner, and T. Pereg-Barnea. Metastable π junction between an $s_{\pm}$-wave and an s-wave superconductor. *Phys. Rev. Lett.*, 106:147003, Apr 2011.

[29] Erez Berg and Ehud Altman. Evolution of the fermi surface of d-wave superconductors in the presence of thermal phase fluctuations. *Phys. Rev. Lett.*, 99:247001, Dec 2007.

[30] Erez Berg, Max A. Metlitski, and Subir Sachdev. Sign-problem–free quantum monte carlo of the onset of antiferromagnetism in metals. *Science*, 338(6114):1606–1609, 2012.

[31] E. Blackburn, J. Chang, M. Hücker, A. T. Holmes, N. B. Christensen, Ruixing Liang, D. A. Bonn, W. N. Hardy, U. Rütt, O. Gutowski, M. v. Zimmermann, E. M. Forgan, and S. M. Hayden. X-Ray Diffraction Observations of a Charge-Density-Wave Order in Superconducting Ortho-II $YBa_2Cu_3\mathbf{O}_{6.54}$ Single Crystals in Zero Magnetic Field. *Phys. Rev. Lett.*, 110:137004, Mar 2013.

[32] Mike Blake and Aristomenis Donos. Quantum critical transport and the hall angle in holographic models. *Phys. Rev. Lett.*, 114:021601, Jan 2015.

[33] S. L. Bud'ko, E. Morosan, and P. C. Canfield. Magnetic field induced non-fermi-liquid behavior in ybagge single crystals. *Phys. Rev. B*, 69:014415, Jan 2004.

[34] S. Bulut, W. A. Atkinson, and A. P. Kampf. Spatially modulated electronic nematicity in the three-band model of cuprate superconductors. *Phys. Rev. B*, 88:155132, Oct 2013.

[35] Sudip Chakravarty, Bertrand I. Halperin, and David R. Nelson. Two-dimensional quantum heisenberg antiferromagnet at low temperatures. *Phys. Rev. B*, 39:2344–2371, Feb 1989.

[36] Sudip Chakravarty and Hae-Young Kee. Fermi pockets and quantum oscillations of the hall coefficient in high-temperature superconductors. *Proceedings of the National Academy of Sciences*, 105(26):8835–8839, 2008.

[37] Sudip Chakravarty, R. Laughlin, Dirk Morr, and Chetan Nayak. Hidden order in the cuprates. *Phys. Rev. B*, 63:094503, Jan 2001.

[38] M. K. Chan, M. J. Veit, C. J. Dorow, Y. Ge, Y. Li, W. Tabis, Y. Tang, X. Zhao, N. Bari**v**sić, and M. Greven. In-plane magnetoresistance obeys kohler's rule in the pseudogap phase of cuprate superconductors. *Phys. Rev. Lett.*, 113:177005, Oct 2014.

[39] J. Chang, E. Blackburn, A. T. Holmes, N. B. Christensen, J. Larsen, J. Mesot, Ruixing Liang, D. A. Bonn, W. N. Hardy, A. Watenphul, M. v. Zimmermann, E. M. Forgan, and S. M. Hayden. Direct observation of competition between superconductivity and charge density wave order in $YBa_2Cu_3O_{6.67}$. *Nat Phys*, 8(12):871–876, 12 2012.

[40] J. Chang, N. B. Christensen, Ch. Niedermayer, K. Lefmann, H. M. Rønnow, D. F. McMorrow, A. Schneidewind, P. Link, A. Hiess, M. Boehm, R. Mottl, S. Pailhés, N. Momono, M. Oda, M. Ido, and J. Mesot. Magnetic-Field-Induced Soft-Mode Quantum Phase Transition in the High-Temperature Superconductor $La_{1.855}Sr_{0.145}CuO_4$: An Inelastic Neutron-Scattering Study. *Phys. Rev. Lett.*, 102:177006, Apr 2009.

[41] C.-C. Chen, J. Maciejko, A. P. Sorini, B. Moritz, R. R. P. Singh, and T. P. Devereaux. Orbital order and spontaneous orthorhombicity in iron pnictides. *Phys. Rev. B*, 82:100504, Sep 2010.

[42] D. Chowdhury and S. Sachdev. The Enigma of the Pseudogap Phase of the Cuprate Superconductors. In J. Jedrzejewski, editor, *QUANTUM CRITICALITY IN CONDENSED MATTER: PHENOMENA, MATERIALS*

AND IDEAS IN THEORY AND EXPERIMENT - 50TH KARPACZ WINTER SCHOOL OF THEORETICAL PHYSICS. Edited by JEDRZEJEWSKI JANUSZ. Published by World Scientific Publishing Co. Pte. Ltd., 2015. ISBN #9789814704090, pp. 1-43, pages 1–43, July 2015.

[43] Debanjan Chowdhury, J. Orenstein, Subir Sachdev, and T. Senthil. Phase transition beneath the superconducting dome in $BaFe_2(As_{1-x}P_x)_2$. *Phys. Rev. B*, 92:081113, Aug 2015.

[44] Debanjan Chowdhury and Subir Sachdev. Density-wave instabilities of fractionalized fermi liquids. *Phys. Rev. B*, 90:245136, Dec 2014.

[45] Debanjan Chowdhury and Subir Sachdev. Feedback of superconducting fluctuations on charge order in the underdoped cuprates. *Phys. Rev. B*, 90:134516, Oct 2014.

[46] Debanjan Chowdhury and Subir Sachdev. Higgs criticality in a two-dimensional metal. *Phys. Rev. B*, 91:115123, Mar 2015.

[47] Debanjan Chowdhury, Brian Swingle, Erez Berg, and Subir Sachdev. Singularity of the london penetration depth at quantum critical points in superconductors. *Phys. Rev. Lett.*, 111:157004, Oct 2013.

[48] Jiun-Haw Chu, James G. Analytis, Kristiaan De Greve, Peter L. McMahon, Zahirul Islam, Yoshihisa Yamamoto, and Ian R. Fisher. In-plane resistivity anisotropy in an underdoped iron arsenide superconductor. *Science*, 329(5993):824–826, 2010.

[49] T.-M. Chuang, M. P. Allan, Jinho Lee, Yang Xie, Ni Ni, S. L. Budko, G. S. Boebinger, P. C. Canfield, and J. C. Davis. Nematic Electronic Structure in the Parent State of the Iron-Based Superconductor $Ca(Fe_{1-x}Co_x)_2As_2$. *Science*, 327(5962):181–184, 2010.

[50] P Coleman and N Andrei. Kondo-stabilised spin liquids and heavy fermion superconductivity. *Journal of Physics: Condensed Matter*, 1(26):4057, 1989.

[51] R. Comin, A. Frano, M. M. Yee, Y. Yoshida, H. Eisaki, E. Schierle, E. Weschke, R. Sutarto, F. He, A. Soumyanarayanan, Yang He, M. Le Tacon, I. S. Elfimov, Jennifer E. Hoffman, G. A. Sawatzky, B. Keimer, and A. Damascelli. Charge Order Driven by Fermi-Arc Instability in $Bi_2Sr_{2-x}La_xCuO_{6+\delta}$. *Science*, 343(6169):390–392, 2014.

[52] R. Comin, R. Sutarto, F. He, E. H. da Silva Neto, L. Chauviere, A. Frano, R. Liang, W. N. Hardy, D. A. Bonn, Y. Yoshida, H. Eisaki, A. J. Achkar, D. G. Hawthorn, B. Keimer, G. A. Sawatzky, and A. Damascelli. Symmetry of charge order in cuprates. *Nat Mater*, 14(8):796–800, 08 2015.

[53] N.J. Curro. NMR Investigations of Inhomogeneous glassy spin fluctuations in Doped $BaFe_2As_2$. *Bulletin of the American Physical Society (http://meetings.aps.org/Meeting/MAR15/Session/T5.7)*, 2015.

[54] J. Custers, P. Gegenwart, C. Geibel, F. Steglich, P. Coleman, and S. Paschen. Evidence for a Non-Fermi-Liquid Phase in Ge-Substituted $YbRh_2Si_2$. *Phys. Rev. Lett.*, 104:186402, May 2010.

[55] Eduardo H. da Silva Neto, Pegor Aynajian, Alex Frano, Riccardo Comin, Enrico Schierle, Eugen Weschke, Andrs Gyenis, Jinsheng Wen, John Schneeloch, Zhijun Xu, Shimpei Ono, Genda Gu, Mathieu Le Tacon, and Ali Yazdani. Ubiquitous interplay between charge ordering and high-temperature superconductivity in cuprates. *Science*, 343(6169):393–396, 2014.

[56] Elbio Dagotto, Eduardo Fradkin, and Adriana Moreo. Su(2) gauge invariance and order parameters in strongly coupled electronic systems. *Phys. Rev. B*, 38:2926–2929, Aug 1988.

[57] Pengcheng Dai, Jiangping Hu, and Elbio Dagotto. Magnetism and its microscopic origin in iron-based high-temperature superconductors. *Nat Phys*, 8(10):709–718, 10 2012.

[58] Andrea Damascelli, Zahid Hussain, and Zhi-Xun Shen. Angle-resolved photoemission studies of the cuprate superconductors. *Rev. Mod. Phys.*, 75:473–541, Apr 2003.

[59] R. Daou, J. Chang, David LeBoeuf, Olivier Cyr-Choiniere, Francis Laliberte, Nicolas Doiron-Leyraud, B. J. Ramshaw, Ruixing Liang, D. A. Bonn, W. N. Hardy, and Louis Taillefer. Broken rotational symmetry in the pseudogap phase of a high-tc superconductor. *Nature*, 463(7280):519–522, 01 2010.

[60] J. C. Séamus Davis and Dung-Hai Lee. Concepts relating magnetic interactions, intertwined electronic orders, and strongly correlated superconductivity. *Proceedings of the National Academy of Sciences*, 110(44):17623–17630, 2013.

[61] Vanuildo S. de Carvalho and Hermann Freire. Evidence of a short-range incommensurate -wave charge order from a fermionic two-loop renormalization group calculation of a 2d model with hot spots. *Annals of Physics*, 348:32 – 49, 2014.

[62] Eugene Demler, Subir Sachdev, and Ying Zhang. Spin-ordering quantum transitions of superconductors in a magnetic field. *Phys. Rev. Lett.*, 87:067202, Jul 2001.

[63] A. P. Dioguardi, J. Crocker, A. C. Shockley, C. H. Lin, K. R. Shirer, D. M. Nisson, M. M. Lawson, N. apRoberts Warren, P. C. Canfield, S. L. Bud'ko, S. Ran,

and N. J. Curro. Coexistence of Cluster Spin Glass and Superconductivity in $Ba(Fe_{1-x}Co_x)_2As_2$ for $0.060 \leq x \leq 0.071$. *Phys. Rev. Lett.*, 111:207201, Nov 2013.

[64] N. Doiron-Leyraud, S. Badoux, S. Renéde Cotret, S. Lepault, D. LeBoeuf, F. Laliberté, E. Hassinger, B. J. Ramshaw, D. A. Bonn, W. N. Hardy, R. Liang, J. H. . Park, D. Vignolles, B. Vignolle, L. Taillefer, and C. Proust. Evidence for a small hole pocket in the Fermi surface of underdoped $YBa_2Cu_3O_y$. *Nat Commun*, 6, 01 2015.

[65] Nicolas Doiron-Leyraud, Cyril Proust, David LeBoeuf, Julien Levallois, Jean-Baptiste Bonnemaison, Ruixing Liang, D. A. Bonn, W. N. Hardy, and Louis Taillefer. Quantum oscillations and the fermi surface in an underdoped high-tc superconductor. *Nature*, 447(7144):565–568, 05 2007.

[66] S. V. Dordevic, D. N. Basov, and C. C. Homes. Do organic and other exotic superconductors fail universal scaling relations? *Scientific Reports*, 3:1713 EP –, 04 2013.

[67] K. B. Efetov, H. Meier, and C. Pepin. Pseudogap state near a quantum critical point. *Nat Phys*, 9(7):442–446, 07 2013.

[68] Chen Fang, Hong Yao, Wei-Feng Tsai, JiangPing Hu, and Steven A. Kivelson. Theory of electron nematic order in lafeaso. *Phys. Rev. B*, 77:224509, Jun 2008.

[69] R. M. Fernandes, A. V. Chubukov, and J. Schmalian. What drives nematic order in iron-based superconductors? *Nat Phys*, 10(2):97–104, 02 2014.

[70] Rafael M. Fernandes, Saurabh Maiti, Peter Wölfle, and Andrey V. Chubukov. How many quantum phase transitions exist inside the superconducting dome of the iron pnictides? *Phys. Rev. Lett.*, 111:057001, Jul 2013.

[71] M. Ferrero, P. S. Cornaglia, L. De Leo, O. Parcollet, G. Kotliar, and A. Georges. Valence bond dynamical mean-field theory of doped mott insulators with nodal/antinodal differentiation. *EPL (Europhysics Letters)*, 85(5):57009, 2009.

[72] Michel Ferrero, Pablo Cornaglia, Lorenzo De Leo, Olivier Parcollet, Gabriel Kotliar, and Antoine Georges. Pseudogap opening and formation of fermi arcs as an orbital-selective mott transition in momentum space. *Phys. Rev. B*, 80:064501, Aug 2009.

[73] Mark H Fischer, Si Wu, Michael Lawler, Arun Paramekanti, and Eun-Ah Kim. Nematic and spin-charge orders driven by hole-doping a charge-transfer insulator. *New Journal of Physics*, 16(9):093057, 2014.

[74] Eduardo Fradkin, Steven A. Kivelson, and John M. Tranquada. *Colloquium* : Theory of intertwined orders in high temperature superconductors. *Rev. Mod. Phys.*, 87:457–482, May 2015.

[75] S. Friedemann, T. Westerkamp, M. Brando, N. Oeschler, S. Wirth, P. Gegenwart, C. Krellner, C. Geibel, and F. Steglich. Detaching the antiferromagnetic quantum critical point from the Fermi-surface reconstruction in $YbRh_2Si_2$. *Nat Phys*, 5(7):465–469, 07 2009.

[76] K. Fujita, Chung Koo Kim, Inhee Lee, Jinho Lee, M. H. Hamidian, I. A. Firmo, S. Mukhopadhyay, H. Eisaki, S. Uchida, M. J. Lawler, E.-A. Kim, and J. C. Davis. Simultaneous transitions in cuprate momentum-space topology and electronic symmetry breaking. *Science*, 344(6184):612–616, 2014.

[77] Kazuhiro Fujita, Mohammad H. Hamidian, Stephen D. Edkins, Chung Koo Kim, Yuhki Kohsaka, Masaki Azuma, Mikio Takano, Hidenori Takagi, Hiroshi Eisaki, Shin-ichi Uchida, Andrea Allais, Michael J. Lawler, Eun-Ah Kim, Subir Sachdev, and J. C. Séamus Davis. Direct phase-sensitive identification of a d-form factor density wave in underdoped cuprates. *Proc. Nat. Acad. Sci.*, 111(30):E3026–E3032, 2014.

[78] G. Ghiringhelli, M. Le Tacon, M. Minola, S. Blanco-Canosa, C. Mazzoli, N. B. Brookes, G. M. De Luca, A. Frano, D. G. Hawthorn, F. He, T. Loew, M. Moretti Sala, D. C. Peets, M. Salluzzo, E. Schierle, R. Sutarto, G. A. Sawatzky, E. Weschke, B. Keimer, and L. Braicovich. Long-Range Incommensurate Charge Fluctuations in $(Y,Nd)Ba_2Cu_3O_{6+x}$. *Science*, 337(6096):821–825, 2012.

[79] R. T. Gordon, H. Kim, N. Salovich, R. W. Giannetta, R. M. Fernandes, V. G. Kogan, T. Prozorov, S. L. Bud'ko, P. C. Canfield, M. A. Tanatar, and R. Prozorov. Doping evolution of the absolute value of the London penetration depth and superfluid density in single crystals of $Ba(Fe_{1-x}Co_x)_2As_2$. *Phys. Rev. B*, 82:054507, Aug 2010.

[80] Emanuel Gull, Olivier Parcollet, and Andrew Millis. Superconductivity and the pseudogap in the two-dimensional hubbard model. *Phys. Rev. Lett.*, 110:216405, May 2013.

[81] N. Harrison and S. Sebastian. Protected nodal electron pocket from multiple-**Q** ordering in underdoped high temperature superconductors. *Phys. Rev. Lett.*, 106:226402, May 2011.

[82] Sean A. Hartnoll, Diego M. Hofman, Max A. Metlitski, and Subir Sachdev. Quantum critical response at the onset of spin-density-wave order in two-dimensional metals. *Phys. Rev. B*, 84:125115, Sep 2011.

[83] Sean A. Hartnoll, Pavel K. Kovtun, Markus Müller, and Subir Sachdev. Theory of the nernst effect near quantum phase transitions in condensed matter and in dyonic black holes. *Phys. Rev. B*, 76:144502, Oct 2007.

[84] Sean A. Hartnoll, Raghu Mahajan, Matthias Punk, and Subir Sachdev. Transport near the ising-nematic quantum critical point of metals in two dimensions. *Phys. Rev. B*, 89:155130, Apr 2014.

[85] K. Hashimoto, K. Cho, T. Shibauchi, S. Kasahara, Y. Mizukami, R. Katsumata, Y. Tsuruhara, T. Terashima, H. Ikeda, M. A. Tanatar, H. Kitano, N. Salovich, R. W. Giannetta, P. Walmsley, A. Carrington, R. Prozorov, and Y. Matsuda. A Sharp Peak of the Zero-Temperature Penetration Depth at Optimal Composition in $BaFe_2(As_{1-x}P_x)_2$. *Science*, 336(6088):1554–1557, 2012.

[86] K. Hashimoto, M. Yamashita, S. Kasahara, Y. Senshu, N. Nakata, S. Tonegawa, K. Ikada, A. Serafin, A. Carrington, T. Terashima, H. Ikeda, T. Shibauchi, and Y. Matsuda. Line nodes in the energy gap of superconducting $BaFe_2(As_{1-x}P_x)_2$ single crystals as seen via penetration depth and thermal conductivity. *Phys. Rev. B*, 81:220501, Jun 2010.

[87] Makoto Hashimoto, Rui-Hua He, Kiyohisa Tanaka, Jean-Pierre Testaud, Worawat Meevasana, Rob G. Moore, Donghui Lu, Hong Yao, Yoshiyuki Yoshida, Hiroshi Eisaki, Thomas P. Devereaux, Zahid Hussain, and Zhi-Xun Shen. Particle-hole symmetry breaking in the pseudogap state of bi2201. *Nat Phys*, 6(6):414–418, 06 2010.

[88] Makoto Hashimoto, Elizabeth A. Nowadnick, Rui-Hua He, Inna M. Vishik, Brian Moritz, Yu He, Kiyohisa Tanaka, Robert G. Moore, Donghui Lu, Yoshiyuki Yoshida, Motoyuki Ishikado, Takao Sasagawa, Kazuhiro Fujita, Shigeyuki Ishida, Shinichi Uchida, Hiroshi Eisaki, Zahid Hussain, Thomas P. Devereaux, and Zhi-Xun Shen. Direct spectroscopic evidence for phase competition between the pseudogap and superconductivity in $Bi_2Sr_2CaCu_2O_{8+\delta}$. *Nat Mater*, 14(1):37–42, 01 2015.

[89] D Haug, V Hinkov, Y Sidis, P Bourges, N B Christensen, A Ivanov, T Keller, C T Lin, and B Keimer. Neutron scattering study of the magnetic phase diagram of underdoped YBa_2Cu_3 O_{6+x}. *New Journal of Physics*, 12(10):105006, 2010.

[90] Lauren E. Hayward, Andrew J. Achkar, David G. Hawthorn, Roger G. Melko, and Subir Sachdev. Diamagnetism and density-wave order in the pseudogap regime of $YBa_2Cu_3O_{6+x}$. *Phys. Rev. B*, 90:094515, Sep 2014.

[91] Lauren E. Hayward, David G. Hawthorn, Roger G. Melko, and Subir Sachdev. Angular Fluctuations of a Multicomponent Order Describe the Pseudogap of $YBa_2Cu_3O_{6+x}$. *Science*, 343(6177):1336–1339, 2014.

[92] Yang He, Yi Yin, M. Zech, Anjan Soumyanarayanan, Michael M. Yee, Tess Williams, M. C. Boyer, Kamalesh Chatterjee, W. D. Wise, I. Zeljkovic, Takeshi Kondo, T. Takeuchi, H. Ikuta, Peter Mistark, Robert S. Markiewicz, Arun Bansil, Subir Sachdev, E. W. Hudson, and J. E. Hoffman. Fermi surface and pseudogap evolution in a cuprate superconductor. *Science*, 344(6184):608–611, 2014.

[93] John A. Hertz. Quantum critical phenomena. *Phys. Rev. B*, 14:1165–1184, Aug 1976.

[94] V. Hinkov, D. Haug, B. Fauqu, P. Bourges, Y. Sidis, A. Ivanov, C. Bernhard, C. T. Lin, and B. Keimer. Electronic Liquid Crystal State in the High-Temperature Superconductor $YBa_2Cu_3O_{6.45}$. *Science*, 319(5863):597–600, 2008.

[95] V. Hinkov, B. Keimer, A. Ivanov, P. Bourges, Y. Sidis, and C. D. Frost. Neutron scattering study and analytical description of the spin excitation spectrum of twin-free $YBa_2Cu_3O_{6.6}$. *ArXiv e-prints*, June 2010.

[96] J. E. Hoffman, E. W. Hudson, K. M. Lang, V. Madhavan, H. Eisaki, S. Uchida, and J. C. Davis. A Four Unit Cell Periodic Pattern of Quasi-Particle States Surrounding Vortex Cores in $Bi_2Sr_2CaCu_2O_{8+\delta}$. *Science*, 295(5554):466–469, 2002.

[97] Tobias Holder and Walter Metzner. Incommensurate nematic fluctuations in two-dimensional metals. *Phys. Rev. B*, 85:165130, Apr 2012.

[98] C. C. Homes, S. V. Dordevic, M. Strongin, D. A. Bonn, Ruixing Liang, W. N. Hardy, Seiki Komiya, Yoichi Ando, G. Yu, N. Kaneko, X. Zhao, M. Greven, D. N. Basov, and T. Timusk. A universal scaling relation in high-temperature superconductors. *Nature*, 430(6999):539–541, 07 2004.

[99] Sungkun Hong, Michael S. Grinolds, Linh M. Pham, David Le Sage, Lan Luan, Ronald L. Walsworth, and Amir Yacoby. Nanoscale magnetometry with nv centers in diamond. *MRS Bulletin*, 38:155–161, 2 2013.

[100] C. Howald, H. Eisaki, N. Kaneko, M. Greven, and A. Kapitulnik. Periodic density-of-states modulations in superconducting $Bi_2Sr_2CaCu_2O_{8+\delta}$. *Phys. Rev. B*, 67:014533, Jan 2003.

[101] Chia-Ren Hu. Midgap surface states as a novel signature for $d_{x^2-y^2}$-wave superconductivity. *Phys. Rev. Lett.*, 72:1526–1529, Mar 1994.

[102] Ding Hu, Xingye Lu, Wenliang Zhang, Huiqian Luo, Shiliang Li, Peipei Wang, Genfu Chen, Fei Han, Shree R. Banjara, A. Sapkota, A. Kreyssig, A. I. Goldman, Z. Yamani, Christof Niedermayer, Markos Skoulatos, Robert

Georgii, T. Keller, Pengshuai Wang, Weiqiang Yu, and Pengcheng Dai. Structural and Magnetic Phase Transitions near Optimal Superconductivity in $BaFe_2(As_{1-x}P_x)_2$. *Phys. Rev. Lett.*, 114:157002, Apr 2015.

[103] Kenneth Hui and A. Nihat Berker. Random-field mechanism in random-bond multicritical systems. *Phys. Rev. Lett.*, 62:2507–2510, May 1989.

[104] Hsiang-Hsuan Hung, Can-Li Song, Xi Chen, Xucun Ma, Qi-kun Xue, and Congjun Wu. Anisotropic vortex lattice structures in the fese superconductor. *Phys. Rev. B*, 85:104510, Mar 2012.

[105] Christoph Husemann and Walter Metzner. Incommensurate nematic fluctuations in the two-dimensional hubbard model. *Phys. Rev. B*, 86:085113, Aug 2012.

[106] N E Hussey. Phenomenology of the normal state in-plane transport properties of high- t c cuprates. *Journal of Physics: Condensed Matter*, 20(12):123201, 2008.

[107] Yoseph Imry and Michael Wortis. Influence of quenched impurities on first-order phase transitions. *Phys. Rev. B*, 19:3580–3585, Apr 1979.

[108] R. Jackiw and C. Rebbi. Solitons with fermion number 1/2. *Phys. Rev. D*, 13:3398–3409, Jun 1976.

[109] A. P. Kampf and J. R. Schrieffer. Spectral function and photoemission spectra in antiferromagnetically correlated metals. *Phys. Rev. B*, 42:7967–7974, Nov 1990.

[110] A. Kanigel, M. R. Norman, M. Randeria, U. Chatterjee, S. Souma, A. Kaminski, H. M. Fretwell, S. Rosenkranz, M. Shi, T. Sato, T. Takahashi, Z. Z. Li, H. Raffy, K. Kadowaki, D. Hinks, L. Ozyuzer, and J. C. Campuzano. Evolution of the pseudogap from fermi arcs to the nodal liquid. *Nat Phys*, 2(7):447–451, 07 2006.

[111] S. Kasahara, H. J. Shi, K. Hashimoto, S. Tonegawa, Y. Mizukami, T. Shibauchi, K. Sugimoto, T. Fukuda, T. Terashima, Andriy H. Nevidomskyy, and Y. Matsuda. Electronic nematicity above the structural and superconducting transition in $BaFe_2(As_{1-x}P_x)_2$. *Nature*, 486(7403):382–385, 06 2012.

[112] S. Kasahara, T. Shibauchi, K. Hashimoto, K. Ikada, S. Tonegawa, R. Okazaki, H. Shishido, H. Ikeda, H. Takeya, K. Hirata, T. Terashima, and Y. Matsuda. Evolution from non-fermi- to fermi-liquid transport via isovalent doping in ${}_{\mathrm{bafe}_2}({}_{\mathrm{As}_{1-x}\mathrm{P}_x})_2$ superconductors. *Phys. Rev. B*, 81:184519, May 2010.

[113] Ribhu Kaul, Alexei Kolezhuk, Michael Levin, Subir Sachdev, and T. Senthil. Hole dynamics in an antiferromagnet across a deconfined quantum critical point. *Phys. Rev. B*, 75:235122, Jun 2007.

[114] Ribhu Kaul, Max Metlitski, Subir Sachdev, and Cenke Xu. Destruction of néel order in the cuprates by electron doping. *Phys. Rev. B*, 78:045110, Jul 2008.

[115] Ribhu K. Kaul, Yong Baek Kim, Subir Sachdev, and T. Senthil. Algebraic charge liquids. *Nat Phys*, 4(1):28–31, 01 2008.

[116] Shinji Kawasaki, Chengtian Lin, Philip L. Kuhns, Arneil P. Reyes, and Guo-qing Zheng. Carrier-Concentration Dependence of the Pseudogap Ground State of Superconducting $Bi_2Sr_{2-x}La_xCuO_{6+\delta}$ revealed by ^{63,65}Cu-Nuclear Magnetic Resonance in Very High Magnetic Fields. *Phys. Rev. Lett.*, 105:137002, Sep 2010.

[117] Hae-Young Kee, Christoph M Puetter, and David Stroud. Transport signatures of electronic-nematic stripe phases. *Journal of Physics: Condensed Matter*, 25(20):202201, 2013.

[118] B. Keimer, N. Belk, R. J. Birgeneau, A. Cassanho, C. Y. Chen, M. Greven, M. A. Kastner, A. Aharony, Y. Endoh, R. W. Erwin, and G. Shirane. Magnetic excitations in pure, lightly doped, and weakly metallic La_2CuO_4. *Phys. Rev. B*, 46:14034–14053, Dec 1992.

[119] B Keimer, SA Kivelson, MR Norman, S Uchida, and J Zaanen. From quantum matter to high-temperature superconductivity in copper oxides. *Nature*, 518(7538):179–186, 2015.

[120] B. Khaykovich, S. Wakimoto, R. J. Birgeneau, M. A. Kastner, Y. S. Lee, P. Smeibidl, P. Vorderwisch, and K. Yamada. Field-induced transition between magnetically disordered and ordered phases in underdoped $La_{2-x}Sr_xCuO_4$. *Phys. Rev. B*, 71:220508, Jun 2005.

[121] Eun-Ah Kim, Michael J. Lawler, Paul Oreto, Subir Sachdev, Eduardo Fradkin, and Steven A. Kivelson. Theory of the nodal nematic quantum phase transition in superconductors. *Phys. Rev. B*, 77:184514, May 2008.

[122] S. A. Kivelson, I. P. Bindloss, E. Fradkin, V. Oganesyan, J. M. Tranquada, A. Kapitulnik, and C. Howald. How to detect fluctuating stripes in the high-temperature superconductors. *Rev. Mod. Phys.*, 75:1201–1241, Oct 2003.

[123] Steven Kivelson, Daniel Rokhsar, and James Sethna. Topology of the resonating valence-bond state: Solitons and high-T_c superconductivity. *Phys. Rev. B*, 35:8865–8868, Jun 1987.

[124] Steven A. Kivelson, Dung-Hai Lee, Eduardo Fradkin, and Vadim Oganesyan. Competing order in the mixed state of high-temperature superconductors. *Phys. Rev. B*, 66:144516, Oct 2002.

[125] Y. Kohsaka, C. Taylor, K. Fujita, A. Schmidt, C. Lupien, T. Hanaguri, M. Azuma, M. Takano, H. Eisaki, H. Takagi, S. Uchida, and J. C. Davis. An intrinsic bond-centered electronic glass with unidirectional domains in underdoped cuprates. *Science*, 315(5817):1380–1385, 2007.

[126] I. Kokanović, D. Hills, M. Sutherland, R. Liang, and J. Cooper. Diamagnetism of $YBa_2Cu_3O_{6+x}$ crystals above T_c: Evidence for Gaussian fluctuations. *Phys. Rev. B*, 88:060505, Aug 2013.

[127] Takeshi Kondo, Ari D. Palczewski, Yoichiro Hamaya, Tsunehiro Takeuchi, J. S. Wen, Z. J. Xu, Genda Gu, and Adam Kaminski. Formation of gapless fermi arcs and fingerprints of order in the pseudogap state of cuprate superconductors. *Phys. Rev. Lett.*, 111:157003, Oct 2013.

[128] Frank Krüger, Sanjeev Kumar, Jan Zaanen, and Jeroen van den Brink. Spin-orbital frustrations and anomalous metallic state in iron-pnictide superconductors. *Phys. Rev. B*, 79:054504, Feb 2009.

[129] B. Lake, H. M. Ronnow, N. B. Christensen, G. Aeppli, K. Lefmann, D. F. McMorrow, P. Vorderwisch, P. Smeibidl, N. Mangkorntong, T. Sasagawa, M. Nohara, H. Takagi, and T. E. Mason. Antiferromagnetic order induced by an applied magnetic field in a high-temperature superconductor. *Nature*, 415(6869):299–302, 01 2002.

[130] M. J. Lawler, K. Fujita, Jhinhwan Lee, A. R. Schmidt, Y. Kohsaka, Chung Koo Kim, H. Eisaki, S. Uchida, J. C. Davis, J. P. Sethna, and Eun-Ah Kim. Intra-unit-cell electronic nematicity of the high-tc copper-oxide pseudogap states. *Nature*, 466(7304):347–351, 07 2010.

[131] David LeBoeuf, Nicolas Doiron-Leyraud, Julien Levallois, R. Daou, J. B. Bonnemaison, N. E. Hussey, L. Balicas, B. J. Ramshaw, Ruixing Liang, D. A. Bonn, W. N. Hardy, S. Adachi, Cyril Proust, and Louis Taillefer. Electron pockets in the fermi surface of hole-doped high-tc superconductors. *Nature*, 450(7169):533–536, 11 2007.

[132] David LeBoeuf, S. Kramer, W. N. Hardy, Ruixing Liang, D. A. Bonn, and Cyril Proust. Thermodynamic phase diagram of static charge order in underdoped $YBa_2Cu_3O_y$. *Nat Phys*, 9(2):79–83, 02 2013.

[133] Junhyun Lee, Philipp Strack, and Subir Sachdev. Quantum criticality of reconstructing fermi surfaces in antiferromagnetic metals. *Phys. Rev. B*, 87:045104, Jan 2013.

[134] Patrick A. Lee. Amperean pairing and the pseudogap phase of cuprate superconductors. *Phys. Rev. X*, 4:031017, Jul 2014.

[135] Patrick A. Lee, Naoto Nagaosa, and Xiao-Gang Wen. Doping a mott insulator: Physics of high-temperature superconductivity. *Rev. Mod. Phys.*, 78:17–85, Jan 2006.

[136] Sung-Sik Lee. Low-energy effective theory of fermi surface coupled with u(1) gauge field in $2+1$ dimensions. *Phys. Rev. B*, 80:165102, Oct 2009.

[137] A. Levchenko, M. G. Vavilov, M. Khodas, and A. V. Chubukov. Enhancement of the london penetration depth in pnictides at the onset of spin-density-wave order under superconducting dome. *Phys. Rev. Lett.*, 110:177003, Apr 2013.

[138] Jian-Xin Li, Chang-Qin Wu, and Dung-Hai Lee. Checkerboard charge density wave and pseudogap of high-T_c cuprate. *Phys. Rev. B*, 74:184515, Nov 2006.

[139] Lu Li, Yayu Wang, Seiki Komiya, Shimpei Ono, Yoichi Ando, G. Gu, and N. Ong. Diamagnetism and cooper pairing above T_c in cuprates. *Phys. Rev. B*, 81:054510, Feb 2010.

[140] Y. Li, V. Baledent, N. Barisic, Y. Cho, B. Fauque, Y. Sidis, G. Yu, X. Zhao, P. Bourges, and M. Greven. Unusual magnetic order in the pseudogap region of the superconductor $HgBa_2CuO_{4+\delta}$. *Nature*, 455(7211):372–375, 09 2008.

[141] E.M. Lifshitz and L.P. Pitaevskii. *Statistical Physics: Theory of the Condensed State (Course of Theoretical Physics Vol. 9)*. Butterworth-Heinemann, 1980.

[142] J. M. Luttinger. Fermi surface and some simple equilibrium properties of a system of interacting fermions. *Phys. Rev.*, 119:1153–1163, Aug 1960.

[143] Akash V. Maharaj, Pavan Hosur, and S. Raghu. Crisscrossed stripe order from interlayer tunneling in hole-doped cuprates. *Phys. Rev. B*, 90:125108, Sep 2014.

[144] Z. Lotfi Mahyari, A. Cannell, E. V. L. de Mello, M. Ishikado, H. Eisaki, Ruixing Liang, D. A. Bonn, and J. E. Sonier. Universal inhomogeneous magnetic-field response in the normal state of cuprate high-T_c superconductors. *Phys. Rev. B*, 88:144504, Oct 2013.

[145] J. Maldacena. The symmetry and simplicity of the laws of physics and the Higgs boson. *ArXiv e-prints*, October 2014.

[146] T. M. McQueen, A. J. Williams, P. W. Stephens, J. Tao, Y. Zhu, V. Ksenofontov, F. Casper, C. Felser, and R. J. Cava. Tetragonal-to-Orthorhombic Structural Phase Transition at 90 K in the Superconductor $Fe_{1.01}Se$. *Phys. Rev. Lett.*, 103:057002, Jul 2009.

[147] S. Medvedev, T. M. McQueen, I. A. Troyan, T. Palasyuk, M. I. Eremets, R. J. Cava, S. Naghavi, F. Casper, V. Ksenofontov, G. Wortmann, and C. Felser. Electronic and magnetic phase diagram of β-$Fe_{1.01}Se$ with superconductivity at 36.7 K under pressure. *Nat Mater*, 8(8):630–633, 08 2009.

[148] Jia-Wei Mei, Shinji Kawasaki, Guo-Qing Zheng, Zheng-Yu Weng, and Xiao-Gang Wen. Luttinger-volume violating fermi liquid in the pseudogap phase of the cuprate superconductors. *Phys. Rev. B*, 85:134519, Apr 2012.

[149] H. Meier, C. Pépin, M. Einenkel, and K. B. Efetov. Cascade of phase transitions in the vicinity of a quantum critical point. *Phys. Rev. B*, 89:195115, May 2014.

[150] Ashot Melikyan and M. R. Norman. Symmetry of the charge density wave in cuprates. *Phys. Rev. B*, 89:024507, Jan 2014.

[151] A. Mesaros, K. Fujita, H. Eisaki, S. Uchida, J. C. Davis, S. Sachdev, J. Zaanen, M. J. Lawler, and Eun-Ah Kim. Topological defects coupling smectic modulations to intra unit-cell nematicity in cuprates. *Science*, 333(6041):426–430, 2011.

[152] Max A. Metlitski, David F. Mross, Subir Sachdev, and T. Senthil. Cooper pairing in non-fermi liquids. *Phys. Rev. B*, 91:115111, Mar 2015.

[153] Max A. Metlitski and Subir Sachdev. Quantum phase transitions of metals in two spatial dimensions. i. ising-nematic order. *Phys. Rev. B*, 82:075127, Aug 2010.

[154] Max A. Metlitski and Subir Sachdev. Quantum phase transitions of metals in two spatial dimensions. ii. spin density wave order. *Phys. Rev. B*, 82:075128, Aug 2010.

[155] T. Micklitz and M. R. Norman. Nature of spectral gaps due to pair formation in superconductors. *Phys. Rev. B*, 80:220513, Dec 2009.

[156] A. J. Millis. Effect of a nonzero temperature on quantum critical points in itinerant fermion systems. *Phys. Rev. B*, 48:7183–7196, Sep 1993.

[157] Seyed Iman Mirzaei, Damien Stricker, Jason N. Hancock, Christophe Berthod, Antoine Georges, Erik van Heumen, Mun K. Chan, Xudong Zhao, Yuan Li, Martin Greven, Neven Bari**v**sić, and Dirk van der Marel. Spectroscopic evidence for fermi liquid-like energy and temperature dependence of the relaxation rate in the pseudogap phase of the cuprates. *Proc. Nat. Acad. Sci.*, 110(15):5774–5778, 2013.

[158] K. Miyake, S. Schmitt-Rink, and C. Varma. Spin-fluctuation-mediated even-parity pairing in heavy-fermion superconductors. *Phys. Rev. B*, 34:6554–6556, Nov 1986.

[159] Y. Mizukami, M. Konczykowski, Y. Kawamoto, S. Kurata, S. Kasahara, K. Hashimoto, V. Mishra, A. Kreisel, Y. Wang, P. J. Hirschfeld, Y. Matsuda, and T. Shibauchi. Disorder-induced topological change of the superconducting gap structure in iron pnictides. *Nat Commun*, 5, 11 2014.

[160] H. A. Mook, M. D. Lumsden, A. D. Christianson, B. C. Sales, R. Jin, M. A. McGuire, A. Sefat, D. Mandrus, S. E. Nagler, T. Egami, and C. de la Cruz. Neutron scattering patterns show Superconductivity in $FeTe_{0.5}Se_{0.5}$ likely results from itinerant electron fluctuations. *ArXiv e-prints*, April 2009.

[161] Eun Gook Moon and Subir Sachdev. Competition between spin density wave order and superconductivity in the underdoped cuprates. *Phys. Rev. B*, 80:035117, Jul 2009.

[162] Eun Gook Moon and Subir Sachdev. Underdoped cuprates as fractionalized fermi liquids: Transition to superconductivity. *Phys. Rev. B*, 83:224508, Jun 2011.

[163] S. J. Moon, Y. S. Lee, A. A. Schafgans, A. V. Chubukov, S. Kasahara, T. Shibauchi, T. Terashima, Y. Matsuda, M. A. Tanatar, R. Prozorov, A. Thaler, P. C. Canfield, S. L. Bud'ko, A. S. Sefat, D. Mandrus, K. Segawa, Y. Ando, and D. N. Basov. Infrared pseudogap in cuprate and pnictide high-temperature superconductors. *Phys. Rev. B*, 90:014503, Jul 2014.

[164] E. M. Motoyama, G. Yu, I. M. Vishik, O. P. Vajk, P. K. Mang, and M. Greven. Spin correlations in the electron-doped high-transition-temperature superconductor $Nd_{2-x}Ce_xCuO_{4+\delta}$. *Nature*, 445(7124):186–189, 01 2007.

[165] Olexei Motrunich and Ashvin Vishwanath. Emergent photons and transitions in the O(3) sigma model with hedgehog suppression. *Phys. Rev. B*, 70:075104, Aug 2004.

[166] David F. Mross, John McGreevy, Hong Liu, and T. Senthil. Controlled expansion for certain non-fermi-liquid metals. *Phys. Rev. B*, 82:045121, Jul 2010.

[167] Yusuke Nakai, Tetsuya Iye, Shunsaku Kitagawa, Kenji Ishida, Shigeru Kasahara, Takasada Shibauchi, Yuji Matsuda, and Takahito Terashima. ^{31}P and ^{75}As NMR evidence for a residual density of states at zero energy in superconducting $BaFe_2(As_{0.67}P_{0.33})_2$. *Phys. Rev. B*, 81:020503, Jan 2010.

[168] M. Nakajima, T. Liang, S. Ishida, Y. Tomioka, K. Kihou, C. H. Lee, A. Iyo, H. Eisaki, T. Kakeshita, T. Ito, and S. Uchida. Unprecedented anisotropic metallic state in undoped iron arsenide $BaFe_2As_2$ revealed by optical spectroscopy. *Proceedings of the National Academy of Sciences*, 108(30):12238–12242, 2011.

[169] S. Nakatsuji, K. Kuga, Y. Machida, T. Tayama, T. Sakakibara, Y. Karaki, H. Ishimoto, S. Yonezawa, Y. Maeno, E. Pearson, G. G. Lonzarich, L. Balicas, H. Lee, and Z. Fisk. Superconductivity and quantum criticality in the heavy-fermion system β-$YbAlB_4$. *Nat Phys*, 4(8):603–607, 08 2008.

[170] Chetan Nayak. Density-wave states of nonzero angular momentum. *Phys. Rev. B*, 62:4880–4889, Aug 2000.

[171] Takuya Nomoto and Hiroaki Ikeda. Effect of magnetic criticality and fermi-surface topology on the magnetic penetration depth. *Phys. Rev. Lett.*, 111:167001, Oct 2013.

[172] M. R. Norman, D. Pines, and C. Kallin. The pseudogap: friend or foe of high t c ? *Advances in Physics*, 54(8):715–733, 2005.

[173] Masaki Oshikawa. Topological approach to luttinger's theorem and the fermi surface of a kondo lattice. *Phys. Rev. Lett.*, 84:3370–3373, Apr 2000.

[174] P.G. Pagliuso, R. Movshovich, A.D. Bianchi, M. Nicklas, N.O. Moreno, J.D. Thompson, M.F. Hundley, J.L. Sarrao, and Z. Fisk. Multiple phase transitions in ce(rh,ir,co)in_5. *Physica B: Condensed Matter*, 312313:129 – 131, 2002. The International Conference on Strongly Correlated Electron Systems.

[175] Arun Paramekanti and Ashvin Vishwanath. Extending luttinger's theorem to Z_2 fractionalized phases of matter. *Phys. Rev. B*, 70:245118, Dec 2004.

[176] Aavishkar A. Patel, Debanjan Chowdhury, Andrea Allais, and Subir Sachdev. Confinement transition to density wave order in metallic doped spin liquids. *Phys. Rev. B*, 93:165139, Apr 2016.

[177] Aavishkar A. Patel and Subir Sachdev. dc resistivity at the onset of spin density wave order in two-dimensional metals. *Phys. Rev. B*, 90:165146, Oct 2014.

[178] D C Peets, J D F Mottershead, B Wu, I S Elfimov, Ruixing Liang, W N Hardy, D A Bonn, M Raudsepp, N J C Ingle, and A Damascelli. Tl_2 Ba_2 $CuO_{6+\delta}$ brings spectroscopic probes deep into the overdoped regime of the high- T c cuprates. *New Journal of Physics*, 9(2):28, 2007.

[179] David Pekker and C.M. Varma. Amplitude/higgs modes in condensed matter physics. *Annual Review of Condensed Matter Physics*, 6(1):269–297, 2015.

[180] Andrea Pelissetto, Subir Sachdev, and Ettore Vicari. Nodal quasiparticles and the onset of spin-density-wave order in cuprate superconductors. *Phys. Rev. Lett.*, 101:027005, Jul 2008.

[181] M. Platé, J. Mottershead, I. Elfimov, D. Peets, Ruixing Liang, D. Bonn, W. Hardy, S. Chiuzbaian, M. Falub, M. Shi, L. Patthey, and A. Damascelli. Fermi Surface and Quasiparticle Excitations of Overdoped $Tl_2Ba_2CuO_{6+\delta}$. *Phys. Rev. Lett.*, 95:077001, Aug 2005.

[182] Matthias Punk, Andrea Allais, and Subir Sachdev. Quantum dimer model for the pseudogap metal. *Proceedings of the National Academy of Sciences*, 112(31):9552–9557, 2015.

[183] Matthias Punk and Subir Sachdev. Fermi surface reconstruction in hole-doped $t - j$ models without long-range antiferromagnetic order. *Phys. Rev. B*, 85:195123, May 2012.

[184] Yang Qi and Subir Sachdev. Effective theory of fermi pockets in fluctuating antiferromagnets. *Phys. Rev. B*, 81:115129, Mar 2010.

[185] Yiming Qiu, Wei Bao, Y. Zhao, Collin Broholm, V. Stanev, Z. Tesanovic, Y. C. Gasparovic, S. Chang, Jin Hu, Bin Qian, Minghu Fang, and Zhiqiang Mao. Spin Gap and Resonance at the Nesting Wave Vector in Superconducting $FeSe_{0.4}Te_{0.6}$. *Phys. Rev. Lett.*, 103:067008, Aug 2009.

[186] S. Raghu, S. A. Kivelson, and D. J. Scalapino. Superconductivity in the repulsive hubbard model: An asymptotically exact weak-coupling solution. *Phys. Rev. B*, 81:224505, Jun 2010.

[187] B. J. Ramshaw, S. E. Sebastian, R. D. McDonald, James Day, B. S. Tan, Z. Zhu, J. B. Betts, Ruixing Liang, D. A. Bonn, W. N. Hardy, and N. Harrison. Quasiparticle mass enhancement approaching optimal doping in a high-tc superconductor. *Science*, 348(6232):317–320, 2015.

[188] N. Read and Subir Sachdev. Large- N expansion for frustrated quantum antiferromagnets. *Phys. Rev. Lett.*, 66:1773–1776, Apr 1991.

[189] T. J. Reber, N. C. Plumb, Z. Sun, Y. Cao, Q. Wang, K. McElroy, H. Iwasawa, M. Arita, J. S. Wen, Z. J. Xu, G. Gu, Y. Yoshida, H. Eisaki, Y. Aiura, and D. S. Dessau. The origin and non-quasiparticle nature of Fermi arcs in $Bi_2Sr_2CaCu_2O_{8+\delta}$. *Nat Phys*, 8(8):606–610, 08 2012.

[190] Scott C. Riggs, O. Vafek, J. B. Kemper, J. B. Betts, A. Migliori, F. F. Balakirev, W. N. Hardy, Ruixing Liang, D. A. Bonn, and G. S. Boebinger. Heat capacity through the magnetic-field-induced resistive transition in an underdoped high-temperature superconductor. *Nat Phys*, 7(4):332–335, 04 2011.

[191] Daniel Rokhsar and Steven A. Kivelson. Superconductivity and the quantum hard-core dimer gas. *Phys. Rev. Lett.*, 61:2376–2379, Nov 1988.

[192] F. Rullier-Albenque, H. Alloul, F. Balakirev, and C. Proust. Disorder, metal-insulator crossover and phase diagram in high-t c cuprates. *EPL (Europhysics Letters)*, 81(3):37008, 2008.

[193] S. Sachdev. *Quantum Phase Transitions*. Cambridge University Press, 2nd Ed., 2011.

[194] Subir Sachdev. Colloquium:. *Rev. Mod. Phys.*, 75:913–932, Jul 2003.

[195] Subir Sachdev. Entangling superconductivity and antiferromagnetism. *Science*, 336(6088):1510–1511, 2012.

[196] Subir Sachdev and Rolando La Placa. Bond order in two-dimensional metals with antiferromagnetic exchange interactions. *Phys. Rev. Lett.*, 111:027202, Jul 2013.

[197] Subir Sachdev, Max Metlitski, Yang Qi, and Cenke Xu. Fluctuating spin density waves in metals. *Phys. Rev. B*, 80:155129, Oct 2009.

[198] Subir Sachdev, Max A Metlitski, and Matthias Punk. Antiferromagnetism in metals: from the cuprate superconductors to the heavy fermion materials. *Journal of Physics: Condensed Matter*, 24(29):294205, 2012.

[199] Jay D. Sau and Subir Sachdev. Mean-field theory of competing orders in metals with antiferromagnetic exchange interactions. *Phys. Rev. B*, 89:075129, Feb 2014.

[200] D. J. Scalapino. A common thread: The pairing interaction for unconventional superconductors. *Rev. Mod. Phys.*, 84:1383–1417, Oct 2012.

[201] D. J. Scalapino, E. Loh, and J. E. Hirsch. *d. Phys. Rev. B*, 34:8190–8192, Dec 1986.

[202] Thomas Schäfer and Kai Schwenzer. Non-fermi liquid effects in qcd at high density. *Phys. Rev. D*, 70:054007, Sep 2004.

[203] Thomas Schäfer and Kai Schwenzer. Low-energy dynamics in ultradegenerate qcd matter. *Phys. Rev. Lett.*, 97:092301, Aug 2006.

[204] Y. Schattner, M. H. Gerlach, S. Trebst, and E. Berg. Competing Orders in a Nearly Antiferromagnetic Metal. *ArXiv e-prints*, December 2015.

[205] Jörg Schmalian, David Pines, and Branko Stojković. Weak pseudogap behavior in the underdoped cuprate superconductors. *Phys. Rev. Lett.*, 80:3839–3842, Apr 1998.

[206] Suchitra E. Sebastian, N. Harrison, F. F. Balakirev, M. M. Altarawneh, P. A. Goddard, Ruixing Liang, D. A. Bonn, W. N. Hardy, and G. G. Lonzarich. Normal-state nodal electronic structure in underdoped high-tc copper oxides. *Nature*, 511(7507):61–64, 07 2014.

[207] Suchitra E Sebastian, Neil Harrison, and Gilbert G Lonzarich. Towards resolution of the fermi surface in underdoped high- t c superconductors. *Reports on Progress in Physics*, 75(10):102501, 2012.

[208] T. Senthil. Theory of a continuous mott transition in two dimensions. *Phys. Rev. B*, 78:045109, Jul 2008.

[209] T. Senthil. On the mass enhancement near optimal doping in high magnetic fields in the cuprates. *ArXiv e-prints*, October 2014.

[210] T. Senthil, Leon Balents, Subir Sachdev, Ashvin Vishwanath, and Matthew Fisher. Quantum criticality beyond the landau-ginzburg-wilson paradigm. *Phys. Rev. B*, 70:144407, Oct 2004.

[211] T. Senthil and Matthew P. A. Fisher. Z_2 gauge theory of electron fractionalization in strongly correlated systems. *Phys. Rev. B*, 62:7850–7881, Sep 2000.

[212] T. Senthil and Patrick A. Lee. Synthesis of the phenomenology of the underdoped cuprates. *Phys. Rev. B*, 79:245116, Jun 2009.

[213] T. Senthil, Subir Sachdev, and Matthias Vojta. Fractionalized fermi liquids. *Phys. Rev. Lett.*, 90:216403, May 2003.

[214] T. Senthil, Ashvin Vishwanath, Leon Balents, Subir Sachdev, and Matthew P. A. Fisher. Deconfined quantum critical points. *Science*, 303(5663):1490–1494, 2004.

[215] T. Senthil, Matthias Vojta, and Subir Sachdev. Weak magnetism and non-fermi liquids near heavy-fermion critical points. *Phys. Rev. B*, 69:035111, Jan 2004.

[216] Kangjun Seo, Han-Dong Chen, and Jiangping Hu. d-wave checkerboard order in cuprates. *Phys. Rev. B*, 76:020511, Jul 2007.

[217] Kyle M. Shen, F. Ronning, D. H. Lu, F. Baumberger, N. J. C. Ingle, W. S. Lee, W. Meevasana, Y. Kohsaka, M. Azuma, M. Takano, H. Takagi, and Z.-X. Shen. Nodal Quasiparticles and Antinodal Charge Ordering in $Ca_{2-x}Na_xCuO_2Cl_2$. *Science*, 307(5711):901–904, 2005.

[218] T. Shibauchi, A. Carrington, and Y. Matsuda. A quantum critical point lying beneath the superconducting dome in iron pnictides. *Annual Review of Condensed Matter Physics*, 5(1):113–135, 2014.

[219] T. Shimojima, F. Sakaguchi, K. Ishizaka, Y. Ishida, T. Kiss, M. Okawa, T. Togashi, C.-T. Chen, S. Watanabe, M. Arita, K. Shimada, H. Namatame, M. Taniguchi, K. Ohgushi, S. Kasahara, T. Terashima, T. Shibauchi, Y. Matsuda, A. Chainani, and S. Shin. Orbital-independent superconducting gaps in iron pnictides. *Science*, 332(6029):564–567, 2011.

[220] H. Shishido, A. F. Bangura, A. I. Coldea, S. Tonegawa, K. Hashimoto, S. Kasahara, P. M. C. Rourke, H. Ikeda, T. Terashima, R. Settai, Y. Ōnuki, D. Vignolles, C. Proust, B. Vignolle, A. McCollam, Y. Matsuda, T. Shibauchi, and A. Carrington. Evolution of the Fermi Surface of $BaFe_2(As_{1-x}\mathbf{P}_x)_2$ on Entering the Superconducting Dome. *Phys. Rev. Lett.*, 104:057008, Feb 2010.

[221] Boris Shraiman and Eric Siggia. Mobile vacancies in a quantum heisenberg antiferromagnet. *Phys. Rev. Lett.*, 61:467–470, Jul 1988.

[222] Boris I. Shraiman and Eric D. Siggia. Spiral phase of a doped quantum antiferromagnet. *Phys. Rev. Lett.*, 62:1564–1567, Mar 1989.

[223] R. R. P. Singh. Exchange Constants and Neutron Spectra of Iron Pnictide Materials. *ArXiv e-prints*, March 2009.

[224] Can-Li Song, Yi-Lin Wang, Peng Cheng, Ye-Ping Jiang, Wei Li, Tong Zhang, Zhi Li, Ke He, Lili Wang, Jin-Feng Jia, Hsiang-Hsuan Hung, Congjun Wu, Xucun Ma, Xi Chen, and Qi-Kun Xue. Direct observation of nodes and twofold symmetry in fese superconductor. *Science*, 332(6036):1410–1413, 2011.

[225] B. I. Spivak and S. A. Kivelson. Negative local superfluid densities: The difference between dirty superconductors and dirty bose liquids. *Phys. Rev. B*, 43:3740–3743, Feb 1991.

[226] J. P. Sun, K. Matsuura, G. Z. Ye, Y. Mizukami, M. Shimozawa, K. Matsubayashi, M. Yamashita, T. Watashige, S. Kasahara, Y. Matsuda, J.-Q. Yan, B. C. Sales, Y. Uwatoko, J.-G. Cheng, and T. Shibauchi. Dome-shaped magnetic order competing with high-temperature superconductivity at high pressures in FeSe. *ArXiv e-prints*, December 2015.

[227] Shouvik Sur and Sung-Sik Lee. Quasilocal strange metal. *Phys. Rev. B*, 91:125136, Mar 2015.

[228] W. Tabis, Y. Li, M. Le Tacon, L. Braicovich, A. Kreyssig, M. Minola, G. Dellea, E. Weschke, M. J. Veit, M. Ramazanoglu, A. I. Goldman, T. Schmitt, G. Ghiringhelli, N. Bariv̌sić, M. K. Chan, C. J. Dorow, G. Yu, X. Zhao, B. Keimer, and

M. Greven. Charge order and its connection with fermi-liquid charge transport in a pristine high-tc cuprate. *Nat Commun*, 5, 12 2014.

[229] Louis Taillefer. Fermi surface reconstruction in high- t c superconductors. *Journal of Physics: Condensed Matter*, 21(16):164212, 2009.

[230] Yukio Tanaka and Satoshi Kashiwaya. Theory of tunneling spectroscopy of d-wave superconductors. *Phys. Rev. Lett.*, 74:3451–3454, Apr 1995.

[231] A. Thomson and S. Sachdev. Charge ordering in three-band models of the cuprates. *ArXiv e-prints*, October 2014.

[232] J. M. Tranquada, B. J. Sternlieb, J. D. Axe, Y. Nakamura, and S. Uchida. Evidence for stripe correlations of spins and holes in copper oxide superconductors. *Nature*, 375(6532):561–563, 06 1995.

[233] A. M. Tsvelik and A. V. Chubukov. Composite charge order in the pseudogap region of the cuprates. *Phys. Rev. B*, 89:184515, May 2014.

[234] Jorden A. van Dam, Yuli V. Nazarov, Erik P. A. M. Bakkers, Silvano De Franceschi, and Leo P. Kouwenhoven. Supercurrent reversal in quantum dots. *Nature*, 442(7103):667–670, 08 2006.

[235] Michael Vershinin, Shashank Misra, S. Ono, Y. Abe, Yoichi Ando, and Ali Yazdani. Local Ordering in the Pseudogap State of the High-Tc Superconductor $Bi_2Sr_2CaCu_2O_{8+\delta}$. *Science*, 303(5666):1995–1998, 2004.

[236] B. Vignolle, A. Carrington, R. A. Cooper, M. M. J. French, A. P. Mackenzie, C. Jaudet, D. Vignolles, Cyril Proust, and N. E. Hussey. Quantum oscillations in an overdoped high-tc superconductor. *Nature*, 455(7215):952–955, 10 2008.

[237] Baptiste Vignolle, David Vignolles, Marc-Henri Julien, and Cyril Proust. From quantum oscillations to charge order in high- copper oxides in high magnetic fields. *Comptes Rendus Physique*, 14(1):39 – 52, 2013. Physics in High Magnetic Fields / Physique en champ magnétique intense.

[238] I. M. Vishik, M. Hashimoto, Rui-Hua He, Wei-Sheng Lee, Felix Schmitt, Donghui Lu, R. G. Moore, C. Zhang, W. Meevasana, T. Sasagawa, S. Uchida, Kazuhiro Fujita, S. Ishida, M. Ishikado, Yoshiyuki Yoshida, Hiroshi Eisaki, Zahid Hussain, Thomas P. Devereaux, and Zhi-Xun Shen. Phase competition in trisected superconducting dome. *Proceedings of the National Academy of Sciences*, 109(45):18332–18337, 2012.

[239] Matthias Vojta. Lattice symmetry breaking in cuprate superconductors: stripes, nematics, and superconductivity. *Advances in Physics*, 58(6):699–820, 2009.

[240] Matthias Vojta. Stripes and electronic quasiparticles in the pseudogap state of cuprate superconductors. *Physica C: Supercon.*, 481(0):178–188, 2012.

[241] Matthias Vojta and Oliver Rösch. Superconducting d-wave stripes in cuprates: Valence bond order coexisting with nodal quasiparticles. *Phys. Rev. B*, 77:094504, Mar 2008.

[242] P. Walmsley, C. Putzke, L. Malone, I. Guillamón, D. Vignolles, C. Proust, S. Badoux, A. I. Coldea, M. D. Watson, S. Kasahara, Y. Mizukami, T. Shibauchi, Y. Matsuda, and A. Carrington. Quasiparticle Mass Enhancement Close to the Quantum Critical Point in $BaFe_2(As_{1-x}P_x)_2$. *Phys. Rev. Lett.*, 110:257002, Jun 2013.

[243] Yuxuan Wang and Andrey Chubukov. Charge-density-wave order with momentum $(2q, 0)$ and $(0, 2q)$ within the spin-fermion model: Continuous and discrete symmetry breaking, preemptive composite order, and relation to pseudogap in hole-doped cuprates. *Phys. Rev. B*, 90:035149, Jul 2014.

[244] X. G. Wen. Mean-field theory of spin-liquid states with finite energy gap and topological orders. *Phys. Rev. B*, 44:2664–2672, Aug 1991.

[245] Xiao-Gang Wen and Patrick A. Lee. Theory of underdoped cuprates. *Phys. Rev. Lett.*, 76:503–506, Jan 1996.

[246] Kenneth G. Wilson and J. Kogut. The renormalization group and the ϵ expansion. *Physics Reports*, 12(2):75 – 199, 1974.

[247] J. Wu, Q. Si, and E. Abrahams. Magnetic and Ising quantum phase transitions in a model for isoelectronically tuned iron pnictides. *ArXiv e-prints*, June 2014.

[248] Tao Wu, Hadrien Mayaffre, Steffen Kramer, Mladen Horvatic, Claude Berthier, W. N. Hardy, Ruixing Liang, D. A. Bonn, and Marc-Henri Julien. Magnetic-field-induced charge-stripe order in the high-temperature superconductor $YBa_2Cu_3O_y$. *Nature*, 477(7363):191–194, 09 2011.

[249] Tao Wu, Hadrien Mayaffre, Steffen Krämer, Mladen Horvatić, Claude Berthier, Philip L. Kuhns, Arneil P. Reyes, Ruixing Liang, W. N. Hardy, D. A. Bonn, and Marc-Henri Julien. Emergence of charge order from the vortex state of a high-temperature superconductor. *Nat Commun*, 4, 07 2013.

[250] Jing Xia, Elizabeth Schemm, G. Deutscher, S. A. Kivelson, D. A. Bonn, W. N. Hardy, R. Liang, W. Siemons, G. Koster, M. M. Fejer, and A. Kapitulnik. Polar kerr-effect measurements of the high-temperature $yba_2cu_3o_{6+x}$ superconductor: Evidence for broken symmetry near the pseudogap temperature. *Phys. Rev. Lett.*, 100:127002, Mar 2008.

[251] Cenke Xu, Markus Müller, and Subir Sachdev. Ising and spin orders in the iron-based superconductors. *Phys. Rev. B*, 78:020501, Jul 2008.

[252] H. B. Yang, J. D. Rameau, P. D. Johnson, T. Valla, A. Tsvelik, and G. D. Gu. Emergence of preformed Cooper pairs from the doped Mott insulating state in $Bi_2Sr_2CaCu_2O_{8+\delta}$. *Nature*, 456(7218):77–80, 11 2008.

[253] H.-B. Yang, J. D. Rameau, Z.-H. Pan, G. D. Gu, P. D. Johnson, H. Claus, D. G. Hinks, and T. E. Kidd. Reconstructed Fermi Surface of Underdoped $B_2Sr_2CaCu_2O_{8+\delta}$ Cuprate Superconductors. *Phys. Rev. Lett.*, 107:047003, Jul 2011.

[254] Kai-Yu Yang, T. M. Rice, and Fu-Chun Zhang. Phenomenological theory of the pseudogap state. *Phys. Rev. B*, 73:174501, May 2006.

[255] Ming Yi, Donghui Lu, Jiun-Haw Chu, James G. Analytis, Adam P. Sorini, Alexander F. Kemper, Brian Moritz, Sung-Kwan Mo, Rob G. Moore, Makoto Hashimoto, Wei-Sheng Lee, Zahid Hussain, Thomas P. Devereaux, Ian R. Fisher, and Zhi-Xun Shen. Symmetry-breaking orbital anisotropy observed for detwinned $Ba(Fe_{1-x}Co_x)_2As_2$ above the spin density wave transition. *Proceedings of the National Academy of Sciences*, 108(17):6878–6883, 2011.

[256] J. J. Ying, X. F. Wang, T. Wu, Z. J. Xiang, R. H. Liu, Y. J. Yan, A. F. Wang, M. Zhang, G. J. Ye, P. Cheng, J. P. Hu, and X. H. Chen. Measurements of the anisotropic in-plane resistivity of underdoped feas-based pnictide superconductors. *Phys. Rev. Lett.*, 107:067001, Aug 2011.

[257] H. Q. Yuan, F. M. Grosche, M. Deppe, G. Sparn, C. Geibel, and F. Steglich. Non-Fermi Liquid States in the Pressurized $CeCu_2(Si_{1-x}Ge_x)_2$ System: Two Critical Points. *Phys. Rev. Lett.*, 96:047008, Feb 2006.

[258] L. Zhang and J.-W. Mei. Reconstructed Fermi surface and quantum oscillation of doped resonating valence bond state with incommensurate charge order in underdoped cuprates. *ArXiv e-prints*, August 2014.

[259] Shou-Cheng Zhang. A unified theory based on so(5) symmetry of superconductivity and antiferromagnetism. *Science*, 275(5303):1089–1096, 1997.

[260] Y. Zhang, A. V. Maharaj, and S. Kivelson. Are there quantum oscillations in an incommensurate charge density wave? *ArXiv e-prints*, October 2014.

[261] Y. Zhang, Z. R. Ye, Q. Q. Ge, F. Chen, Juan Jiang, M. Xu, B. P. Xie, and D. L. Feng. Nodal superconducting-gap structure in ferropnictide superconductor $BaFe_2(As_{0.7}P_{0.3})_2$. *Nat Phys*, 8(5):371–375, 05 2012.

[262] J. Zinn-Justin. *Quantum Field Theory and Critical Phenomena*. Clarendon Press, Oxford, 2001.